

**DEVELOPMENT OF *IN VITRO* SCREENING
APPROACHES TO OPTIMISE FORMULATION
PERFORMANCE.**

ANDRZEJ GALLAS, mgr farm.

**Thesis submitted to the University of Nottingham
for the degree of Doctor of Philosophy.**

September 2013

Abstract.

The pharmaceutical industry has been criticised for a lack of innovation associated with the drug discovery and development process, for example when compared with the computer or music industries. In fact, bringing a new medicine to the market requires, on average, the screening of up to 10 000 molecules, an expense in the range of \$500 million-\$2 billion and roughly 10-15 years of research. Such a situation not only has a direct impact on the health and life expectancy of every single human being on the planet, but also indicates that alternative strategies for drug development should be investigated.

In this thesis, studies of direct formulation-membrane interactions, both in a high throughput (HT) manner and at a nanometre scale, were initially identified as an important approach that could offer advantages for *in vitro-in vivo* correlations of in-man drug behaviours. Subsequently, supported lipid bilayers (SLBs) of physiologically-relevant lipid compositions were indicated as experimental models of preference for pre-clinical drug development. For that reason, the characterisation and assessment of physicochemical and behavioural properties of the model SLBs at a nanometre scale, as well as development of an SLB microarray for HT applications were the focus of this research. Here, the optimisation and characterisation of model lipid films was performed using atomic force microscopy (AFM), time-of-flight secondary ion mass spectrometry (ToF-SIMS) and X-ray photoelectron spectroscopy (XPS). Additionally, the AFM-investigated assessment of the interactions between model SLBs and formulation components (*e.g.* Pluronic[®], siRNA, DNA polyplexes) enabled both the correlation of *in vitro* observations with literature-reported *in vivo* performances of the components of interest and the development of hypotheses with regards a number of phenomena in biology. Furthermore, the development of a SLB microarray prototype suitable for HT applications is reported.

Directly, this research improves: the understanding of SLB behaviours and experimental investigation at a nanometre scale of the mechanisms of interactions between membranes and: Pluronic[®], nucleic acids and their complexes, as well as the technology of SLB microarray development. Indirectly, this research contributes towards the progress in a number of research areas within pharmaceutical sciences, potentially resulting in new scientific disciplines, such as immunolipidomics or nanopharmacology.

Acknowledgements.

I would like to thank EPSRC, AstraZeneca and University of Nottingham for funding.

I would like to thank my supervisors: Dr Stephanie Allen, Prof. Cameron Alexander, Prof. Morgan Alexander, Prof. Martyn Davies and Dr Sanyogitta Puri for help and guidance throughout the project.

I would like to thank Prof. Xinyong Chen, Dr David Scurr, Mrs Emily Smith, Dr Andrew Hook, Dr Adam Celiz, Dr Francisco Fernandez-Trillo and other members of the Laboratory of Biophysics and Surface Analysis and the Drug Delivery groups for advice and hands-on help in laboratory.

Mamo, Tato, Haniu, Leszku, babciu Zosiu i Mirciu, dziadku Stasiu i Jurku – serdecznie dziękuję za wsparcie, pomoc i wszystko co umożliwiło mi zrobienie tego doktoratu.

I would also like to thank Mrs Christine Grainger-Boulton, Mr Paul Cooling, Mrs Julia Crouch, Dr Christina Grindon and Dr Claudia Matz for technical support during my PhD.

I would particularly like to thank Sarah, Gökçen, Vanessa, Marek, Alim, Selina and Beppe for friendship and support throughout my time in Nottingham.

Finally, I would like thank my assessors: Prof. Clive Roberts and Dr Patrick Gunning for feedback and time they spent on improving this thesis.

Andrzej Gallas.

List of Contents.

Title Page.....	1
Abstract.....	2
Acknowledgements.....	3
List of Contents.....	4
List of Figures.....	7
List of Tables.....	10
Preface.....	11

1 Chapter 1: Introduction and Aims.

Supported lipid bilayers as models for pre-clinical development of new drugs.....	12
1.1. Abstract.....	12
1.2. Introduction.....	13
1.3. The importance of membrane interactions in pharmaceutical sciences.....	14
1.4. Models for membrane interactions: development and types.....	17
1.5. SLBs as a model for membrane interactions.....	21
1.6. Current limitations associated with SLBs.....	26
1.7. Conclusions and future prospects.....	27
1.8. References.....	30

2 Chapter 2: Materials and Methods.

2.1. Materials.....	33
2.2. Methods.....	36
2.2.1. Preparation of supported lipid bilayers.....	36
2.2.1.1. Calculation of lipid amounts for liposome preparation.....	36
2.2.1.2. Bilayer self-spreading technique (BSST).....	36
2.2.1.3. Vesicle deposition technique (VDT).....	36
2.2.2. Atomic Force Microscopy (AFM)	37
2.2.2.1. Background.....	37
2.2.2.2. Experimental.....	38
2.2.2.2.1. Basic SLB imaging (chapter 3 and 4).....	38
2.2.2.2.2. SLB interaction studies (chapter 5).....	38
2.2.2.2.3. SLB air stability studies (chapter 1 and 6)	39
2.2.2.2.4. SLB microarray imaging (chapter 6)	39
2.2.2.2.5. Imaging of Polyphosphonium-DNA polyplexes (chapter 5)	39
2.2.2.2.6. Preparation and imaging of FluidArray®-like surfaces (chapter 6)	40
2.2.2.2.7. AFM data analysis.....	40
2.2.2.2.7.1. Evaluation of SLB thickness.....	40
2.2.2.2.7.2. Quantification of SLB coverage.....	41
2.2.2.2.7.3. Evaluation of particle size.....	41
2.2.3. Time-of-Flight Secondary Ion Mass Spectrometry (ToF-SIMS).....	41
2.2.3.1. Background.....	41
2.2.3.2. Experimental.....	42
2.2.3.3. ToF-SIMS: data analysis.....	42
2.2.4. X-ray Photoelectron Spectroscopy (XPS).....	43
2.2.4.1. Background.....	43
2.2.4.2. Experimental.....	44
2.2.4.2.1. XPS: sample preparation.....	44
2.2.4.2.2. XPS: data analysis.....	45
2.2.4.2.2.1. Calculation of the theoretical lipid content and ratio between: -N ⁺ (CH ₃), =N ⁺ (H ₂) and -NH- nitrogen groups for lipid film samples analysed with XPS in the N1s region.....	46
2.2.4.2.2.2. Calculation of theoretical intensity of the P2p peak for lipid film samples analysed with XPS in the P2p region.....	47
2.2.5. Dynamic Light Scattering (DLS).....	47
2.2.5.1. Background.....	47

List of Contents.

2.2.5.2.	Experimental.....	48
2.2.5.2.1.	DLS: sample preparation.....	48
2.2.5.2.2.	DLS: data analysis.....	48
2.2.6.	Piezoelectric inkjet print head technology.....	48
2.2.6.1.	Background.....	48
2.2.6.2.	Experimental.....	49
2.2.7.	Preparation of Pluronic® solutions (chapter 4 and 6).....	50
2.2.8.	Preparation of DNA complexes (chapter 5).....	50
2.2.9.	Preparation of text and figures.....	51
2.3.	References.....	51

3 Chapter 3: Fabrication and Characterisation of Model SLBs.

Advanced surface analysis techniques for the development of a supported lipid bilayer model.....

	53
3.1	Abstract.....	53
3.2	Introduction.....	54
3.3	Materials and Methods.....	54
3.4	Results and Discussion.....	55
3.4.1	Studying SLB morphology and composition.....	55
3.4.1.1	AFM: optimisation of model SLB fabrication protocols.....	55
3.4.1.2	ToF-SIMS: qualitative and semi-quantitative evaluation of model lipid films.....	57
3.4.1.3	XPS: quantitative evaluation of model lipid films.....	62
3.4.2	AFM: studying SLB behaviour.	71
3.5	Conclusion.....	79
3.6	References.....	79

4 Chapter 4: Model SLBs-Excipient Interaction Studies.

Supported lipid bilayers to aid understanding of pharmaceutical excipient performances *in vitro*.....

	81
4.1	Abstract.....	81
4.2	Introduction.....	82
4.3	Materials and Methods.....	82
4.4	Results and Discussion.....	83
4.5	Conclusion.....	93
4.6	References.....	93

5 Chapter 5: Model SLBs-Nucleic Acid Formulation Interaction Studies.

Supported lipid bilayers: stop-change in nucleic acid pharmacology.....

	94
5.1	Abstract.....	94
5.2	Introduction.....	95
5.3	Materials and Methods.....	96
5.4	Results and Discussion.....	96
5.4.1	Nucleic acid-SLB interactions.....	96
5.4.2	DNA polyplex-SLB interactions.....	106
5.5	Conclusion.....	111
5.6	References.....	112

6 Chapter 6: Development of SLB Microarray for Nano-HTS Applications.

Development of supported lipid bilayer microarray for high throughput screening applications at nanoscale.....

	114
6.1	Abstract.....	114
6.2	Introduction.....	115

List of Contents.

6.3	Materials and Methods.....	115
6.4	Results and Discussion.....	116
6.4.1	Optimisation of SLB fabrication method on microscope slide-sized mica sheets.....	116
6.4.2	AFM studies of dry, model SLBs in high humidity environments.....	119
6.4.3	Optimisation of the piezoelectric inkjet printing methodology for SLB microarray development.....	122
6.4.4	Optimisation of the ToF-SIMS chemical imaging of the SLB microarrays.....	126
6.5	Conclusion.....	131
6.6	References.....	132
	Chapter 7: Concluding Remarks and Future Prospects.....	133
	References.....	136
	Appendix I: Analysis of AFM Images.....	137
	Appendix II: Supporting Information on AFM Studies.....	145
	Appendix III: Molecular Ion Assignments for ToF-SIMS Spectra of Single Lipids.....	154
	Appendix IV: Chemistry and Formulations for siRNA therapeutics.....	165

List of Figures.

1. Chapter 1: Introduction and Aims.	
1.1. The graphical summary of the factors involved in the development of the supported lipid bilayer (SLB)-based model for studying formulation-membrane interactions.....	12
1.2. Illustration depicting the importance of interactions between drugs (or formulations) and membranes (or lipids) in pharmaceutical sciences.....	15
1.3. Graphical summary of the factors involved in the development of the Parallel Artificial Membrane Permeability Assay (PAMPA).....	17
1.4. Strategies providing air stability for SLBs.....	27
2. Chapter 2: Materials and Methods.	
2.1. The chemical structures of lipids, PEO-PPO-PEO (Pluronic) tri-block co-polymers and 19bp DNA strand.....	35
2.2. The schematic of AFM operation principle.....	38
2.3. The schematic of ToF-SIMS operation principle.....	42
2.4. The schematic of XPS operation principle.....	44
2.5. The schematic of DLS operation principle.....	48
2.6. The schematic of piezoelectric inkjet print head technology operation principle.....	49
3. Chapter 3: Fabrication and Characterisation of Model SLBs.	
3.1. Graphic indicating the nature of studies discussed in chapter 3.....	53
3.2. AFM images of BSST-fabricated model SLBs and VDT-fabricated model lipid films.....	56
3.3. ToF-SIMS spectra for mica and both model lipid film samples in the 0 – 300 u mass regions.....	57
3.4. The ToF-SIMS chemical images presenting the spatial distributions of single lipid-representative peaks within the model lipid film samples.....	60
3.5. Graphs presenting the semi-quantitative evaluation of single lipid-representative peak intensities within the ToF-SIMS spectra of the model lipid films in both positive and negative modes.....	61
3.6. Wide-scan XPS spectra indicating the elemental compositions of the solid support (MICA) and two model lipid film (BSST, VDT) samples.....	62
3.7. The graph and equation depicting the calculations of the lipid film coverage for both model lipid film samples prepared using vesicle deposition (VDT) and bilayer self-spreading (BSST) techniques.....	64
3.8. XPS spectra in the N1s region indicating the peaks associated with the presence of nitrogen on the solid support (MICA), egg-phosphatidyl choline (EPC), sphingomyelin (SPM), cholesterol (CHOL), dioleoylphosphatidyl ethanolamine (DOPE), dioleoylphosphatidyl serine (DOPS) and two model lipid film (BSST, VDT) samples.....	66
3.9. The graph indicating the XPS spectra in the N1s region for mica, single lipid and model lipid film samples.....	67
3.10. XPS spectra in the P2p region indicating the peaks associated with the presence of phosphorous on the solid support (MICA), egg-phosphatidyl choline (EPC), sphingomyelin (SPM), cholesterol (CHOL), dioleoylphosphatidyl ethanolamine (DOPE), dioleoylphosphatidyl serine (DOPS) and two model lipid film (BSST, VDT) samples.....	69
3.11. AFM images presenting the instances of phase separation occurrence within the model SLBs.....	72
3.12. The chemical structure of cholesterol (CHOL).....	73
3.13. The chemical structures of ionic and non-ionic mesomers of sphingomyelin (SPM).....	74
3.14. Illustration of the 'sphingomyelin (SPM) trap' hypothesis.....	75
3.15. The chemical and three-dimensional structures of DNA - deoxyribonucleic acid and RNA - ribonucleic acid molecules.....	77
4. Chapter 4: Model SLB-Excipient Interaction Studies.	
4.1. Graphical abstract indicating the experimental focus of chapter 4.....	81
4.2. AFM images presenting steps of the interactions between model SLBs of different bilayer qualities and Pluronic® L-62 monitored over time.....	84

List of Figures.

4.3.	AFM images presenting steps of interactions between model SLBs of different bilayer qualities and Pluronic® L-64 monitored over time.....	85
4.4.	AFM images presenting steps of interactions between model SLBs of different bilayer qualities and Pluronic® F-68 monitored over time.....	86
4.5.	Schematic illustration of two basic pore types in a lipid bilayer: hydrophilic and hydrophobic.....	87
4.6.	The graph presenting the changes of the coverage for patch-like, model SLBs over time, after exposure to 0.001% (w/v) Pluronics®: L-62, L-64 and F-68 in PBS.....	88
4.7.	The graph presenting changes of the coverage of porous, model SLBs over time, after exposure to 0.0001% (w/v) Pluronics®: L-62, L-64 and F-68 in PBS.....	90
4.8.	Schematic illustration of possible interaction mechanism between phase separated SLBs and Pluronics® of different polyethylene oxide block content.....	92
5. <u>Chapter 5: Model SLB-Nucleic Acid Formulation Interaction Studies.</u>		
5.1.	Graphical abstract depicting the spontaneous formation of DNA/sphingomyelin/cholesterol (DNA/SPM/CHOL) lipoplexes.....	94
5.2.	The AFM images and graphs presenting the qualitative and quantitative changes to the uniform, model SLBs: before and after exposure to a 2.5 µg/ml DNA solution.....	97
5.3.	The AFM images and the analysis of L ₀ domain thickness throughout the interaction of the model SLB and 5 µg/ml DNA, indicating three phases.....	98
5.4.	The AFM images and graphs presenting the qualitative and quantitative changes to the non-phase separated, model SLBs over time after exposure to: 5, 10, 62 [µg/ml] DNA solutions.....	100
5.5.	Graphs illustrating the quantitative relationship: DNA concentration vs. the increases of SLB coverage over time.....	100
5.6.	The illustration of the key steps of the interaction between DNA and a model SLB.....	102
5.7.	The illustration of the siRNA-cell interaction mechanism based on the AFM-observed 19bp DNA-model SLB interaction.....	104
5.8.	An illustration indicating the directions for future research as an implication of the spontaneous DNA-sphingomyelin-cholesterol (DNA/SPM/CHOL) lipoplex formation phenomenon.....	106
5.9.	The illustration of a polyphosphonium polyplex with 19-bp DNA (right) and the chemical structure of PPP - phosphonium polymer.....	107
5.10.	AFM images presenting the changes in the behaviour of the non-phase separated, model SLBs after exposure to: 5 (A), 10 (B), 50 (C) [µgDNA/ml] polyphosphonium polyplexes with 19-bp DNA and 90 µg/ml phosphonium polymer solutions (D).....	108
5.11.	The graphs illustrating the quantitative relationship: DNA concentration vs. the increases of SLB coverage over time for the model SLB-polyphosphonium DNA polyplex interactions.....	109
5.12.	The illustration of the anticipated cell transfection mechanism for polyphosphonium-DNA polyplexes.....	111
6. <u>Chapter 6: Development of SLB Microarray for Nano-HTS Applications.</u>		
6.1.	Graphical abstract indicating the supported lipid bilayer (SLB) microarray approach that has been studied in chapter 6.....	114
6.2.	The graphics and AFM images presenting the engineering approaches for the optimisation of mica sheet preparation before the exposure to lipid material and lipid film morphologies recorded for both approaches, respectively.....	118
6.3.	AFM images indicating the behaviour of model SLBs once the liquid excess has been removed from the surface at three different relative humidity (RH) values: ~25 %, ~50 % and ~70 %.....	122
6.4.	The optical image of an AFM probe approaching the liquid-excess-free, SLB-coated mica surface incubated in a ~70% relative humidity environment at RT.....	123

List of Figures.

6.5.	Optical images presenting ink-jet printed spots on mica sheets surfaces incubated at 70% relative humidity and 28°C temperature of the sample stage.....	125
6.6.	The Illustration presenting ToF-SIMS chemical images that have been collected from glass slide-attached mica sheets of tilted surface topography.....	127
6.7.	ToF-SIMS images of an SLB-Pluronic® interaction in a microarray format.....	128
6.8.	AFM images and illustration depicting the FluidArray® surface-based preliminary studies.....	130

List of Tables.

Chapter 1: Introduction and Aims.

1.1	Examples of drug-membrane interactions of clinical importance.....	16
1.2	Examples of <i>in silico</i> , <i>in vitro</i> and <i>in vivo</i> models in pre-clinical drug development.....	19
1.3	Experimental and theoretical models for studying drug-membrane interactions.....	20
1.4	Comparison of cell membranes and supported lipid films.....	22
1.5	Key techniques employed for SLB characterisation studies.....	23
1.6	Examples demonstrating alterability of SLB properties.....	23
1.7	Key techniques used to fabricate SLBs.....	25

Chapter 3: Fabrication and Characterisation of Model SLBs.

3.1	The single lipid-representative peaks within the ToF-SIMS C ₆₀ spectra of model lipid films.....	59
3.2	The XPS-measured lipid content ratios within the model lipids films.....	68

Chapter 4: Model SLBs-Excipient Interaction Studies.

4.1	The physicochemical and cell viability parameters for the representative Pluronics®.....	83
-----	--	----

Preface.

Dear Reader,

First of all, thank you for having a look at my thesis. Hopefully, you will manage to find something useful.

You are about to read a thesis that summarises 3 years of laboratory-based work of a candidate for a PhD in pharmacy.

Since pharmacy is a fairly broad science discipline, the overall aim throughout writing this thesis was to present data, conclusions and hypotheses as clearly, and as concisely, as possible. For that reason, special attention was divided to figures depicting discussions in text. Also, since this PhD project underpinned many scientific disciplines, introductions and descriptions regarding some of the theoretical background were kept to the minimum. In my opinion, this would help to both achieve an appropriate flow of the text and prevent you from falling asleep. I consider these as factors detrimental to the overall scientific focus that is required for reading.

As the English language is not my mother tongue, I have also tried to express thoughts in a logical manner, keeping the sentences short, wherever possible. However, I understand that some expressions may sound a bit unfamiliar to a native speaker. Therefore, I encourage you to direct all questions that you may have to me via email.

Although I spent a significant amount of time editing the text in order to avoid errors, I anticipate that it could be further improved. Nevertheless, it is my hope that the quality of this thesis would enable you to understand: what I was working on, how I have achieved it and why it was important from a pharmacy point of view.

I look forward to helping you with any questions that may arise and I sincerely hope that you will find this thesis useful.

Kind regards,

Andrzej Gallas

email: andrzej.gallas@gmail.com

Supported lipid bilayers as models for the pre-clinical development of new drugs.

1.1 Abstract

The currently employed *in vitro-in vivo* correlation methodologies often fail to fully elucidate the in-man toxicity and efficacy of a drug. This results in an inefficient, expensive and time consuming drug discovery and development process, and hence the need for predictive *in vitro* screening approaches to facilitate such correlations is an urgent priority. The interactions between active pharmaceutical ingredients (APIs) and biological membranes had repeatedly been demonstrated to be able to elucidate the mechanisms behind toxicities, modes of action, as well as pharmacokinetic properties of drugs. Therefore, it is anticipated that approaches enabling high throughput screening of API-membrane interactions may provide a useful platform for the prediction of *in vivo* performance of new chemical entities (NCE) at an early development stage.

In this chapter, the importance of drug-membrane interactions and *in vitro-in vivo* correlation models are briefly overviewed. The properties of various *in vitro* models involving lipid-based systems are assessed for their potential to be used to screen API-membrane interactions. Particular focus is directed toward the advantages and limitations of supported lipid bilayers (SLBs), as emerging tools for investigations of drug-membrane interactions. To conclude, achievable goals and directions for the future work are outlined. Additionally, aims of this thesis are explained.

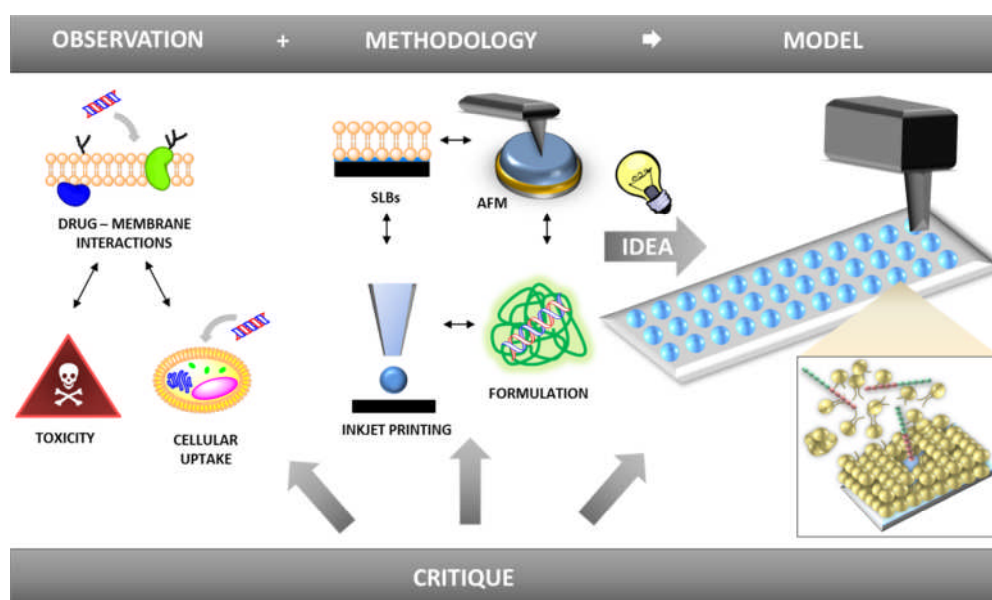


Figure 1.1. A graphical summary of the factors involved in the development of the supported lipid bilayer (SLB)-based model for studying formulation-membrane interactions. Since drug-membrane interactions have been correlated with toxicity and efficacy of a drug, combining automated liquid dispensing systems (ink-jet printing) with advanced surface analysis techniques (AFM – atomic force microscopy) and SLBs as membrane models, may provide a useful approach to study *in vitro* formulation performance both in a high throughput manner and at a nanometre scale. Details have been reviewed in chapter 1.

Abbreviations:

3R- replacement, reduction, refinement; ADME – absorption, distribution, metabolism, elimination; AFM – atomic force microscopy; API – active pharmaceutical ingredient; CYP-450 – cytochrome P-450; D – distribution; GFP – green fluorescent protein; HTS – high throughput screening; P – partition; PAMPA – parallel artificial permeability assay; PKPD – pharmacokinetics and pharmacodynamics; PBS – phosphate buffer saline; QbD – quality by design; MDR – multidrug resistance; NCE – new chemical entity PEG – polyethylene glycol; RH – relative humidity; SLB – supported lipid bilayer; SPBs – supported phospholipid bilayers; SUV – small unilamellar vesicle; tBLMs – tethered bilayer lipid membranes; ToF-SIMS – time-of-flight secondary ion mass spectrometry; XPS – X-ray photoelectron spectroscopy.

1.2 Introduction

Although correlating the clinical performance of pharmaceutical formulations with their behaviour *in vitro* has been a research focus for many years, it remains a significant challenge¹. As a result, bringing a new medicine to market requires, on average, the screening of up to 10 000 molecules², an expense in the range of \$500 million - \$2 billion³ and roughly 10-15 years⁴ of research, directly affecting the health and life expectancy of every single human being on the planet.

Since the unpredicted toxicity and the targeted delivery of APIs have emerged as the key obstacles for the development of new medicines⁵, the need for scientific model(s) enabling *in vitro-in vivo* correlations for both of these issues has become an urgent priority⁶. Here, studies on direct interactions between cellular membranes and pharmaceutical formulations had been repeatedly demonstrated to provide scientific explanation for clinically observed drug behaviours⁷.

In this chapter, the importance of drug-membrane interactions and the theory of scientific model development are briefly reviewed. Subsequently, the literature-reported models for studying drug-membrane interactions are investigated. A particular focus is directed at supported lipid bilayers (SLBs) as emerging tools for the drug-membrane interaction studies. Both the advantages and limitations are thoroughly examined. To conclude, the directions for further research are considered.

The development of a screening model that enables correlation of the *in vitro* behaviour of pharmaceuticals with their performance *in vivo* would have a direct impact on the time and expense associated with the discovery and development of drugs, as well as on the replacement, reduction and refinement (3Rs) of animal model use in the pharmaceutical sciences. Additionally, an improved understanding of drug-membrane interaction

mechanisms would benefit the rational design of new APIs, not only impacting on quality by design (QbD) approaches in drug development, but also increasing the efficiency of bringing therapeutics to the market.

1.3 The importance of membrane interactions in pharmaceutical sciences.

The interaction of drugs (or formulations) with membranes is important for many aspects of drug development as thoroughly reviewed in ref.8. Briefly, APIs interact with membranes at all pharmacokinetic stages: absorption, distribution, metabolism and elimination (ADME). During drug absorption *e.g.* from intestines into the bloodstream, APIs have to permeate through a set of membranes associated with intestinal cells, as well as blood vessels before they reach blood or lymph⁸. Once in the blood or lymph, APIs can be distributed into its effector (*e.g.* organ, tissue, cell), metabolism (*e.g.* liver) or elimination (*e.g.* kidneys) sites. In each case, before the APIs reach the molecular targets, undergo CYP-450-catalysed metabolism or are excreted with urine, they must yet again overcome a few membrane barriers *en route*, *for instance*: epithelial cells of the blood vessels (*e.g.* blood brain barrier if targeted against the central nervous system), cytoplasmic membranes of the destination cells in order to reach an intracellular target or intracellular CYP-450 enzymes, as well as membranes associated with elimination processes (*e.g.* ultrafiltration, secretion and reabsorption of the drug). In addition, drug release may be affected by interactions with lipids *e.g.* in gastrointestinal fluid, foods or lipid-based formulations indicating the role at the drug liberation stage. Pharmacodynamically, drug-membrane interactions are essential for a detailed understanding of the processes triggered by the APIs at their active sites, such as modes of action, mechanisms of multidrug resistance (MDR), drug transport into or within the cell cytoplasm, as well as toxicity (immunogenicity) of drugs or excipients^{7a}. Figure 1.2 and table 1.1 summarise those considerations and indicate some examples of drug membrane interactions of pharmacological importance. Without a doubt, a detailed understanding of the drug-membrane interactions in various microenvironments is essential in order to uncover drug behaviour *in vivo*.

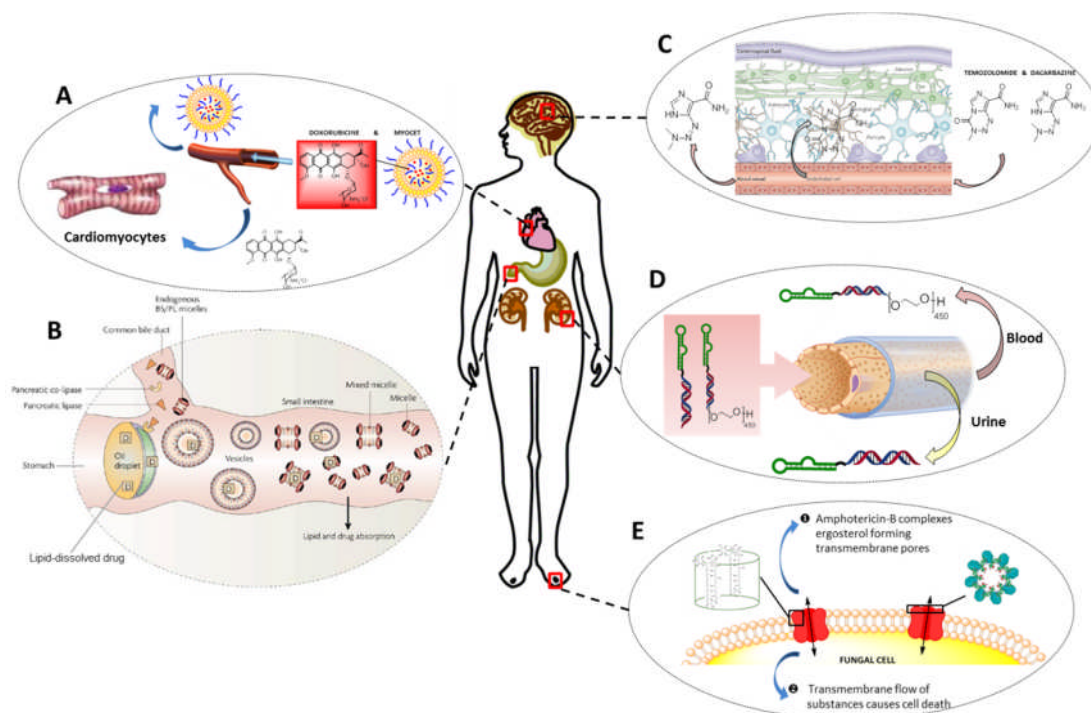
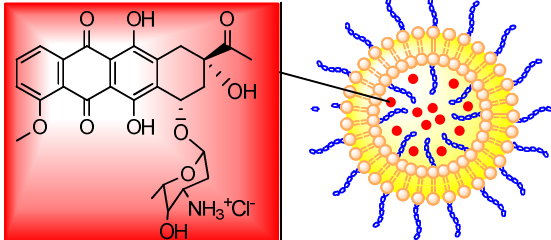
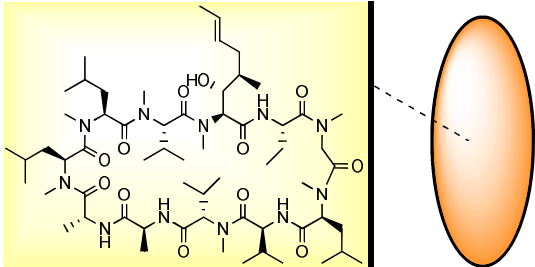
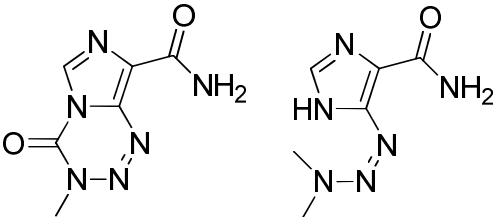
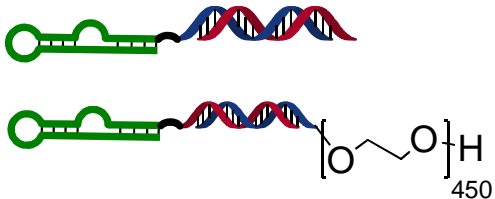
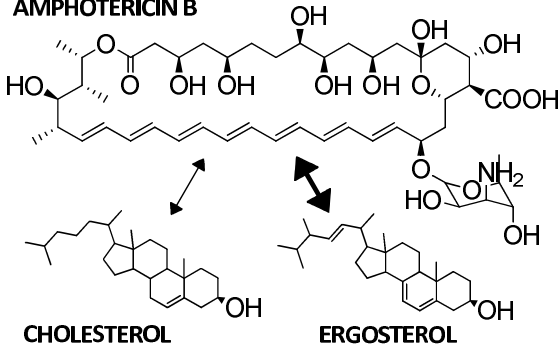


Figure 1.2. Illustration depicting the importance of interactions between drugs (or formulations) and membranes (or lipids) in pharmaceutical sciences. The drug release into and absorption from the gastrointestinal fluid is strongly affected by the bile-triggered fat emulsification for lipid-based formulations (B). Small changes in chemical structure can influence the distribution of a drug across the blood-brain barrier (C) or the elimination of a drug with urine through the fenestrations in kidney capillaries (D). Liposome encapsulation of doxorubicin prevents direct binding of the drug with membranes of various organs decreasing the overall toxicity (A). Drug-membrane interactions can also elucidate modes of action for many therapeutics, such as anti-fungal medicines (E). More details can be found in table 1.1. Figure elements adapted from the following references: ⁸⁻⁹.

Table 1.1 | Examples of drug-membrane interactions of clinical importance.

Name and structure		Interaction
<p>DOXORUBICIN & MYOCET</p>  <p>The image shows the chemical structure of Doxorubicin on the left, which is a tetracyclic anthracycline. On the right, a diagram of Myocet liposomes is shown, consisting of a spherical bilayer of phospholipids with hydrophilic heads and hydrophobic tails, containing several Doxorubicin molecules (represented as red dots) encapsulated within.</p>	<p>Encapsulation of doxorubicin in liposomes not only limits the direct interaction with membranes, but also increases the effective size of the drug circulating in the human body. Thus, non-specific organ uptake and kidney elimination are lower for Myocet than for conventional doxorubicin and explains why the administration of Myocet results in lower cardiotoxicity, longer biological half-life and better targeting of leaky tumour tissue¹⁰.</p>	
<p>CYCLOSPORIN A & NEORAL CAPSULES</p>  <p>The image shows the complex cyclic peptide structure of Cyclosporin A on the left. On the right, a diagram of a Neoral capsule is shown, which is a lipid-based formulation used for oral administration.</p>	<p>Encapsulation of cyclosporin in a lipid-based formulation provides more consistent absorption from the intestines making it less variable across patients and less dependent on food and bile presence¹¹. Orally-administered lipid-based formulations affect drug liberation and absorption from intestines through three mechanisms: changes to the composition of intestinal milieu, recruitment of lymphatic drug transport and direct interactions with enterocyte-based drug absorption and metabolism.⁸</p>	
<p>TEMOZOLOMIDE & DACARBAZINE</p>  <p>The image shows the chemical structures of Temozolomide (left) and Dacarbazine (right). Both are pyrimidine derivatives, but Temozolomide has a methyl group at the 5-position and a methylamino group at the 2-position, while Dacarbazine has a methyl group at the 5-position and a methylamino group at the 4-position.</p>	<p>Temozolomide permeates well through the blood-brain barrier, while the chemically similar compound, dacarbazine¹², does not. Thus, temozolomide¹³ is used as a therapeutic for brain and dacarbazine for systemic tumours. This example indicates how small changes in chemical structure can affect the drug-membrane interactions, distribution and therefore therapeutic profile of a drug.</p>	
<p>Aptamer-siRNA chimeras</p>  <p>The diagram shows an aptamer-siRNA chimera. It consists of a green aptamer structure, a blue and red siRNA double-strand, and a polyethylene glycol (PEG) chain represented as a repeating unit of $[-O-CH_2-CH_2-O-]_n$ with a terminal hydrogen atom, where $n = 450$.</p>	<p>PEGylated siRNA-aptamer chimeras are less likely to undergo ultrafiltration through kidney membranes than non-PEGylated ones, resulting in a longer biological half-life ($t_{1/2}$). <i>In vivo</i> studies using mouse models revealed an increase from $t_{1/2} < 35$ min to $t_{1/2} > 30$ h for the non-PEG- and PEGylated systems, respectively⁵.</p>	
<p>AMPHOTERICIN B</p>  <p>The image shows the chemical structure of Amphotericin B, a polyene macrolide. Below it, two steroid structures are shown: Cholesterol (left) and Ergosterol (right). Arrows indicate the interaction of Amphotericin B with the hydroxyl group at the C3 position of the steroid ring system, which is more prominent in ergosterol than in cholesterol.</p>	<p>Since amphotericin B binds ergosterol in fungal cell membranes with higher affinity than cholesterol in human cell membranes, the destabilisation of fungal cell membranes is more likely. At the same time, a lower cholesterol binding affinity implicates the preferential interaction of amphotericin B with fungal cells over human cell membranes and justifies its low toxicity profile^{7a}.</p>	

1.4 Models for membrane interactions: development and types.

Since direct investigations of drug-membrane interactions are difficult in complex biological environments, such as within the human body, the development of experimental models has been an essential part of research in this field for many years^{7b}. By definition, the purpose of a model is the simplified representation of empirical phenomena, processes or objects, logically and objectively, using a number of different approaches and data sets. Unfortunately, due to the simplicity of scientific models, the inherent falsities, as well as scientific dispute (critique) are inseparable companions of both model development and applicability¹⁴. Figure 1.3 presents a successful model development using the Parallel Artificial Membrane Permeability Assay (PAMPA)¹⁵ as an example case study.

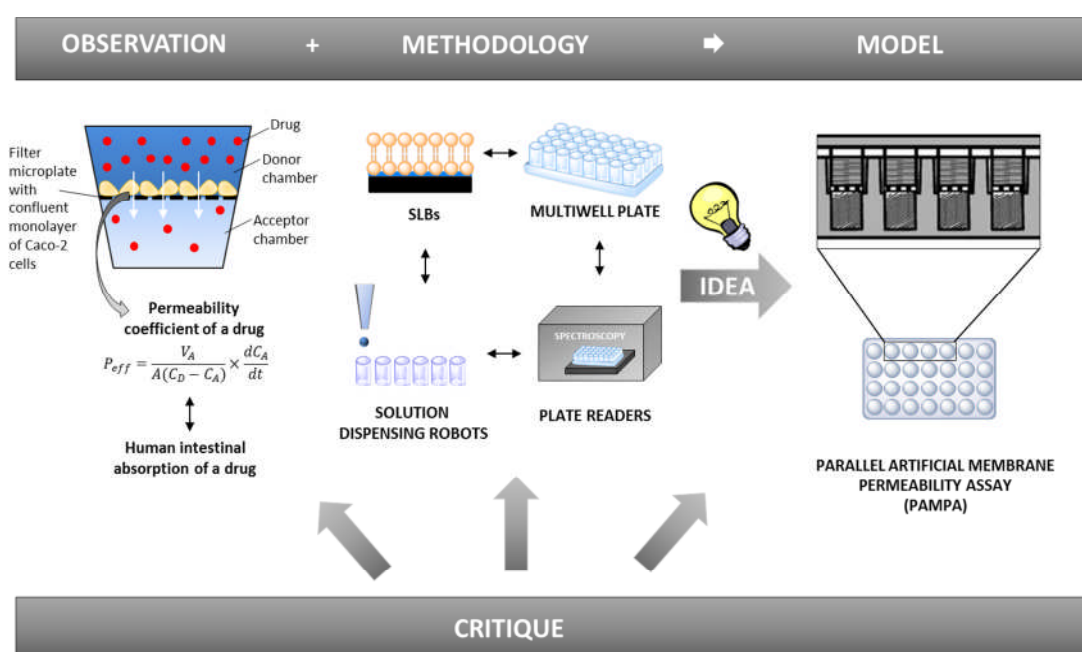


Figure 1.3. Graphical summary of the factors involved in the development of the Parallel Artificial Membrane Permeability Assay (PAMPA). The ability of Caco-2 cells to mimic intestinal drug absorption (left), supported lipid bilayer science (middle), as well as methods employed for high throughput screening approaches (middle) all contributed to the development of PAMPA¹⁶ in its current form (left). Additionally, scientific dispute (critique) had been indicated as an important constituent influencing PAMPA development at all stages. A figure element adapted from reference 24.

PAMPA is used as a method in pre-clinical drug development for predicting the passive permeability of drugs through a desired physiological barrier. Due to good biomimetic properties, reproducibility, low cost and high throughput design, PAMPA has now partially replaced Caco-2 assays (see table 1.2). However, as a simplified model, PAMPA is limited to predictions associated with passive drug diffusion and does not account for active or

paracellular transport mechanisms. For this reason, further developments on PAMPA are ongoing¹⁷.

Apart from PAMPA, pre-clinical drug development employs numerous approaches (models) integrating computational, chemical, physical and biological data sets in order to predict the drug behaviour *in vivo*. Table 1.2 lists a few examples of such models demonstrating that establishing *in vitro-in vivo* relationships through modelling is possible.

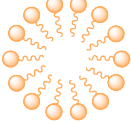
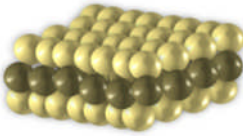
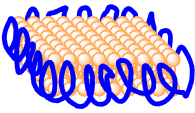
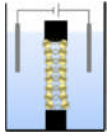
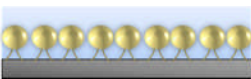
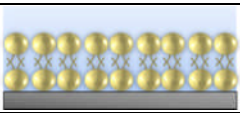
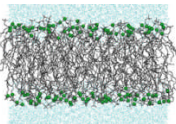
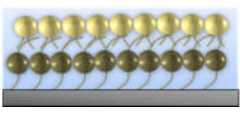
With regards the modelling of drug-membrane interactions, experimental or theoretical model development is focussed on phase separated systems, where one phase typically consists of a polar liquid (*e.g.* water, buffer) and the other, amphiphilic molecules (*e.g.* octanol, lipids)¹⁸. Key examples of systems that are employed to study such interactions are presented in table 1.3. As can be noted, the vast majority of these approaches focus on direct interactions between drugs and lipid bilayers, since both the chemical composition and double leaflet-type design are expected to mimic the cell membrane behaviours more closely. Apart from mimicking the membrane behaviour, an additional advantage of lipid bilayers as models is the potential to be enriched with other types of molecules (*e.g.* proteins¹⁹, carbohydrates²⁰) and thus used as tools for more complex interaction studies. In contrast the water/octanol system is limited to only partition and permeability studies. Out of all the lipid-based examples for drug-membrane interactions, supported lipid bilayers hold the highest potential as tools for *in vitro-in vivo* correlation studies, as discussed in the following section.

Table 1.2 | Examples of *in silico*, *in vitro* and *in vivo* models in pre-clinical drug development¹⁷.

	Model name	Brief description	Applications
<i>In silico</i>	In vitro – in vivo correlation (IVIVC)	Tool enabling the correlation between dissolution and pharmacokinetic parameters for a dosage form.	Predictions for human studies; support for validation of dissolution methods, formulation manufacturing and selection of appropriate dosage form.
	Physiologically Based Biokinetic (PBBK) modelling	Platform integrating <i>in vitro</i> drug metabolism data with physiological characteristics of various animal species and humans.	Predictions of dose- and specie-dependent pharmacokinetics of a drug; extrapolation of starting dose for human studies.
	Benchmark Dose (BMD) software	Software enabling expression of dose-response data as mathematical equations.	Establishment of drug dose, giving a standard response for animal and human studies.
	Quantitative structure-activity relationship (QSAR)	Tool relating structural or physicochemical properties of a molecule to the potency of its biological response as a mathematical expression.	Identification of chemical structures of the most potent activity and lowest toxicity, prediction of physicochemical parameters of a drug (<i>e.g.</i> logP, pKa), quantitative analysis of various interactions (<i>e.g.</i> drug-active site or between two protein domains)
<i>In vitro</i>	Fluorescent Cell Culture models for protein knockdown studies (GFP-, Luc-expressing cells)	Cells that are able to change the levels of fluorescence once exposed to siRNAs targeted against green fluorescent protein (GFP) or luciferase (Luc).	Assessment of siRNA formulation efficacy.
	Cell viability assays (MTS, MTT, XTT, WST)	Colorimetric assays measuring the amount of tetrazolium dye reduction in living cells after exposure to a xenobiotic.	Assessment of cytotoxicity profiles for different molecules.
	Cell Culture Models for drug permeability assessments (Caco-2, MDCK, LLC-PK1, HT-29, TC-7, IEC-18)	Confluent cell monolayer on a filter microplate separating two fluid chambers in a multiple well format. Concentrations of the drug moving from the top to the bottom chamber are recorded over time.	Modelling of human, intestinal drug absorption.
<i>In vivo</i>	Animal Models (rats, rabbits, dogs, monkeys)	Pharmacokinetic and pharmacodynamics (PKPD) testing of various aspects of drug behaviour <i>in vivo</i> .	Extrapolation of results to humans, <i>e.g.</i> non-human primates for drug metabolism, rabbits and rats for safety profiles and dogs for oral absorption studies of a drug.
	Cancer-affected humans (Phase 0 clinical trials)	First-in-human testing of API behaviours at subtherapeutic doses.	Assessment of PKPD relationships and establishment of drug-target effects for future phases of clinical trials.

Chapter 1: Introduction and Aims.

Table. 1.3 | Experimental and theoretical models for studying drug-membrane interactions.

Name	Depiction	Comments
Water-octanol system ¹⁸		Model mimicking water/biological membrane phase equilibrium. Used to measure partition/distribution coefficient (LogP/LogD) values of a compound distributed between equal volumes of water and octanol. Data helps to predict the PK drug behaviour ⁶ .
Lipid micelles ²¹		2-30 nm-sized nanoparticles composed of assembled lipid molecules with the hydrophilic head facing the solvent and hydrophobic tails the core. Used as delivery systems ²² or for purification and studies on membrane proteins ²³ .
Bicells ²⁴		Around 50 nm-sized lipid bilayer fragments consisting usually of two lipids; one forming bilayer (yellow) and the other micelle-like assemblies with the bilayer at the edge (brown). Used as delivery systems ²⁵ or for studies of membrane amphiphiles and proteins ²⁶ .
Bilayer Nanodiscs ²⁷		Around 10 nm-sized lipid bilayer fragments encapsulated in an amphipathic protein scaffold around the edge. Used as delivery systems ²⁸ or for studies of membrane protein functions ²⁹ .
Liposomes ³⁰		20nm – 1µm-sized lipid bilayer(s) rolled up in a spherical shell format; may vary in bilayer number (uni- or multilamellar) or overall vesicle size (small, giant). Used as delivery systems or for studies of cell membrane behaviour.
Black lipid membranes (BLMs) ³¹		A short-living lipid bilayer patch attached to the pore edges of a hydrophobic plate that is immersed in liquid, creating two chambers. Used for electrophysiological and structural studies of membranes and membrane proteins.
Lipid Self-assembled Monolayers (SAMs) ³²		Lipid monolayer spontaneously adsorbed on the surface of a solid support into organised domains of different sizes. Used for studies of membrane properties or cell-lipid interactions.
Supported lipid bilayers (SLBs) ³³		An organised double leaflet lipid film deposited on a solid support. Used for membrane behaviour and interaction studies.
NanoSLBs ³⁴		SLBs deposited on the surface of spherical nanoparticles. Used as delivery systems and biosensors.
Multi-scale simulations ³⁵		Computer-based calculations of lipid behaviours on a certain level based on information from different levels. Used for simulating the molecular dynamics of membrane-drug interactions. Figure adapted from ref. 44.
Tethered Bilayer Lipid Membranes (t-BLMs) ³⁶		Models composed of lipid mono- or bilayers associated with SAMs of thiolipids that are covalently attached to the solid support. Used for membrane behaviour and interaction studies.
Microfluidic systems ³⁷		Models of a various design focusing on interactions of lipid films with small and precisely controlled volumes of fluids. Used for membrane behaviour and interaction studies in liquid environments. Figure adapted from ref. 46.

1.5 SLBs as a model for membrane interactions.

Supported lipid bilayers (SLBs) or supported phospholipid bilayers (SPBs) could be defined as organised lipid films that are deposited on a solid support. Biophysical studies often employ SLBs as research tools to investigate the behaviour and properties of cellular membranes, when exposed to xenobiotics for several reasons:

Firstly, since SLBs display a number of structural and behavioural similarities when compared with membranes in the cell, they are often considered a representative model for the *in vivo* behaviour of phospholipid membranes. Table 1.4 summarises the similarities that can be noted between cell membranes and SLBs³⁸. Although SLBs may be criticised for loss of the 'complexity' present in cellular membranes, it is the point of a model to simplify and uncover components of the interactions between the complex structures (*e.g.* cell membrane) and acting agents (*e.g.* drugs) that are not well understood. For those reasons, SLBs indeed seem to be a reasonable model for studying and possibly correlating the behaviour and responses of a cell membrane *in vivo* after exposure to a drug.

Secondly, since research into SLBs is extensive, characterisation of SLB model composition can be performed with a wide range of techniques. Additionally, since SLBs are surface deposits, high resolution techniques such as ToF-SIMS³⁹, XPS⁴⁰ or AFM⁴¹ can be employed. These techniques enable characterisation of SLB chemical composition and observation of its behaviour at a nanometre scale, making investigations of membrane-drug interactions at a molecular level possible. Table 1.5 lists key techniques that are used for SLB characterisation studies.

Thirdly, the SLBs are easily alterable systems; both the components of the experimental environment and SLB can be easily modified. On the one hand, the number and types of lipids in the model composition can be simply chosen. In addition, SLBs can be functionalised with alternative chemical structures, *e.g.* proteins, carbohydrates, fluorophores, polymers, which increase the complexity of SLB model and enable measurement(s) of the desired interaction(s). Furthermore, both the surrounding liquid environment and solid support are also relatively easy to adjust. Providing the liquid is polar and the solid support is flat enough, any desired environment may be introduced. These properties make SLBs very potent candidates for high throughput applications of interest. Some examples of such alterability are presented in table 1.6.

Table 1.4 | Comparison of cell membranes and supported lipid films.

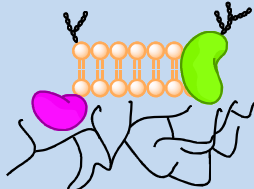
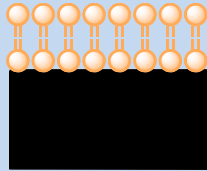
Property	Cell membrane	Supported lipid film
Scheme:		
Chemical composition:	Two lipid leaflets with proteins and carbohydrates.	Two lipid leaflets; attachment of other chemistries possible ³³ .
Surround environment:	Supported by cytoskeleton (bottom); suspended in physiological buffers (top & bottom).	Supported by a solid support (bottom); suspended in a polar liquid (top & bottom).
Film quality:	Continuous or porous films (membranes considered continuous, while lipid film a porous bilayer with holes for transmembrane proteins).	Various ⁴² (continuous, porous, patch-like film qualities).
Number of bilayers:	Usually, one bilayer per membrane; each cell is a multi-bilayer environment.	Various ³⁸ (bilayer or multilayer topographies).
Spatial lipid distribution:	Unclear whether distribution is homogenous or organised in domains (rafts) ⁴³ .	Both homogenous and phase separated morphologies possible. ⁴⁴
Lipid distribution across two leaflets:	Membrane asymmetry present for some lipids ⁴⁵ .	Preparation of asymmetric structures possible. ⁴⁶
Membrane dynamics:	Lateral and vertical mobility of lipids present (fluidic mosaic model ⁴⁷ & flip-flop ⁴⁸ phenomenon).	Lateral mobility present ³⁸ . Flip-flop phenomenon reported. ⁴⁹
Behaviour when exposed to a xenobiotic:	Complex and difficult to measure at nanoscale.	Simplified and possible to measure at nanoscale ⁵⁰ .

Table 1.5 | Key techniques employed for SLB characterisation studies.

Property	Techniques
SLB morphology & lipid behaviour:	Scanning probe (NSOM ⁵¹ , AFM, SICM ⁵²), electron (TEM ⁵³ , SEM ⁵⁴) fluorescence (FLICM ⁵⁵ , TIRFM ⁵⁶) or optical (RICM ⁵⁷) microscopy, neutron ⁵⁸ & X-ray ⁵⁹ scattering, neutron ⁶⁰ reflectometry, X-ray ⁶¹ reflectivity & ellipsometry ⁶²), fluorescence (SPT ⁶³ , FRET ⁶⁴ or FCS ⁶⁵ , FRAP ⁶⁶ , SPR ⁶⁷), optical (DPI ⁶⁸ , OWLS ⁶⁹) techniques, QCM-D ⁷⁰ , computational simulations ⁷¹ .
SLB chemical composition:	ToF-SIMS, XPS ⁴⁰ , NMR ⁷²
Electrical properties:	EIS ⁷³ and other DC and AC measurements ⁷⁴
Vibrational properties:	Ultrafast spectroscopy ⁷⁵ , computational modelling
Mechanical properties:	AFM or other scanning probe techniques ⁷⁶

Abbreviations: NSOM – near-field scanning optical microscopy; AFM – atomic force microscopy; SICM – scanning ion-conductance microscopy; TEM – transmission electron microscopy; SEM – scanning electron microscopy; SPT – single particle tracking; FRET – Foerster resonance energy transfer; FCS – fluorescence correlation spectroscopy; FRAP – fluorescence recovery after photobleaching; SPR – surface plasmon resonance; FLICM – fluorescence interference contrast microscopy; TIRFM – total interference reflection fluorescence microscopy; DPI – dual polarisation interferometry; RICM – reflection interference contrast microscopy; OWLS – optical waveguide lightmode spectroscopy; QCM-D – quartz crystal microbalance with dissipation; ToF-SIMS – time-of-flight secondary ion mass spectrometry; XPS – X-ray photoelectron spectroscopy; NMR – nuclear magnetic resonance; EIS – electrochemical impedance spectroscopy; DC – direct current; AC – alternating current

Table 1.6 | Examples demonstrating alterability of SLB properties.

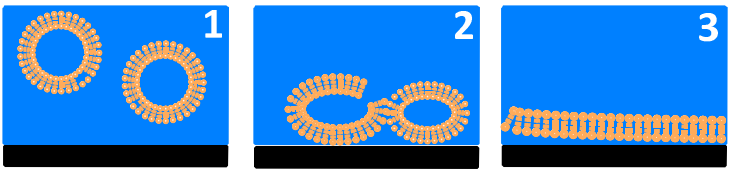
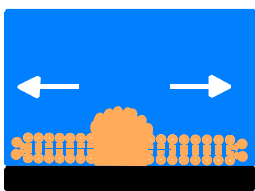
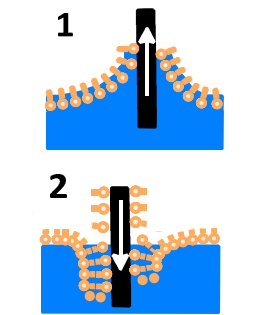
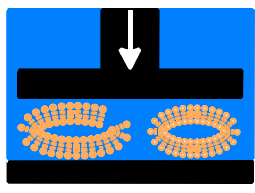
Variable	Adjustment	Result
Lipid number or type:	Addition of 5-15% CHOL to DOPC/SPM-composed SLBs ⁷⁷ .	Changes in bilayer morphology and behaviour.
Protein:	Insertion of a transmembrane protein phospholamban into SLBs ¹⁹ .	Studies of protein-antibody interaction profiles.
Carbohydrate:	Insertion of glycan-lipid conjugates into SLBs at various densities ²⁰ .	Studies of cell-bilayer adhesion profiles or protein-glycan interactions.
Fluorophore:	Insertion of α -parinaric acid into SLBs ⁷⁸ .	Studies of membrane phase transition behaviour.
Polymer:	Insertion of PEG-lipid conjugates into SLBs ⁷⁹ .	Provision of air stability for SLBs enabling membrane interaction studies.
Biotin:	Insertion of biotin-lipid conjugates into SLBs ⁸⁰ .	Immobilisation of protein, vesicles, bilayers on the bilayer surface <i>via</i> streptavidin for further studies.
Liquid environment:	Exposure of DMPC-composed SLBs to 0-0.1 M sodium chloride media ⁸¹ .	Changes in frictional properties of SLBs.
Solid support:	Exposure of SLBs to different surfaces and surface topologies ⁸² .	Studying behavioural changes of bilayer lipids.

Abbreviations: SLB – supported lipid bilayer; CHOL – cholesterol; DOPC – dioleoylphosphatidyl choline; SPM – sphingomyelin; DMPC – dimyristoylphosphatidyl choline; PEG – polyethylene oxide;

On the other hand, SLBs enable the development of lipid films of both: different qualities (or edge lengths), including continuous, porous and patch-like qualities, and also the number of lipid layers (*e.g.* bi- or multilayers). SLBs of desired properties can be achieved through a variety of fabrication methods that are briefly detailed in table 1.7. It is worth mentioning that the simplicity and range of fabrication techniques available for SLBs, as well as other aspects of alterability are the key advantages of SLBs over the other lipid-based model systems (*e.g.* tethered bilayer membranes).

Finally, SLBs hold the potential to be studied in a high throughput manner. Although several approaches for SLB microarray development have already been reported in the literature, there is still a lack of commercial tests that enable the direct screening of direct formulation/API-membrane interactions in a routine high throughput manner. Apart from PAMPA, liposomes⁸³ and a few automated lipid-based detection systems targeted mainly at the research community (Biacore Life Sciences⁸⁴, Nanion Inc.⁸⁵, Oxford NanoLabs⁸⁶), the potential of lipid bilayers for high throughput screening (HTS) remains to be discovered. The most likely cause of this situation is due to several limitations associated with SLBs, as discussed in the section below.

Table 1.7 | Key techniques used to fabricate SLBs.

Technique	Principle	Comments
<p>Vesicle deposition⁸⁷</p> 	<p>Liposomes adsorb at the surface (1), deform and/or fuse with each other (2) and open forming a bilayer (3).</p>	<ul style="list-style-type: none"> • Popular technique. • Quick and easy to handle. • Provides controlled fabrication of various film qualities. • Excessive liposomes may be problematic to remove. • Suitable for preparation of complex compositions.
<p>Bilayer self-spreading⁸⁸</p> 	<p>Once immersed in a polar environment above the transition temperature, bulk lipids start to self-spread on a solid support forming a bilayer.</p>	<ul style="list-style-type: none"> • Quick and easy to handle. • Provides clean and continuous lipid bi- and multilayers with limited control. • Lipids in a mixture may not spread evenly. • Complex bilayer compositions may need to be fabricated through post-functionalization of the bilayer
<p>Langmuir-Blodgett⁸⁹ (Langmuir-Schaeffer)</p> 	<p>First bilayer leaflet is formed through the adsorption of lipids at the surface after emersion of a solid support from a lipid monolayer that is assembled at a liquid surface (1). Second leaflet is formed through the immersion of the support in liquid with another lipid monolayer at the surface (2).</p>	<ul style="list-style-type: none"> • Requires advanced knowledge and equipment to handle. • Enables controlled fabrication of clean and continuous lipid bi- and multilayers. • Operation in horizontal immersion direction possible. • Complex bilayer compositions may need to be fabricated through bilayer post-functionalization of the bilayer.
<p>Contact Printing⁹⁰</p> 	<p>Liposomes are forced to break and form bilayers under the mechanistic force of the stamp.</p>	<ul style="list-style-type: none"> • Requires advanced knowledge and equipment to handle. • Fabrication of various film qualities with limited control. • Excessive liposomes problematic to remove.
<p>Spin coating⁹¹</p> 	<p>Bilayer forms through spreading of lipids in a high humidity chamber after pipetting of lipid solution in organic solvent onto a spinning surface.</p>	<ul style="list-style-type: none"> • Requires advanced knowledge and equipment to handle. • Fabrication of clean and continuous lipid bi- and multilayers with limited control. • Disc-shaped surfaces preferred. • Complex bilayer compositions mainly through bilayer functionalization.

1.6 Current limitations associated with SLBs.

Unfortunately, there are several limitations associated with SLBs as models for the *in vitro* screening of API-membrane interactions.

Firstly, the two leaflet structure is only present in an aqueous (or any other polar) environment. Shortly after SLBs are dried and exposed to air, the bilayer structure gradually loses stability causing the SLB lipids to collapse and form alternative structures due to the amphiphilic nature of lipid molecules (*e.g.* lipid aggregates, mono- or multilayers non-specifically adsorbed on the surface)⁹². The lack of air stability is therefore an issue, when the complex mechanisms between membranes and formulations are investigated limiting such studies to liquid environments which provide the maintenance of a double leaflet structure. For that reason, the development of air stable SLBs has been a research focus for a while. Here, several approaches have been proposed, including: covering SLBs with moisturising agents (trehalose and other sugars⁹², proteins⁹³, hydrophilic polymers⁷⁹) or the deposition of SLBs on specific solid supports¹⁹ (figure 1.4). Alternatively, incubation of SLBs in high humidity environments may provide the required stability⁹⁴. From a microarray perspective, the solid support and high humidity approaches appear to be particularly useful, since they would enable development of an SLB platform that could be manufactured and studied *via* fully automated liquid dispensing systems (*e.g.* piezoelectric inkjet print head technology). Such systems are of interest, as they assure high precision and accuracy for liquid handling-associated applications⁹⁵. Here, the presence of moisturising agents in the API-membrane environment may interfere with the API-SLB interaction or affect the printing process.

Secondly, SLB handling and optimisation are often not an easy task to achieve. Since the behaviour of SLBs depends on many factors (*e.g.* room temperature, membrane composition and film qualities, type of solid support and solution, bilayer mechanics, phase behaviour or lipid crystalline structures within the mixture), various parameters need to be monitored and/or considered in order to develop an SLB-based screening platform that is well understood. For this reason, an advanced knowledge of lipid chemistry and biophysics, as well as membrane research is essential for appropriate interpretation of model SLB behaviours.

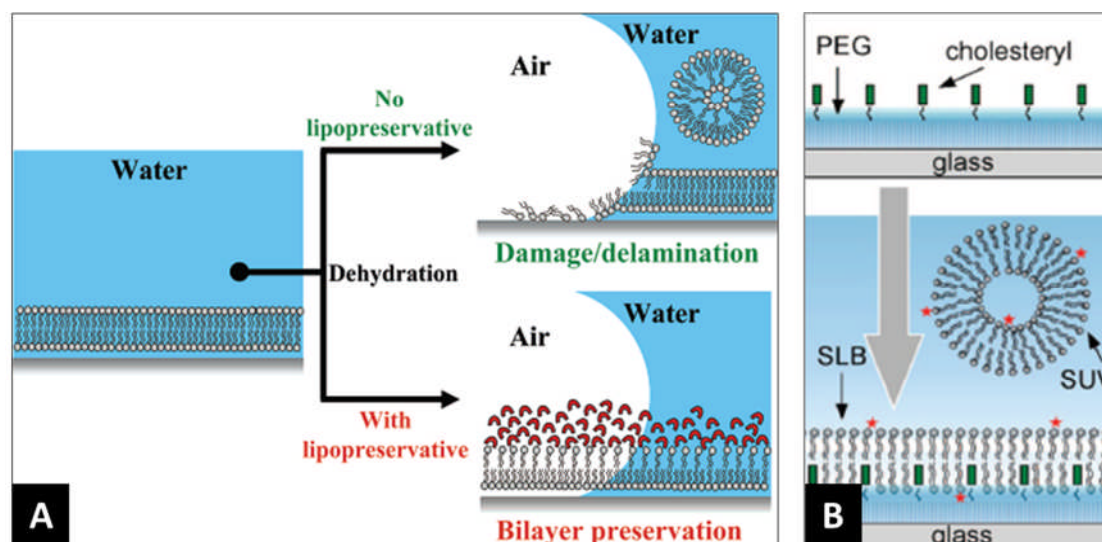


Figure 1.4. Strategies providing air stability for SLBs. In order to assure air stability, SLBs are coated with lipopreservatives, such as trehalose or other carbohydrates, hydrophilic proteins and polymers or their conjugates with lipids before exposure to air (A). Alternatively, deposition of SLBs on solid supports of advanced chemistry (e.g. FluidArray®) have been reported to provide air stability (B). Figures were adapted from ref. 102 and 28.

Finally, the literature related to SLBs is impressive and plentiful. On the one hand, this is the reason why SLBs are considered very attractive research tools, as indicated above. However, on the other hand, the inconsistencies in terms of the types and number of lipids within the SLBs, terminologies of lipid-based models, as well as SLB fabrication and characterisation methodologies make it difficult to find and compare results and extract unambiguous conclusions across different papers, authors or research groups. Furthermore, the vast majority of the SLB research in the literature is performed using systems composed of only one or two lipid molecules⁷⁷, while the SLB models employing more complex lipid compositions are less popular⁵⁰. Interestingly, a critique may be raised that an increase in the amount and types of lipids could unnecessarily boost the complexity of a model SLB. However, it had also been demonstrated that studies on SLBs of oversimplified structure may result in misleading observations^{7c}. For that reason, investigations into more complex lipid compositions of physiological relevance seem to be a reasonable compromise in order to correlate the SLB interactions of APIs with their performance *in vivo*.

1.7 Conclusion and aims.

Clearly, the development of screening model(s) enabling correlation of the *in vivo* and *in vitro* behaviours of a pharmaceutical formulation is not an easy task and without further research, progress will not be made. However, since the approaches currently used in

pharmaceutical sciences are either too basic or too complex to fully elucidate the toxicity and targeted delivery of biopharmaceuticals in the human body, it is fair to state that a more detailed understanding of drug behaviours in physiologically-relevant environments at a molecular level would be beneficial. Here, analysis techniques such as AFM, ToF-SIMS or XPS that enable the observations of *in situ* drug behaviours at nanometre scales hold considerable potential.

Furthermore, since direct drug-cell membrane interactions have enabled the elucidation of the mechanisms behind the behaviours of APIs *in vivo*, the studies of drug-SLB interactions using the techniques above are a reasonable starting point for model development. Here, an important factor to consider is the model lipid composition of an SLB, so that it reflects the behaviour of lipids in biological membranes more closely. For this purpose, it is sensible to investigate bilayers with lipid compositions close to the ones of cell membranes in the first instance, *e.g.* lung epithelial cell, blood-brain barrier or even erythrocyte (as a more general model) membrane lipid compositions. Investigations into the latter may be particularly useful for assessing the general modelling potential of SLBs that are composed of several different lipids. In terms of the APIs introduced to SLBs, the interactions of bilayers with biopharmaceutical formulations, such as nucleic acid therapeutics, antibodies or polymer-enhanced delivery systems remain a fairly undiscovered area. Hence, the elucidation of mechanisms behind such interactions may be of significant interest from a pharmaceutical point of view.

In parallel, development of an SLB microarray that enables a high throughput screening of the SLB-formulation interactions would also be of interest. Such microarrays would facilitate rapid assessments of interactions between a range of formulations or APIs and a range of physiologically-relevant lipid compositions. This may provide useful insights into API behaviours at various lipid-based barriers in biological systems and improve the general understanding of API/formulation performance *in vivo* in a high throughput manner. However, such limitations as SLB air instability or consideration of rapid readout methodology may need to be primarily addressed.

To conclude, SLBs seem to hold a realistic potential as an *in vitro* screening approach to study drug-membrane interactions. Since appropriate understanding of such interactions is vital for predicting the API performance *in vivo*, thorough research into this interesting, yet challenging field may be worth the effort.

Chapter 1: Introduction and Aims.

For this reason, this thesis aims to develop and assess SLBs of physiologically-relevant lipid compositions, as tools for high throughput screening of pharmaceutical formulation-membrane interactions.

In chapter 2, the methodology and experimental approaches for the investigations of SLBs at a nanometre scale (*e.g.* AFM, ToF-SIMS, XPS) are briefly explained.

In chapter 3, the development and characterisation of model SLBs that are composed of five natural lipids is performed using the methods above. Here, since such investigations, to the author's knowledge, have not been attempted previously, the innovative approaches towards qualitative and quantitative data analysis are indicated. Additionally, the two SLB fabrication techniques: vesicle deposition (VDT) and bilayer self-spreading (BSST) are assessed with regards to the SLB microarray development.

In chapters 4 and 5, the model SLBs are used for the elucidation of interaction mechanisms between biological membranes and pharmaceutical formulation components. Chapter 4 focuses on a recently re-discovered class of polymer excipients: Pluronics®, not only revealing their likely performances and interaction mechanisms *in vivo*, but also indicating further advantages of SLBs as experimental models for excipient-membrane interaction studies. The focus of chapter 5 is directed towards the AFM investigations of model SLB-biopharmaceutical formulation interactions. Studies on models for siRNA therapeutics at a nanometre scale are correlated with the literature-reported *in vivo* performances and toxicities of nucleic acid therapeutics. In addition, the performance of basic siRNA-like polyplexes is assessed highlighting the need for the development of an SLB-based screening approach that is suitable for commercial applications.

For this reason, the development of an SLB microarray prototype is attempted and reported in chapter 6. The method development, as well as technological issues associated with the optimisation processes are described in order to assure both repeatability and reproducibility of such approach.

Finally, the research is concluded and the directions for further investigations are outlined in chapter 7. In addition, two potential research disciplines that may emerge from this research are identified.

Since the nature of this PhD project is fairly multidisciplinary, it is the author's hope that this thesis would significantly contribute towards a general progress within the pharmaceutical

sciences. For this reason, the consideration of the discussion and hypotheses presented in this thesis is encouraged to everybody, who is interested in pharmaceutical research.

1.8 References

1. Kostewicz, E. S.; Abrahamsson, B.; Brewster, M.; Brouwers, J.; Butler, J.; Carlert, S.; Dickinson, P. A.; Dressman, J.; Holm, R.; Klein, S.; Mann, J.; McAllister, M.; Minekus, M.; Muenster, U.; Mullertz, A.; Verwei, M.; Vertzoni, M.; Weitschies, W.; Augustijns, P., In vitro models for the prediction of in vivo performance of oral dosage forms. *European journal of pharmaceutical sciences : official journal of the European Federation for Pharmaceutical Sciences* **2013**.
2. pharma.org Drug Discovery and Development. Understanding the R&D process. (accessed 16/09/2013).
3. Adams, C. P.; Brantner, V. V., Estimating the cost of new drug development: is it really 802 million dollars? *Health affairs* **2006**, *25* (2), 420-8.
4. (a) Kaitin, K. I., Deconstructing the Drug Development Process: The New Face of Innovation (vol 87, pg 356, 2010). *Clinical Pharmacology & Therapeutics* **2011**, *89* (1), 148-148; (b) Kaitin, K. I., Deconstructing the Drug Development Process: The New Face of Innovation. *Clinical Pharmacology & Therapeutics* **2010**, *87* (3), 356-361.
5. Gallas, A.; Alexander, C.; Davies, M. C.; Puri, S.; Allen, S., Chemistry and formulations for siRNA therapeutics. *Chemical Society reviews* **2013**.
6. Ying Lu, S. K., Kinam Park,, In vitro-in vivo correlation: Perspectives on model development. *International journal of pharmaceutics* **2011**, *418* (1), 142-148.
7. (a) Lucio, M.; Lima, J. L.; Reis, S., Drug-membrane interactions: significance for medicinal chemistry. *Current medicinal chemistry* **2010**, *17* (17), 1795-809; (b) Pignatello, R.; Musumeci, T.; Basile, L.; Carbone, C.; Puglisi, G., Biomembrane models and drug-biomembrane interaction studies: Involvement in drug design and development. *Journal of pharmacy & bioallied sciences* **2011**, *3* (1), 4-14; (c) Peetla, C.; Stine, A.; Labhasetwar, V., Biophysical interactions with model lipid membranes: applications in drug discovery and drug delivery. *Molecular pharmaceutics* **2009**, *6* (5), 1264-76.
8. Porter, C. J.; Trevasakis, N. L.; Charman, W. N., Lipids and lipid-based formulations: optimizing the oral delivery of lipophilic drugs. *Nature reviews. Drug discovery* **2007**, *6* (3), 231-48.
9. (a) Kim, K. S., Mechanisms of microbial traversal of the blood-brain barrier. *Nature reviews. Microbiology* **2008**, *6* (8), 625-34; (b) MedilinePlus (accessed 16/09/13); (c) Joshi, M. Blood vessel-blocking drug may delay prostate cancer progression. (accessed 16/09/2013); (d) Baginski, M.; Sternal, K.; Czub, J.; Borowski, E., Molecular modelling of membrane activity of amphotericin B, a polyene macrolide antifungal antibiotic. *Acta biochimica Polonica* **2005**, *52* (3), 655-8; (e) Kozmin, S. A., Chemical "knockout" challenges the amphotericin B channel model. *Nature chemical biology* **2008**, *4* (1), 19-20; (f) College, O. Human Anatomy and Physiology. (accessed 16/09/13).
10. Limited, C. U. (accessed 16/09/13).
11. Ltd., N. P. U. Neoral Soft Gelatin Capsules, Neoral Oral Solution. (accessed 16/03/13).
12. GmbH, m. Dacarbazine 100mg, 200mg, 500mg, 1000mg. (accessed 16/09/13).
13. Limited, M. S. D. Temodal Capsules. (accessed 16/09/13).
14. Roman Frigg, S. H., Models in Science. In *Stanford Encyclopedia of Philosophy*, <http://plato.stanford.edu/entries/models-science/>, 2012.
15. Kansy, M.; Senner, F.; Gubernator, K., Physicochemical high throughput screening: parallel artificial membrane permeation assay in the description of passive absorption processes. *Journal of medicinal chemistry* **1998**, *41* (7), 1007-10.
16. (a) Chen, X.; Murawski, A.; Patel, K.; Crespi, C. L.; Balimane, P. V., A novel design of artificial membrane for improving the PAMPA model. *Pharmaceutical research* **2008**, *25* (7), 1511-20; (b) Seddon, A. M.; Casey, D.; Law, R. V.; Gee, A.; Templer, R. H.; Ces, O., Drug interactions with lipid membranes. *Chemical Society reviews* **2009**, *38* (9), 2509-19.
17. Gad, S. C., In *Preclinical Development Handbook: ADME and Biopharmaceutical Properties (Pharmaceutical Development Series)*, Gad, S. C., Ed. 2008.
18. Joachim K. Seydel, M. W., Drug-Membrane Interactions: Analysis, Drug Distribution, Modeling. ©2002 Wiley-VCH Verlag GmbH & Co. KGaA: http://onlinelibrary.wiley.com/doi/10.1002/3527600639.fmatter_indsup/pdf. (accessed 16/9/13).
19. Deng, Y.; Wang, Y.; Holtz, B.; Li, J. Y.; Traaseth, N.; Veglia, G.; Stottrup, B. J.; Elde, R.; Pei, D. Q.; Guo, A.; Zhu, X. Y., Fluidic and air-stable supported lipid bilayer and cell-mimicking microarrays. *J Am Chem Soc* **2008**, *130* (19), 6267-6271.
20. Zhu, X. Y.; Holtz, B.; Wang, Y. N.; Wang, L. X.; Orndorff, P. E.; Guo, A., Quantitative Glycomics from Fluidic Glycan Microarrays. *J Am Chem Soc* **2009**, *131* (38), 13646-13650.
21. Mazer, N. A.; Benedek, G. B.; Carey, M. C., Quasielastic light-scattering studies of aqueous biliary lipid systems. Mixed micelle formation in bile salt-lecithin solutions. *Biochemistry-Us* **1980**, *19* (4), 601-15.
22. Torchilin, V. P., Lipid-core micelles for targeted drug delivery. *Current drug delivery* **2005**, *2* (4), 319-27.
23. Franzin, C. M.; Gong, X. M.; Thai, K.; Yu, J.; Marassi, F. M., NMR of membrane proteins in micelles and bilayers: the FXFD family proteins. *Methods* **2007**, *41* (4), 398-408.
24. Durr, U. H.; Gildenberg, M.; Ramamoorthy, A., The magic of bicelles lights up membrane protein structure. *Chem Rev* **2012**, *112* (11), 6054-74.
25. Rubio, L.; Alonso, C.; Rodriguez, G.; Cocera, M.; Lopez-Iglesias, C.; Coderch, L.; De la Maza, A.; Parra, J. L.; Lopez, O., Bicellar systems as new delivery strategy for topical application of flufenamic acid. *International journal of pharmaceutics* **2013**, *444* (1-2), 60-69.
26. Whiles, J. A.; Deems, R.; Vold, R. R.; Dennis, E. A., Bicycles in structure-function studies of membrane-associated proteins. *Bioorganic chemistry* **2002**, *30* (6), 431-42.
27. Denisov, I. G.; Grinkova, Y. V.; Lazarides, A. A.; Sligar, S. G., Directed self-assembly of monodisperse phospholipid bilayer Nanodiscs with controlled size. *J Am Chem Soc* **2004**, *126* (11), 3477-87.
28. Murakami, T., Phospholipid nanodisc engineering for drug delivery systems. *Biotechnology journal* **2012**, *7* (6), 762-7.
29. Ritchie, T. K.; Grinkova, Y. V.; Bayburt, T. H.; Denisov, I. G.; Zolnerciks, J. K.; Atkins, W. M.; Sligar, S. G., Chapter 11 - Reconstitution of membrane proteins in phospholipid bilayer nanodiscs. *Methods in enzymology* **2009**, *464*, 211-31.
30. Jesorka, A.; Orwar, O., Liposomes: technologies and analytical applications. *Annual review of analytical chemistry* **2008**, *1*, 801-32.
31. Winterhalter, M., Black lipid membranes. *Curr Opin Colloid In* **2000**, *5* (3-4), 250-255.
32. Love, J. C.; Estroff, L. A.; Kriebel, J. K.; Nuzzo, R. G.; Whitesides, G. M., Self-assembled monolayers of thiolates on metals as a form of nanotechnology. *Chem Rev* **2005**, *105* (4), 1103-1169.
33. Castellana, E. T.; Cremer, P. S., Solid supported lipid bilayers: From biophysical studies to sensor design. *Surf Sci Rep* **2006**, *61* (10), 429-444.
34. Ashley, C. E.; Carnes, E. C.; Phillips, G. K.; Padilla, D.; Durfee, P. N.; Brown, P. A.; Hanna, T. N.; Liu, J.; Phillips, B.; Carter, M. B.; Carroll, N. J.; Jiang, X.; Dunphy, D. R.; Willman, C. L.; Petsev, D. N.; Evans, D. G.; Parikh, A. N.; Chackerian, B.; Wharton, W.; Peabody, D. S.; Brinker, C. J., The targeted delivery of multicomponent cargos to cancer cells by nanoporous particle-supported lipid bilayers. *Nature materials* **2011**, *10* (5), 389-97.

35. Khandelia, H.; Kaznessis, Y. N., Structure of the antimicrobial beta-hairpin peptide protegrin-1 in a DLPC lipid bilayer investigated by molecular dynamics simulation. *Biochimica et biophysica acta* **2007**, *1768* (3), 509-20.
36. Cornell, B. A.; Braach-Maksvytis, V. L.; King, L. G.; Osman, P. D.; Raguse, B.; Wieczorek, L.; Pace, R. J., A biosensor that uses ion-channel switches. *Nature* **1997**, *387* (6633), 580-3.
37. Goluch, E. D.; Shaw, A. W.; Sligar, S. G.; Liu, C., Microfluidic patterning of nanodisc lipid bilayers and multiplexed analysis of protein interaction. *Lab Chip* **2008**, *8* (10), 1723-1728.
38. Ferrari, M., *BioMEMS and biomedical nanotechnology*. Springer: New York, 2006.
39. Prinz, C.; Hook, F.; Malm, J.; Sjoval, P., Structural effects in the analysis of supported lipid bilayers by time-of-flight secondary ion mass spectrometry. *Langmuir* **2007**, *23* (15), 8035-8041.
40. Michel, R.; Subramaniam, V.; McArthur, S. L.; Bondurant, B.; D'Ambruso, G. D.; Hall, H. K.; Brown, M. F.; Ross, E. E.; Saavedra, S. S.; Castner, D. G., Ultra-high vacuum surface analysis study of rhodopsin incorporation into supported lipid bilayers. *Langmuir* **2008**, *24* (9), 4901-4906.
41. Morandat, S.; Azouzi, S.; Beauvais, E.; Mastouri, A.; El Kirat, K., Atomic force microscopy of model lipid membranes. *Analytical and bioanalytical chemistry* **2013**, *405* (5), 1445-1461.
42. Richter, R. P.; Berat, R.; Brisson, A. R., Formation of solid-supported lipid bilayers: An integrated view. *Langmuir* **2006**, *22* (8), 3497-3505.
43. Pike, L. J., The challenge of lipid rafts. *J Lipid Res* **2009**, *50* Suppl, S323-8.
44. Elson, E. L.; Fried, E.; Dolbow, J. E.; Genin, G. M., Phase separation in biological membranes: integration of theory and experiment. *Annu Rev Biophys* **2010**, *39*, 207-26.
45. GM., C., Structure of the Plasma Membrane. In *The Cell: A Molecular Approach. 2nd edition.*, Sunderland (MA): Sinauer Associates; <http://www.ncbi.nlm.nih.gov/books/NBK9898/>, 2000.
46. Stanglmaier, S.; Hertrich, S.; Fritz, K.; Moulin, J. F.; Haese-Seiller, M.; Radler, J. O.; Nickel, B., Asymmetric distribution of anionic phospholipids in supported lipid bilayers. *Langmuir* **2012**, *28* (29), 10818-21.
47. Singer, S. J.; Nicolson, G. L., The fluid mosaic model of the structure of cell membranes. *Science* **1972**, *175* (4023), 720-31.
48. Kornberg, R. D.; McConnell, H. M., Inside-outside transitions of phospholipids in vesicle membranes. *Biochemistry-U S* **1971**, *10* (7), 1111-20.
49. Nakanishi, M.; Matsumoto, K.; Takahashi, S., Binding of macrophages and phospholipid flip-flop in supported lipid bilayers. *FEBS letters* **1985**, *192* (1), 66-70.
50. Soliman, M.; Nasanit, R.; Allen, S.; Davies, M. C.; Briggs, S. S.; Seymour, L. W.; Preece, J. A.; Alexander, C., Interaction of reducible polypeptide gene delivery vectors with supported lipid bilayers: pore formation and structure-function relationships. *Soft Matter* **2010**, *6* (11), 2517-2524.
51. Hollars, C. W.; Dunn, R. C., Submicron structure in L-alpha-dipalmitoylphosphatidylcholine monolayers and bilayers probed with confocal, atomic force, and near-field microscopy. *Biophys J* **1998**, *75* (1), 342-353.
52. Jonsson, P.; McColl, J.; Clarke, R. W.; Ostanin, V. P.; Jonsson, B.; Klenerman, D., Hydrodynamic trapping of molecules in lipid bilayers. *P Natl Acad Sci USA* **2012**, *109* (26), 10328-10333.
53. Diociaiuti, M.; Ruspantini, I.; Molinari, A.; Cianfriglia, M.; Gaudiano, C.; Chistolini, P.; Ippoliti, R.; Lendaro, E.; Arancia, G., Immunogold localisation of P-glycoprotein in supported lipid bilayers by transmission electron microscopy and atomic force microscopy. *Proceedings of the 5th Multinational Congress on Electron Microscopy* **2001**, 171-172.
54. Han, X.; Pradeep, S. N.; Critchley, K.; Sheikh, K.; Bushby, R. J.; Evans, S. D., Supported bilayer lipid membrane arrays on photopatterned self-assembled monolayers. *Chemistry* **2007**, *13* (28), 7957-64.
55. Crane, J. M.; Kiessling, V.; Tamm, L. K., Measuring lipid asymmetry in planar supported bilayers by fluorescence interference contrast microscopy. *Langmuir* **2005**, *21* (4), 1377-88.
56. Dewa, T.; Sugiura, R.; Suemori, Y.; Sugimoto, M.; Takeuchi, T.; Hiro, A.; Iida, K.; Gardiner, A. T.; Cogdell, R. J.; Nango, M., Lateral organization of a membrane protein in a supported binary lipid domain: direct observation of the organization of bacterial light-harvesting complex 2 by total internal reflection fluorescence microscopy. *Langmuir* **2006**, *22* (12), 5412-8.
57. Monzel, C.; Fenz, S. F.; Merkel, R.; Sengupta, K., Probing biomembrane dynamics by dual-wavelength reflection interference contrast microscopy. *Chemphyschem : a European journal of chemical physics and physical chemistry* **2009**, *10* (16), 2828-38.
58. Armstrong, C. L.; Kaye, M. D.; Zamponi, M.; Mamontov, E.; Tyagi, M.; Jenkins, T.; Rheinstadter, M. C., Diffusion in single supported lipid bilayers studied by quasi-elastic neutron scattering. *Soft Matter* **2010**, *6* (23), 5864-5867.
59. Balgavy, P.; Uhríkova, D.; Karlovska, J.; Dubnickova, M.; Kucerka, N.; Devinsky, F.; Lacko, I.; Cizmarik, J.; Lohner, K.; Degovics, G.; Rapp, G.; Yadaikin, S.; Kiselev, M.; Islamov, A.; Gordeliy, V., X-ray diffraction and neutron scattering studies of amphiphile - Lipid bilayer organization. *Cell Mol Biol Lett* **2001**, *6* (2A), 283-290.
60. Shen, H. H.; Hartley, P. G.; James, M.; Nelson, A.; Defendi, H.; McLean, K. M., The interaction of cubosomes with supported phospholipid bilayers using neutron reflectometry and QCM-D. *Soft Matter* **2011**, *7* (18), 8041-8049.
61. Wang, S. T.; Fukuto, M.; Yang, L., In situ x-ray reflectivity studies on the formation of substrate-supported phospholipid bilayers and monolayers. *Phys Rev E* **2008**, *77* (3).
62. Howland, M. C.; Szmodis, A. W.; Sanii, B.; Parikh, A. N., Characterization of physical properties of supported phospholipid membranes using imaging ellipsometry at optical wavelengths. *Biophys J* **2007**, *92* (4), 1306-1317.
63. Poudel, K. R.; Keller, D. J.; Brozik, J. A., Single Particle Tracking Reveals Corraling of a Transmembrane Protein in a Double-Cushioned Lipid Bilayer Assembly. *Langmuir* **2011**, *27* (1), 320-327.
64. Castellana, E. T.; Cremer, P. S., Imaging large arrays of supported lipid bilayers with a microscope. *Biointerphases* **2007**, *2* (2), 57-63.
65. Bag, N.; Sankaran, J.; Paul, A.; Kraut, R. S.; Wohland, T., Calibration and Limits of Camera-Based Fluorescence Correlation Spectroscopy: A Supported Lipid Bilayer Study. *Chemphyschem : a European journal of chemical physics and physical chemistry* **2012**, *13* (11), 2784-2794.
66. Weng, K. C.; Kanter, J. L.; Robinson, W. H.; Frank, C. W., Fluid supported lipid bilayers containing monosialoganglioside GM1: a QCM-D and FRAP study. *Colloids and surfaces. B, Biointerphases* **2006**, *50* (1), 76-84.
67. Margheri, G.; D'Agostino, R.; Becucci, L.; Guidelli, R.; Tiribilli, B.; Del Rosso, M., Surface plasmon resonance as detection tool for lipids lateral mobility in biomimetic membranes. *Biomed Opt Express* **2012**, *3* (12).
68. Ho, J. A.; Kuo, T. Y.; Yu, L. G., Dual polarization interferometric and capillary electrophoretic analysis of supported lipid bilayer constructed on silica-based surface: Evaluation of its anti-protein adsorption effect. *Anal Chim Acta* **2012**, *714*, 127-133.
69. Horvath, R.; Fricsovsky, G.; Papp, E., Application of the optical waveguide lightmode spectroscopy to monitor lipid bilayer phase transition. *Biosens Bioelectron* **2003**, *18* (4), 415-428.
70. Wang, K. F.; Nagarajan, R.; Mello, C. M.; Camesano, T. A., Characterization of Supported Lipid Bilayer Disruption By Chrysoptin-3 Using QCM-D. *J Phys Chem B* **2011**, *115* (51), 15228-15235.
71. Lin, X. B.; Wang, C. L.; Wang, M.; Fang, K.; Gu, N., Computer Simulation of the Effects of Nanoparticles' Adsorption on the Properties of Supported Lipid Bilayer. *J Phys Chem C* **2012**, *116* (33), 17960-17968.
72. Gaede, H. C.; Lockett, K. M.; Polozov, I. V.; Gawrisch, K., Multinuclear NMR studies of single lipid bilayers supported in cylindrical aluminum oxide nanopores. *Langmuir* **2004**, *20* (18), 7711-7719.
73. Sugihara, K.; Delai, M.; Szendro, I.; Guillaume-Gentil, O.; Voros, J.; Zambelli, T., Simultaneous OWLS and EIS monitoring of supported lipid bilayers with the pore forming peptide melittin. *Sensor Actuat B-Chem* **2012**, *161* (1), 600-606.

Chapter 1: Introduction and Aims.

74. Sabo, J.; Ottova, A.; Laputkova, G.; Legin, M.; Vojcikova, L.; Tien, H. T., A combined AC-DC method for investigating supported bilayer lipid membranes. *Thin Solid Films* **1997**, *306* (1), 112-118.
75. Gruenbaum, S. M.; Skinner, J. L., Vibrational spectroscopy of water in hydrated lipid multi-bilayers. I. Infrared spectra and ultrafast pump-probe observables. *J Chem Phys* **2011**, *135* (7).
76. Steltenkamp, S.; Muller, M. M.; Deserno, M.; Hennessal, C.; Steinem, C.; Janshoff, A., Mechanical properties of pore-spanning lipid bilayers probed by atomic force microscopy. *Biophys J* **2006**, *91* (1), 217-226.
77. S. Morandat, K. E. K., Exploring the Properties and Interactions of Supported Lipid Bilayers on the Nanoscale by Atomic Force Microscopy. In *MICROSCOPY: SCIENCE, TECHNOLOGY, APPLICATIONS AND EDUCATION*, formatex.org, Ed. <http://www.formatex.info/microscopy4/1925-1939.pdf>, 2010.
78. Sklar, L. A.; Miljanich, G. P.; Dratz, E. A., Phospholipid Lateral Phase-Separation and the Partition of Cis-Parinaric Acid and Trans-Parinaric Acid among Aqueous, Solid Lipid, and Fluid Lipid Phases. *Biochemistry-US* **1979**, *18* (9), 1707-1717.
79. Albertorio, F.; Diaz, A. J.; Yang, T.; Chapa, V. A.; Kataoka, S.; Castellana, E. T.; Cremer, P. S., Fluid and air-stable lipopolymer membranes for biosensor applications. *Langmuir* **2005**, *21* (16), 7476-82.
80. Murray, D. H.; Tamm, L. K.; Kiessling, V., Supported double membranes. *J Struct Biol* **2009**, *168* (1), 183-189.
81. Oncins, G.; Garcia-Manyes, S.; Sanz, F., Study of frictional properties of a phospholipid bilayer in a liquid environment with lateral force microscopy as a function of NaCl concentration. *Langmuir* **2005**, *21* (16), 7373-7379.
82. Xing, C.; Faller, R., Interactions of lipid bilayers with supports: a coarse-grained molecular simulation study. *J Phys Chem B* **2008**, *112* (23), 7086-94.
83. Winterhalter, M.; Frederik, P. M.; Vallner, J. J.; Lasic, D. D., Stealth(R) liposomes: From theory to product. *Adv Drug Deliver Rev* **1997**, *24* (2-3), 165-177.
84. biacore.com Sensor Chip L1. (accessed 22/09/13).
85. Walz, W., *Patch-Clamp Analysis Advanced Techniques*. Humana Press, Totowa New Jersey: <http://link.springer.com/book/10.1007/978-1-59745-492-6/page/1>, 2007; Vol. 38.
86. Hwang, W. L.; Holden, M. A.; White, S.; Bayley, H., Electrical behavior of droplet interface bilayer networks: Experimental analysis and Modeling. *J Am Chem Soc* **2007**, *129* (38), 11854-11864.
87. Seifert, U., Configurations of fluid membranes and vesicles. *Adv Phys* **1997**, *46* (1), 13-137.
88. Radler, J.; Strey, H.; Sackmann, E., Phenomenology and Kinetics of Lipid Bilayer Spreading on Hydrophilic Surfaces. *Langmuir* **1995**, *11* (11), 4539-4548.
89. (a) Tamm, L. K.; Mcconnell, H. M., Supported Phospholipid-Bilayers. *Biophys J* **1985**, *47* (1), 105-113; (b) Liu, J.; Conboy, J. C., Structure of a gel phase lipid bilayer prepared by the Langmuir-Blodgett/Langmuir-Schaefer method characterized by sum-frequency vibrational spectroscopy. *Langmuir* **2005**, *21* (20), 9091-9097.
90. Majd, S.; Mayer, M., Hydrogel stamping of arrays of supported lipid bilayers with various lipid compositions for the screening of drug-membrane and protein-membrane interactions. *Angew Chem Int Edit* **2005**, *44* (41), 6697-6700.
91. Mennicke, U.; Salditt, T., Preparation of solid-supported lipid bilayers by spin-coating. *Langmuir* **2002**, *18* (21), 8172-8177.
92. Albertorio, F.; Chapa, V. A.; Chen, X.; Diaz, A. J.; Cremer, P. S., The alpha,alpha-(1-->1) linkage of trehalose is key to anhydrobiotic preservation. *J Am Chem Soc* **2007**, *129* (34), 10567-74.
93. Holden, M. A.; Jung, S. Y.; Yang, T. L.; Castellana, E. T.; Cremer, P. S., Creating fluid and air-stable solid supported lipid bilayers. *J Am Chem Soc* **2004**, *126* (21), 6512-6513.
94. Kuhner, M.; Tampe, R.; Sackmann, E., Lipid mono- and bilayer supported on polymer films: composite polymer-lipid films on solid substrates. *Biophys J* **1994**, *67* (1), 217-26.
95. Calvert, P., Inkjet printing for materials and devices. *Chem Mater* **2001**, *13* (10), 3299-3305.

Abbreviations:

3D – three dimensional; A – deoxyadenylate; AFM – atomic force microscopy; AUC – area under the curve; bp – base-pair; BSST – bilayer self-spreading technique; ; C – deoxycytidilate (with regards to nucleic acid) or carbon; C₆₀ – fullerene; Ca – calcium; Calc – calculated; CHOL – cholesterol; CPS – counts per second; DE – Germany; DLS – dynamic light scattering; DNA – deoxyribonucleic acid; DOPC – dioleoylphosphatidyl choline; DOPE – dioleoylphosphatidyl ethanolamine; DOPS – dioleoylphosphatidyl serine; DPPC – dipalmitoylphosphatidyl choline; EPC – egg phosphatidyl choline; F – flakes (with regards to Pluronic®); f_o – resonant frequency (with regard to AFM probe); FW – formula weight; G – deoxyguanylate; HPLC – high-performance liquid chromatography; k – spring constant (with regard to AFM probe); K – potassium; L – liquid or length (with regards to Pluronic® or AFM probe, respectively); MALDI – matrix-assisted laser desorption/ionization; Mg – magnesium; MS – Microsoft; N – nitrogen; Na – sodium; P – phosphorous; PBS – phosphate buffer saline; Pcode – product code; PEO – polyethylene oxide; PPO – polypropylene oxide; PPP – phosphonium polymer; QELS – quasi-elastic light scattering; RH – relative humidity; RT – room temperature; s.c. – so called; SD – standard deviation; SLB – supported lipid bilayer; SPM – sphingomyelin; ToF-SIMS – time-of-flight secondary ion mass spectrometry; UHV – ultrahigh vacuum; UK – United Kingdom; US – United States of America; T – thymidylate or thickness (with regard to DNA or AFM probe, respectively); VDT – vesicle deposition technique; W – width (with regard to AFM probe); XPS – X-ray photoelectron spectroscopy.

2.1 Materials.

Lipids: egg phosphatidyl choline (EPC), cholesterol (CHOL) were purchased from Sigma-Aldrich (UK), while dioleoylphosphatidyl serine (DOPS), dioleoylphosphatidyl ethanolamine (DOPE), sphingomyelin (SPM), dipalmitoylphosphatidyl choline (DPPC), dioleoylphosphatidyl choline (DOPC) were purchased from Avanti Polar Lipids (US). Cholesteryl chloroformate was purchased from Fluka (UK). Polymers: Pluronics® L-62; L-64; F-68 have been obtained from Martin Redhead (University of Nottingham); the polyphosphonium polymer (PPP) from collaboration with Vanessa Loczenski (University of Nottingham). 19 base-pair (bp) oligomers were purchased from biomers.net (DE). PBS was purchased from PAA The Cell Culture Company (UK), Tris from Sigma-Aldrich and magnesium chloride from Sigma-Aldrich. Organic solvents (pyridine, DMF, dichloromethane) were purchased from English or German suppliers, as listed below. 14 mm mica discs, microscope slide-sized mica sheets and metal disc specimens were purchased from Agar Scientific (UK). FluidArray®-type surfaces were purchased from MicroSurfaces, Inc. (US). AFM probes: SCANASYST-FLUID+, RTESPA and MCLS were purchased from Bruker Nano (UK). Chemicals and consumables were used as received, unless otherwise stated. The structures of the key chemicals are presented in figure 2.1. The structure of PPP has been presented in figure 5.9. Product details are listed below:

Chapter 2: Materials and Methods.

- EPC – L- α -Phosphatidylcholine from egg yolk, Type XI-E, 100mg/mL in chloroform; (P-2772-250MG; Pcode: 101021317; Lot# HMBB7405V).
- CHOL – Cholesterol; (C8667-5G; Lot# 010M5303)
- DOPS - 1,2- Dioleoyl-sn-Glycero-3-[Phospho-L-Serine] (Sodium Salt); 25mg/mL in chloroform; (840035C; Lot# 181PS-313).
- DOPE - 1,2-Dioleoyl-sn-Glycero-3-Phosphoethanolamine; 25mg/mL in chloroform; (850725C; Lot# 181PE-351).
- SPM - Sphingomyelin (Egg, Chicken); 25mg/ml in chloroform; (860061C; Lot# ESM-106)
- DOPC - 1,2-Dioleoyl-sn-Glycero-3-Phosphocholine; 10mg/mL in chloroform; (850975C; Lot# 181PC-189).
- DPPC - 1,2-Dipalmitoyl-sn-Glycero-3-Phosphocholine; 10mg/mL in chloroform; (850355C; Lot# 160PC-258).
- 19bp oligonucleotides: 5'-gagatgtaaggccaggccg-3' (HPLC purified, FW (Calc) = 5904 g/mol; FW (MALDI found) = 5903 g/mol; T_m = 54°C, Length: 19bp); 5'-ctctacattccgggtccggc-3' (HPLC purified, FW (Calc) = 5717 g/mol; FW (MALDI found) = 5718 g/mol; T_m = 54°C, Length: 19bp).
- PBS – Dulbecco's Phosphate Buffer Saline (1x) without Ca⁺⁺ and Mg⁺⁺ (500ml; Cat No: H15-002; Lot: H00211-2880).
- Tris – Trizma[®] pre-set crystals pH7.4: Sigma-Aldrich (T7693-100G; Batch No: 114K5466).
- Magnesium Chloride – Anhydrous; Sigma-Aldrich (M-82661KG; Lot# 100K0176).
- Mica disc 14mm - Agar Scientific (10x) (F7019).
- Mica sheets - 3" x 1" Mica, Agar Scientific (20x) (G250-1).
- Metal disc specimen – SPM Specimen Discs 15mm, Agar Scientific (50x) (F7003).
- SCANASSYST-FLUID+ - silicon Tip on Nitride Lever with coat of Ti/Au 45 nm coat at the back side (Cantilever: T: 600 nm; f₀: 120-180 kHz; k: 0.7 N/m).
- RTESPA probe - 0.01-0.025 Ohm-cm Antimony (n) doped Si with 50 +/- 10 nm Al coat at the back side (Part: MPP-11120-10; Cantilever: T: 3.5-4.5 μ m; f₀: 347 – 393 kHz; k: 20-80 N/m; L: 115-135 μ m; W: 30-40 μ m).
- MCLT probe – silicon nitride tip 45 nm Ti/Au coat at the back side (Cantilever: T: 500-600 nm; f₀: 90-160 kHz; k: 0.3-1.2 N/m; L: 80-90 μ m; W: 13-23 μ m).
- Cholesteryl chloroformate – Fluka; 10g powder; \geq 99 %; Mr = 449.12 g/mol; Pcode: 26790; Lot & Filling code: 1259298 & 11706081.
- Pyridine – Riedel-de Haën; 1l; \geq 99.5%; Pcode: 33553; M = 79.10 g/mol; Lot: 52170.
- DMF – N,N-dimethyl formamide; Sigma-Aldrich; Pcode: 270547-1L; \geq 99.9%; FW = 73.09; Batch# STBB7278.
- Dichloromethane – Sigma-Aldrich; Pcode: 270997-1L; \geq 99.8%; MW: 84.93 g/mol; Lot# STBD2904V.
- FluidArray[®]-type surface – MicroSurfaces, Inc.; COOH_02_GS, Acid Glass Slide (High Density); Lot: 2005635; Density of COOH groups: (10¹⁴ per cm² \pm 5%).

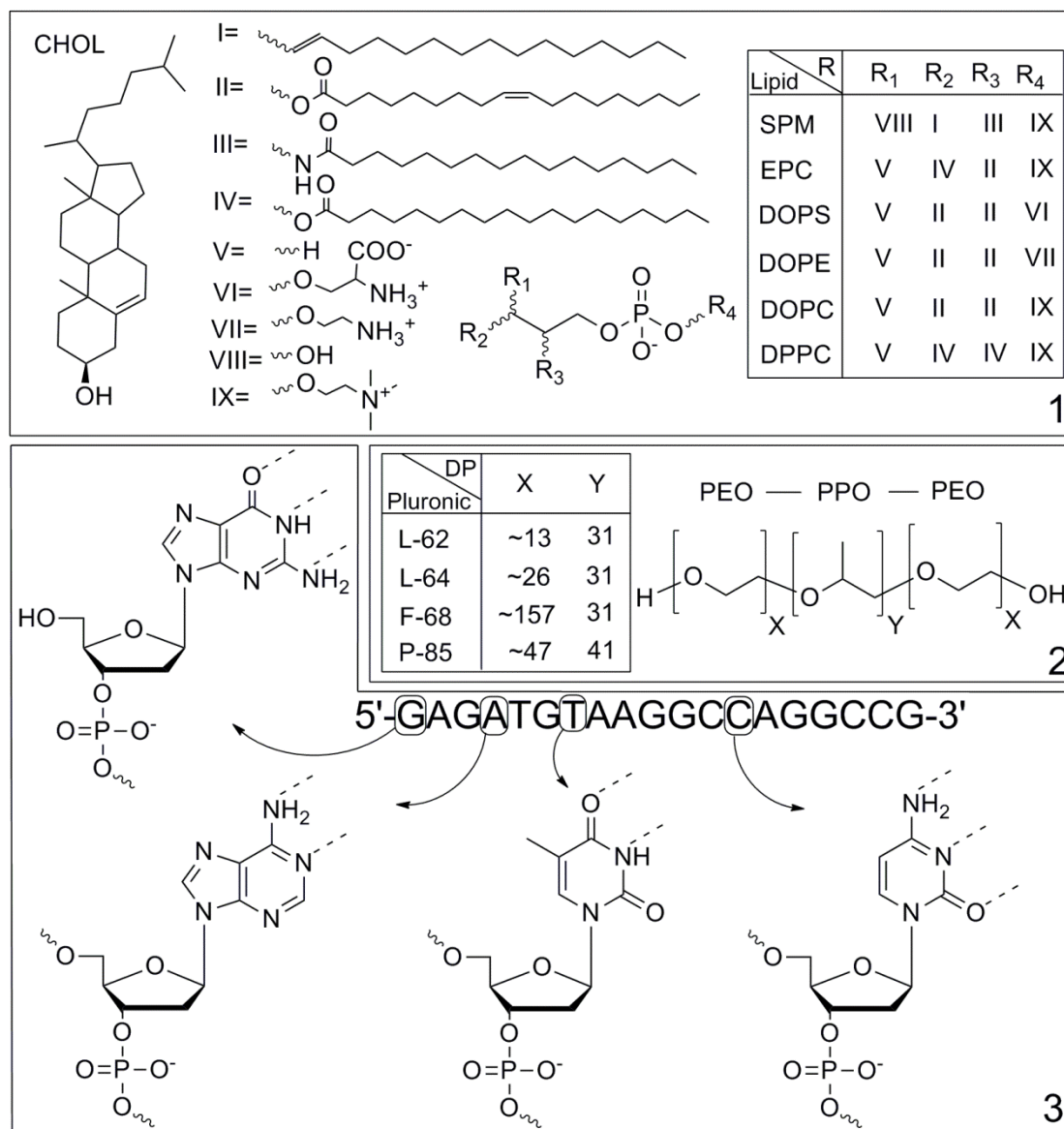


Figure 2.1. The chemical structures of lipids (1), PEO-PPO-PEO (Pluronic®) tri-block copolymers (2) and 19bp DNA strand (3). Abbreviations: CHOL – cholesterol; SPM – sphingomyelin; EPC – egg phosphatidyl choline; DOPS – dioleoylphosphatidyl serine; DOPE – dioleoylphosphatidyl ethanolamine; DOPC – dioleoylphosphatidyl choline; DPPC – dipalmitoylphosphatidyl choline; PEO – polyethylene oxide; PPO – polypropylene oxide; A – deoxyadenylate; G – deoxyguanylate; C – deoxycytidilate; T – thymidylate; DP – degree of polymerisation. Curly bonds are shown to indicate break in covalent bonds (1 and 3), whilst dashed lines are drawn to indicate the functionalities that form hydrogen bonds to other DNA bases (3).

2.2 Methods.

2.2.1 Preparation of supported lipid bilayers.

2.2.1.1 Calculation of lipid amounts for liposome preparation.

13 mM liposome solutions of the (%w/w): 23% CHOL (F.W. = 386.65 g/mol), 18% SPM (F.W. = 703.03 g/mol), 18% DOPE (F.W. = 744.04 g/mol), 7% DOPS (F.W. = 810.03 g/mol) and 33% EPC (F.W. = 768 g/mol) lipid mixture were used for SLB preparation¹. Therefore, 1 g of lipid mixture contains: 230 mg CHOL, 180 mg SPM, 180 mg DOPE, 70 mg DOPS and 330 mg EPC. If expressed in moles (mass of lipid/molecular weight of lipid), the 1g mixture of: 0.5949 mmol CHOL, 0.2560 mmol SPM, 0.2419 mmol DOPE, 0.0864 mmol DOPS and 0.4297 mmol EPC, would contain 1.6089 mmol lipid mixture molecules. Since 13 mM (0.013 moles of all lipids in 1000 ml solution) is required for the liposome solution, 0.0048 mmol (or 1.8586 mg) CHOL, 0.0021 mmol (or 1.4542 mg) SPM, 0.0020 mmol DOPS (or 1.4543 mg) DOPE, 0.0007 mmol (or 0.5655 mg) DOPS and 1.6089 mmol (or 2.6665 mg) EPC should be mixed together [as an example: 0.0048 mmol CHOL = (0.013 mmol lipids x 0.5949 mmol CHOL)/1.6089 mmol lipid or 1.8586 mg CHOL = 0.0048 mmol CHOL x 386.65 g/mol]. Effectively, 74.3 μ l 25 mg/ml CHOL, 58.2 μ l 25 mg/ml SPM, 58.2 μ l 25 mg/ml DOPE, 22.6 μ l 25 mg/ml DOPS and 26.7 μ l 25 mg/ml EPC chloroform lipid stock solutions were mixed, evaporated and resuspended in 4 ml 0.2 μ m Millipore water to give 2 mg/ml liposome stock.

2.2.1.2 Bilayer self-spreading technique (BSST)².

Chloroform solutions of lipids were mixed. 10 μ g lipid mixture was pipetted onto the centre of freshly cleaved 14 mm mica discs, glued to a metal disc specimen (Agar Scientific) and dried under a gentle stream of argon. Subsequently, the sample was pre-heated at 45°C on a hotplate for 5 minutes and incubated for 45 minutes under saturated liquid-vapour conditions after gentle addition of 100 μ l Millipore water onto the sample surface. Finally, the SLB-coated surface was rinsed in a gentle or vigorous manner in order to fabricate continuous or patch-like lipid film qualities, respectively.

2.2.1.3 Vesicle deposition technique (VDT)³.

The unilamellar lipid vesicles were prepared using extrusion method. Briefly, chloroform solutions of lipids were mixed and dried under argon to form a thin film in a round bottom flask. Subsequently, lipids were suspended in Millipore water at 2 mg/ml and exposed to 10 freeze-thaw cycles. The suspension was extruded 21 times through 100 nm polycarbonate membrane filters (Whatman) using hand-held system (Avanti Polar Lipids) to obtain unilamellar mixed lipid vesicles and stored at 4°C for a maximum of 30 days unless otherwise stated.

14 mm mica discs were glued to metal disc specimens and left overnight to settle. Freshly cleaved mica was pre-incubated with 10 mM magnesium chloride for 5 min at RT, rinsed once with Millipore water, heated up to 35°C on a hot plate with metal support providing even heat distribution and exposed to 160 µl 0.5 mg/ml suspension of liposomes for 45 minutes under saturated liquid-vapour conditions. Finally, the SLB-coated surface was gently rinsed with PBS three times at RT in order to produce porous film qualities. For continuous and multilayer film qualities the same protocol was followed using 60- and 100-minute incubation at 35°C, respectively. The patch-like topographies were produced through one vigorous and two gentle PBS rinses at the end of the protocol. The 60 minute incubation of 1.5 ml liposome solution with mica sheets glued to a glass microscope slide was used to prepare the microscope-sized model lipid films of porous qualities. The same protocol with the incubation at or above 45-50°C was used in order to obtain phase separated model SLBs.

2.2.2 Atomic Force Microscopy (AFM).

2.2.2.1 Background.

AFM or SFM (Scanning Force Microscopy) is a piezoelectric technique used for imaging, manipulating and measuring matter at the nanometre scale. Prof. Gerd Binnig, Prof. Calvin Quate and Prof. Christoph Gerber invented the first AFM in 1986⁴. Two major AFM applications are imaging⁵ and force measurements⁶. The principle behind AFM operation is depicted and explained in figure 2.2. Nanometre resolution, ability to analyse a wide range of materials in both air and liquid environments and little requirements for sample preparation are often mentioned as key strengths, whilst small scan size and low speed of imaging, image artefacts, destruction of fragile materials and difficult handling as common weaknesses of AFM⁷. AFM is frequently used in many disparate scientific areas, including biophysics⁸, material and surface sciences⁹, earth sciences¹⁰, food sciences^{5, 11}, crystallography¹² or metallurgy¹³. AFM can operate in a number of modes, such as contact, tapping or PeakForce® Tapping. Tapping mode is less destructive towards the sample of interest than contact mode. PeakForce® Tapping mode enables the use of reduced and controlled forces without the loss of resolution whilst *e.g.* imaging the sample of interest¹⁴.

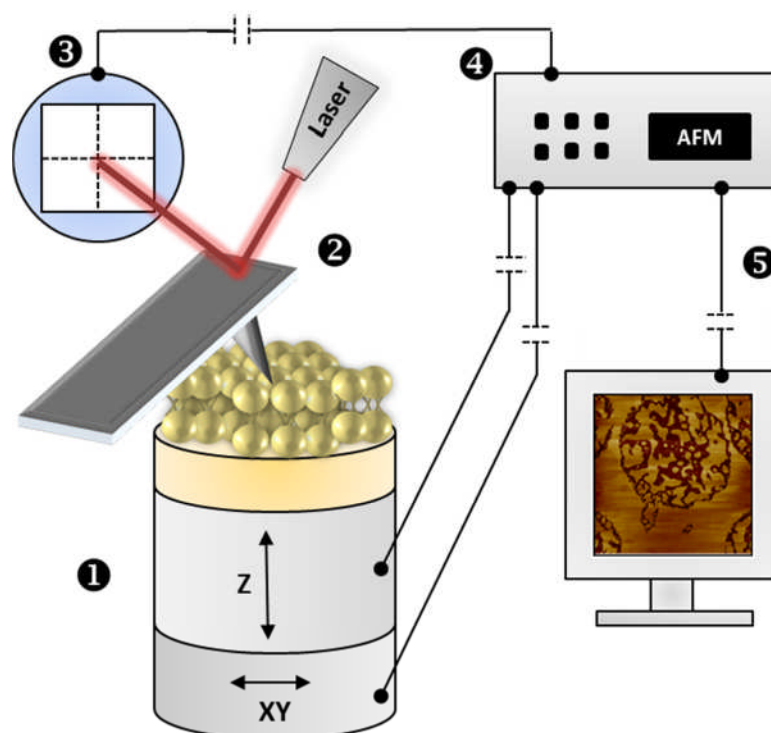


Figure 2.2 The schematic of AFM operation principle. (1) The AFM probe operates in X-Y-Z directions at or very close to the sample surface depending on the imaging mode. The X-Y positions are controlled through raster scanning signals applied to X-Y piezos, whilst the AFM feedback loop output signal adjusts the Z position. (2) In the resting state the laser beam is reflected off the back side of the AFM cantilever and focused onto centre of a photosensitive position detector. (3) In its basic mode of operation, throughout imaging interactions between the probe and sample result in changes in the cantilever deflection, and hence the position of the laser on the photodetector. (4) In constant-force imaging a feedback loop contradicts these changes and moves the z-piezo up or down to maintain constant cantilever deflection. (5) The AFM controller plus software translate the feedback signal into high resolution images. Figure elements are not in scale for presentation purposes.

2.2.2.2 Experimental.

2.2.2.2.1 Basic SLB imaging (chapter 3 and 4).

A MultiMode scanning probe microscope with Nanoscope IIIa controller (Bruker) and E-scanner (Bruker) was used in tapping mode to acquire images of 3-5 μm -sized sample areas (512 x 512 pixel resolutions) in aqueous buffer environments. Images were acquired using 'SCANASYST-FLUID+' AFM probes (Bruker) and the following parameters: 440V Z limit, 2.5-10 kHz sweep width, 26-40 kHz drive frequency, 800-1500 mV drive amplitude, 0.5-2 mV amplitude setpoint, 0.1-0.5 integral, proportional and look ahead gains, 1-3.05 Hz scan rate. Sample areas with a minimum of 50% SLB coverage were chosen and monitored over time.

2.2.2.2.2 SLB interaction studies (chapter 5).

A MultiMode scanning microscope with Nanoscope V controller (Bruker) and E-scanner (Bruker) was used in PeakForce® Tapping mode to acquire images of 3-5 μm -sized areas (512

x 512 pixel resolutions) in liquid environments. Images were acquired using 'SCANASYST-FLUID+' AFM probes (Bruker) and the following parameters: 2.3-3.1 μm Z limit, 4 V deflection limit, 8-10 nm amplitude, 0.05-0.15 V setpoint, 0.3-0.5 nm noise threshold, 1 Hz scan rate and automatically controlled feedback gains. Initially, sample areas with a minimum of 50% SLB coverage were chosen and briefly monitored. Subsequently, the excessive liquid on the sample was replaced with an appropriate solution of interacting agent and the AFM probe was re-introduced as soon as possible.

2.2.2.2.3 SLB air stability studies (chapter 1 and 6).

An EnviroScope scanning microscope with Nanoscope IIIa controller (Bruker) and humidity chamber (Triton Technology Ltd, UK), was used in tapping mode to acquire images of 3-5 μm -sized sample areas (512 x 512 pixel resolution) in either liquid or high humidity environments. Images in liquid were acquired using the F tip of 'MLCT' AFM cantilevers (Bruker) and the following manually-adjusted parameters: 440V Z limit, 2.5-5 kHz sweep width, 26-40 kHz drive frequency, 800-1500 mV drive amplitude, 0.5-2 mV amplitude setpoint, 0.1-0.5 integral, proportional and look ahead gains, 1-3.05 Hz scan rate. Images in air were acquired using 'RTESPA' AFM probes (Bruker) and the auto-tuned parameters as above apart from: 290-330 kHz drive frequency, 70-250 mV drive amplitude, 0.1-0.3 Hz amplitude setpoint, 0.5-4 gains. Initially, sample areas with a minimum of 50% SLB coverage were chosen and briefly monitored in liquid environments. Subsequently, the AFM probe was replaced, and a high humidity environment introduced and the excess of liquid on the sample removed. The AFM probe was re-introduced as soon as the remainder of the liquid on the sample surface had been evaporated using sample stage (Bruker) at 28 °C.

2.2.2.2.4 SLB microarray imaging (chapter 6).

A Dimension scanning microscope with a Nanoscope IIIa controller (Bruker) was used in tapping mode to acquire images from a minimum of three 10-25 μm -sized areas (512 x 512 pixel resolution) in liquid environments. Images were acquired using the F of 'MLCT' AFM cantilevers (Bruker) and the following parameters: 440V Z limit, 2.5-10 kHz sweep width, 26-40 KHz drive frequency, 500-3000 mV drive amplitude, 1-4 V amplitude setpoint, 0.1-0.8 integral, proportional and look ahead gains, 1-2 Hz scan rate.

2.2.2.2.5 Imaging of phosphonium-DNA polyplexes (chapter 5).

Particle imaging was performed as in section 2.2.2.2.2. Appropriate area scan sizes were chosen according to the particles size. For particle imaging mica was cleaved each time, pre-incubated with a freshly prepared 10mM 0.2 μm magnesium chloride solution, rinsed with 0.2 μm PBS and inserted into the AFM cell. Assessment of mica surface was performed

before the addition of particle solutions. Particle solutions were pipetted onto the mica surface using a Gilson's pipette.

2.2.2.2.6 Preparation and imaging of FluidArray®-like surfaces (chapter 6).

Acid Surface high density PEG-coated glass slides were purchased from MicroSurfaces, Inc. (US). Slides were stored at -20°C until used. The removal of the manufacturer packing, as well as resealing of the remaining slides was performed in a glove box saturated with argon, as recommended by the manufacturer. A single slide was used for all experiments.

The slide was immersed in 30 mM cholesteryl chloroformate DMF/dichloromethane (1:1 volume ratio) solution in a glass Petri dish, a catalytic amount of pyridine was added and the petri dish was incubated for 3.5 hours at RT on a rocking device. Next, the slide was rinsed with a number of solutions on the rocking device, in order to remove the remainder of the reagents: two 5-minute rinses with DMF/dichloromethane (1:1) and four 10-minute rinses with 0.2 µm Millipore water. Subsequently, the slide was dried under a gentle stream of argon and stored in desiccator for 12 hours until imaged with AFM. All AFM images were collected using a Dimension scanning microscope with a Nanoscope IIIa controller (Bruker). Imaging was performed in tapping mode in either air ('RTESPA' AFM probes) or liquid ('F' tip of 'MCLT' probes) environments in the same manner as reported above. In each step, several areas of the slide were imaged. Initially, the slide was imaged in air. Next, the slide was incubated with 2 ml of fresh, 0.5 mg/ml liposome solution at 35°C for 45 minutes, in order to coat the slide with a model SLB through the VDT protocol and imaged with AFM in a liquid environment. Subsequently, the slide was dried and incubated in a desiccator at RT for 23 hours and imaged with AFM in air. Finally, the 0.2 µm PBS solution was gently pipetted onto the slide surface and imaged with AFM in liquid.

2.2.2.2.7 AFM data analysis.

Images were processed using NanoScope Analysis software ver. 1.20 (Bruker). Each image was flattened (1st-2nd order, automatic threshold) and analysed.

2.2.2.2.7.1 Evaluation of SLB thickness.

'Section Analysis' was employed to evaluate the changes in SLB heights. Each marker line was drawn horizontally. The marker points were set at the average height for each feature within the marker line and vertical distance between the points was recorded. Each reported value was an average of 10 separate readings per image and expressed as $(\bar{x}_{15} \pm SD)^*$ nm. SD was calculated using stdev.p function in MS Excel 2007. An example of such analysis was depicted in appendix I.

* \bar{x}_{15} stand for an average of 15 measurements.

2.2.2.2.7.2 Quantification of SLB coverage.

'Particle Analysis' was employed to quantify SLB coverage for each image. The average number of particles (= pixels) within the SLB uncovered areas (including edge particles) was recorded through threshold adjustments according to the best possible fit, subtracted from the average total amount of particles within the image, expressed in percent and plotted against time. Each value was an average of separate three measurements and expressed as $(\bar{y}_3 \pm \Delta y)$. Measurement errors were calculated using total differential method and the equation below. See appendix I for a step-by-step guide for this approach.

$$(y_i = \frac{100 \cdot a_i}{a_{100}} \pm \Delta y_i = \left| \frac{100}{a_{100}} \right| \cdot \Delta a_i + \left| \frac{100 \cdot a_i}{a_{100}^2} \right| \cdot \Delta a_{100})$$

y_i – SLB coverage at i time point [%]

Δy_i – error of SLB coverage at i time point [%]

100 – multiplication factor [%]

a_i – average number of particles within the SLB covered area at i time point [-]

a_{100} – average total number of particles within the recorded area [-]

Δa_i – standard deviation of a_i [-]

| ... | - absolute value

2.2.2.2.7.3 Evaluation of particle size.

'Section Analysis' was used to evaluate the changes in particle size. Each marker line was drawn in 3 directions: horizontally, vertically and in diagonal (from left to right at 45° angle against the horizontal). The marker points were set half-way at both sides of each peak and the horizontal distances were recorded. Each reported value was an average of 3 separate readings per image for all particle images obtained and expressed as $(\bar{x}_{6.8} \pm SD)$ nm. SD was calculated using stdev.p function in MS Excel 2007. An example of such analysis was depicted in appendix I.

2.2.3 Time-of-Flight Secondary Ion Mass Spectrometry (ToF-SIMS).

2.2.3.1 Background.

ToF-SIMS is an analytical technique used for studying first two nanometres of material surfaces. Prof. Alfred Benninghoven is considered as one of the key ToF-SIMS inventors¹⁵. ToF-SIMS allows to: establish qualitative (and rarely quantitative) composition of material surfaces, visualise the distribution of chemical species on the surface and determine the distribution of chemical species as a function of depth from the surface. The principle behind ToF-SIMS operation is depicted and explained in figure 2.3. High mass resolution, high sensitivity and capability of sub-micron scale chemical mapping are often mentioned as key

strengths, whilst poor ability to quantify chemical species, image shift when changing between positive and negative modes, the requirement for charge compensation of the primary ion-beam ionized sample surface with electron flood gun and complex data analysis as common weaknesses of ToF-SIMS. ToF-SIMS is frequently used in material and surface sciences¹⁶, earth sciences¹⁷, high throughput applications¹⁸, forensics¹⁹ and pharmacy²⁰. Depending on the application, various primary ion sources may be used, e.g. bismuth (I), fullerene (C₆₀).

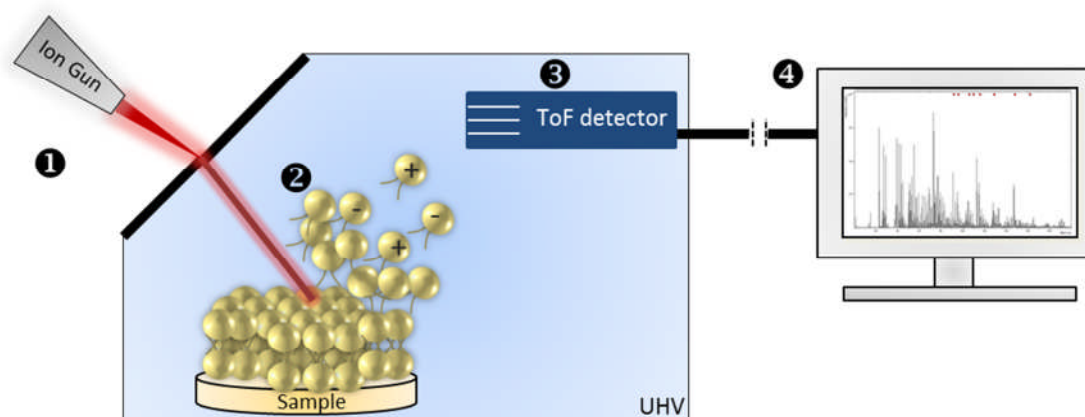


Figure 2.3. The schematic of ToF-SIMS operation principle. (1) The ion gun generates a primary ion beam through short pulses. (2) The energy of primary ions is dissipated within the first 2 nm of the sample surface triggering both series of binary collisions and ejection (sputtering) of so called secondary chemical species (e.g. ions, neutral molecules) originating from the surface. It is approximated that 1 primary ion disrupts 10 nm² of the surface (s.c. static limit). (3) Secondary ions are accelerated onto a mass spectrometer via high voltage potential between the mass analyser and sample surface and travel through a time-of-flight (ToF) detector before reaching the mass analyser. The secondary ions of different masses arrive to the mass analyser at different times, because their velocities in ultrahigh vacuum (UHV) are different. These arrival times are measured for each secondary ion. (4) ToF-SIMS software generates spectra based on the time to mass conversions for all secondary ions captured by the ToF detector. Since the primary ion-surface interaction is limited to a small area around the ion beam, a precise control over the primary ion beam enables collecting chemical spectra from every pixel of the targeted surface area of the sample through a raster scanning approach. This is transferred onto a chemical image via ToF-SIMS software. Figure elements are not in scale for presentation purposes.

2.2.3.2 Experimental.

2.2.3.2.1 ToF-SIMS: sample preparation.

After preparation samples were rinsed once with Millipore water, dried in air and inserted onto the ToF-SIMS sample stage. ION-TOF IV Time-of-Flight Secondary Ion Mass Spectrometer was used to obtain spectra of dry lipid films on mica surfaces, using a C₆₀ primary ion sources (two 500 µm x 500 µm surface areas per sample) in both positive and negative modes.

2.2.3.2.2 ToF-SIMS: data analysis.

SurfaceLab 6 (ION-TOF) software was used to analyse ToF-SIMS spectra. Initially, all spectra were calibrated against: in a positive and ions in a negative mode. The presence of key peaks for EPC, CHOL, DOPS, DOPE and SPM single lipid samples was confirmed through comparisons against literature, as well as chemical structures for each lipid or their fragments using ChemBioDraw software. Due to structural similarities of secondary ions for single lipid samples, a list of lipid-specific peaks within the model lipid films was identified *via* manual, peak-by-peak comparisons of lipid mixture spectra with the single lipid spectra for each mode. This enabled to establish the single lipid-representative peak list (table 3.1). Next, the peak lists was used to rebuild the images of chemical distribution of lipids within the model lipid films. Subsequently, the images of the highest mass counts were selected for presentation purposes. Also, the list of representative peaks was used for semi-quantitative evaluation of lipid content within the mixture. For that purpose, the areas under the peaks were calculated using 'Statistics' button in IONTOF software as an absolute count value for each peak, divided by the total count value for each spectrum and plotted as a bar chart. Each normalised peak intensity value was an average of two data points and was expressed as ($\bar{x}_2 \pm SD$). SD values were plotted using MS Excel 2007 and stdev.p function. Graph was prepared using GraphPad software.

2.2.4 X-ray Photoelectron Spectroscopy (XPS).

2.2.4.1 Background.

XPS (or ESCA – Electron Spectroscopy for Chemical Analysis) is a quantitative analytical technique used for studying first 10 nanometers of material surfaces. Kai M.B. Siegbahn received Nobel Prize in 1924 for discoveries and research on XPS²¹. XPS allows to: establish the elemental composition of or element distribution within material surfaces, measure the chemical and electronic state of surface elements, as well as calculate empirical formulas and/or contaminations of pure materials. The principle behind XPS operation is depicted and explained in figure 2.4. High quantitative accuracy and relatively short analysis time and roughly 100 ppm detection limit are often mentioned as key strengths, whilst sample degradation during analysis and changes in sample morphology due to the presence of vacuum as common weaknesses of XPS. XPS is frequently used in material and surface sciences²², earth sciences²³, metallurgy²⁴, forensic science²⁵ and medicine²⁶. It is worth adding that X-ray photoelectron spectrometers enable setting the exact energy and time, at which the X-rays are contacting the sample surface, therefore spectra within both the wide and narrow regions of binding energies of the chemical bonds can be collected.

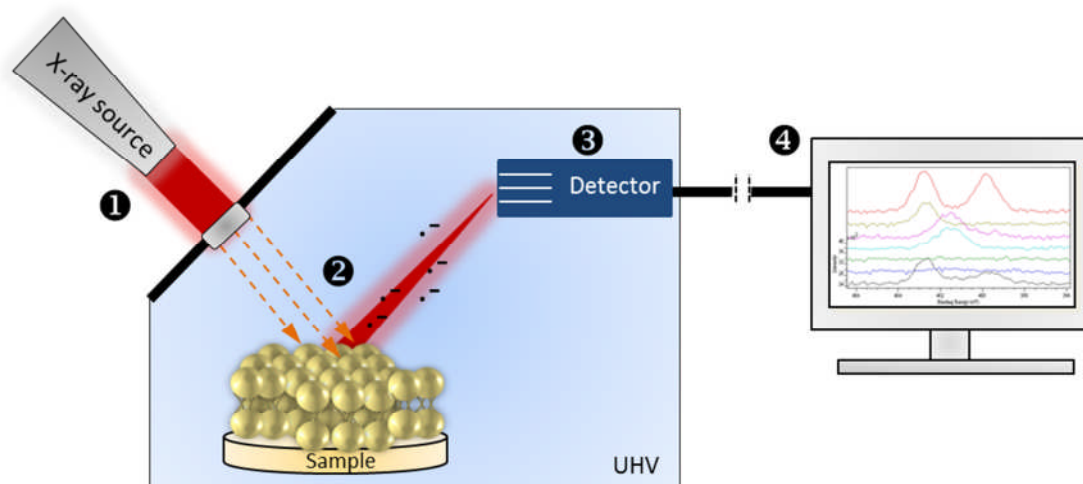


Figure 2.4. The schematic of XPS operation principle. (1) The X-ray source generates a beam of photons (X-rays), electrons and radiation heat. Those travel through a monochromator in order to purify the photoelectrons that are transmitted onto the sample. (2) Once the X-rays reach the sample, their energy is transferred onto the sample atoms resulting in the release of photoelectrons from the sample (s.c. photoelectric effect) under the ultra-high vacuum (UHV). Only photoelectrons from the first 5-10 nm of the sample surface (s.c. core level) reach the photodetector. (3) Detector measures kinetic energies and number of electrons originating from the samples surface. Here, electrons may or may not lose their kinetic energy on the way to the photodetector, which is manifested as a background noise or specific peak on the XPS spectrum, respectively. (4) The XPS software generates spectra as a function of binding energy (kinetic energy) vs. number of counts for each photoelectron originating from the sample elements. Here, since the number of count per second (CPS) for each chemical specie on the surface is proportional to the amount of the specie in the sample, as well as the binding energy values are specific not only for each element (e.g. oxygen, carbon, nitrogen), but also for each functional group (e.g. amine, ammonium groups), a quantitative information about the content of both functional groups and chemical elements on the sample can be extracted from XPS spectra, based on both peak fitting analysis and comparison of normalised peak intensity values (areas under the curve). Figure elements are not in scale for presentation purposes.

2.2.4.2 Experimental.

2.2.4.2.1 XPS: sample preparation.

After preparation SLBs were rinsed once with Millipore water, dried in air, inserted onto the XPS sample stage and analyzed using a Kratos Ultra Axis X-Ray Photoelectron Spectrometer. High-resolution spectra in N1s region were acquired from surfaces using mono-chromated Aluminium X-ray gun with a charge-compensating electron flood (three 300 μm x 700 μm surface areas per sample for 301 s).

2.2.4.2.2 XPS: data analysis.

XPS spectra were analysed using CasaXPS ver. 2.3.10 software (Neal Fairley). Initial calibration of the spectra was performed using kratos.lib file (University of Nottingham). The

background lines were established for each peak at appropriate binding energy regions. Each peak was labelled and highlighted with a light-green band available through software. The calculation of the SLB thickness was based on the method developed by Seale and Spencer²⁷. For XPS-measured calculation of sample coverage (thickness), the K2p and C1s peak intensities on XPS spectra of both lipid film samples in the wide region were initially extracted from the software as CPS values. Next, the values were plotted (figure 3.7) and the linear correlation equations were calculated. The extrapolated intercept values for these equations were assigned to I_c^∞ parameter, while the C1s peak intensities to I_c parameter in the equation below. The lipid film thickness values were expressed as $(\bar{x}_3 \pm SD)$ nm, based on three XPS spectra in the wide region. All calculations were performed in MS Excel 2007 using average and stdev.p functions.

$$d_c = -L_c(E_c) \cdot \cos \theta \cdot \ln \left[1 - \left(\frac{I_c}{I_c^\infty} \right) \right]$$

d_c – thickness of the lipid film [nm].

$L_c(E_c)$ – effective attenuation length at the energy of the C1s core level [nm].

Value 3.6 nm was taken from the literature²⁷.

θ – take-off angle between the normal to the surface and the plane of the analyser [°]. Value 50° was established manually between 20-60°.

I_c – intensity of the C1s core level [CPS].

I_c^∞ – intensity of an infinitely thick layer of the same lipid film at the same spectrometer [CPS].

For the N1s spectra, appropriate functional group populations were identified as components for every sample, basing on reference binding energy values for nitrogen functional groups²⁸. The percentage content of each component within the peak was established using manual fitting analysis available through software. Since three separate spectra were obtained during the XPS analysis, each component value within the ratio was averaged and expressed as $(\bar{x}_3 \pm SD)$ %. SD values were calculated using stdev.p function in MS Excel 2007. The empirical ratios were compared with the theoretically-expected ratio that was calculated in the following section.

For P2p spectra the procedure was similar. The peak intensity values for each spectrum were extracted from the CasaXPS software as CPS values and further calculations were performed in MS Excel 2007. Again, each peak intensity value was expressed as $(\bar{x}_3 \pm SD)$ CPS, since three separate measurements were performed during XPS analysis. SD values were calculated as above. The theoretically-expected intensity of the lipid film samples was calculated in the section below.

2.2.4.2.2.1 Calculation of the theoretical lipid content and ratio between: $-N^+(CH_3)$, $=N^+(H_2)$ and $-NH-$ nitrogen groups for lipid film samples analysed with XPS in the N1s region.

Since the peaks within XPS N1s spectra represent the total amount of electrons originating from nitrogen-containing lipid molecules, the experimentally established ratios are equivalent to the ratio between the contents (in per cent) of the numbers of moles of nitrogen atoms organised in three populations: $-N^+(CH_3)$, $=N^+(H_2)$ and $-NH-$. Therefore, in order to establish the theoretical ratio between the $-N^+(CH_3)$, $=N^+(H_2)$ and $-NH-$ groups, the number of moles of nitrogen atoms per lipid in each sample were calculated, classified in an appropriate population and expressed as a per cent of the total number of such moles. Since 160 μ l 0.5 mg/ml liposome solution was used to prepare each model SLB using VDT, 80 μ g of lipid mixture was used per each sample. 80 μ g of lipid mixture was equivalent to mixing: 18.586 μ g CHOL, 5.655 μ g DOPS, 26.665 μ g EPC, 14.543 μ g DOPE and 14.452 μ g SPM. The CHOL molecule did not contain nitrogen atoms; hence it did not contribute towards the total number of moles of nitrogen atoms in the sample. Therefore, CHOL was not considered for further calculations. The single lipid masses, once divided by molecular weight for each lipid, were equivalent to: 6.9815 nmol DOPS (F.W. = 810.03 g/mol), 19.5455 nmol DOPE (F.W. = 744.04 g/mol), 20.5567 nmol SPM (F.W. = 703.03 g/mol) and 34.7201 nmol EPC (F.W. = 768 g/mol) in each sample. Since the single lipids contained 1,1,2,1 moles of nitrogen atoms per one mole of a lipid molecule, each lipid in the sample was equivalent to: 6.9815 nmol, 19.5455 nmol, 41.1134 nmol and 34.7201 nmol of nitrogen atoms for the amount of DOPS, DOPE, SPM, EPC in the sample, respectively. Therefore, the total number of moles of nitrogen atoms per sample was 102.3605 nmol. Since this sum was 100% of the moles of nitrogen atoms per sample and according to the XPS all $-NH-$; $=N^+(H_2)$ and $-N^+(CH_3)_3$ groups originated from: 45% SPM + 13% DOPS (0.45 x 41.1134 nmol SPM + 0.13 x 6.9815 nmol DOPS); 100% DOPE + 87% DOPS + 8% SPM (1 x 19.5455 nmol DOPE + 0.87 x 6.9815 nmol DOPS + 0.08 x 41.1134 nmol SPM) and 100% EPC + 47% SPM (1 x 34.7201 nmol EPC + 0.47 x 41.1134 nmol SPM), the molar content [%] of $-NH-$; $=N^+(H_2)$ and $-N^+(CH_3)$ in the lipid mixture equalled: 19 %, 28 % and 53 %, respectively. Percentage content of each lipid within a peak population was also calculated, e.g. the SPM content within the amine population is 18%, as $18\% = [(0.45 \times 41.1134) \text{ nmol SPM} \times 100\%] / 102.3605 \text{ nmol lipids}$. The calculations starting from 10 μ g (equivalent to the amount of lipids used for BSST) led to the same ratio, because the molar content values are independent of the total mass of lipids that are used for the sample preparation.

2.2.4.2.2.2 Calculation of theoretical intensity of the P2p peak for lipid film samples analysed with XPS in the P2p region.

Since the single phosphorous peaks on the lipid film spectra in the P2p regions correlate quantitatively with the amounts of phosphorous within the sample, the XPS-reported intensities for phosphorous within the single lipid samples corrected by their concentration in the lipid mixture could have been summed, indicating the peak intensity for phosphorous in the lipid mixture. Since 80 μg of lipids pipetted on the surface was equivalent to: 6.9815 nmol DOPS, 19.5455 nmol DOPE, 20.5567 nmol SPM and 34.7201 nmol EPC and each of the lipids had 1 mole of phosphorous atoms per 1 mole of lipid molecule, the total amount of moles of phosphorous per sample was 81.8038 nmol. If expressed in per cent, the molar content of phosphorous atoms of DOPS, SPM, DOPE and EPC in the lipid mixture was: 9 %, 25 %, 24 % and 42 %, respectively. Since the mean peak intensities for single lipid P2p spectra were: (548 \pm 18) CPS for DOPS, (430 \pm 9) CPS for SPM, (318 \pm 15) CPS for DOPE and (197 \pm 88) CPS for EPC, the counts per second of each lipid in the lipid mixture were: (49 \pm 2) CPS for DOPS, (107 \pm 2) CPS for SPM, (76 \pm 4) CPS for DOPE and (83 \pm 37) CPS for EPC, respectively (*e.g.* for DOPS: 49 = 0.09 x 548 CPS and 2 = 0.09 x 18). The sums of these intensity and error values were (316 \pm 44).

2.2.5 Dynamic Light Scattering (DLS).

2.2.5.1 Background.

DLS (or QELS - quasi-elastic light scattering or photon correlation spectroscopy) is an analytical technique used for studying the size and behaviour of molecules and particles dispersed in liquid environments. Prof. Bruno H. Zimm's work pioneered the development of DLS²⁹. DLS allows to measure particle or molecular size, as well as size distribution. The principle behind DLS is depicted and explained in figure 2.5. Short analysis time, user-friendliness and system automation are often mentioned as key strengths, whilst requirements for dust-free and laser-transparent solutions as common weaknesses of DLS. DLS is frequently used in life sciences³⁰, particle engineering³¹ and many industries.

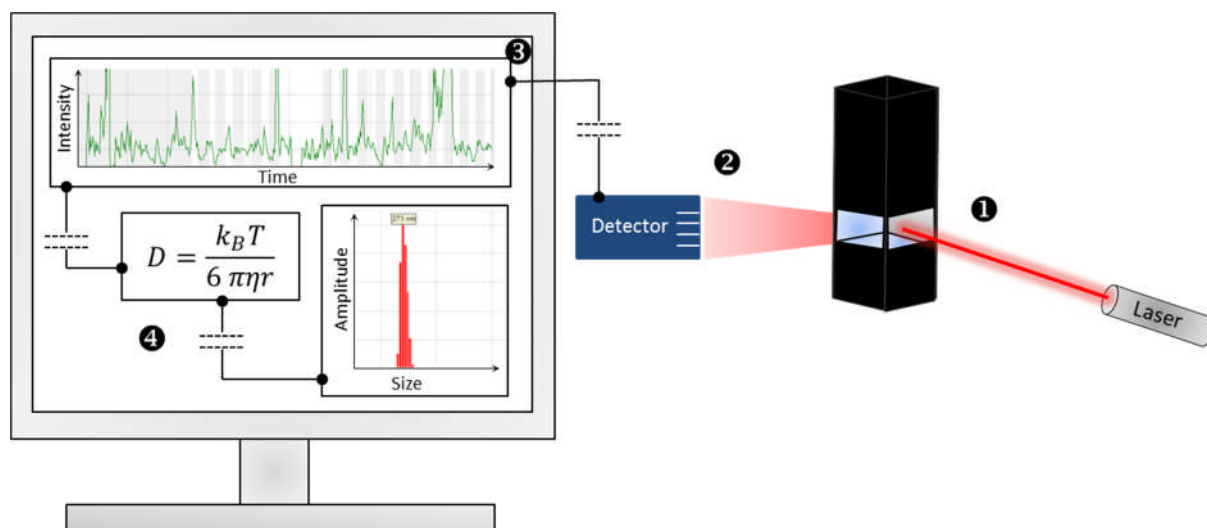


Figure 2.5. The schematic of DLS operation principle. (1) A laser beam is scattered in all directions once it hits a dispersion of maximally 250-nm-sized particles. (2) The Brownian motions of the particles trigger constructive or destructive interferences of the scattered light beams. (3) Photodetector records the intensity fluctuations of the scattered light over time. (4) The software calculates the hydrodynamic radius of the particle, based on the Stokes-Einstein relation. Figure elements are not in scale for presentation purposes.

2.2.5.2 Experimental.

2.2.5.2.1 DLS: sample preparation.

10 μg DNA/150ul of particle dispersion was pipetted into a clean DLS-suitable quartz cuvette and inserted into Viscotec DLS Model 802 (Viscotec) sample stage. Measurements were recorded at 300-1000 k counts laser intensity stabilized through the adjustments of sample transparency at 20 °C. All solutions used for sample preparation were pre-filtered through 0.2 μm carbon filters.

2.2.5.2.2 DLS: data analysis.

OmniSIZE ver. 3.0.0.295 (Malvern) software was used for data analysis. A minimum of 30 readings were used to evaluate the o diameter radius of the particles, based on the number distribution values. DLS measurements were performed directly before the AFM studies. Particle size values were averaged and expressed as ($\bar{x}_6 \pm \text{SD}$). SD values were calculated in MS Excel 2007 using stdev.p function.

2.2.6 Piezoelectric inkjet print head technology.

2.2.6.1 Background.

Piezoelectric inkjet print head technology is a non-contact dispensing technique used for an automated deposition of picolitre volumes of low viscosity solutions on material surfaces. A Japanese company Epson is considered a world-wide pioneer of this technology. Piezoelectric inkjet print head technology allows to: coat surface materials with many

substances using a desired amount of layers (2D and 3D printing), perform chemical reactions at picolitre scales (in-drop reactions) or create microarrays for high throughput screening applications. The principle behind the piezoelectric inkjet print head operation is depicted and explained in figure 2.6. High precision and accuracy, small amounts of materials and automation with regards to liquid handling are often mentioned as key strengths, whilst the requirements for low viscosity and small particle size solutions, common nozzle blockages and high cost of equipment as common weaknesses of this technique. Piezoelectric inkjet print head technology is frequently used in material and surface sciences^{16, 32}, arts and graphics³³, as well as in biotechnology³⁴ and pharmaceutical industries³⁵.

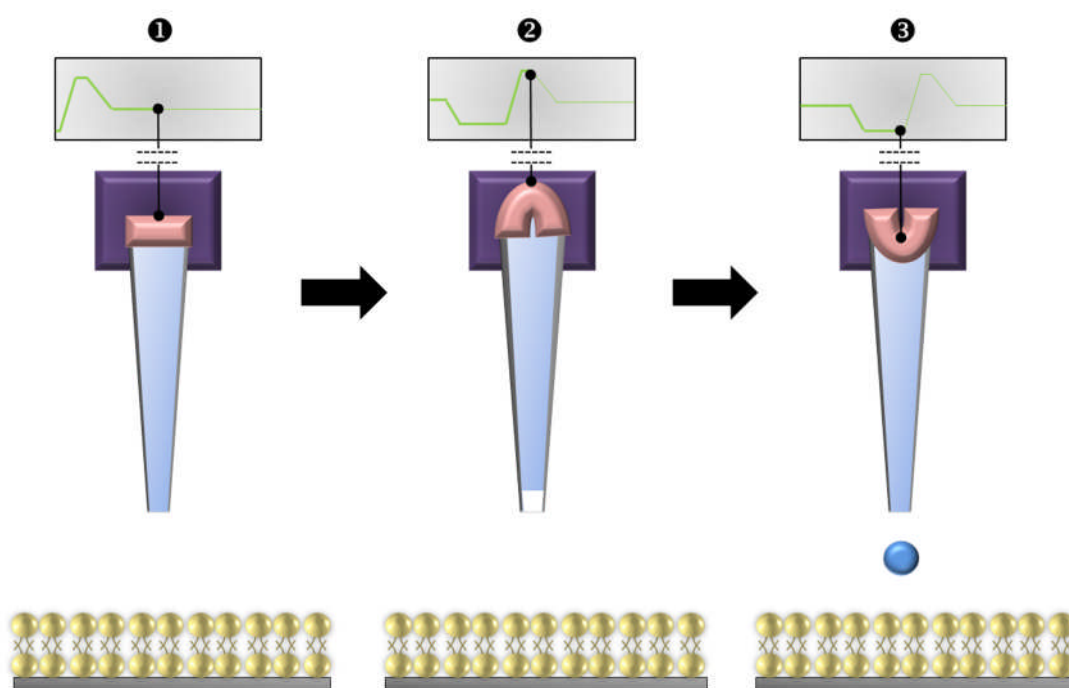


Figure 2.6. *The schematic of piezoelectric inkjet print head technology operation principle. (1) The nozzle is filled with liquid in the steady state. (2) As soon as electric charge is applied the piezoelectric material changes shape. (3) Dramatic decrease of the electric charge applied causes the piezoelectric material to bend in opposite direction and triggers propelling a precise volume of the liquid out of the nozzle. Figure elements are not in scale for presentation purposes.*

2.2.6.2 Experimental.

The excess of liquid on freshly prepared slide-sized model lipid films through the vesicle deposition protocol was removed and the samples were quickly placed onto a 28-30°C sample stage at 70 % relative humidity environment of the ink-jet printing chamber. Once the remaining water was evaporated, the stage temperature was decreased to 2-3°C above the theoretical dew point. Subsequently, six 195 nl spots were printed in one row 2 mm

apart (149 V, 25 μ s, Z = 700 μ m), as presented in figure 6.5B, on the lipid film using clean and patent Delivery Piezo Dispense Capillary (ID: 8561) and the sciFlexarrayer S5 (Scienion, DE). Finally, the solution drops were incubated for 1 hour with the film at 70 % humidity; one slide was immersed in copious amounts of Millipore water. Next, both slides were transferred onto the ToF-SIMS sample stage.

2.2.7 Preparation of Pluronic solutions (chapter 4 and 6).

The required amount of a polymer was weighted out using a laboratory balance and a glass vial, exposed to a gentle stream of argon for 10 minutes and dissolved in a sterile, 0.2 μ m PBS (chapter 4) or Millipore water (chapter 6) through vortexing. Once the bubbles disappeared from the liquid surface, appropriate dilutions were prepared using the solvent of interest. Each solution was prepared fresh before the experiment.

2.2.8 Preparation of DNA complexes (chapter 5).

The amounts of DNA and polymer were calculated, as follows. In order to obtain a polyplex at 1:1 P:P ratio, each mole of DNA phosphate groups required 1 mole of phosphonium groups within a polymer (or in other words 1 mole of monomer). Since 1 μ g DNA has 3 nmol of phosphate groups³⁶, a sample containing 10 μ g DNA (30 nmol phosphate groups) required 30 nmol phosphonium groups in order to form a complex at 1:1 ratio. The amount of DNA [μ g] in the sample was found from the molecular mass of DNA ($M_{DNA} = 11625$ g/mol), which was calculated as a sum of molecular weights of oligonucleotides reported by a manufacturer ($M_A = 5907.5$ g/mol; $M_B = 5717.5$ g/mol). The amount of polymer used for complexation was found, based on the molecular mass of the monomer used as a substrate for polymerisation. The equation below was established to simplify the calculations:

$$m_{polymer} = 3 \cdot 10^{-9} \cdot C_{DNA} \cdot V_{DNA} \cdot M_{DNA} \cdot R \cdot M_{monomer}$$

- $m_{polymer}$ – mass of the polymer needed for DNA polyplex at R ratio [μ g]
- C_{DNA} – molar concentration of DNA aliquot solution [μ M]
- V_{DNA} – volume of DNA aliquot solution [μ l]
- M_{DNA} – molecular weight of DNA molecule [g/mol]
- R – P:P monomer/DNA ratio for complex formation [-]
- $M_{monomer}$ – molecular weight of the monomer [g/mol]
- 3×10^{-9} – multiplication factor

DNA stock solutions (100 μ M) was prepared following the manufacturer protocol and stored at -20°C until used. Before use, 20 μ M aliquots of the stock solution were prepared in sterile PBS and stored at +4°C for up to a month. Polymer stock solution (2 mg/ml) was prepared

through dissolution of an appropriate mass of polymer in sterile PBS and filtered through 20 μm carbon filters.

75 μl dilutions of DNA and phosphonium polymer at appropriate concentrations were prepared in sterile PBS. DNA was gently pipetted into the polymer solution, vortexed for 60 seconds, left on a roller for 30 minutes and used for DLS and AFM studies. Eppendorf tubes with DNA polyplexes were stored on ice whenever possible. Particle dilutions for the AFM kinetic studies were prepared using one particle solution and sterile 0.2 μm PBS.

2.2.9 Preparation of text and figures.

The thesis was written using the Microsoft Word 2010 software. References were included using the EndNote X-5 add-in for Microsoft Word available through the University of Nottingham. All figures and graphs were drawn using one or more of the following computer programs: Microsoft PowerPoint 2010, ChemBioDraw 2010 and ChemBio3DDraw 2010, Gimp 2, Microsoft Excel 2010, OriginPro8, GraphPad Prism 6 available online either as freeware or through the University of Nottingham.

2.3 References

1. Soliman, M.; Nasanit, R.; Allen, S.; Davies, M. C.; Briggs, S. S.; Seymour, L. W.; Preece, J. A.; Alexander, C., Interaction of reducible polypeptide gene delivery vectors with supported lipid bilayers: pore formation and structure-function relationships. *Soft Matter* **2010**, *6* (11), 2517-2524.
2. Radler, J.; Strey, H.; Sackmann, E., Phenomenology and Kinetics of Lipid Bilayer Spreading on Hydrophilic Surfaces. *Langmuir* **1995**, *11* (11), 4539-4548.
3. Seifert, U., Configurations of fluid membranes and vesicles. *Adv Phys* **1997**, *46* (1), 13-137.
4. (a) Binnig, G.; Quate, C. F.; Gerber, C., Atomic Force Microscope. *Physical review letters* **1986**, *56* (9), 930-933; (b) Binnig, G.; Gerber, C.; Stoll, E.; Albrecht, T. R.; Quate, C. F., Atomic Resolution with Atomic Force Microscope. *Europhys Lett* **1987**, *3* (12), 1281-1286.
5. Gunning, A. P.; Wilde, P. J.; Clark, D. C.; Morris, V. J.; Parker, M. L.; Gunning, P. A., Atomic force microscopy of interfacial protein films. *J Colloid Interf Sci* **1996**, *183* (2), 600-602.
6. Gunning, A. P.; Kirby, A. R.; Fuell, C.; Pin, C.; Tailford, L. E.; Juge, N., Mining the "glycocode"-exploring the spatial distribution of glycans in gastrointestinal mucin using force spectroscopy. *Faseb J* **2013**, *27* (6), 2342-2354.
7. Carpick, R. W.; Salmeron, M., Scratching the surface: Fundamental investigations of tribology with atomic force microscopy. *Chem Rev* **1997**, *97* (4), 1163-1194.
8. Alessandrini, A.; Facci, P., AFM: a versatile tool in biophysics. *Meas Sci Technol* **2005**, *16* (6), R65-R92.
9. Magonov, S. N.; Reneker, D. H., Characterization of polymer surfaces with atomic force microscopy. *Annu Rev Mater Sci* **1997**, *27*, 175-222.
10. Rachlin, A. L.; Henderson, G. S.; Goh, M. C., An Atomic Force Microscope (Afm) Study of the Calcite Cleavage Plane - Image Averaging in Fourier Space. *Am Mineral* **1992**, *77* (9-10), 904-910.
11. Gunning, A. P.; Kirby, A. R.; Parker, M. L.; Cross, K. L.; Morris, V. J., Utilizing ATOMIC FORCE MICROSCOPY in Food Research. *Food Technol-Chicago* **2010**, *64* (12), 32-37.
12. McPherson, A.; Malkin, A. J.; Kuznetsov, Y. G.; Plomp, M., Atomic force microscopy applications in macromolecular crystallography. *Acta Crystallogr D* **2001**, *57*, 1053-1060.
13. Yin, X.; Miller, J. D., Wettability of kaolinite basal planes based on surface force measurements using atomic force microscopy. *Miner Metall Proc* **2012**, *29* (1), 13-19.
14. Foster, B., New Atomic Force Microscopy (AFM) Approaches Life Sciences Gently, Quantitatively, and Correlatively. *Am Lab* **2012**, *44* (4), 24-+.
15. (a) Herzog, R. F. K.; Viehbock, F. P., Ion Source for Mass Spectrography. *Phys Rev* **1949**, *76* (6), 855-856; (b) Liebl, H. J.; Herzog, R. F. K., Sputtering Ion Source for Solids. *J Appl Phys* **1963**, *34* (9), 2893-8; (c) Benninghoven, A., Observing surface oxidation of molybdenum with the static method of secondary ion mass spectroscopy. *Chem Phys Lett* **1970**, *6* (6), 626-628.
16. Celiz, A. D.; Hook, A. L.; Scurr, D. J.; Anderson, D. G.; Langer, R.; Davies, M. C.; Alexander, M. R., ToF-SIMS imaging of a polymer microarray prepared using ink-jet printing of acrylate monomers. *Surf Interface Anal* **2013**, *45* (1), 202-205.
17. Thiel, V.; Sjoval, P., Using Time-of-Flight Secondary Ion Mass Spectrometry to Study Biomarkers. *Annu Rev Earth Pl Sc* **2011**, *39*, 125-156.
18. (a) Hook, A. L.; Chang, C. Y.; Yang, J.; Scurr, D. J.; Langer, R.; Anderson, D. G.; Atkinson, S.; Williams, P.; Davies, M. C.; Alexander, M. R., Polymer microarrays for high throughput discovery of biomaterials. *Journal of visualized experiments : JoVE* **2012**, (59), e3636; (b) Hook, A. L.; Scurr, D. J.; Anderson, D. G.; Langer, R.; Williams, P.; Davies, M.; Alexander, M., High throughput discovery of thermo-responsive materials using water contact angle measurements and time-of-flight secondary ion mass spectrometry. *Surf Interface Anal* **2013**, *45* (1), 181-184; (c) Scoutaris, N.; Hook, A. L.; Gellert, P. R.; Roberts, C. J.; Alexander, M. R.; Scurr, D. J., ToF-SIMS analysis of chemical heterogeneities in inkjet micro-array printed drug/polymer formulations. *Journal of materials science. Materials in medicine* **2012**, *23* (2), 385-91; (d) Scurr, D. J.; Horlacher, T.; Oberli, M. A.; Werz, D. B.; Kroeck, L.; Bufali, S.; Seeberger, P. H.; Shard, A. G.; Alexander, M. R., Surface Characterization of Carbohydrate Microarrays. *Langmuir* **2010**, *26* (22), 17143-17155.

Chapter 2: Materials and Methods.

19. Brewer, L. N.; Ohlhausen, J. A.; Kotula, P. G.; Michael, J. R., Forensic analysis of bioagents by X-ray and TOF-SIMS hyperspectral imaging. *Forensic Sci Int* **2008**, *179* (2-3), 98-106.
20. (a) Boxer, S. G.; Kraft, M. L.; Weber, P. K., Advances in Imaging Secondary Ion Mass Spectrometry for Biological Samples. *Annu Rev Biophys* **2009**, *38*, 53-74; (b) Johansson, B., ToF-SIMS imaging of lipids in cell membranes. *Surf Interface Anal* **2006**, *38* (11), 1401-1412.
21. (a) Hagstrom, S.; Nordling, C.; Siegbahn, K., Electron Spectroscopy for Chemical Analysis. *Phys Lett* **1964**, *9* (3), 235-236; (b) Siegbahn, H., Electron-Spectroscopy for Chemical-Analysis of Liquids and Solutions. *J Phys Chem-Us* **1985**, *89* (6), 897-909; (c) Siegbahn, K., Electron Spectroscopy for Chemical Analysis (Esca). *Philos Tr R Soc S-A* **1970**, *268* (1184), 33-&.
22. (a) Li, Y. J.; Huang, X. Q.; Li, Y. J.; Xu, Y. X.; Wang, Y.; Zhu, E. B.; Duan, X. F.; Huang, Y., Graphene-hemin hybrid material as effective catalyst for selective oxidation of primary C-H bond in toluene. *Scientific reports* **2013**, *3*; (b) Ogaki, R.; Andersen, O. Z.; Jensen, G. V.; Kolind, K.; Kraft, D. C. E.; Pedersen, J. S.; Foss, M., Temperature-Induced Ultradense PEG Polyelectrolyte Surface Grafting Provides Effective Long-Term Bioresistance against Mammalian Cells, Serum, and Whole Blood. *Biomacromolecules* **2012**, *13* (11), 3668-3677.
23. Vercaemst, R.; Poelman, D.; Fiermans, L.; Vanmeirhaeghe, R. L.; Laflere, W. H.; Cardon, F., A Detailed Xps Study of the Rare-Earth Compounds Eus and Euf3. *J Electron Spectrosc* **1995**, *74* (1), 45-56.
24. Ingo, G. M.; Scoppio, L., Small-Area Xps and Xaes Study of Early Iron Metallurgy Slags. *Surf Interface Anal* **1992**, *18* (7), 551-554.
25. Watts, J. F., The potential for the application of X-ray photoelectron spectroscopy in forensic science. *Surf Interface Anal* **2010**, *42* (5), 358-362.
26. Wollin, T. A.; Tieszer, C.; Riddell, J. V.; Denstedt, J. D.; Reid, G., Bacterial biofilm formation, encrustation, and antibiotic adsorption to ureteral stents indwelling in humans. *J Endourol* **1998**, *12* (2), 101-111.
27. Seah, M. P.; Spencer, S. J., Ultrathin SiO₂ on Si. I. Quantifying and removing carbonaceous contamination. *J Vac Sci Technol A* **2003**, *21* (2), 345-352.
28. Gilmore, I.; Vickerman, J. C., *Surface analysis : the principal techniques*. Chichester : Wiley, 2009.: 2009.
29. (a) Zimm, B. H., Molecular Theory of the Scattering of Light in Fluids. *Phys Rev* **1945**, *67* (5-6), 201-201; (b) Zimm, B. H., The Scattering of Light and the Radial Distribution Function of High Polymer Solutions. *J Chem Phys* **1948**, *16* (12), 1093-1099.
30. (a) Nobbmann, U.; Connah, M.; Fish, B.; Varley, P.; Gee, C.; Mulot, S.; Chen, J.; Zhou, L.; Lu, Y.; Shen, F.; Yi, J.; Harding, S. E., Dynamic light scattering as a relative tool for assessing the molecular integrity and stability of monoclonal antibodies. *Biotechnology & genetic engineering reviews* **2007**, *24*, 117-28; (b) Kaszuba, M.; Connah, M. T.; McNeil-Watson, F. K.; Nobbmann, U., Resolving concentrated particle size mixtures using dynamic light scattering. *Part Part Syst Char* **2007**, *24* (3), 159-162.
31. Mittal, V.; Matsko, N. B., Microscopic analysis of the surface functionalization of polymer particles and subsequent grafting of polymer chains from the surface. *Journal of electron microscopy* **2012**, *61* (6), 367-80.
32. Calvert, P., Inkjet printing for materials and devices. *Chem Mater* **2001**, *13* (10), 3299-3305.
33. Le, H. P., Progress and trends in ink-jet printing technology. *J Imaging Sci Techn* **1998**, *42* (1), 49-62.
34. Boland, T.; Xu, T.; Damon, B.; Cui, X., Application of inkjet printing to tissue engineering. *Biotechnology journal* **2006**, *1* (9), 910-7.
35. Scoutaris, N.; Alexander, M. R.; Gellert, P. R.; Roberts, C. J., Inkjet printing as a novel medicine formulation technique. *Journal of Controlled Release* **2011**, *156* (2), 179-185.
36. invitrogen.com Conversion Factors, Units, and Abbreviations. (accessed 22/09/13).

Advanced surface analysis techniques for the development of a supported lipid bilayer model.

3.1 Abstract

Since biological membranes are a vital part of the human body, understanding of their behaviour at a molecular level is important. Hence, in this chapter, atomic force microscopy (AFM), time-of-flight secondary ion mass spectrometry (ToF-SIMS) and X-ray photoelectron spectroscopy (XPS) have been employed to study the physicochemical and behavioural properties of supported lipid bilayer (SLB)-based models for biological membranes. As the model SLBs were both surface deposits and compositions of five naturally occurring lipids mixed at physiologically-relevant ratios, not only were they hypothesised to be representative of biological membranes, but also could be studied at a nanometre scale. Such studies allowed optimisation of the SLB fabrication protocols and provided insights into how cellular membranes may behave *in vivo*. Both aspects of this work have been presented in chapter 3 in order to set the scene for the findings presented in the following thesis chapters.

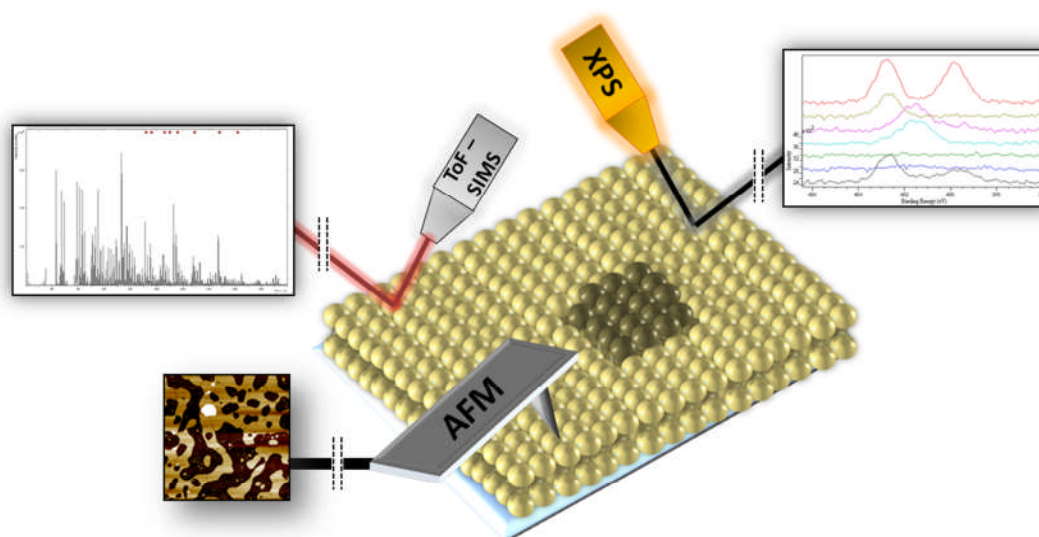


Figure 3.1: Graphic indicating the nature of the studies discussed in chapter 3. Three advanced surface analysis techniques: atomic force microscopy (AFM), time-of-flight secondary ion mass spectrometry (ToF-SIMS) and X-ray photoelectron spectroscopy (XPS) were used not only to develop, optimise and understand the supported lipid bilayer (SLB)-based model of interest, but also to study the phase separation behaviour, as might occur within biological membranes, *in vivo*.

Abbreviations:

3D – three dimensional; AFM – atomic force microscopy; Al – aluminium; AUC – area under the curve; BSST – bilayer self-spreading technique; C – carbon; C₆₀ – fullerene; Ca – calcium; CHOL – cholesterol; CPS – counts per second; DNA – deoxyribonucleic acid; DOPC – dioleoylphosphatidyl choline; DOPE – dioleoylphosphatidyl ethanolamine; DOPS – dioleoylphosphatidyl serine; DPPC – dipalmitoylphosphatidyl choline; EPC – egg phosphatidyl choline; eV – electronvolt; F – fluorine; H – hydrogen; IUPAC – International Union of Pure and Applied Chemistry; K – potassium; L_D – liquid-disordered; L_O – liquid-ordered; Mg – magnesium; N – nitrogen; Na – sodium; O – oxygen; P – phosphorous; PBS – phosphate buffer saline; RH – relative humidity; RNA – ribonucleic acid; RT – room temperature; Si – silica; SLB – supported lipid bilayer; SPM – sphingomyelin; ToF-SIMS – time-of-flight secondary ion mass spectrometry; UHV – ultrahigh vacuum; VDT – vesicle deposition technique; XPS – X-ray photoelectron spectroscopy.

3.2 Introduction

Despite many years of research using various lipid-based models for biological membranes, the current understanding of biological membranes has not yet been fully elucidated¹. Here, as indicated in chapter 1, supported lipid bilayers (SLBs) of compositions close to the ones in cellular membranes hold a considerable potential to improve this understanding².

In chapter 3, the manufacture and characterisation of SLBs that are composed of five, naturally-occurring lipids were investigated. Such model SLBs were both fabricated using two techniques: vesicle deposition (VDT)³ and bilayer self-spreading (BSST)⁴ and characterised with three advanced surface analysis techniques: atomic force microscopy (AFM), time-of-flight secondary ion mass spectrometry (ToF-SIMS) and X-ray photoelectron spectroscopy (XPS). Not only did such studies improve an understanding of the model SLBs, but they also helped to establish several hypotheses regarding the behaviour of biological membranes *in vivo*.

This research demonstrates the important value of advanced surface analysis techniques in SLB research. The model SLB preparation and characterisation protocols studied throughout this chapter can be easily applied across a wide range of alternative lipid compositions, enabling the optimisation of any model SLB of interest to be performed more rapidly. Also, the hypothesis with regards to the phase separation behaviour that is proposed in this chapter may have important implications for a number of disciplines within pharmaceutical research.

3.3 Materials and Methods – see chapter 2

3.4 Results and Discussion

3.4.1 Studying SLB morphology and composition.

Since limited studies have been performed on SLBs of physiologically relevant lipid compositions² and the exact mechanisms behind the formation of SLBs are still not fully understood⁵, advanced surface analysis techniques such as AFM, ToF-SIMS and XPS were employed to investigate the quality and composition of model lipid films* at a nanometre scale.

One of the objectives of this thesis was the development of an SLB microarray. For that reason, two SLB fabrication techniques were initially considered. The bilayer self-spreading (BSST)⁴ and vesicle deposition (VDT)³ were chosen as fabrication techniques of preference, due to their user-friendly manner (see table 1.7).

A lipid composition close to the one in erythrocyte membranes was chosen as a model for several reasons. Red blood cell membranes are commonly used as models for cellular membranes^{2, 6} and the biophysical and chemical properties of the lipid ingredients have been viewed as beneficial for studying lipid bilayer behaviour *in situ*. Briefly, the bilayer surface was composed of both positively (SPM, DOPE) and negatively (EPC, DOPS) charged, as well as neutral (CHOL) lipid head groups. Additionally, lipids of different phases, such as gel (CHOL, SPM), liquid (EPC, DOPE, DOPS) lamellar (DOPS, EPC) and non-lamellar (SPM, DOPE) phases may co-exist within the bilayer structure⁷. Also, the presence of CHOL supported the bio-relevant mechanistic properties of the model SLB⁸. Accordingly, PBS (pH = 7.4/RT) solution was selected as a liquid environment for the AFM imaging of SLBs and mica as an AFM-suitable solid support. For XPS and ToF-SIMS studies, PBS was replaced with Millipore water in order to avoid potential interferences with the sample chemistries.

3.4.1.1 AFM: optimisation of model SLB fabrication protocols.

The initial optimisation of the VDT and BSST fabrication protocols for the model lipid composition was based on AFM studies in liquid environments with either dioleoylphosphatidyl choline (DOPC) or dipalmitoylphosphatidyl choline (DPPC)-composed supported lipid films. Such films on mica surfaces have been used as liquid- and gel-phase bilayer models, respectively⁹. These studies have been summarised in appendix II.

* Since drying in air destabilises the SLB structure, the term 'model lipid films' (as opposed to 'model SLBs') is used to describe both the air-dried films of model lipid composition on mica supports that have been used for ToF-SIMS and XPS analyses, as well as model supported lipid multilayers for AFM studies in liquid environments.

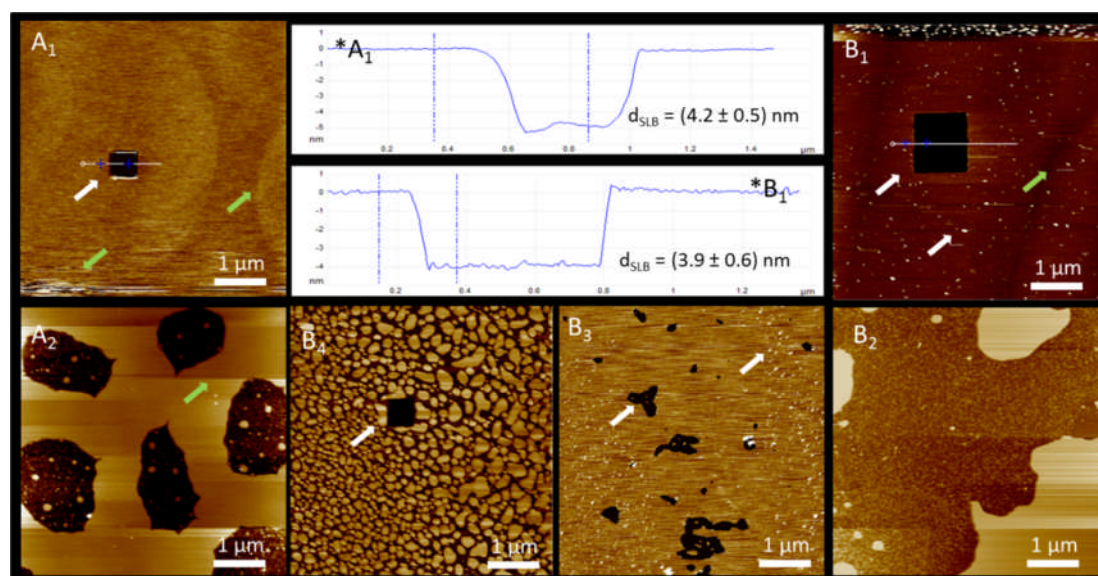


Figure 3.2. The AFM images of BSST-fabricated model SLBs (A) and VDT-fabricated model lipid films (B). Images (A) represent the uniform continuous (1) or porous (2) SLBs that have been rinsed once with PBS in a gentle or vigorous manner, respectively, before AFM imaging in liquid environments has been performed. Images B represent continuous (1) patch-like (2), porous (3) SLBs or supported lipid multilayers (4) that have been deposited on the mica surface throughout 60-, 30-, 45-, 90-minute incubation with 0.5 mg/ml liposome solutions at 35°C before imaging. The square features on A₁, B₁, B₄ were generated with AFM probes through a scratch test (see appendix II) in order to both demonstrate the presence and measure the heights (*) of the lipid films on the surface. Black and brown areas on AFM each image correspond to lipid film-uncovered and covered surface areas, respectively. Z-scale bars have been removed for clarity purposes (average range 0-10 nm). White arrows indicate some of the characteristic lipid film features (see text) and the scratch test squares, whilst green arrows common AFM image artefacts.

The preliminary AFM investigations on model lipid compositions revealed that BSST resulted in uniform and continuous SLBs (figure 3.2A₁), whilst VDT resulted in lipid films of various qualities, such as porous, continuous bilayers and multilayers, depending on the liposome-mica incubation times at an appropriate temperature (figure 3.2: B₃, B₁, B₄, respectively). Additionally, it was observed that BSST resulted in lipid excess-free SLBs, whilst additional lipid material was present at the VDT-fabricated SLB surfaces (figure 3.2A₁ and B₁, respectively)^{5b}. Also, it was demonstrated that BSST may result in porous or in VDT patch-like topographies, if rinsed vigorously with PBS after the preparation procedure (figure 3.2: A₂ or B₂, respectively). In order to confirm presence and thickness of lipid films, an AFM-based scratch test was developed and used as a control (appendix II). The thickness of BSST- and VDT-fabricated SLBs was (4.2 ± 0.5) nm and (3.9 ± 0.6) nm, respectively (figure 3.2*A₁ and *B₁), consistent with previous studies². The parameters above were established for

model SLBs deposited on freshly-cleaved mica discs (14 mm in diameter) that were glued to metal disc specimens.

3.4.1.2 ToF-SIMS: qualitative and semi-quantitative evaluation of model lipid films.

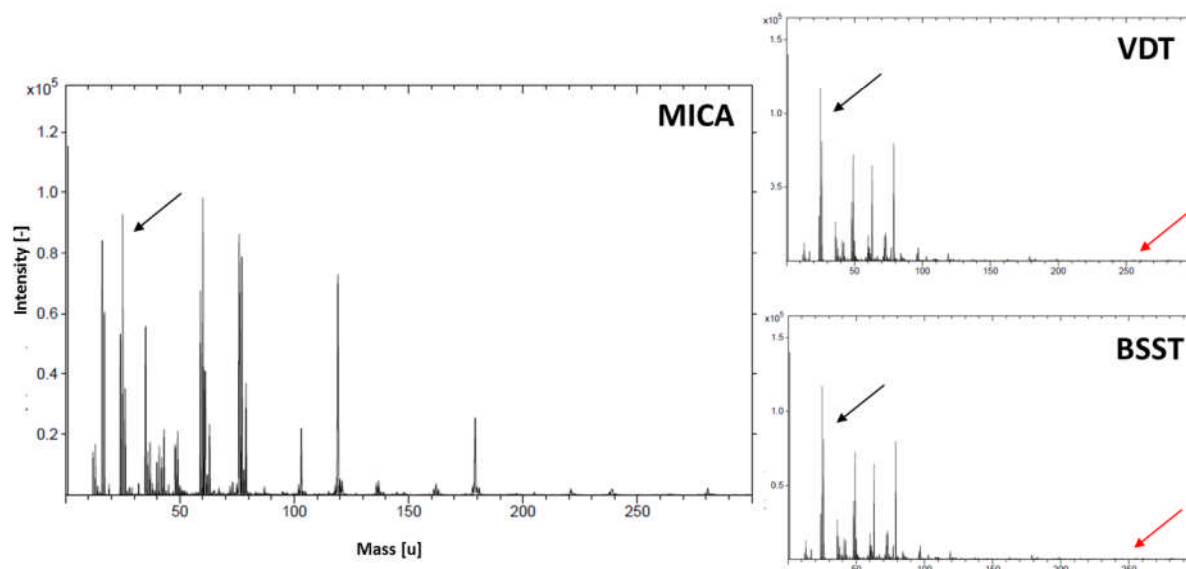


Figure 3.3. ToF-SIMS spectra for mica and both model lipid film samples in the 0 – 300 u mass regions. The model lipid films have been prepared using vesicle deposition (VDT) and bilayer self-spreading (BSST) techniques and dried in air before insertion into the ToF-SIMS ultrahigh vacuum chamber. The spectra have been collected using C_{60} as primary ion source in the negative mode. Black and red arrows have been added to demonstrate the intensities of mica-associated peaks and the intensities of peaks that have been identified as single lipid-representative peaks within the lipid mixture, respectively.

ToF-SIMS was used to study the chemical compositions of model SLBs. Since the ToF-SIMS requires ultrahigh vacuum (UHV) conditions, studies were performed on dry model lipid films deposited on 14 mm mica discs. Both the single lipid samples and the VDT- and BSST-fabricated model lipid films were studied with ToF-SIMS. A C_{60} primary ion source was selected for such studies, due to the literature-indicated advantages for studying samples of such chemistries¹⁰. The preliminary analysis of the ToF-SIMS spectra of the model supported lipid films indicated the presence of two peak populations in terms of the intensity: high and low in intensity. The high intensity peaks were correlated with the chemistries specific for mica, whilst the majority of the low intensity peaks with the lipid chemistries. This was expected, as the total amount of lipids on the surface of the solid support was likely much less than 10 μg and 80 μg on BSST and VDT samples, respectively. Also, since the air-dried lipid films may not have had a uniform coverage across the sample surface and the ToF-SIMS analysis depth limit (~ 2 nm) is only slightly lower than the lipid matter (~ 4 nm for lipid films in liquid environments), it is likely that the mica-specific ions are present everywhere on the

sample surfaces. The fragments of ToF-SIMS spectra for mica, VDT and BSST are presented in figure 3.3.

The analysis of ToF-SIMS spectra for single lipids enabled the identification of the specific peaks for each lipid within the mixture (see appendix III for details). Subsequently, the lipid-specific peaks were compared with the supported lipid samples indicating that the majority of the peaks specific for the triglyceride-type lipid chemistries within the model lipid film spectra could not easily be correlated to a single lipid. This is likely, because the chemical structures of triglycerides used in the lipid mixture were very similar and therefore the interaction of such lipids with the primary ion source undergoes through similar destruction pathways, resulting in very similar or even identical products (secondary ions) that are recognised in the ToF detector. In the model SLB composition, 3 out of 5 lipid molecules contain an unsaturated oleoyl group as a key component of lipid hydrophobic chains and 4 out of 5 lipids [O-(2-aminoethyl)-O-propylphosphate] group as a key component of lipid head groups. For that reason, the interferences on ToF-SIMS lipid film spectra were likely to occur in between the vast majority lipid peaks initially identified on single lipid ToF-SIMS spectra. This suggested that the identification of single lipid-representative peaks within lipid film spectra may be based on small amount of peaks of very low intensity. Also, since lipids were mixed within the model lipid composition at a different molar ratio (EPC > CHOL > DOPE \approx SPM > DOPS), the effective amounts of secondary ions that originate from each lipid chemistry per surface area unit for the lipid film samples was expected to be different (assuming the homogenous distribution of the lipid molecules within the lipid film). Therefore, the contribution of the peaks originating from *e.g.* DOPS was thought to be substantially different from the contribution originating from *e.g.* EPC. These and the overall low intensity of lipid-specific peaks within the lipid film spectra implied that the statistical, peak-intensity-based approaches for the identification of secondary ion peaks representative for each lipid chemistry (*e.g.* principal component analysis¹¹) may not be the best strategy for qualitative analysis of the spectra. Since such approaches involve the initial adjustment of a threshold level with regards to the peak intensity of interest, the low intensities of lipid-specific peaks would most likely be identified as noise within the lipid film spectra. Additionally, the C_{60} ion source-associated broadness of peaks within the ToF-SIMS spectra further discouraged the statistical analysis approaches. For these reasons, the identification of the peaks that were representative for the single lipids within the lipid film spectra, was performed manually through peak-by-peak comparisons with the ToF-SIMS spectra of the single lipid samples. Such a comparative analysis resulted in the identification

of a number of lipid-specific peaks and their assignments within the lipid film samples, which are presented in table 3.1. The molecular ion assignments for the peaks in the table were based on the comparisons between the IONTOF software-indicated options and molecular masses of possible secondary ions that have been anticipated using BioChemDraw software. The IONTOF-indicated deviation for the molecular ion assignments was not higher than 1000 ppm.

Table 3.1. The single lipid-representative peaks within the ToF-SIMS C_{60} spectra of model lipid films.

Lipid	Molecular Mass [Da]	Molecular ion assignment	Molecular Mass [Da]	Molecular ion assignment
EPC	253.2	$C_{16}H_{31}NO^-$	256.2	$C_{15}H_{30}NO_2^-$
	145.1	$C_{11}H_{13}^+$	275.3	$C_{20}H_{35}^+$
CHOL	146.1	$C_{11}H_{14}^+$	367.4	$C_{27}H_{43}^+$
	159.1	$C_{12}H_{15}^+$	369.4	$C_{27}H_{45}O^+$
	160.1	$C_{12}H_{16}^+$	384.3	$C_{27}H_{44}O^-$
	161.2	$C_{12}H_{17}^+$	386.3	$C_{27}H_{46}O^+$
DOPE	124.0	$C_2H_7NO_3P^+$	339.3	$C_{22}H_{43}O_2^+$
	214.1	$C_5H_{13}NO_6P^-$		
DOPS	206.0	$C_3H_6NO_6PNa^-$	269.8	$C_{21}H_{18}^+$
	246.0	$C_6H_{10}NO_6PNa^-$	288.8	$C_{19}H_{13}O_3^+$
	255.1	$C_{16}H_{18}O_3^+$		
SPM	104.1	$C_5H_{14}NO^+$	254.0	$C_{16}H_{32}NO^-$
	167.9	$C_{10}H_{18}NO^+$	404.2	$C_{20}H_{39}NO_5P^-$
	168.0	$C_9H_{12}O_3^-$	598.3	$C_{34}H_{65}NO_5P^-$
	186.1	$C_5H_{17}NO_4P^+$	600.5	$C_{34}H_{67}NO_5P^-$
	198.1	$C_3H_4O_7Na^+$	616.5	$C_{34}H_{67}NO_6P^-$
	224.1	$C_8H_{17}PO_5^+$	642.4	$C_{36}H_{65}NO_6P^-$
	225.1	$C_8H_{18}PO_5^+$		

Abbreviations: EPC – egg phosphatidyl choline, CHOL – cholesterol, DOPE – dioleoylphosphatidyl ethanolamine, DOPS – dioleoylphosphatidyl serine, SPM – sphingomyelin.

Next, the list of single lipid-representative peaks was used for the assessment of the spatial distributions of single lipids within the BSST and VDT model lipid films. The examples of ToF-SIMS chemical images presenting the spatial distributions of the single lipids within both lipid film samples are presented in figure 3.4. The peak distributions of the highest intensity within the sample area have been presented. In addition, the semi-quantitative evaluation of the key peak intensities has been performed and presented in figure 3.5.

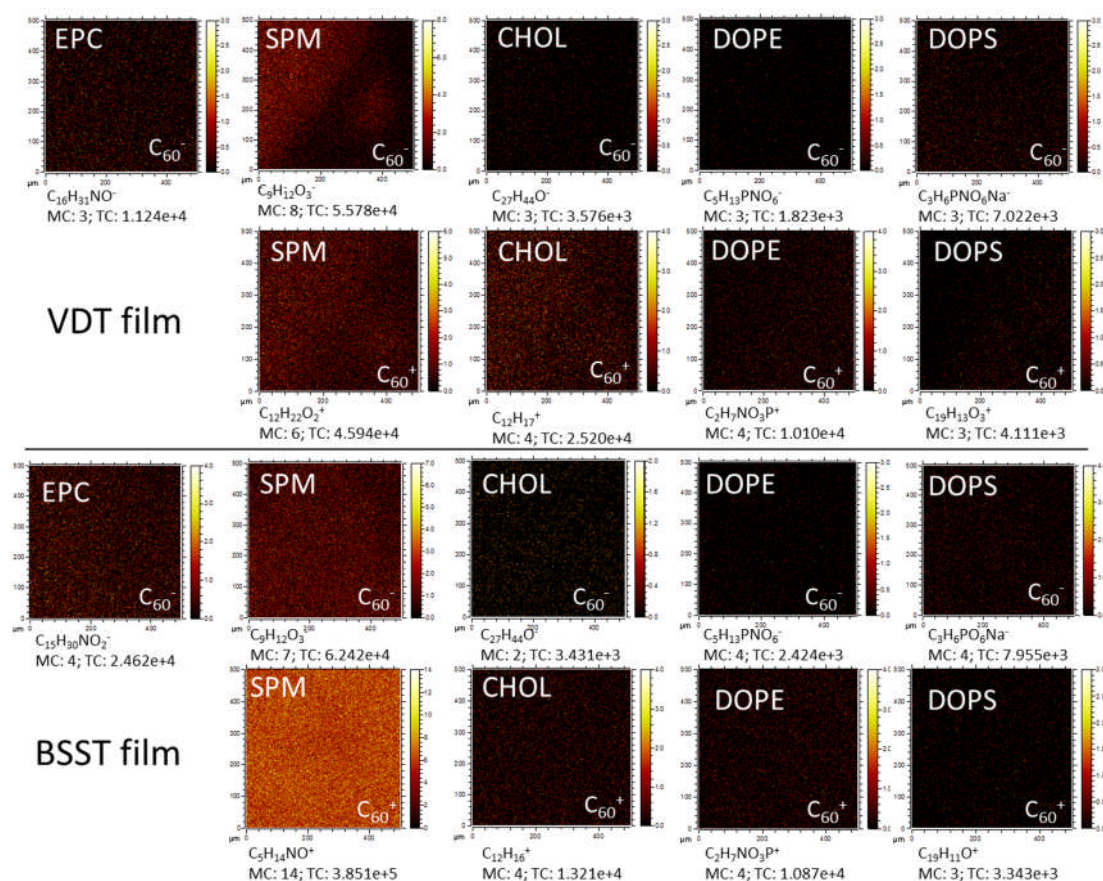


Figure 3.4. The ToF-SIMS chemical images presenting the spatial distributions of single lipid-representative peaks within the model lipid film samples. The model lipid films have been prepared using the vesicle deposition technique (VDT) and bilayer self-spreading technique (BSST) protocols and dried in air. C_{60} has been used as a primary ion source for ToF-SIMS imaging. Molecular ion assignments have been assigned to a specific lipid through IONTOF and ChemBioDraw software-based comparisons, as it has been described in the text.

Analyses of ToF-SIMS images and single lipid-representative peaks within VDT- and BSST-fabricated model lipid films have indicated an overall low intensity of DOPE and DOPS-specific secondary ions. Such low intensities of DOPE and DOPS-specific secondary ion peaks within the lipid film spectra may be misleading and therefore the ToF-SIMS-based evaluation of the DOPE and DOPS distributions within the model lipid films was not conclusive. The low intensity of DOPS and DOPE peaks is likely to be triggered by several factors. Firstly, DOPS and DOPE lipids have very similar chemical structures; hence, due to the peak interferences, the identification of lipid-representative peaks within the mixture was based on the low intensity peaks. Secondly, the theoretical DOPS content within the mixture is around 7 %; hence the low amounts of this lipid within the scan areas have been expected. Thirdly, DOPE as a lipid forming non-lamellar conformations may not be fully incorporated into bilayer structure throughout the bilayer fabrication process for both protocols¹². Since this has not

been clear, the quantitative assessment of supported lipid films for both protocols has been performed using XPS, as it has been discussed in the following section.

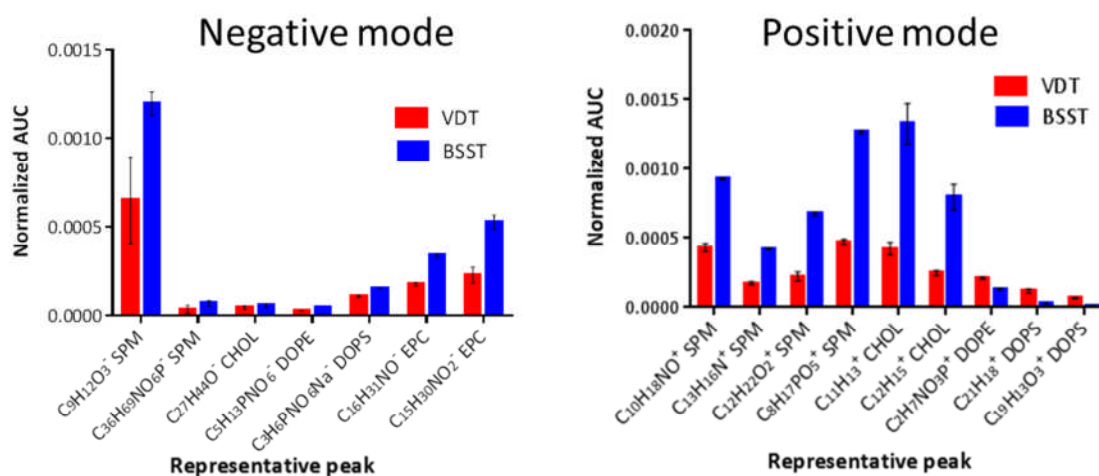


Figure 3.5. Graphs presenting the semi-quantitative evaluation of single lipid-representative peak intensities within the ToF-SIMS spectra of the model lipid films in both positive and negative modes. The mean normalised areas under the curves (AUCs) for each single lipid-representative peak have been calculated and plotted for the ToF-SIMS spectra of both: vesicle deposition technique (VDT)- and bilayer self-spreading technique (BSST)-fabricated model lipid films. ToF-SIMS spectra were collected using C_{60} as a primary ion source from two separate sample areas.

The analysis of the spatial distributions of SPM, EPC and CHOL-specific peaks within the lipid film spectra suggested that the distribution of these lipids within the supported lipid films is uniform. However, for SPM and CHOL a degree of organisation was observed within the VDT samples. This may be associated with the AFM-observed presence of lipid excess attached to the model SLBs in liquid environments. Since the ToF-SIMS images were of lipid film samples that have been dried in air, the formation of alternative, non-bilayer structures on the mica surface is likely to have occurred (figure 3.2B₃). For the BSST samples, which exert lipid excess-free SLB morphologies in liquid environments, the formation of such structures is likely to occur in a similar manner in all areas of the sample surface, resulting in a uniform lipid distribution on ToF-SIMS chemical images. However, for VDT samples, the lipid excess at the bilayer surfaces in liquid environments is likely to be organised in small lipid bulk populations across the sample surface, once the samples are dried. This results in a non-homogenous distribution of single lipids within the ToF-SIMS chemical images of lipid film samples. Such a degree of organisation has not been observed for EPC, which may suggest the presence of SPM/CHOL aggregates in the VDT samples, as it has been hypothesized later in the chapter.

In addition to the qualitative analysis, ToF-SIMS enables to compare the content of the material across different samples in a quantitative manner. The semi-quantitative evaluation of lipid-specific peak intensities has suggested that BSST-fabricated supported lipid films contain more SPM, CHOL and EPC lipids per surface unit than the VDT films. This has indicated that the lipids within the BSST films are packed more densely than the lipids within the VDT films. Such a conclusion has correlated with the AFM-reported morphologies of the model SLBs in liquid environments after 45-minute incubation in liquid at an elevated temperature. According to AFM data, not only were bilayer film qualities continuous for BSST samples and porous for VDT samples, but also the SLB thicknesses were slightly higher (by roughly 0.5 nm) for BSST samples than for VDT bilayers.

3.4.1.3 XPS: quantitative evaluation of model lipid films.

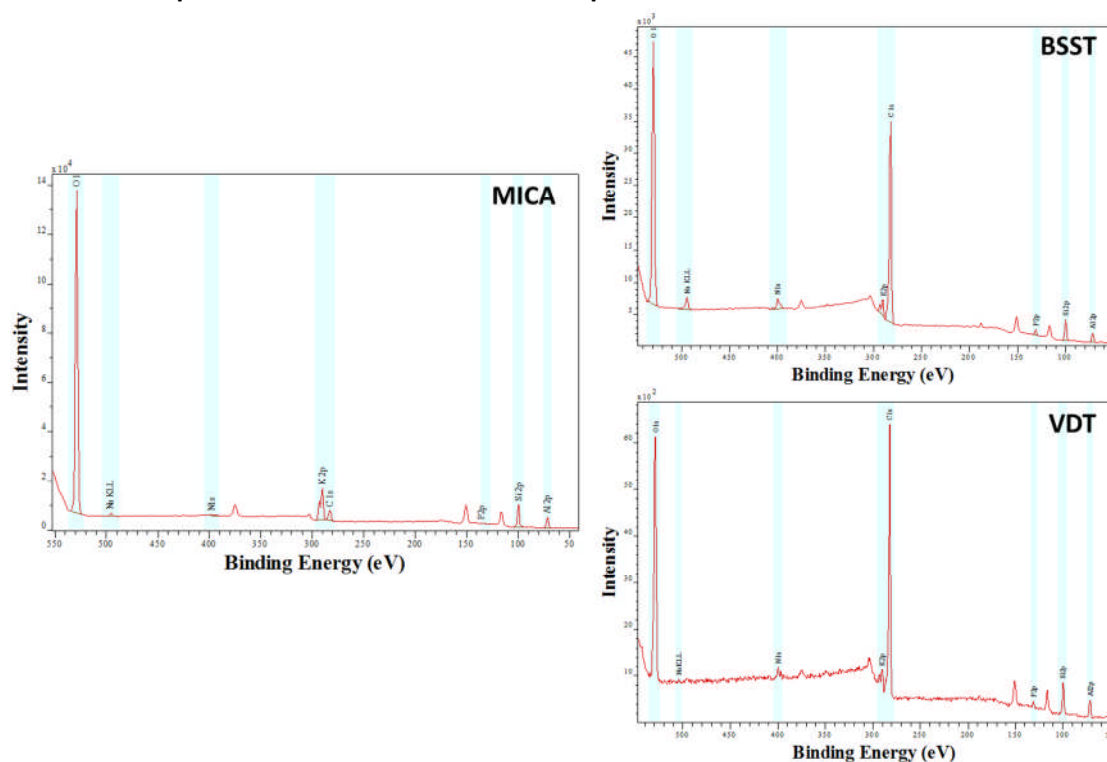


Figure 3.6. Wide-scan XPS spectra indicating the elemental compositions of the solid support (MICA) and two model lipid film (BSST, VDT) samples. Both films have been prepared using bilayer self-spreading (BSST) and vesicle deposition (VDT) techniques and were dried in air before insertion into the XPS ultrahigh vacuum chamber. The peaks correlating to oxygen (O1s), sodium (NaKLL), nitrogen (N1s), potassium (K2p), carbon (C1s), phosphorous (P2p), silica (Si2p) and aluminium (Al2p) have been labelled and highlighted with light-green band available through CasaXPS software package.

XPS has been used to study the elemental compositions of the model supported lipid films. Due to similar sample preparation requirements for XPS and ToF-SIMS, XPS analysis has

been performed on dry model lipid films that had been prepared similarly to the ToF-SIMS-analysed films, facilitating therefore the comparisons between both experimental techniques.

Initial analysis has revolved around the comparison of the wide-scan XPS spectra for mica, VDT and BSST samples. As presented in figure 3.6, mica-specific elements (*e.g.* aluminium (Al) as Al_{2p} at ~70 eV, silica (Si) as Si_{2p} at ~100 eV, potassium (K) as K_{2p} at 290 eV) were noticed with XPS on the control (mica) and the supported lipid film samples alike. This is likely, because lipid films were 3-5 nm thick and XPS spectra were collected from the first 10 nm of the surface in depth. Interestingly, this phenomenon was used for establishing the surface coverage of the sample, based on the comparison between the peak intensities that are characteristic for the solid support and the surface lipid coating on the supported lipid film samples. This was successfully attempted for K_{2p} and C_{1s} peak intensities within VDT and BSST samples and has indicated that the areas of the sample surfaces analysed with XPS have been fully covered with the lipid film, because the calculated thicknesses of the lipid film layers have been established at (3.1 ± 0.1) nm and (5.2 ± 0.1) nm for BSST and VDT samples, respectively (figure 3.7). Although this observation did not initially seem to correspond with both ToF-SIMS and AFM results, the overall conclusion that the BSST resulted in more densely packed lipid films than the VDT was the same for all techniques, as it has been explained below. This contradiction for XPS-reported lipid film thicknesses is likely associated with the lipid excess present on the VDT samples. Since XPS has a five times higher depth analysis limit than ToF-SIMS, the XPS-reported sample coverage seems to account for lipids forming both the bilayer and the lipid excess in the VDT samples when studied in liquid environments with AFM. Here, as the XPS samples were dried in air and therefore the lipid excess had collapsed on the surface above the original bilayer, the XPS would account for more lipids within the first 10 nanometres of the surface than *e.g.* ToF-SIMS that enables the study of only the first 2 nanometres of a material surface. This however was not entirely clear, because the XPS-thickness measurements were based on C_{1s} peak intensities and may have been caused by sample contamination throughout the VDT fabrication protocol, which involves more steps than BSST protocol (*e.g.* liposome extrusion).

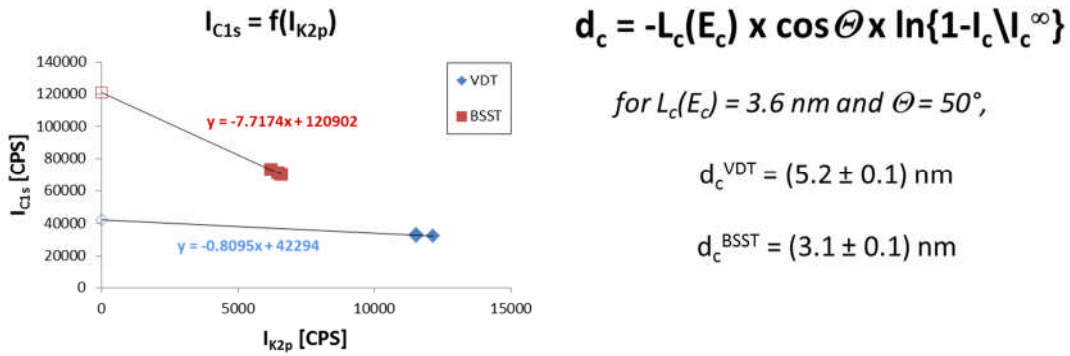


Figure 3.7. The graph and equation depicting the calculations of the lipid film coverage for both model lipid film samples prepared using vesicle deposition (VDT) and bilayer self-spreading (BSST) techniques. Intensities (I) of K2p and C1s peaks within the XPS spectra in the wide regions were calculated and plotted for three different areas within the samples collected using increasing number of scans per spectrum. The linear correlation equations and the trendline were calculated using Microsoft Excel 2007. The intercept values have been assigned to the I_c^∞ parameter, whilst the I_{C1s} values as I_c parameter in the equation. Effectively, the mean lipid film thickness values (d_c) for $L_c(E_c) = 3.6$ nm and $\Theta = 50^\circ$ have been calculated for three separate areas of each lipid film sample. The error values have been calculated as a standard deviation using *stdev.p* function in Excel. The symbols within the equation have been explained in chapter 2.

Additionally, since all lipid molecules are composed of C, O, P, Na and N elements, the qualitative assessment of their presence within the wide XPS spectra for all samples was performed. The wide XPS spectra for mica samples indicated that significant amounts of C (C1s at ~ 280 eV) and O (O1s at ~ 530 eV) atoms were present on the pure solid support. The presence of C elements on mica surface was most likely due to the contamination from air (dust) throughout sample handling. The presence of oxygen on mica may have originated from both dust and the support itself, as the chemical structure of mica is: $X_2Y_4-6Z_8O_{20}(OH,F)_4$, where most commonly X is K, Na or Ca, Y is Al, Si or magnesium (Mg), while Z was Al or Si, all depending on the mineral source the mica discs had been obtained from (H and F stand for hydrogen and fluorine, respectively). Therefore, since the overall amount of both O and C elements on lipid samples was affected by the interferences from the solid support, the C1s and O1s regions were not suitable candidates for the high resolution XPS analysis. Similarly, Na (NaKLL at ~ 500 eV) regions were not indicative, as the presence of Na within the wide XPS spectra for pure mica control was observed.

However, mica support does not contain any N or P elements (N1s at ~ 400 eV or P2p at ~ 130 eV, respectively). This implies that the XPS narrow scan analysis in the P2p and N1s regions should not be affected by the interferences either from the solid support or aerial contamination and might be used to assess the quantitative relationships between the lipids

within the supported lipid films. This was studied further. Here, it is worth adding that the extraction of further quantitative information about the model lipid films, based on the narrow XPS scans of the C1s and O1s regions may be possible, especially if mica was replaced as the solid support. Due to the overall nature of this work aiming to develop and assess SLBs as tools for *in vitro* screening of the drug-membrane interactions in high throughput, the further characterisation of the model supported lipid films with XPS was not however, pursued.

As presented in figure 3.8, XPS spectra in the N1s region for EPC and DOPE have indicated the presence of single peaks at (402.7 ± 0.1) eV and 401.5 eV, respectively. According to the values available in the literature, these have corresponded to the nitrogen atoms in the trimethylammonium ($-N^+(\text{CH}_3)_3$) and ammonium ($-\text{NH}_3^+$) within EPC and DOPE structures¹³. Interestingly, for SPM and DOPS samples, the presence of several peak populations per spectrum has been observed at 401.5 eV and (399.4 ± 0.1) eV for DOPS or at 402.7 eV, 401.4 eV and 399.8 eV for SPM. On the one hand, DOPS contains the α -amino acid; serine in its structure and therefore nitrogen may exist in both protonated ammonium ($-\text{NH}_3^+$) and non-protonated amino ($-\text{NH}_2$) forms¹³. This correlates with the atom assignments for XPS spectra in the N1s region, suggesting that the content ratio between those groups within DOPS molecules was $(87 \pm 2) \% : (13 \pm 2) \%$, respectively. On the other hand, the presence of two dominant, almost symmetrical peaks on the SPM spectra are equivalent to the nitrogen atoms in trimethylammonium ($-N^+(\text{CH}_3)_3$) at 402.7 eV and amine ($-\text{NH}-$) at 399.8 eV groups within the structure of this lipid¹³. The small peak at 401.4 eV is likely associated with the ionic mesomer of the amide group ($-\text{HN}^+=\text{C}(\text{O}^-)$), not only because this correlates with the literature-indicated values¹³, but also the XPS-measured content ratio between the groups: $(47 \pm 1) \% : (45 \pm 1) \% : (8 \pm 1) \%$ for $-N^+(\text{CH}_3)_3 : (-\text{NH}-) : (-\text{HN}^+=\text{C}(\text{O}^-))$ has suggested so (compare SPM structures in figure 3.13). The presence of N for mica and CHOL samples has been assumed as non-existent, because the peak intensities for those samples are considerably low.

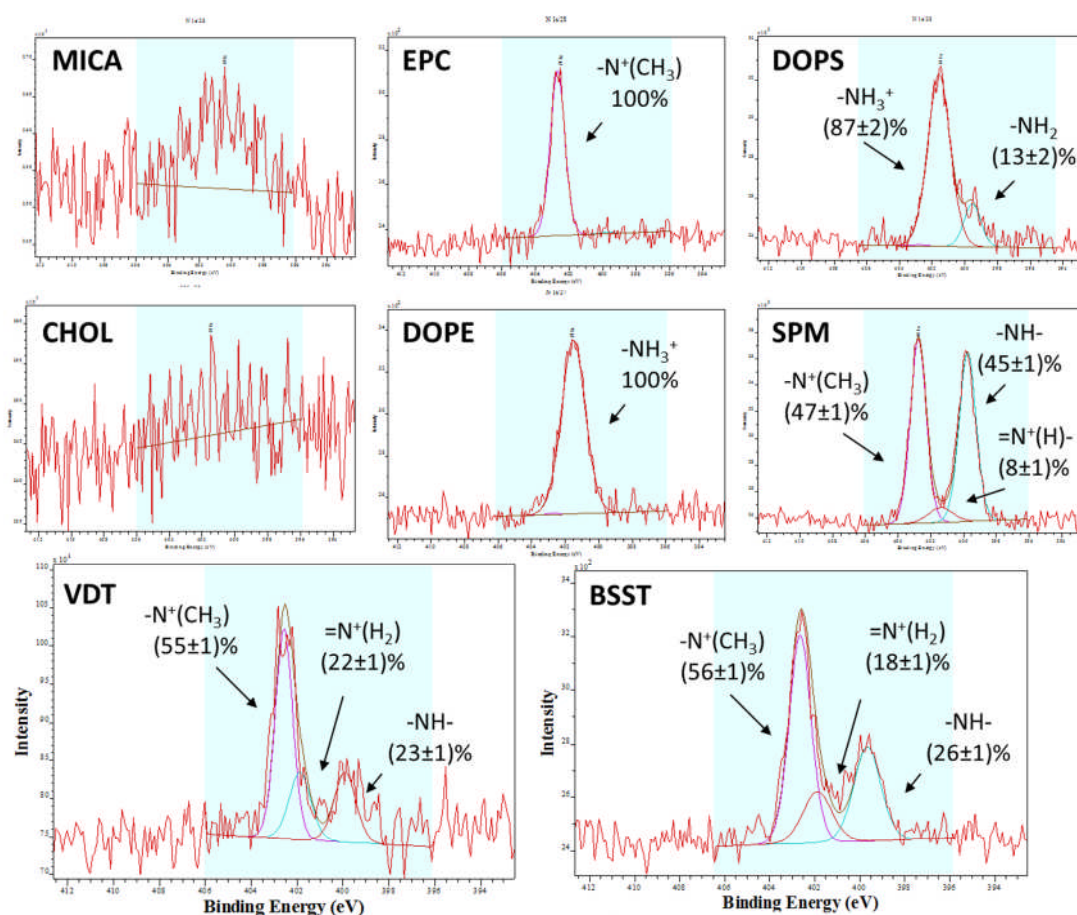


Figure 3.8. XPS spectra in the N1s region indicating the peaks associated with the presence of nitrogen on the solid support (MICA), egg-phosphatidyl choline (EPC), sphingomyelin (SPM), cholesterol (CHOL), dioleoylphosphatidyl ethanolamine (DOPE), dioleoylphosphatidyl serine (DOPS) and two model lipid film (BSST, VDT) samples. The films were prepared using bilayer self-spreading (BSST) and vesicle deposition (VDT) techniques and were dried in air before insertion into the XPS ultrahigh vacuum (UHV) chamber. Single lipid samples were prepared through deposition of lipid bulks on mica surfaces. The peaks correlating with nitrogen (N1s) were labelled and highlighted with a light-green band available through CasaXPS software package. The group populations and their contents within each peak corresponding to appropriate nitrogen atoms for each lipid molecule were also indicated for the relevant spectra. Labels on X and Y axes of single lipid spectra are written in small font for presentation purposes and correspond to Binding Energy (eV) and Intensity, respectively.

Since amide bonds (or amino acids) bonds are known to exist in ionised forms not only in a solution¹⁴, but also in a solid state¹⁵, the ultrahigh vacuum conditions for XPS seem to provide appropriate conditions for such observations¹⁶. Additionally, the possibility of establishing the quantitative relationships between such conformers implies that XPS studies in the N1s region may be a useful approach for an empirical establishment of N group conformations within lipids and possibly other molecules. The reason behind this phenomenon is associated with the small differences in binding energies for N atoms in

different group conformations that, as it has been demonstrated above, can be distinguished through XPS narrow scan measurements.

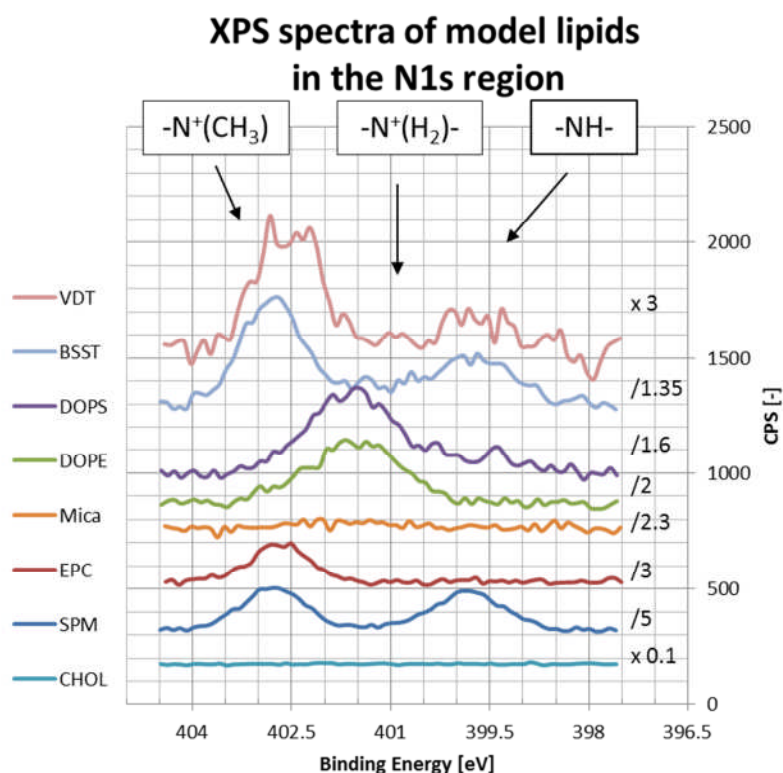


Figure 3.9. Graph indicating the XPS spectra in the N1s region for mica, single lipid and model lipid film samples. For clarity purposes the spectra from figure 3.8. have been presented as a single graph. The functional group populations at ~402 eV, ~401 eV and ~399 eV Binding Energy have also been indicated. Since the background level for each spectrum has been similar, for the purpose of presentation, the intensity values for each sample have been multiplied (x) or divided (/) by a factor indicated on the graph.

As indicated in figure 3.9, once the single lipids were compared with the XPS spectra in the N1s region for supported lipid film samples, it became apparent that all N-containing functional groups in the lipid mixture may be grouped into 3 populations at ~402 eV, ~401 eV and ~399 eV corresponding to nitrogen atoms in: trimethylammonium (-N⁺(CH₃)₃), ammonium (-N⁺(H₂)-) and amine (-NH-) groups, respectively. Here, the trimethylammonium population within the SLB has originated from all EPC and 47% SPM, the ammonium population from 87% DOPS, 8% SPM and 100% DOPE, whilst the amine population from 45% SPM and 13% DOPS nitrogen atoms, based on the theoretical calculations. Since the overall content of single lipids within the model SLB varied (23% CHOL, 18% SPM, 18% DOPE, 7% DOPS and 33% EPC), it was helpful to assume that the vast majority of ammonium groups originated from DOPE, whereas the vast majority of amine groups were from SPM within the

model lipid composition. With regards to the trimethylammonium population, all EPC and a bit less than half of the SPM nitrogen atoms contributed towards the N1s peak intensities. This also explains why the ~402 eV population has a significantly larger area than the ~401 eV and ~399 eV populations. Based on the peak fitting analysis of the XPS spectra of the model supported lipid film samples in the N1s regions, the quantitative ratios between the peak populations were found and compared with a theoretically expected ratio (table 3.2). As the establishment of such theoretical ratio may cause difficulties, the author's calculation approach is explained in detail in chapter 2.

Table 3.2: | The XPS-measured lipid content ratios within the model lipids films.

Binding Energy [eV]:	~402		~401		~399
Peak population:	$[(-N^+(CH_3)_3)]$:	$[(=N^+(H_2))]$:	$[(-NH-)]$
Theoretical ratio:	53 %	:	28 %	:	19 %
	(34% EPC + 19% SPM)		(19% DOPE + 6% DOPS + 3% SPM)		(18% SPM + 1% DOPS)
Ratio in VDT film:	$(55 \pm 1) \%$:	$(22 \pm 1) \%$:	$(23 \pm 1) \%$
Ratio in BSST film:	$(56 \pm 1) \%$:	$(18 \pm 1) \%$:	$(26 \pm 1) \%$

Abbreviations: VDT – vesicle deposition technique; BSST – bilayer self-spreading technique; EPC – egg phosphatidyl choline; SPM – sphingomyelin; DOPE – dioleoylphosphatidyl ethanolamine; DOPS – dioleoylphosphatidyl serine.

As indicated in table 3.2, both the VDT and BSST empirical ratios were similar to the theoretical ratio suggesting that the molar contents of DOPE, SPM, DOPS and EPC lipids in the studied model lipid film were close to the theoretical expectations. However, a slightly decreased content of ammonium groups for the empirical ratios, as well as slightly elevated values for the other two group populations suggested that a loss of DOPE is likely to occur for both VDT- and BSST-fabricated model lipid films. The loss of DOPE for BSST was slightly higher than the loss for the VDT films. This is likely, as DOPE crystallises in the H_{II} polymorphic phase (inverted cone shape; non-lamellar)¹². Hence, its behaviour is different than the behaviour of other model lipids and has not incorporated effectively into a bilayer structure for both VDT and BSST samples. Such behaviour has been observed previously for different application^{12, 17}. This phenomenon additionally explains the low intensity of DOPE peak signals within the ToF-SIMS spectra, despite the fact that the theoretical content of DOPE was expected at the same level as SPM (both 18 %).

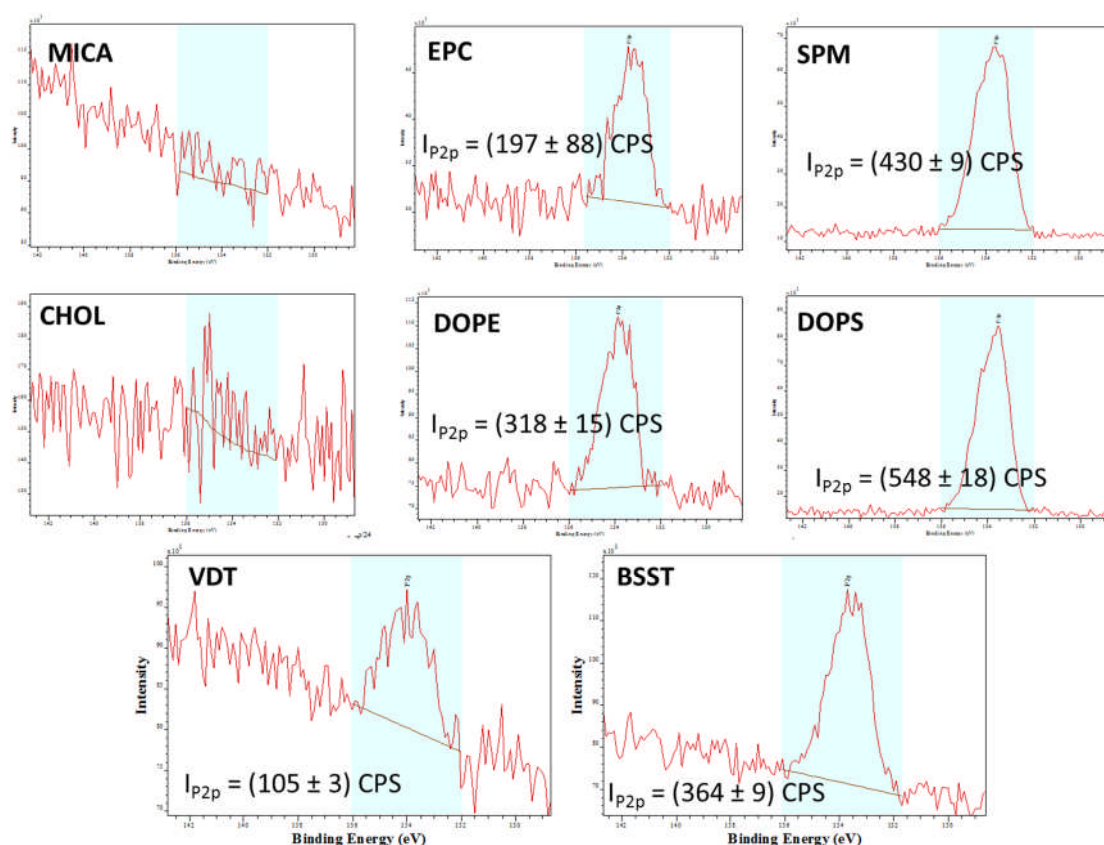


Figure 3.10. XPS spectra in the P2p region indicating the peaks associated with the presence of phosphorous on the solid support (MICA), egg-phosphatidyl choline (EPC), sphingomyelin (SPM), cholesterol (CHOL), dioleoylphosphatidyl ethanolamine (DOPE), dioleoylphosphatidyl serine (DOPS) and two model lipid film (BSST, VDT) samples. Both films were prepared using bilayer self-spreading (BSST) and vesicle deposition (VDT) techniques and were dried in air before insertion into the XPS vacuum chamber. Single lipid samples were prepared through deposition of a lipid bulk on a mica surface. The peaks correlating with phosphorous (P2p) were labelled and highlighted with light green band available through CasaXPS software package. Peak intensities were also indicated for each sample. Labels on X and Y axes of single lipid spectra are written in small font for presentation purposes and correspond to Binding Energy (eV) and Intensity, respectively.

As indicated in figure 3.10, the XPS spectra of EPC, DOPE, SPM and DOPS single lipid samples in the P2p region have indicated the presence of a single peak at 132-136 eV Binding Energy which agrees with that expected for phosphorous in lipid phosphate groups¹³. This has not been observed for mica and CHOL spectra confirming the expected lack of phosphorous in these samples. The model lipid film spectra indicated the presence of single peaks at the same binding energy values suggesting that all phosphorous atoms within the lipid mixture originated from phosphate groups. Unfortunately, due to the same shape of the peaks for all phosphorous-containing samples, the quantification of lipids based on peak fitting analysis was not successful. Since all phosphorous atoms within the head groups of model lipids have

the same chemistries, the differences in kinetic energies for such bonds were very small and did not seem to be distinguishable *via* XPS measurements. However, the comparison of peak intensities between VDT and BSST spectra suggested that the overall amount of phosphorous on the VDT samples was roughly 3.5 times lower than the phosphorous amount on BSST samples. Interestingly, according to the sample coverage calculations above (figure 3.7.), VDT films were slightly thicker than BSST lipid films. Also, the overall mass of lipids used for SLB preparation is 8 times higher for VDT than for BSST (see chapter 2). Therefore, the significantly lower amounts of phosphorous within the VDT films have been related to the lipid film density. As established with AFM, a 45-minute incubation of liposomes on mica surfaces resulted in liposome-attached porous SLBs, whilst a similar incubation for BSST resulted in liposome-free continuous film qualities. The ToF-SIMS semi-quantitative analysis indicated that the content of SPM, CHOL and EPC per surface area unit of the model lipid films was higher for BSST than for VDT. For that reason, the overall amount of phosphorous per surface area on the samples would likely be higher for BSST and lower for VDT samples, if solely based on ToF-SIMS and AFM data. This has correlated with the XPS observations, with regards the overall amount of phosphorus per area unit of the surface for both BSST and VDT samples, indicating that the lipids within the BSST films were packed more densely. This was an interesting observation, because it has demonstrated that XPS measurements may help to establish the quality of lipid films deposited on the surface, in addition to the quantitative information of the lipid content, as demonstrated for the N1s regions earlier.

It is also worth mentioning that the theoretical intensity of the phosphorous peak within the lipid film has been calculated from the mean peak intensities of the single lipid samples. Details on author's calculation approach are summarised in chapter 2. Such a theoretical value of the phosphorous peak within the model lipid film was calculated at (316 ± 44) CPS and was in the same range as the value found for BSST samples: (364 ± 9) CPS and above the value for VDT samples: (105 ± 3) CPS. The slightly higher values for BSST films are attributed to the higher lipid (phosphate group) content per unit area of the lipid film surface, whilst the lower values for VDT to lower density of lipids (phosphorous) per surface unit. This is interesting, because the single lipid samples that have been used for the calculation of the theoretically expected intensity, were lipid bulks deposited on the mica surface. Since the mathematical calculations assumed the homogenous mixing of lipids, the fact that BSST values were close to the theoretical values suggested homogenous distribution of phosphate groups within the XPS-studied surface areas (at the scale of observation). It also suggests

that XPS studies on lipids deposited on the surface as a bulk may serve for the predictions of lipids deposited on a surface in a form of a thin lipid film. However, further studies would need to be performed in order to confirm this hypothesis.

To summarise, the analysis of XPS spectra has suggested that the VDT protocol resulted in films of a more accurate composition of model lipids (table 3.2). Also, XPS analysis indicated that the BSST protocol resulted in films of higher density of lipid molecules per square metre of the lipid film surface. Both observations were consistent with the previous AFM and ToF-SIMS studies. It is worth mentioning that the innovative analysis approach of the XPS spectra in the N1s region can be applied across various lipid compositions of supported lipid films.

3.4.2 AFM: studying SLB behaviour.

In addition to the optimisation of fabrication methodologies, the AFM enabled studies of the behaviours of the model lipid films *in situ*, at a nanometre scale. Since the following chapters also focused on such studies, the aim of this section is to introduce the reader to the hypotheses associated with the phase separation behaviours within the model SLBs.

Since the model lipid composition consisted of five lipids of various transition temperatures, the ability of the model SLB system to produce phase separated film morphologies was investigated by AFM. The summary of such investigations is presented in figure 3.11.

The AFM investigations enabled visualising that phase separation within the model SLBs occurred in three instances: (i), when the model lipid bilayers were heated above 45°C using the VDT fabrication protocol; (ii), when the model SLBs were fabricated using liposomes of different ages and (iii), once the model SLBs were dried and incubated in high humidity environments over time.

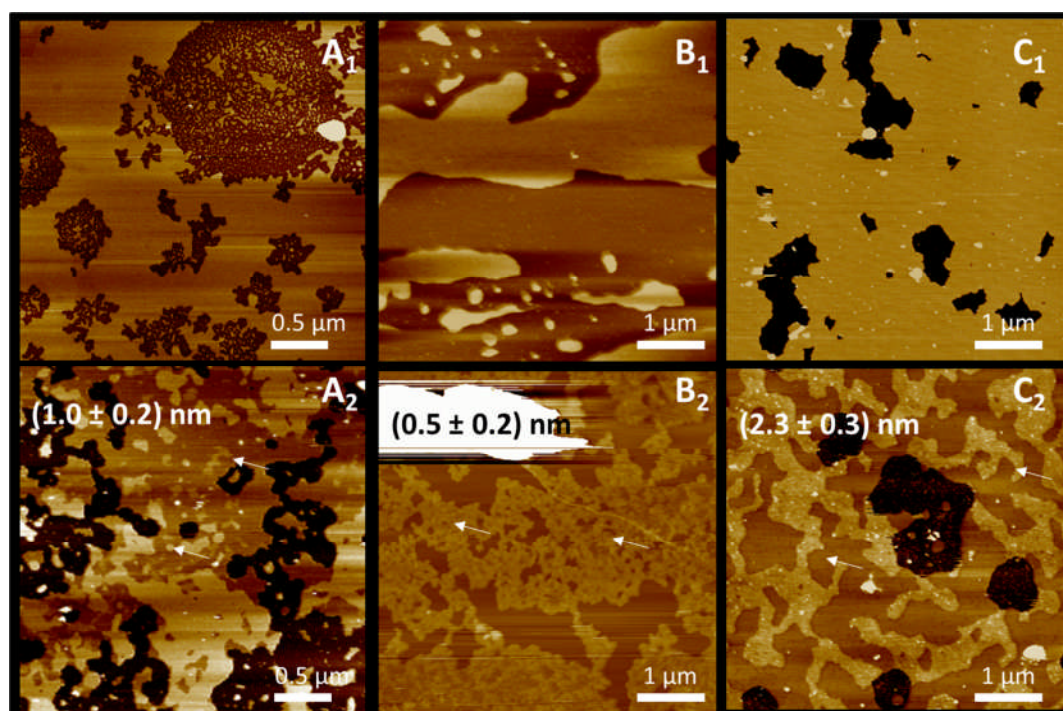


Figure 3.11. AFM images presenting the instances of phase separation occurrence within the model SLBs. A_1 presents the morphology of the model SLB prepared after incubation at 35°C, while A_2 the morphology after incubation above 45°C using vesicle deposition protocol. B_1 presents the morphology of model SLBs imaged in liquid environments, while B_2 the morphology after 52-minute incubation of dry, model SLBs at 70 % relative humidity and 28°C sample stage temperature. C_1 and C_2 indicate the morphologies of model SLBs prepared using standard vesicle deposition protocol at 35°C and liposomes 9 days and 71 days following preparation. Liquid-ordered domains (L_O) on images with phase separated morphologies (2) have been indicated with arrows. The mean thickness of the L_O domains in each instance has also been indicated. Z-scale bars were removed for clarity purposes (average range 0-10 nm).

Currently, the exact mechanism of phase separation (or liquid-ordered (L_O)* domain formation) within complex lipid bilayer models is not clear¹⁸. Therefore, the interpretation of the AFM results has been based on consideration of lipid and bilayer physicochemical properties, as well as the experimental observations that are discussed later in the thesis. However, it is well established that phase separation is associated with two phenomena; an increase of the L_O domain thickness¹⁹ and changes to spatial distribution of SPM and CHOL lipids within the bilayer (assembly)²⁰. These lipids have been identified as the two main components of the L_O domains¹⁹. Therefore, in order to explain the temperature-triggered phase separation mechanism the chemical structures of CHOL and SPM were initially studied.

* The terms: liquid-ordered (L_O) and liquid disordered (L_D) domains are synonymous to liquid-condensed (L_C) and liquid-expanded (L_E) domains, respectively.

Analysis of the chemical structure of CHOL in a three dimensional (3D) format indicated that the most stable conformation of this molecule resembles a boomerang morphology, as it is presented in figure 3.12.

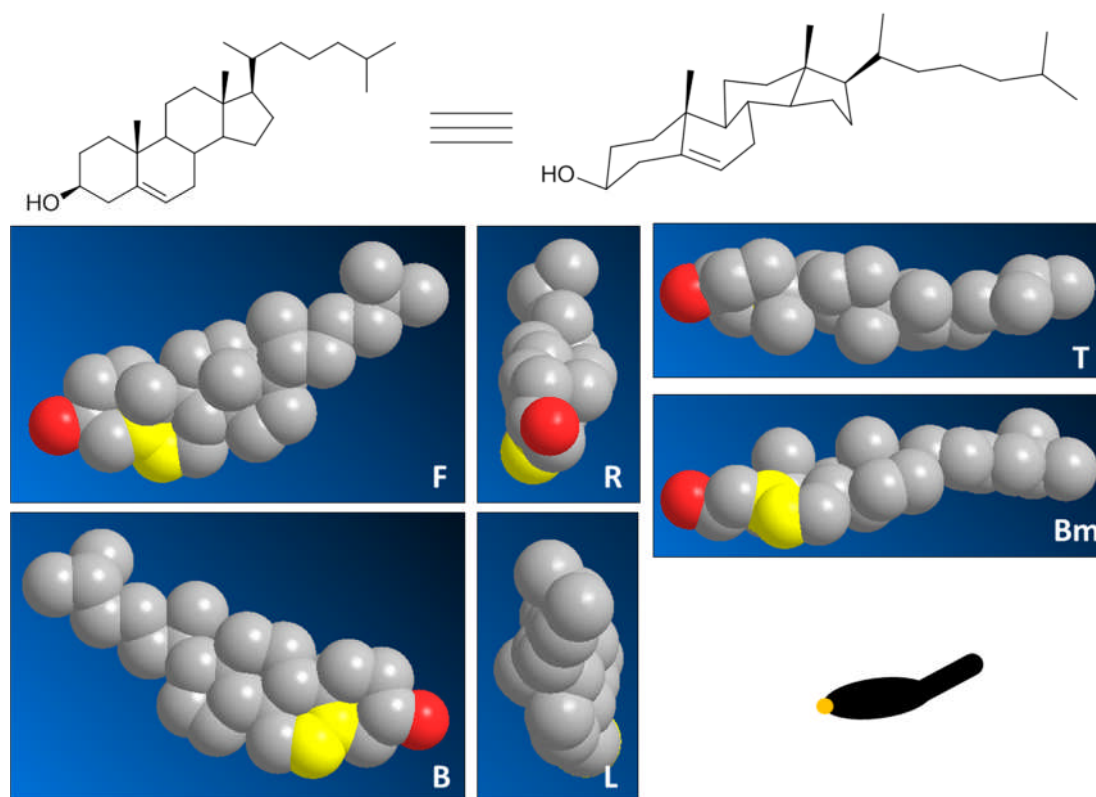


Figure 3.12. The chemical structure of cholesterol (CHOL). Top structures indicate the conformation of the molecule according to IUPAC. 3D images of the most stable cholesterol conformation are presented in all planes: coronal (F- front; B - back), sagittal (R – right; L- left) and transverse (T-top; Bm-bottom). Images were generated automatically using ChemBio3D Ultra 12.0 software. Double bond and oxygen atom have been coloured in yellow and red, respectively. Bottom right cartoon indicates the boomerang-like morphology of CHOL with hydrophilic (yellow) and hydrophobic (black) regions. Hydrogen atoms have been hidden for clarity reasons.

With regards to SPM, since an amide group is present in its structure, two critical resonance structures; ionic and non-ionic mesomers were considered. Similar analysis for both SPM mesomers suggested that the two most stable SPM 3D conformations are significantly different. This has implied that a dramatic change in the molecule geometry is associated with the transition from non-ionic into ionic mesomers, as depicted in figure 3.13. Here, since various studies have suggested different shapes for SPM without a clear scientific proof^{7c}, software enabling the visualisation of the organic chemistries in various hybridisation states (e.g. sp^1 , sp^2 , sp^3) was applied in order to assess the most stable conformations for both lipids.

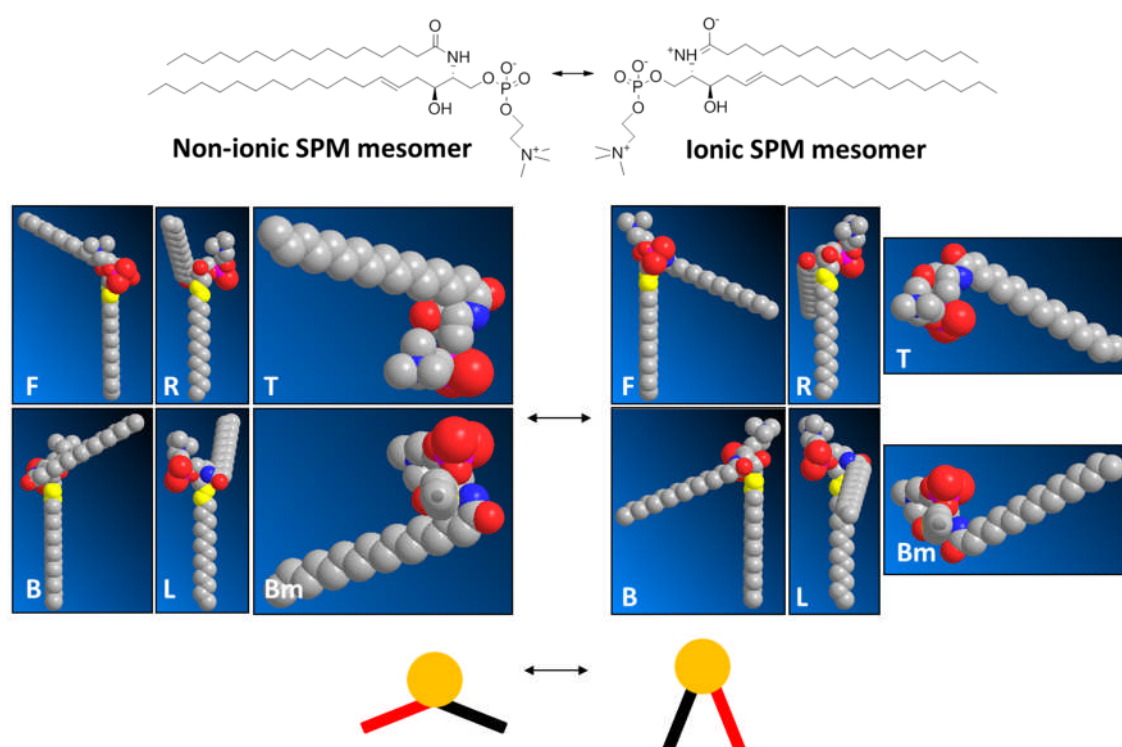


Figure 3.13. The chemical structures of ionic and non-ionic mesomers of sphingomyelin (SPM). Top structures indicate the chemical structures of both SPM mesomers. 3D images of the most stable conformations for both SPM mesomers are presented in all planes: coronal (F- front; B – back), sagittal (R – right; L-left) and transverse (T-top; Bm-bottom). Images were generated automatically using ChemBio3D Ultra 12.0 software. Double bond, nitrogen and oxygen atoms are coloured in yellow, blue and red, respectively. The bottom cartoon indicates the change in morphology associated with the transition between mesomer structures for SPM; hydrophilic head group (yellow) and hydrophobic alkenyl (black) and acyl (red) chains are indicated. Hydrogen atoms are hidden for clarity reasons.

Currently, neither the exact structure of a SPM/CHOL aggregate, nor the aggregation mechanism have been clarified. However, the fact that both molecules associate has been well established¹⁹. Literature has indicated that the most likely stoichiometric molar ratios have been either 1:1²¹ or 2:1²² CHOL:SPM, which is stabilised *via* several bond types. In addition, the aggregation of both molecules is associated with an increase in the thickness of the L_0 domains during phase separation of the membrane, suggesting the involvement of the ionic mesomer in the L_0 - and non-ionic mesomer in the L_D - domain (L_D – liquid disordered domain).

Taking the above into consideration, the author has proposed a hypothesis to explain both the most likely mechanism of the SPM-CHOL interaction and the possible structure of the SPM/CHOL aggregates. An ‘SPM trap’ is suggested as the name for hypothesis that is depicted and explained in figure 3.14.

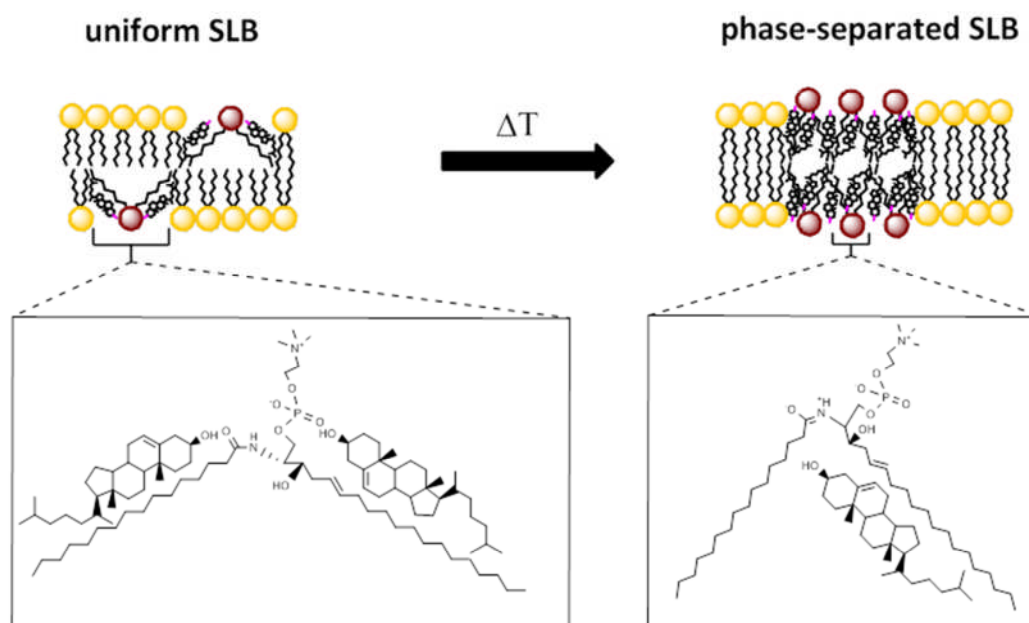


Figure 3.14. Illustration of the 'sphingomyelin (SPM) trap' hypothesis. Within a non-phase separated lipid bilayer, the non-ionised SPM mesomers are associated with two cholesterol (CHOL) molecules through hydrogen bonds, hydrophobic interaction and possibly π -bonds, which stabilise SPM mesomer conformation and assure the uniform morphology of the bilayer. Once the bilayer is heated reaching the phase transition temperature, one of the CHOL molecules inserts into the gap between both hydrocarbon chains within the SPM molecule and stabilizes the ionic mesomer through hydrogen (or even electrostatic) bonds with the amide group, hydrophobic interactions and π -bonds, causing an increase in the overall lipid height. The second CHOL is released from the initial hydrogen bonds and most likely acts as a gluing agent, attracting other SPM/CHOL aggregates through hydrophobic interactions and possibly π -stacking. The change in mesomer structure explains the increase in height, whilst the release of CHOL from a hydrogen bond and subsequent assembly of SPM/CHOL aggregates; the changes in spatial distribution of the lipids in a phase separated bilayer.

The above hypothesis is supported by several facts. It has been well established that the presence of amide groups within a molecular structure is associated with a significant increase of the boiling point. Since the transition temperature (T_t) of ceramides (e.g. SPM) is generally higher than the T_t for the other phospholipids, it is likely that amide groups significantly influence the properties of this class of molecules in addition to the presence of the long fatty acid chains in their structure²³. The presence of hydrogen bonding donor ($=N^+H^-$, $-NH-$, $-OH$) and acceptor ($-C=O$, $-C-O^-$) groups is thought to be the reason behind the higher boiling point of amides. Such groups enable forming hydrogen bonds with the external environment, which results in higher energy requirements for amides in order to reach melting point. In the lipid bilayer environment below the T_t , such hydrogen bonds might originate both from water molecules above the bilayer, and the polar head groups of the

ceramide molecule or other neighbouring lipids within. For that reason, the SPM resonance structures are likely to be dominant within a non-phase separated lipid bilayer and be involved in the interactions with the surrounding environment. Here, the XPS spectra in the N1s region of SPM lipid bulk support this claim, as according to the XPS spectrum on the pure SPM sample (lipid bulk pipetted on the surface) the vast majority of amide groups has been in the -NH- (non-ionic) rather than =N⁺(H)- (ionic) conformation (figure 3.8). Interestingly, since the morphologies of the non-phase separated SLBs were uniform, the equilibrium between the resonant structures appears to be shifted towards the non-ionised structure. For that reason, hydrogen bonding-based stabilisation of non-ionised SPM mesomer through CHOL at 1:2 (SPM:CHOL) ratio is proposed for the non-phase separated bilayer environment.

Once the temperature has been elevated, increasing the thermodynamic free energy of the bilayer system, the molecular movements are accelerated, hydrogen bonds begin to break and SPM molecules seek the most thermodynamically stable conformations. Here, both SPM resonant structures have been allowed, as it has been well established that amide groups are likely to change the structure with temperature.

According to the hypothesis, once the system has reached the phase transition temperature, the CHOL molecule that has been initially associated with the unsaturated SPM chain, forms bonds with the positively charged nitrogen in amide group. This event would effectively stabilise the ionized SPM structure through either hydrogen bonding or electrostatic interactions between CHOL hydroxyl and SPM amide groups, π -stacking between unsaturated CHOL and SPM groups, as well as hydrophobic interactions between the CHOL and SPM hydrocarbyl chains. Such a conformation would provide the best conformational fit between two molecules after careful consideration of the 3D thermodynamically stable conformations of both molecules, independently. This SPM/CHOL 'trap' would stabilize the SPM conformation associated with the ionised mesomer, bringing SPM hydrophobic chains as close as possible to each other, which would explain both the increase in thickness of the L₀ domains and high level of lipid packing within the L₀ domain structure reported in the literature¹⁹. Also, since effectively a new bond is formed between two lipids, the boiling point would significantly increase, explaining why the L₀ domains would 'crystallise' within the bilayer structure at a room temperature. The lateral self-assembly of SPM/CHOL aggregate would occur most likely through the released CHOL molecules from the initial aggregate however, the mechanism has not been clarified²⁴. If this hypothesis is true, the

confusion in terms of literature-reported stoichiometric ratios for CHOL-SPM aggregates would also be elucidated.

The assumed, elliptical cone conformation of the aggregate would fit the conclusions drawn from the AFM-observed phenomenon of spontaneous particle formation during the interaction of DNA with the phase separated model SLBs (chapter 5). The elliptical cone shape of SPM/CHOL aggregates may also fit well into the gaps associated with the grooves within the deoxyribonucleic acid (DNA) or ribonucleic acid (RNA) structures²⁵ (figure 3.15).

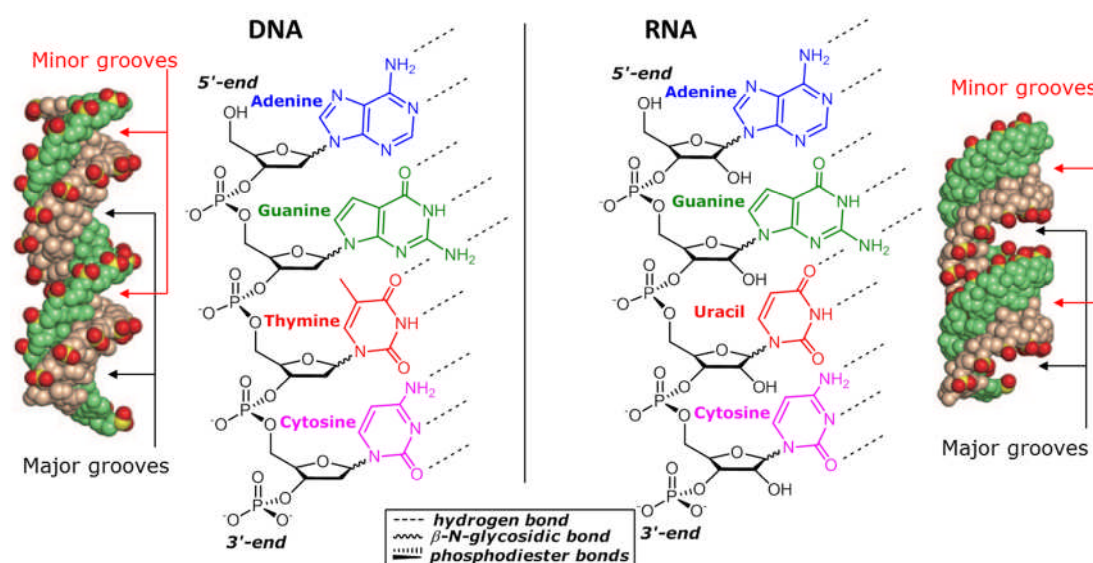


Figure 3.15. The chemical and three-dimensional structures of DNA - deoxyribonucleic acid (left) and RNA - ribonucleic acid (right) molecules. Each DNA and RNA molecule is composed of two strands associated and stabilised through hydrogen bonds forming A- or B-form helical structures, respectively. Major and minor grooves are present in both structures. Each strand is composed of phosphate-pentose-base units called nucleotides. Phosphate groups (PO_4^-) are responsible for negative charge of the nucleic acids in a solution. Deoxyribose and ribose are the pentose structures within DNA and RNA, respectively. Their conformations are the molecular reason behind the differences in morphology between both nucleic acids. Adenine (blue), guanine (green), cytosine (purple) are bases that DNA and RNA have in common. Thymine (red) is present only in DNA, whilst uracil (red) only in RNA. The bond types present in both nucleic acids are also presented. Three dimensional structures of DNA and RNA have been adapted from ref. 39.

It is thought that the electrostatic DNA-SPM interactions and the hydrogen bonds between lipid head groups and DNA core, as well as hydrophobic inter-lipid interactions may be involved in the stabilisation of DNA/SPM/CHOL lipoplex. Also, the proposed hypothesis would correlate with the observations regarding kinetic changes to the model SLB throughout the AFM studies. Since the conformations of SPM/CHOL aggregates have been different in a non- and phase-separated bilayer, lipids would provide a different

stereochemical fit for DNA strands; the better being the elliptical cone shape in phase separated bilayers. For that reason, the changes of SLB behaviour would happen gradually for uniform SLBs and quite suddenly, directly above the L_0 domains (see figures 5.2 and 5.3 later in this thesis).

This 'SPM trap' hypothesis would also help to explain the liposome age-related phase separation observed throughout the model SLB development. As indicated in figure 3.11, the older the liposomes are, the more likely the SLB fabrication using VDT results in phase separated SLB morphologies, at temperatures lower than 45-50°C, forming L_0 domains of higher heights and overall lower surface areas within the image. This implied that the formation and self-assembly of SPM/CHOL aggregates into more tightly packed domains occurred gradually over time within a bilayer structure. If this conclusion was true, the age-related phase separation of a lipid membrane would be a phenomenon playing an important role in membrane, liposome and cell aging mechanisms. It is well established that the stability of liposomes decreases with time²⁶. Since liposomes are spherical structures with a high bilayer curvature, the gradual formation of tightly-packed and rigid L_0 domains within a liposomal membrane would significantly affect lipid fluidity effectively making the liposomes more prone to break. Also, the formation of 1-3 nanometre-thick edges within the liposome surface would contribute, if not trigger, the fusion of liposomes in a solution due to the edge effect (see chapter 4). In a native biological membrane, where the formation of SPM/CHOL aggregates is likely to be decelerated *via* protein and/or carbohydrate components of the membranes, the formation of L_0 domains may occur even slower possibly indicating the reason for unclear existence of lipid rafts in biological membranes. However, if the L_0 domains formed within a biological membrane of a certain age, the cellular environments would most likely change, directing cells with such membranes onto necrosis or apoptosis pathways. Since SPM lipids are identified as key determinants involved in cell death²⁷, as well as the presence of lipid rafts has been associated with cellular senescence-related signalling²⁸, such a hypothesis is possible. Interestingly, aging of an erythrocyte (eryptosis) is also associated with changes related to the plasma membranes²⁹.

Finally, the 'SPM trap' hypothesis would also be in agreement with the phase separation mechanism observed throughout the incubation of dry SLBs in a high humidity chamber (chapter 6). This phenomenon is most likely associated with the gradual structural reorganisation of bilayer lipids. Once the amount of water-lipid head group hydrogen bonds was decreased, the forces involved in inter-lipid interactions would start playing the

dominant role as factors providing the most energetically stable organisation of lipid molecules. For that reason, the formation of SPM/CHOL aggregates and their self-assembly would occur initially within the model bilayer, until the SLB lipids start forming bulk and micelle-like structures, resulting eventually in the delamination of the bilayer³⁰. Both phenomena have been manifested as the gradual appearance of L_0 domains, as well as the appearance of particular structures directly above the model SLBs, over time, as presented in figures 3.11. and 6.3. Such a mechanism is unlikely to be observed *in vivo*, due to the presence of membrane-stabilizing proteins and carbohydrates in a biological membrane however, it has indicated that the incubation of SLBs in high humidity environments could increase the overall stability of the model SLBs when exposed to air. This was identified as being beneficial in terms of SLB microarray development, as discussed in chapter 6.

3.5 Conclusion

In conclusion, the advanced surface analysis techniques, such as ToF-SIMS, XPS and AFM have been confirmed as very important techniques for SLB-related research. ToF-SIMS and XPS investigations allowed the qualitative and quantitative characterisation of the lipid compositions of the model SLBs, improving the general understanding of such membrane models at a molecular level. AFM studies enabled not only the development and optimisation of model SLB fabrication protocols, but also the comparison of the SLB behavioural properties at a nanometre scale, with the behaviours of cellular membranes *in vivo* demonstrating again that SLBs are valid models for membrane studies. Here, a new hypothesis regarding the aggregation of SPM and CHOL within model SLBs has been proposed. Since these lipids are associated with both lipid rafts and the L_0 domains of lipid bilayers, it is anticipated that subsequent research verifying the considerations may significantly impact the currently unclear role, existence and formation mechanisms associated with phase separation of lipid bilayers, lipid rafts and the protein ingredients within.

Finally, the development of an SLB model was successfully performed, hence, further assessment with regards both formulation-SLB interaction performance, as well as the throughput SLB-based applications has been studied and presented in the following chapters.

3.6 References

1. Feigenson, G. W., Phase behavior of lipid mixtures. *Nature chemical biology* **2006**, 2 (11), 560-563.

Chapter 3: Fabrication and Characterisation of Model SLBs.

2. Soliman, M.; Nasanit, R.; Allen, S.; Davies, M. C.; Briggs, S. S.; Seymour, L. W.; Preece, J. A.; Alexander, C., Interaction of reducible polypeptide gene delivery vectors with supported lipid bilayers: pore formation and structure-function relationships. *Soft Matter* **2010**, *6* (11), 2517-2524.
3. Seifert, U., Configurations of fluid membranes and vesicles. *Adv Phys* **1997**, *46* (1), 13-137.
4. Radler, J.; Strey, H.; Sackmann, E., Phenomenology and Kinetics of Lipid Bilayer Spreading on Hydrophilic Surfaces. *Langmuir* **1995**, *11* (11), 4539-4548.
5. (a) Castellana, E. T.; Cremer, P. S., Solid supported lipid bilayers: From biophysical studies to sensor design. *Surf Sci Rep* **2006**, *61* (10), 429-444; (b) Ferrari, M., *BioMEMS and biomedical nanotechnology*. Springer: New York, 2006; (c) Johnson, J. M.; Ha, T.; Chu, S.; Boxer, S. G., Early steps of supported bilayer formation probed by single vesicle fluorescence assays. *Biophys J* **2002**, *83* (6), 3371-9; (d) Weirich, K. L.; Israelachvili, J. N.; Fygenson, D. K., Bilayer edges catalyze supported lipid bilayer formation. *Biophys J* **2010**, *98* (1), 85-92; (e) Reimhult, E.; Hook, F.; Kasemo, B., Intact vesicle adsorption and supported biomembrane formation from vesicles in solution: Influence of surface chemistry, vesicle size, temperature, and osmotic pressure. *Langmuir* **2003**, *19* (5), 1681-1691.
6. (a) Redhead, M.; Mantovani, G.; Nawaz, S.; Carbone, P.; Gorecki, D. C.; Alexander, C.; Bosquillon, C., Relationship between the Affinity of PEO-PPO-PEO Block Copolymers for Biological Membranes and Their Cellular Effects. *Pharmaceutical research* **2012**, *29* (7), 1908-1918; (b) GM., C., Structure of the Plasma Membrane. In *The Cell: A Molecular Approach. 2nd edition.*, Sunderland (MA): Sinauer Associates; <http://www.ncbi.nlm.nih.gov/books/NBK9898/>, 2000; (c) Roelofsen, B., Molecular Architecture and Dynamics of the Plasma-Membrane Lipid Bilayer - the Red-Blood-Cell as a Model. *Infection* **1991**, *19*, S206-S209.
7. (a) Luzzati, V.; Tardieu, A., Lipid Phases - Structure and Structural Transitions. *Annu Rev Phys Chem* **1974**, *25*, 79-94; (b) van Meer, G., Membrane lipids, where they are and how they behave: Sphingolipids on the move. *Faseb J* **2010**, *24*; (c) van Meer, G.; Voelker, D. R.; Feigenson, G. W., Membrane lipids: where they are and how they behave. *Nat Rev Mol Cell Bio* **2008**, *9* (2), 112-124; (d) Kaiser, H. J.; Lingwood, D.; Levental, I.; Sampaio, J. L.; Kalvodova, L.; Rajendran, L.; Simons, K., Order of lipid phases in model and plasma membranes. *P Natl Acad Sci USA* **2009**, *106* (39), 16645-16650.
8. (a) de Meyer, F.; Smit, B., Effect of cholesterol on the structure of a phospholipid bilayer. *P Natl Acad Sci USA* **2009**, *106* (10), 3654-3658; (b) Corvera, E.; Mouritsen, O. G.; Singer, M. A.; Zuckermann, M. J., The Permeability and the Effect of Acyl-Chain Length for Phospholipid-Bilayers Containing Cholesterol - Theory and Experiment. *Biochimica et biophysica acta* **1992**, *1107* (2), 261-270; (c) Needham, D.; Nunn, R. S., Elastic-Deformation and Failure of Lipid Bilayer-Membranes Containing Cholesterol. *Biophys J* **1990**, *58* (4), 997-1009; (d) Owen, J. S.; Bruckdorfer, K. R.; Day, R. C.; McIntyre, N., Decreased Erythrocyte-Membrane Fluidity and Altered Lipid-Composition in Human-Liver Disease. *J Lipid Res* **1982**, *23* (1), 124-132; (e) Nissen, J.; Gritsch, S.; Wiegand, G.; Radler, J. O., Wetting of phospholipid membranes on hydrophilic surfaces - Concepts towards self-healing membranes. *Eur Phys J B* **1999**, *10* (2), 335-344.
9. Leonenko, Z. V.; Finot, E.; Ma, H.; Dahms, T. E.; Cramb, D. T., Investigation of temperature-induced phase transitions in DOPC and DPPC phospholipid bilayers using temperature-controlled scanning force microscopy. *Biophys J* **2004**, *86* (6), 3783-93.
10. Ostrowski, S. G.; Szakal, C.; Kozole, J.; Roddy, T. P.; Xu, J.; Ewing, A. G.; Winograd, N., Secondary ion MS imaging of lipids in picoliter vials with a buckminsterfullerene ion source. *Analytical chemistry* **2005**, *77* (19), 6190-6.
11. Pacholski, M. L., Principal component analysis of TOF-SIMS spectra, images and depth profiles: an industrial perspective. *Appl Surf Sci* **2004**, *231*, 235-239.
12. Loew, M.; Forsythe, J. C.; McCarley, R. L., Lipid Nature and Their Influence on Opening of Redox-Active Liposomes. *Langmuir* **2013**, *29* (22), 6615-6623.
13. Gilmore, I.; Vickerman, J. C., *Surface analysis : the principal techniques*. Chichester : Wiley, 2009.: 2009.
14. Kemnitz, C. R.; Loewen, M. J., "Amide resonance" correlates with a breadth of C-N rotation barriers. *J Am Chem Soc* **2007**, *129* (9), 2521-2528.
15. Tycko, R., Biomolecular solid state NMR: Advances in structural methodology and applications to peptide and protein fibrils. *Annu Rev Phys Chem* **2001**, *52*, 575-606.
16. Johnson, P. S.; Cook, P. L.; Liu, X. S.; Yang, W. L.; Bai, Y. Q.; Abbott, N. L.; Himpfel, F. J., Universal mechanism for breaking amide bonds by ionizing radiation. *J Chem Phys* **2011**, *135* (4).
17. Kirpotin, D.; Hong, K. L.; Mullah, N.; Papahadjopoulos, D.; Zalipsky, S., Liposomes with detachable polymer coating: Destabilization and fusion of dioleoylphosphatidylethanolamine vesicles triggered by cleavage of surface-grafted poly(ethylene glycol). *FEBS letters* **1996**, *388* (2-3), 115-118.
18. (a) Heberle, F. A.; Feigenson, G. W., Phase Separation in Lipid Membranes. *Csh Perspect Biol* **2011**, *3* (4); (b) Simons, K.; Sampaio, J. L., Membrane Organization and Lipid Rafts. *Csh Perspect Biol* **2011**, *3* (10).
19. Ohvo-Rekila, H.; Ramstedt, B.; Leppimaki, P.; Slotte, J. P., Cholesterol interactions with phospholipids in membranes. *Prog Lipid Res* **2002**, *41* (1), 66-97.
20. Slotte, J. P., Sphingomyelin-cholesterol interactions in biological and model membranes. *Chem Phys Lipids* **1999**, *102* (1-2), 13-27.
21. Zidar, J.; Merzel, F.; Hodoscek, M.; Rebolj, K.; Sepcic, K.; Macek, P.; Janezic, D., Liquid-Ordered Phase Formation in Cholesterol/Sphingomyelin Bilayers: All-Atom Molecular Dynamics Simulations. *J Phys Chem B* **2009**, *113* (48), 15795-15802.
22. Bittman, R.; Kasireddy, C. R.; Mattjus, P.; Slotte, J. P., Interaction of Cholesterol with Sphingomyelin in Monolayers and Vesicles. *Biochemistry-US* **1994**, *33* (39), 11776-11781.
23. Coderch, L.; Lopez, O.; de la Maza, A.; Parra, J. L., Ceramides and skin function. *American journal of clinical dermatology* **2003**, *4* (2), 107-29.
24. Korade, Z.; Kenworthy, A. K., Lipid rafts, cholesterol, and the brain. *Neuropharmacology* **2008**, *55* (8), 1265-73.
25. Rana, T. M., Illuminating the silence: understanding the structure and function of small RNAs. *Nature reviews. Molecular cell biology* **2007**, *8* (1), 23-36.
26. Hernandez-Caselles, T.; Villalain, J.; Gomez-Fernandez, J. C., Stability of liposomes on long term storage. *The Journal of pharmacy and pharmacology* **1990**, *42* (6), 397-400.
27. Green, D. R., Apoptosis and sphingomyelin hydrolysis. The flip side. *The Journal of cell biology* **2000**, *150* (1), F5-7.
28. Ohno-Iwashita, Y.; Shimada, Y.; Hayashi, M.; Inomata, M., Plasma membrane microdomains in aging and disease. *Geriatrics & gerontology international* **2010**, *10* Suppl 1, S41-52.
29. Lang, F.; Lang, E.; Foller, M., Physiology and pathophysiology of eryptosis. *Transfusion medicine and hemotherapy : offizielles Organ der Deutschen Gesellschaft fur Transfusionsmedizin und Immunhamatologie* **2012**, *39* (5), 308-14.
30. Albertorio, F.; Chapa, V. A.; Chen, X.; Diaz, A. J.; Cremer, P. S., The alpha, alpha-(1->1) linkage of trehalose is key to anhydrobiotic preservation. *J Am Chem Soc* **2007**, *129* (34), 10567-74.

Supported lipid bilayers to aid understanding of pharmaceutical excipient performances *in vitro*.

4.1 Abstract

Since pharmaceutical excipients are an inseparable part of a medicine, proper understanding of their bioactivities is very important. In this chapter, the mechanisms of interactions between cell membrane models and polymer excipients: PEO-PPO-PEO tri-block co-polymer surfactants are investigated. Atomic force microscopy (AFM) is successfully used to assess the changes within model supported lipid bilayers (SLBs) after exposure to Pluronics® L-62, L-64 and F-68. The possible mechanisms underlying such interactions are proposed. Additionally, unique properties of model SLBs as scientific tools for exploring the mechanisms of such interactions are identified.

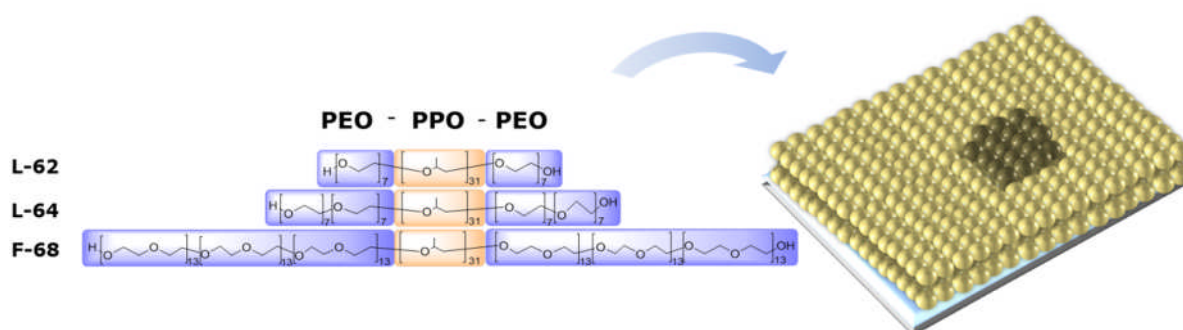


Figure 4.1. Graphical abstract indicating the experimental focus of chapter 4. The interactions between model supported lipid bilayers (SLBs) and three Pluronics® of the same polypropylene oxide (PPO) and different polyethylene oxide (PEO) block lengths: L-62, L-64, and F-68 are studied with atomic force microscopy (AFM).

Abbreviations:

AFM – atomic force microscopy; API – active pharmaceutical ingredient; CHOL – cholesterol; CMC – critical micellar concentration; DP – degree of polymerisation; F – flakes (with regards to Pluronic®); HLB – hydrophilic/lipophilic balance; L – liquid (with regards to Pluronic®); L_D – liquid disordered; L_O – liquid-ordered; MDR – multi-drug resistance; MTS – 3-(4,5-dimethylthiazol-2-yl)-5-(3-carboxymethoxyphenyl)-2-(4-sulphonyl)-2H-tetrazolium; PBS – phosphate buffer saline; PEO – polyethylene oxide; PPO – polypropylene oxide; SLB – supported lipid bilayer; SPM – sphingomyelin; w/v – weight/volume.

4.2 Introduction

Pharmaceutical excipients are an inseparable part of a formulation and not infrequently, the key reason for an active pharmaceutical ingredient (API) turning into a medication¹. In spite of a common definition of an excipient as an inactive substance, a number of studies have shown that pharmaceutical excipients are not biologically inert and may trigger either beneficial or detrimental bioresponses depending on the dose and application². For instance, PEO-PPO-PEO tri-block co-polymer surfactants (Pluronic®, Synperionics®, poloxamers) are common excipients in healthcare products³ and were reported to affect gene expression and function of membrane proteins that are involved in multi-drug resistance (MDR) phenomena⁴. Therefore, PEO-PPO-PEO tri-block co-polymers have gained a renewed interest as promising adjuvants for various drug delivery applications and an accurate understanding of their bioactivity profile has become an urgent priority⁵.

In this chapter, the mechanisms of interactions between Pluronic® and cell membrane models were investigated with atomic force microscopy (AFM). AFM studies on supported lipid bilayers (SLBs) of biorelevant lipid compositions were employed as an experimental approach to model behaviours of cellular membranes at a nanometre scale⁶. Experiments were performed using Pluronic® L-62, L-64 and F-68, as these were initially identified as representatives of the class of PEO-PPO-PEO tri-block co-polymers (figure 4.1).

This research has provided useful insights into structure-activity relationships for Pluronic®, as a class of polymers and has indicated the likely mechanism of their interactions with a cellular membrane. In addition, the impact of SLBs on exploring excipient-triggered changes of cell membrane behaviours has been demonstrated, revealing the importance of SLBs as scientific tools for formulation-membrane interaction studies.

4.3 Materials and Methods – see chapter 2

4.4 Results and Discussion

Initially, Pluronics® L-62, L-64, F-68 were identified as polymers representative of the class of PEO-PPO-PEO tri-block co-polymer surfactants. The three polymers were identified as Pluronics® of both similar structure (%PEO content as the only changing variable; figure 2.1) and significant differences in cytotoxicity profiles (table 4.1). Additionally, hydrophobicity profiles were taken into consideration: hydrophobic L-62 ($DP_{PPO} > DP_{PEO}$), amphiphilic L-64 ($DP_{PPO} \approx DP_{PEO}$) and hydrophilic F-68 ($DP_{PPO} < DP_{PEO}$). Therefore, it was hypothesized that interactions of these three chemistries with models for cell membranes at a molecular level may provide useful insights into the mechanisms of poloxamer-membrane interactions. Since concentrations of Pluronics® at or above critical micellar concentrations (CMC) caused experimental challenges (*e.g.* bubble formation whilst AFM imaging or pipetting) and previous *in vitro* studies reported no impact of CMC on cellular toxicity^{5a}, the AFM experiments were performed at concentrations below the CMC values, *i.e.* 0.001 % - 0.0001 % (%w/v). Relevant cell viability and physicochemical parameters for the representative poloxamers, which had been extracted from the literature, were summarised in table 4.1.

Table 4.1. | **The physicochemical and cell viability parameters for the representative Pluronics®.**

Pluronic name	DP_{PPO}	DP_{PEO}	F.W. [kDa]	M_n^{PPO} [kDa]	M_n^{PEO} [kDa]	% _{w/w} PEO [-]	CMC [%w/v]	HLB [-]	Integrated MTS score (Caco-2)
L-62	31	13±3	2.5	1.8	0.6±0.1	24±4	0.001	1 - 7	-0.04603
L-64	31	26±1	2.9	1.8	1.2±0.1	39±1	0.1	12 - 18	0.020236
F-68	31	157±7	8.4	1.8	7.0±0.3	79±1	7	29	0.86001

**Since the theoretical and manufacturer-reported molecular weights of the co-polymers (F.W.) are inconsistent, the degree of polymerisation for PEO block (DP_{PEO}), PEO block content (%_{w/w}PEO) and molecular weight of PEO block (M_n^{PEO}) were averaged and expressed as ($\bar{a}_2 \pm SD$); CMC (critical micellar concentration) of aqueous solutions at 40 °C were measured using DPH spectroscopy method⁷ (CMC for L-62 were extrapolated, based on CMC values reported for F-68, P-65, L-64); hydrophilic-lipophilic balance (HLB) values were indicated by manufacturer (Sigma-Aldrich and BASF); Integrated MTS scores, based on cell viability studies were taken from ref. 12.*

The composition of model SLB was selected for the reasons discussed in chapter 3. The AFM interaction studies between the Pluronics® and model SLBs were performed using three different bilayer qualities: continuous, patch-like and porous. The summary of AFM investigations for each polymer was depicted in figures 4.2., 4.3. and 4.4.

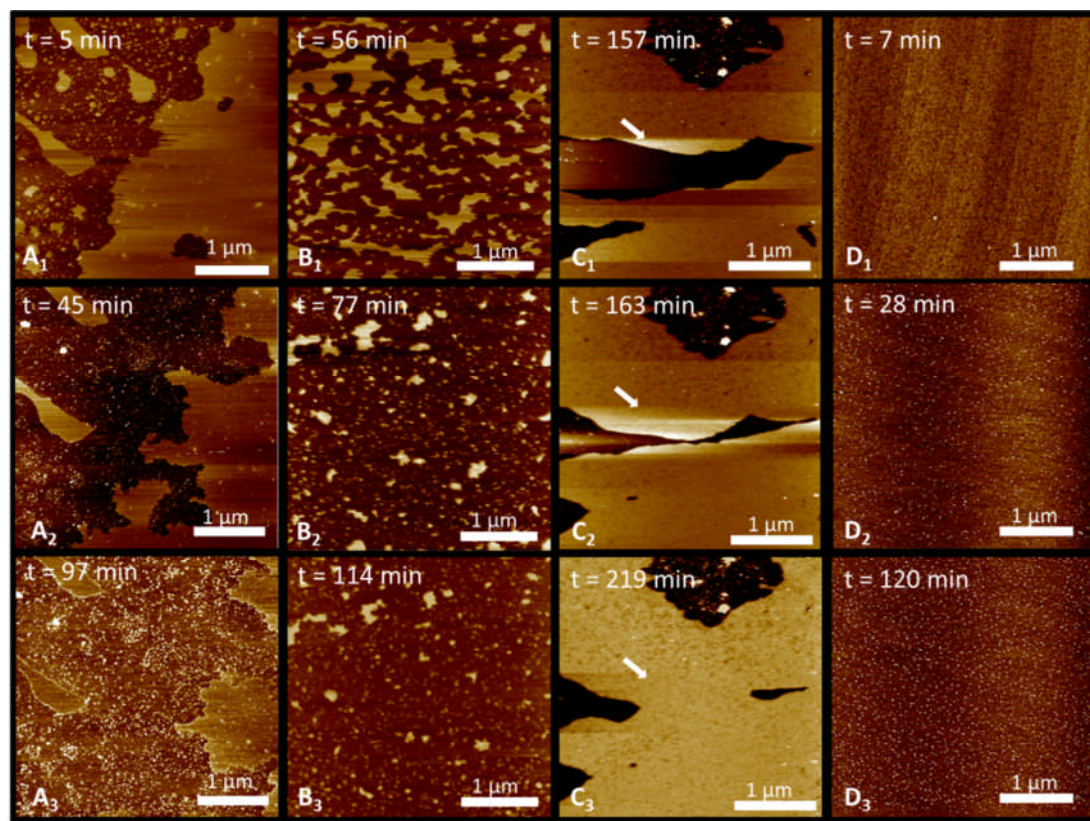


Figure 4.2. AFM images presenting steps of the interactions between model SLBs of different bilayer qualities and Pluronic® L-62 monitored over time. A_{1-3} and B_{1-3} indicate gradual desorption of model SLB patches after exposure to 0.001 % (w/v) and 0.0001 % (w/v) polymer solutions, respectively. C_{1-3} indicate gradual closure of SLB pores after prolonged exposure to 0.0001% (w/v) polymer solution. D_{1-3} present gradual solubilisation of continuous model SLB incubated with 0.001% (w/v) polymer solution. Arrows were added to indicate important observations explained throughout the text. Z-scale bars were removed for clarity purposes (average range 0-10 nm). Images are recorded in liquid environments.

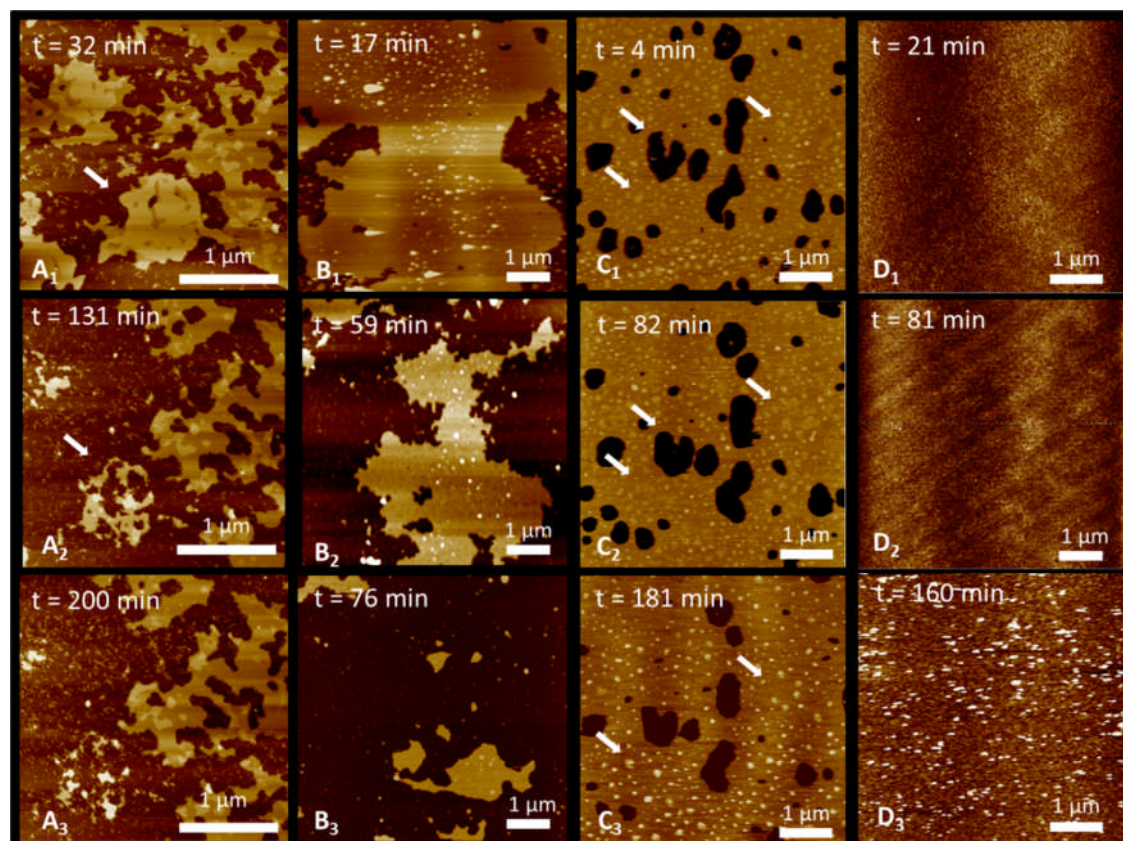


Figure 4.3. AFM images presenting steps of interactions between model SLBs of different bilayer qualities and Pluronic® L-64 monitored over time. A_{1-3} and B_{1-3} indicate gradual desorption of model SLB patches after exposure to 0.001 % (w/v) and 0.0001 % (w/v) polymer solutions, respectively. C_{1-3} indicate gradual closure of SLB pores and changes to liquid-ordered domains after exposure to 0.0001% (w/v) polymer solution. D_{1-3} present gradual solubilisation of a continuous model SLB incubated with 0.001% (w/v) polymer solution. Arrows were added to indicate important observations explained throughout the text. Z-scale bars were removed for clarity purposes (average range 0-10 nm). Images are recorded in liquid environments.

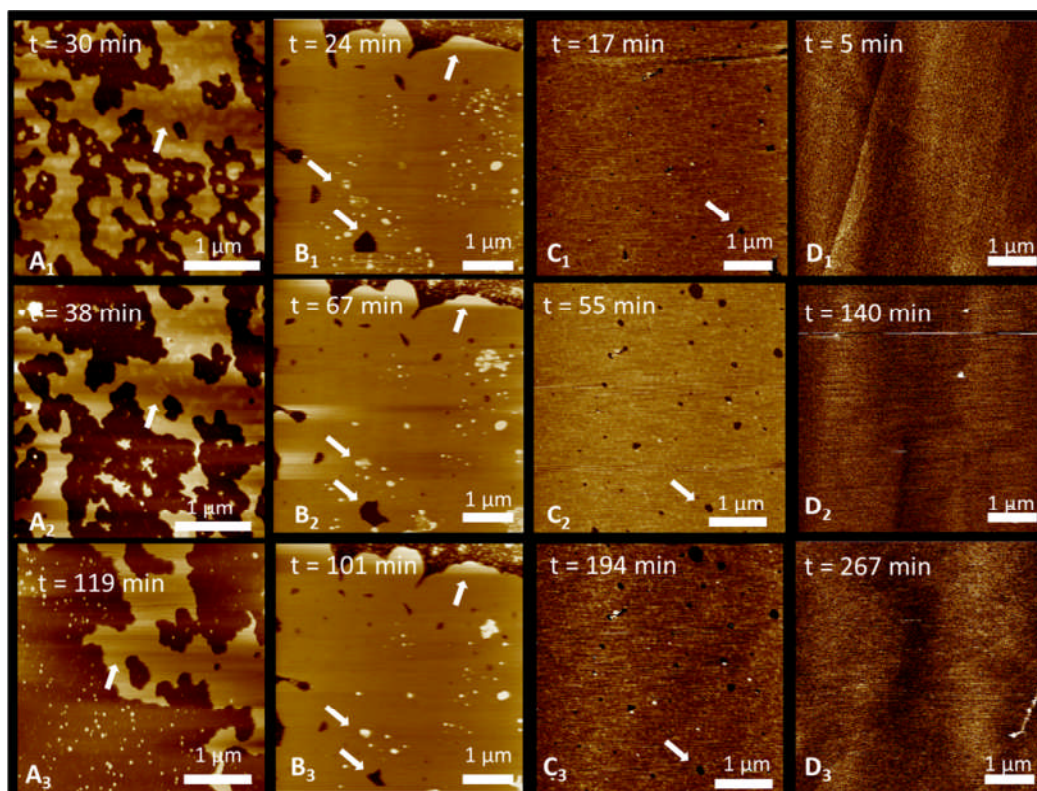


Figure 4.4. AFM images presenting steps of interactions between model SLBs of different bilayer qualities and Pluronic® F-68 monitored over time. A₁₋₃ indicate gradual desorption and changes to liquid-ordered domains within model SLB patches after exposure to 0.001 % (w/v) polymer solution. B₁₋₃ indicate both pore closure/extension and changes to L₀ domains within a porous model SLB patch, after exposure to 0.001 % (w/v) polymer solution. C₁₋₃ indicate gradual pore extension within a model SLB of non-phase separated morphology after exposure to 0.0001% (w/v) polymer solution. Images D₁₋₅ present lack of apparent changes in the morphology of continuous model SLB exposed to 0.001% (w/v) polymer solution. Arrows were added to indicate important observations explained throughout the text. Z-scale bars were removed for clarity purposes (average range 0-10 nm). Images are recorded in liquid environments.

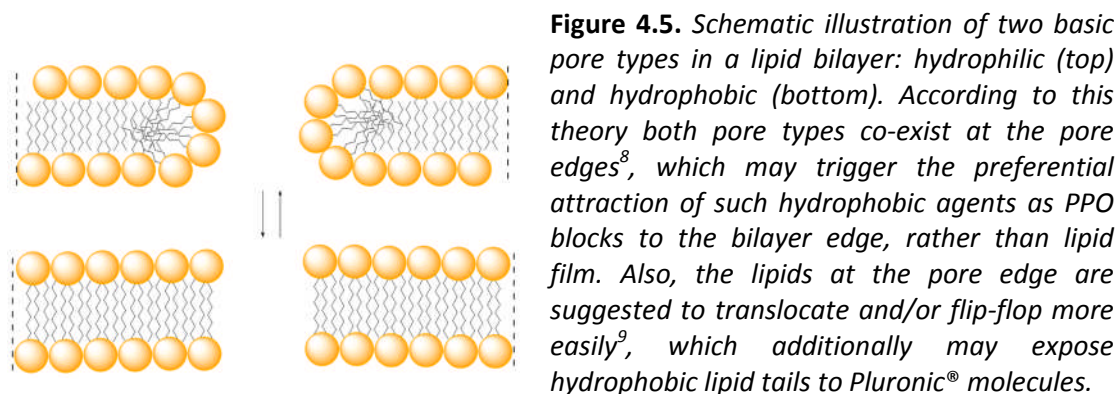
Although the morphology of continuous model SLBs with a uniform gel phase distribution was thought to be most relevant to the morphology of cellular membranes, the incubation of such SLBs with Pluronic® representatives provided limited information (figures 4.2-4.4D), suggesting that this would not be an informative model for exploring the mechanisms of membrane-poloxamer interactions. Therefore, alternative SLB morphologies were employed.

Throughout the AFM experimentation with patch-like and porous model SLB film qualities, it was observed that the addition of L-62 solution triggered changes in the environment, which critically affected imaging performance. Directly after the exposure of SLBs to L-62 solutions, the AFM probe was retracted from the surface and its rapprochement to the initial scan area

caused difficulties. For this reason, images obtained for the L-62 interaction studies were often significantly delayed. Such critical changes were not observed after gentle injections of the L-64 and F-68 solutions into the AFM environments.

Such critical changes in the imaging environment were most likely triggered by the hydrophobicity of L-62, which seemed to trigger immediate solubilisation of the model SLB and therefore disturbances in AFM imaging. Interestingly, such an effect was not observed for the continuous SLBs (figure 4.2D). This suggested that the presence of a bilayer edge in the model SLB was critical for such interaction studies and most likely the Pluronic® L-62 molecules were interacting with SLB edges in the first instance.

This hypothesis corresponded well with *in vitro* cellular toxicity studies and the theories within the lipid bilayer mechanics, according to which lipid molecules at bilayer edges are packed in a different manner than the lipids within the bilayer leaflet⁸. Since the hydrophobic lipid tails of the edge lipid (or line tension) were more likely to be exposed to polar, aqueous environments, the energy of edge lipids was increased (figure 4.5). Therefore, Pluronics®, as tension-lowering agents, may be attracted to the bilayer edge more easily.



Accordingly, the higher the edge energy of a lipid bilayer was, the more likely it desorbed from the surface, once exposed to a surfactant solution. In order to test the applicability of such hypothesis for the model SLBs, the bilayers of a patch-like topography were exposed to the surfactant solutions of interest and SLB desorption was monitored over time (figure 4.6). As presented on the graph, F-68 triggered much slower SLB desorption than L-62 and L-64, which indicated its weak performance as a surfactant. L-62 and L-64 solubilised patch-like SLBs at a similar rate, before the plateau was reached. However, L-62 reached the plateau faster than L-64 for both concentrations. Since these observations corresponded with the

lipophilicity profiles based on HLB values for the three polymers, patch-like SLB designs are proposed to serve as models predictive of Pluronic® surfactant performances.

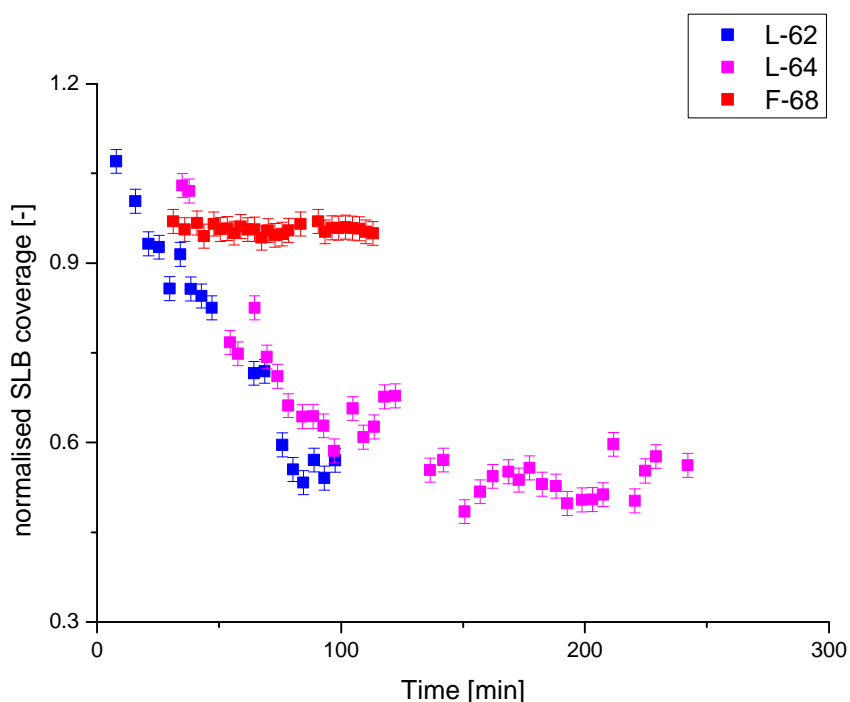


Figure 4.6. Graph presenting the changes of the coverage for patch-like, model SLBs over time, after exposure to 0.001% (w/v) Pluronic®: L-62 (blue), L-64 (purple) and F-68 (red) in PBS. The exposure of patch-like, model SLBs to L-62, L-64 and F-68 solutions results in decrease of SLB coverage over time, which is manifested as dissolution of the bilayer patches on AFM images (compare figures 4.2.A, 4.3A and 4.4.A). However, the kinetics of such interactions are different for each polymer: L-62 and L-64 trigger dramatic decrease in the SLB coverage over time, while F-68 acts as a mild surfactant decreasing the SLB coverage more slowly. Each value of SLB coverage is divided (normalised) by the SLB coverage value at the first time point of the interaction in order to highlight the differences between three Pluronic®. This is performed, because the SLB coverage values at the first recorded time point are different for each interaction causing difficulties for comparison of polymer performances. See appendix III for control studies.

Similar conclusions were drawn from the observations of the behaviour of the phase-separated, model SLBs after exposure to the three surfactants. The cholesterol/sphingomyelin (CHOL/SPM)-rich liquid-ordered (L_0) domains in model SLBs were disappearing independently of the liquid-ordered (L_0) domains, after the patch-like films of model SLBs were exposed to L-64 and F-68 (figures 4.3A and 4.4A, respectively). This implied that polymer surfactants were attracted to the L_0 edges and triggered interactions at the phase borders. Initially present L_0 domains were not identified in any of the samples after the exposure to L-62 solutions (see appendix II for the AFM image of model SLB before

addition of the Pluronics® L-62). Although this observation was strongly affected by the delay in imaging, it was reasonable to hypothesize that L-62 molecules were initially attracted to the phase separation border, as well. Also, since phase separation was not present for continuous SLBs, apparent changes in continuous SLB morphologies were less noticeable with AFM (figure 4.2D).

Intriguingly, the changes in phase separation for porous SLBs were less critical. As indicated in figures 4.3C₁₋₃, lipid phases disappeared gradually over time. Since L_O were slightly thicker than the L_D domains, it was reasonable to hypothesize that the lipids at the L_O-L_D border were of similar conformation to the lipids at the pore edge and the hydrophilic/hydrophobic pore model applied. Here, the gradual disappearance confirmed again the critical role of edge lipids for SLB-Pluronic® interactions and suggested that the phase separation borders may act as specific insertion points for the PPO polymer blocks. AFM imaging of porous SLBs exposed to L-62 was again delayed and limited data was obtained. The changes in phase separation were also noticed for Pluronic® F-68 and discussed below.

Surprisingly, the mica-bordering pores were observed to gradually decrease in size for the L-64-exposed porous SLBs (figures 4.3C and 4.7). A similar effect occurred even more rapidly for L-62 samples after prolonged incubation with fairly disrupted SLB patches (figures 4.2C). A quantitative evaluation of SLB desorption kinetics is presented in figure 4.7.

Since L-62 and L-64 acted as more efficient surfactants than F-68 on patch-like SLBs, the observations on porous SLBs were primarily unexpected. After careful consideration, the phenomenon of pore closure was hypothesized to be due to the poloxamer-triggered increase in the fluidity of model SLBs. Here, as the incubation with the polymer was causing gradual L_O domain disappearance (figure 4.3C), it was likely that the amphiphilic L-64 polymer molecules, after initial attraction and insertion across the bilayer at the L_O domain edges, were washing away the gel phase lipids from the SLBs, effecting in an improved overall lateral mobility of lipids within the bilayer leaflets. As an implication, the fluidity of the bilayer films increased, which was manifested as a gradual pore closure that was recorded with AFM (figure 4.3C). The pore closure for L-62-exposed SLBs suggested that the lipophilic polymer was able to exert increase of bilayer fluidity as well (figure 4.2C). However, this effect was noticed after prolonged exposure of porous SLBs to L-62 and multiple attempts to find an SLB-covered area for AFM imaging. For this reason, it was anticipated that this effect was recorded for SLB fragments most adhesive to the mica surface that were not solubilised with L-62 in the first instance¹⁰. If that was the case, the

uneven SLB adherence across the surface of a solid support could be viewed as another useful property of SLBs to obtain a fuller picture of the interactions at a cellular membrane.

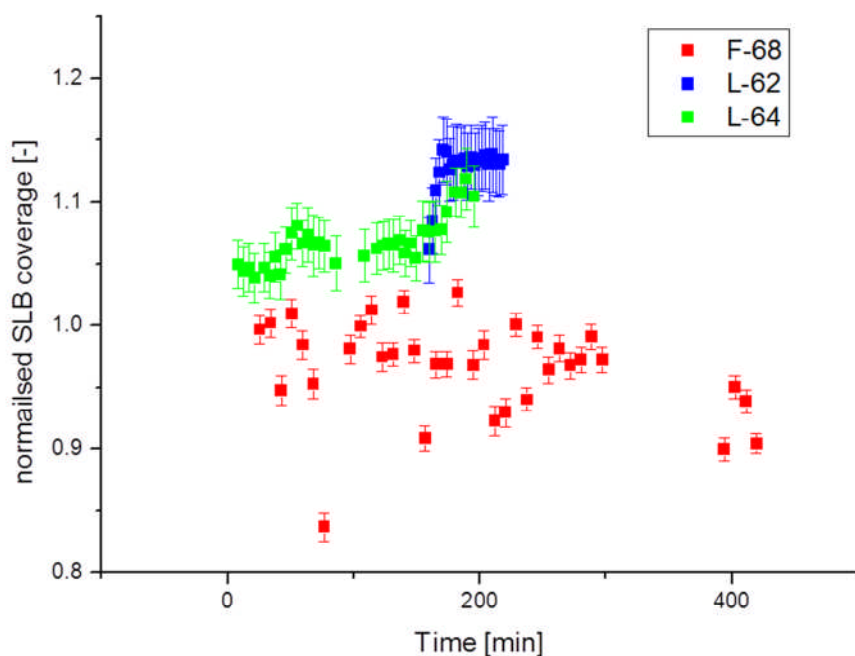


Figure 4.7. Graph presenting changes of the coverage of porous model SLBs over time after exposure to 0.0001% (w/v) Pluronic[®]: L-62 (blue), L-64 (green) and F-68 (red) in PBS. The exposure of porous, model SLBs to L-62 and L-64 solutions results in an increase of SLB coverage over time, which is manifested as a gradual pore closure on AFM images (compare figures 4.2.C and 4.3.C). The exposure of a porous, model SLB to an F-68 solution results in gradual decrease of SLB coverage, which is manifested as a gradual extension of the pores (compare figures 4.4.B and C). Each value of SLB coverage is divided (normalised) by the SLB coverage value at the first time point of the interaction in order to highlight the differences between three Pluronic[®]. This is performed, because the SLB coverage values at the first recorded time point are different for each interaction causing difficulties for comparison of polymer performances. See appendix III for control studies.

As initially hypothesized, the use of AFM imaging enabled the observations that were consistent with both cytotoxicity studies, and molecular modelling for L-64 and L-62 polymers⁵. On the one hand, continuous SLBs (most relevant to cell membrane environment) indicated faster dissolution of the bilayer for L-62 than L-64 which agreed with integrated MTS scores (table 4.1). On the other hand, the L-62- and L-64-triggered increase in bilayer fluidities indicated the involvement of transmembrane insertion mechanism proposed by Nawaz *et al.*^{5b} for both polymers.

Interestingly, Pluronic® F-68 was demonstrated to trigger both pore enlargement and closure for porous SLBs (figure 4.4B). This suggested that the bilayer interaction profile for F-68 was affected by factors additional to the edge effect. Pluronic® F-68, as a large molecule with long hydrophilic PEO chains, once attracted to the pore or L_0 domain edges, was likely not to insert the PPO block into the bilayer structure as easily as L-62 and L-64. Instead, F-68 adhered to the SLB surface and, as a mild surfactant, was gradually pulling out the L_0 domain lipids (figure 4.4B). This in turn, increased the local bilayer fluidity of lipids within the L_0 phase and resulted in local pore closure within porous lipid film. In parallel, at the SLB edges greatly exposed to mica support, F-68 triggered partial, slow bilayer dissolution, probably because F-68 molecules adhered to the mica support in a non-specific manner resulting in a higher local concentration of PPO blocks around the pore edges. This implied that the bilayer solubilisation was likely to be affected by a non-specific adsorption of F-68 to the mica support, as well as distribution of L_0 phases across the bilayer. In order to test this hypothesis, additional experiments with porous model SLBs of non-phase separated morphologies were performed. Such morphologies were expected to provide the attraction of F-68 molecules to the pore edges, without the interferences triggered by the presence of L_0 domains. As indicated in figure 4.4C, exposure of such SLBs to F-68 polymer solution resulted in a gradual pore expansion. This indicated that F-68 did not act as a sealant once exposed to non-phase separated SLB morphologies. This was expected, because the only process occurring at the bilayer edges of such morphologies was adsorption of the polymer molecule and gradual dissolution of the bilayer film. The local increase in bilayer fluidity (that was observed for the phase separated morphologies) was not present in this case. Therefore, the experiments above suggested that Pluronic® F-68 can act both as a sealant and as a mild surfactant depending on its accessibility to edge lipids, adsorption to solid supports and the L_0 domain distribution within the bilayer.

It is worth adding that the AFM-based interaction studies between F-68 and continuous SLBs, as the most *in vitro*-relevant systems indicated no, or very slow, bilayer desorption (figure 4.4D). This correlated with F-68 cytotoxicity profile and inability to haemolyse erythrocytes^{5a}. Sealant properties for F-68 were previously reported for studies employing liposome-based systems¹¹.

To summarise, a hypothesis underlying a possible mechanism of model SLB-polyoxamer interactions was drawn, based on the AFM studies, as presented in figure 4.8.

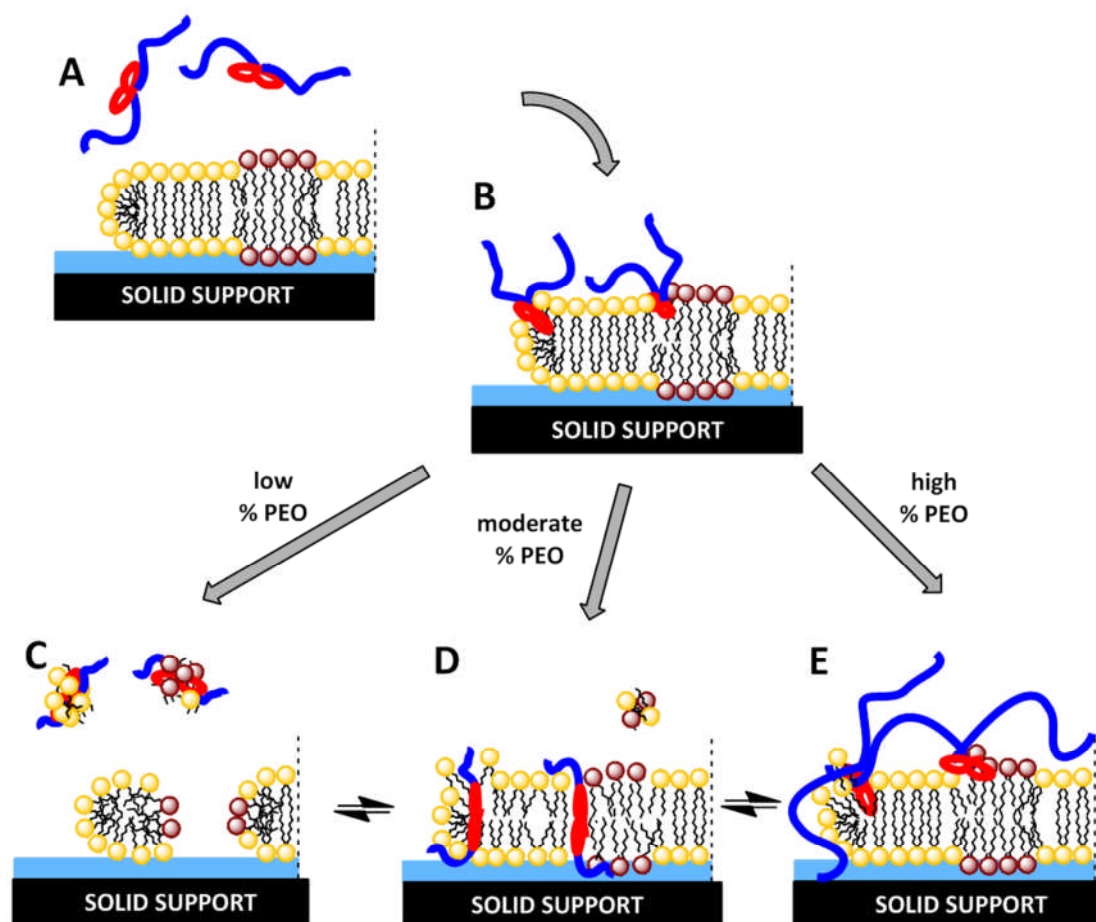


Figure 4.8. Schematic illustration of possible interaction mechanism between phase separated SLBs and Pluronic® of different polyethylene oxide block content (%PEO). (A) indicates free polymer molecules floating in liquid (white) above the edge of model supported lipid bilayers (SLBs) of phase separated morphologies (orange, brown for liquid and gel phase lipids, respectively). (B) indicates the attraction and insertion of a PPO blocks (red) into the edge lipids of a liquid-disordered or liquid-ordered phases. (C) indicates poloxamers with low %PEO that primarily trigger solubilisation of SLBs through desorption of lipids from the support. Such poloxamers may additionally insert across the bilayer causing increase in the fluidity of SLB fragments that strongly adhere to the solid support (black) surface (not shown). (D) indicates poloxamers with a moderate content of PEO (blue) which primarily insert across the membrane and increase SLB fluidity through a gradual desorption of lipids from the bilayer. (E) indicates poloxamers with high %PEO which adsorb to the bilayer and solid support surfaces through non-specific interactions with long PEO chains and trigger slow reorganisation of lipid distribution within the SLB structure. This may result in both increase of the local bilayer fluidity and lipid desorption from the surface. The monolayer of liquid environment in between the surface of solid support and bilayer film was presented in light-blue colour. The relative scales between the size of polymer molecules (~10-20nm) and bilayer thickness (~5 nm), as well as the likely conformation of polymer (as a globule) are omitted on the cartoon for the presentation purposes.

4.5 Conclusion

Model SLBs were employed to study the interactions between representatives of PEO-PPO-PEO tri-block co-polymer surfactants and models for biological membranes. This enabled hypothesizing the possible structure-activity relationship for Pluronic®, which agrees with available literature.

In addition, SLBs were demonstrated to have several advantages over the cell culture-based models, as scientific tools to investigate such interactions. For instance, SLBs can be easily studied with high resolution imaging techniques, such as AFM. In addition, the simplicity of SLB structures significantly improves the ability to study and interpret bilayer behaviour after exposure to the excipients of interest. Furthermore, since SLB morphologies can be altered (*e.g.* lipid film quality or distribution of gel phase lipids), more detailed information regarding the interaction mechanisms can be obtained. Also, uneven adherence of SLBs to solid supports may offer additional advantages for such studies. For those reasons, AFM-based excipient-SLB interaction studies may be a useful approach to study and optimise the excipient performance *in vitro*.

Interestingly, oversimplified structure, the presence of phase separation or porosity within SLBs may be criticised for their irrelevance to biological environments. As this study indicates, these properties are advantageous, providing the behaviour of model SLBs employed is well understood.

4.6 References

1. Leuenberger, H., From "functional excipients towards "drug carrier systems"". *Chim Oggi* **2006**, *24* (5), 64-66.
2. (a) Kalasz, H.; Antal, I., Drug Excipients. *Current medicinal chemistry* **2006**, *13* (21), 2535-2563; (b) Golightly, L. K.; Smolinske, S. S.; Bennett, M. L.; Sutherland, E. W.; Rumack, B. H., Pharmaceutical Excipients - Adverse-Effects Associated with Inactive Ingredients in Drug Products .2. *Med Toxicol Adv Drug* **1988**, *3* (3), 209-240; (c) Golightly, L. K.; Smolinske, S. S.; Bennett, M. L.; Sutherland, E. W.; Rumack, B. H., Pharmaceutical Excipients - Adverse-Effects Associated with Inactive Ingredients in Drug Products .1. *Med Toxicol Adv Drug* **1988**, *3* (2), 128-165.
3. (a) Schmolka, I. R., Review of Block Polymer Surfactants. *J Am Oil Chem Soc* **1977**, *54* (3), 110-116; (b) Batrakova, E. V.; Kabanov, A. V., Pluronic block copolymers: Evolution of drug delivery concept from inert nanocarriers to biological response modifiers. *Journal of Controlled Release* **2008**, *130* (2), 98-106.
4. (a) Kabanov, A. V.; Batrakova, E. V.; Alakhov, V. Y., Pluronic((R)) block copolymers for overcoming drug resistance in cancer. *Adv Drug Deliver Rev* **2002**, *54* (5), 759-779; (b) Kabanov, A. V.; Batrakova, E. V.; Alakhov, V. Y., Pluronic (R) block copolymers as novel polymer therapeutics for drug and gene delivery. *Journal of Controlled Release* **2002**, *82* (2-3), 189-212; (c) Kabanov, A. V.; Alakhov, V. Y., Pluronic (R) block copolymers in drug delivery: From micellar nanocontainers to biological response modifiers. *Crit Rev Ther Drug* **2002**, *19* (1), 1-72; (d) Bronich, T. K.; Kabanov, A. V.; Eisenberg, A.; Kabanov, V. A., Block ionomer complexes: Implications for drug delivery. *Abstr Pap Am Chem S* **2002**, *223*, U438-U438; (e) Kabanov, A. V.; Lemieux, P.; Vinogradov, S.; Alakhov, V., Pluronic((R)) block copolymers: novel functional molecules for gene therapy. *Adv Drug Deliver Rev* **2002**, *54* (2), 223-233.
5. (a) Redhead, M.; Mantovani, G.; Nawaz, S.; Carbone, P.; Gorecki, D. C.; Alexander, C.; Bosquillon, C., Relationship between the Affinity of PEO-PPO-PEO Block Copolymers for Biological Membranes and Their Cellular Effects. *Pharmaceutical research* **2012**, *29* (7), 1908-1918; (b) Nawaz, S.; Redhead, M.; Mantovani, G.; Alexander, C.; Bosquillon, C.; Carbone, P., Interactions of PEO-PPO-PEO block copolymers with lipid membranes: a computational and experimental study linking membrane lysis with polymer structure. *Soft Matter* **2012**, *8* (25), 6744-6754.
6. (a) Peetla, C.; Stine, A.; Labhasetwar, V., Biophysical interactions with model lipid membranes: applications in drug discovery and drug delivery. *Molecular pharmaceuticals* **2009**, *6* (5), 1264-76; (b) Lucio, M.; Lima, J. L.; Reis, S., Drug-membrane interactions: significance for medicinal chemistry. *Current medicinal chemistry* **2010**, *17* (17), 1795-809; (c) Pignatello, R.; Musumeci, T.; Basile, L.; Carbone, C.; Puglisi, G., Biomembrane models and drug-biomembrane interaction studies: Involvement in drug design and development. *Journal of pharmacy & bioallied sciences* **2011**, *3* (1), 4-14.
7. Alexandridis, P.; Holzwarth, J. F.; Hatton, T. A., Micellization of Poly(Ethylene Oxide)-Poly(Propylene Oxide)-Poly(Ethylene Oxide) Triblock Copolymers in Aqueous-Solutions - Thermodynamics of Copolymer Association. *Macromolecules* **1994**, *27* (9), 2414-2425.
8. Weaver, J. C.; Chizmadzhev, Y. A., Theory of electroporation: A review. *Bioelectroch Bioener* **1996**, *41* (2), 135-160.
9. Taupin, C.; Dvalitzky, M.; Sauterey, C., Osmotic-Pressure Induced Pores in Phospholipid Vesicles. *Biochemistry-Us* **1975**, *14* (21), 4771-4775.
10. Ferrari, M., *BioMEMS and biomedical nanotechnology*. Springer: New York, 2006.
11. (a) Wang, J. Y.; Marks, J.; Lee, K. Y. C., Nature of Interactions between PEO-PPO-PEO Triblock Copolymers and Lipid Membranes: (I) Effect of Polymer Hydrophobicity on Its Ability to Protect Liposomes from Peroxidation. *Biomacromolecules* **2012**, *13* (9), 2616-2623; (b) Wang, J. Y.; Chin, J. M.; Marks, J. D.; Lee, K. Y. C., Effects of PEO-PPO-PEO Triblock Copolymers on Phospholipid Membrane Integrity under Osmotic Stress. *Langmuir* **2010**, *26* (15), 12953-12961.

Supported lipid bilayers: stop-change in nucleic acid pharmacology.

5.1 Abstract

Although siRNA therapeutics hold significant potential as next-generation medicines, a lack of a detailed understanding of their behaviour *in vivo* currently decelerates the achievement of a commercial product. Studies of siRNA-membrane interactions at a nanometer scale are expected to provide useful insights into siRNA pharmacology. In this chapter, a spontaneous formation of nucleic acid-sphingomyelin-cholesterol lipoplexes is observed *via* AFM studies of the interactions between the models for lipid membranes and siRNAs. The *in vivo* implications of this phenomenon is discussed uncovering novel research directions for nucleic acid pharmacology. In addition, the mode of action and performance of polyphosphonium siRNA-type polyplexes are assessed and highlight an important role of supported lipid bilayers (SLBs) in the pharmaceutical sciences.

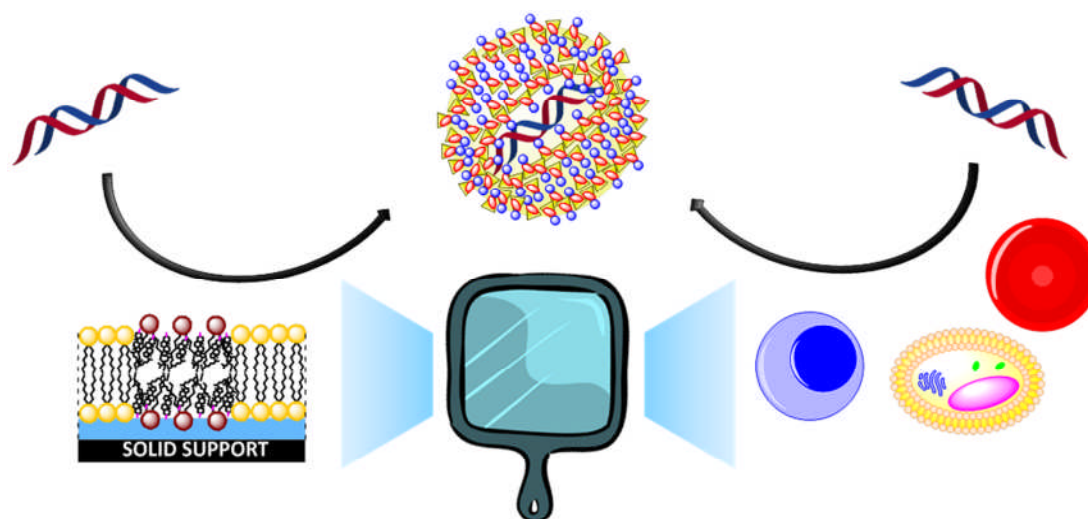


Figure 5.1. Graphical abstract depicting the spontaneous formation of DNA/sphingomyelin/cholesterol (DNA/SPM/CHOL) lipoplexes. AFM-observed phenomenon of spontaneous lipoplex formation has been correlated and discussed with the *in vivo* performance of siRNA therapeutics not only indicating the likely mechanisms involved in siRNA toxicity and cellular uptake, but also confirming the significant role of model SLBs at an early stage of drug discovery and development.

Abbreviations:

AFM – atomic force microscopy; bp – base-pair; CHOL – cholesterol; DNA – deoxyribonucleic acid; DP – degree of polymerisation; ECM – extracellular matrix; GeRPs – β -(1,3)-d-glucan-encapsulated siRNA particles; ICM – intercellular matrix; L_o – liquid-ordered; PBS – phosphate buffer saline; PPP – polyphosphonium polymer; PEG – polyethylene glycol; PEI – polyethyleneimine; RH – relative humidity; RISC – RNA-induced silencing complex; siRNA – short (small) interfering ribonucleic acid; SLB – supported lipid bilayer; SNALPs – stable nucleic acid lipid particles; SPM – sphingomyelin; TRL – Toll-like receptor.

5.2 Introduction

The formulation strategies, delivery routes and barriers for targeted delivery of short interfering ribonucleic acid (siRNA) therapeutics have been studied for many years, as thoroughly reviewed in reference 1¹ (attached as appendix IV). Unfortunately, progress has been slow with very few medicines reaching the market, which is partially due to a lack of detailed understanding of the behaviour of nucleic acid therapeutics both *in vitro* and *in vivo*. In particular, toxicity and low transfection efficacy seem to be the significant barriers that have not been addressed to date. For this reason, investigations of direct membrane interactions at a molecular level may uncover important², but hitherto uncharacterised phenomena with significant implications for drug delivery.

In chapter 5, the interactions between scientific models for siRNA therapeutics and biological membranes were investigated with atomic force microscopy (AFM). Since AFM enables studying processes at a nanometre scale, it was hypothesized that the observation of direct interactions between the siRNA formulation components and supported lipid bilayers (SLBs) of a biorelevant lipid composition³ may improve the understanding of mechanisms behind gene transfection and toxicity *in vivo*. To the author's knowledge, such studies were not performed previously; hence the interactions of both nucleic acid formulation and its components were investigated independently. In addition, such investigations were expected to enable further assessment of SLBs as models for the *in vitro* optimisation of pharmaceutical formulation performance.

The unexpected phenomena observed during these studies have potentially important implications for the pharmacology of nucleic acid-based therapeutics. Directly, this work highlights the potential of SLBs in pharmaceutical sciences, demonstrates a novel analysis approach for the assessment of formulation-bilayer interactions studied with AFM and indicates possible phenomena underlying formulation performance of nucleic acids *in vivo*. Indirectly, the focus for future research across a number of areas within life sciences is

outlined, hopefully leading to the new effective therapeutics, innovation in the drug development process and discoveries relating to how materials function in the human body.

5.3 Materials and Methods – see chapter 2.

5.4 Results and Discussion

5.4.1 Nucleic acid-SLB interactions

The interactions between the model SLBs and siRNA models were studied with AFM using porous bilayers and an unbound 19 base pair (bp), double-stranded DNA at a wide range of concentrations, in order to reflect the concentrations used for *in vitro* studies⁴. AFM PeakForce® Tapping mode was chosen as an imaging technique for liquid environments in order to both study the interactions at scales of several nanometres and minimise AFM probe-triggered damage of the sample⁵. The model SLBs and imaging in liquid environments were chosen for the reasons discussed in chapters 1 and 3. The controls for liquid injection-associated SLB disruption within the AFM system were also based on previous data (appendix II). The 19bp DNA was chosen as a model for siRNA, as it was expected to exhibit close physicochemical and behavioural similarities with siRNA molecules without the associated high cost and chemical stability issues. Although DNA and RNA structures are stereochemically different, negative charges along the strand backbones, hydrogen bonds in the core of both helices, as well as major and minor grooves within the double strands are present for both chemistries (see figure 3.15)⁶. For that reason, it was fair to anticipate that the dynamics behind the interactions between either DNA or RNA strands and significantly smaller, lipid molecules would be similar and the extrapolation of DNA-lipid interactions onto RNA-lipid interactions does not involve significant errors⁷. The model DNA sequence was designed in order to prevent self-complexation of DNA strands throughout the experimentation.

Initial imaging of the model SLBs exposed to DNA resulted in two clear phenomena. Firstly, DNA-exposure triggered an increase in the SLB fluidity when compared against non-exposed samples. This was manifested as gradual pore closure within the model SLBs that were exposed to DNA. The quantitative analysis of changes in SLB coverage over time indicated that the increase may be considered linear (figure 5.2).

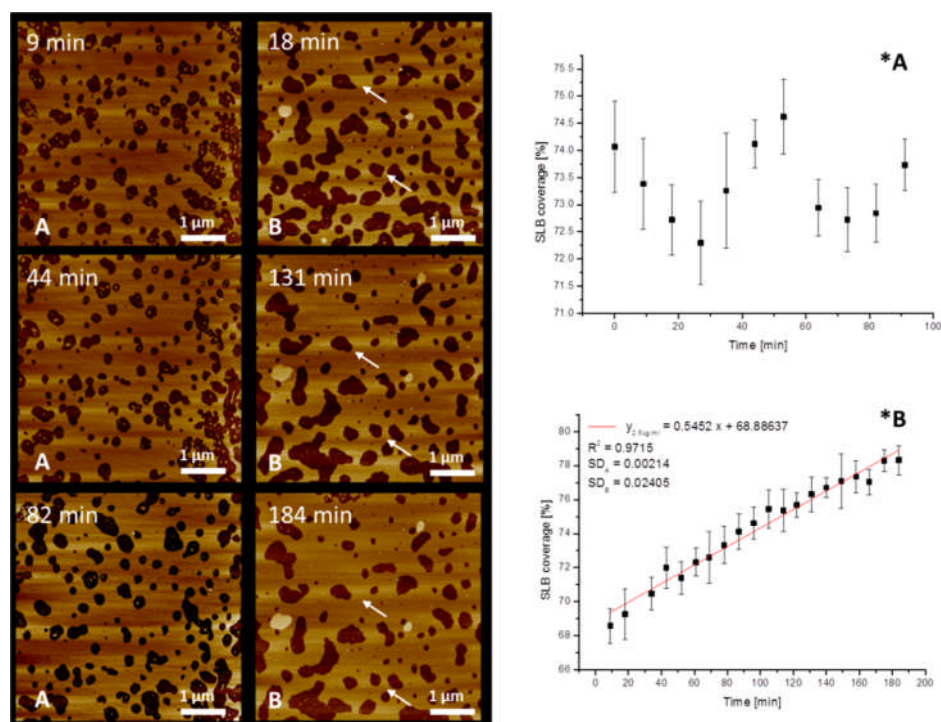


Figure 5.2. AFM images and graphs presenting the qualitative and quantitative changes to the uniform, model SLBs: before (A) and after (B) exposure to a 2.5 $\mu\text{g}/\text{ml}$ DNA solution. Control experiments (A) indicate lack of PBS or AFM probe-associated pore closure. The fluctuations of SLB coverage over time (*A) are due to image drift. Gradual pore closure is observed for DNA-exposed SLBs (B) with the linear increase in SLB coverage over time (*B). Arrows are added on (B) to demonstrate the gradual pore closure within model SLBs after exposure to DNA. Z-scale bars are removed from the images for clarity purposes Z-scale bars have been removed for clarity purposes (average range 0-10 nm). See appendix III for control studies.

Secondly, exposure of phase-separated, model SLBs to DNA resulted in significant morphological changes of the liquid-ordered (L_0) domains over time. Details regarding L_0 domain formation within the model SLBs were explained in chapter 3. As presented in figure 5.3, shortly after introduction of the DNA to the experimental environment, a spontaneous formation of the non-spherical particles [mean diameter: (117 ± 7) nm] directly above the L_0 domains was observed, leading eventually to bilayers of an altered morphology. Quantitative analysis of the changes to the L_0 domain height throughout the interaction suggested that the process could be divided into three phases: lifting L_0 domain lipids, particle formation and bilayer remodelling. In the bilayer remodelling phase, two types of isle-like domains may be distinguished: one (0.6 ± 0.1) nm and the second (2.3 ± 0.3) nm thick. The latter domain was associated with non-spherical particles of (45 ± 4) nm mean diameter. The particles formed both during particle formation and remodelling phases had similar three-dimensional structures as demonstrated by their size consistency when

measured over time of interaction vertically: (84 ± 5) nm and (28.8 ± 0.4) nm, respectively; horizontally: (140 ± 19) nm and (67 ± 11) nm, respectively; and in a diagonal direction: (108 ± 11) nm and (39 ± 11) nm, respectively. See appendix I for an example image presenting the cross section analysis on a particle during the particle formation phase.

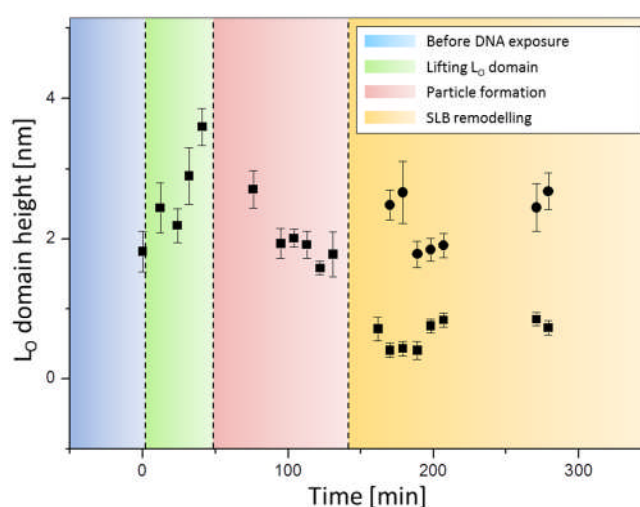
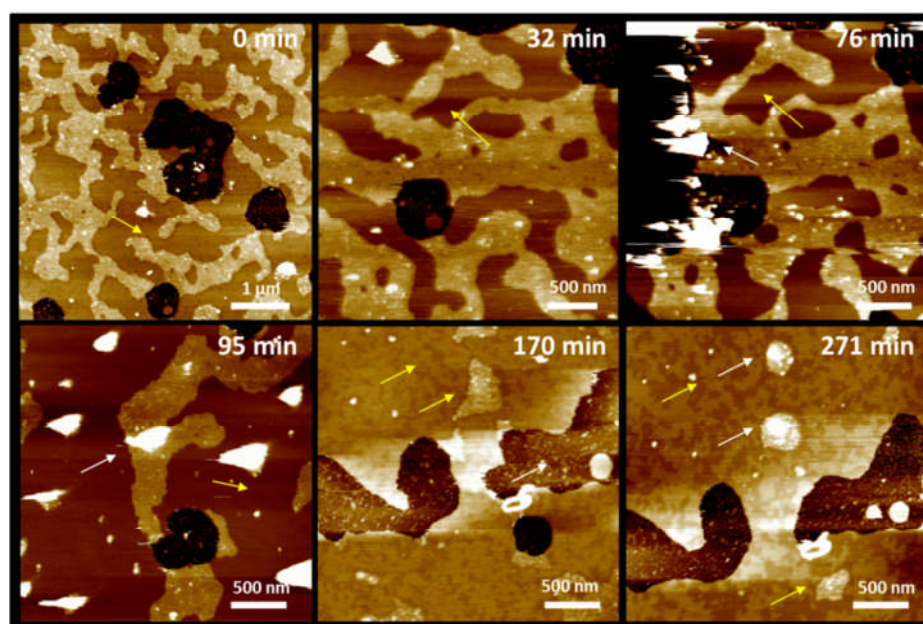


Figure 5.3. The AFM images (top) and the analysis of L_0 domain thickness (bottom) throughout the interaction of the model SLB and $5 \mu\text{g/ml}$ DNA, indicating three phases. Within the first 70 minutes after the injection of DNA into an AFM cell a gradual increase in L_0 domain height can be observed (green). Subsequently, the spontaneous formation of particles $[(117 \pm 7) \text{ nm}]$ occurs decreasing the L_0 domain height (red). After 170 min L_0 domains of two heights can be observed: (0.6 ± 0.1) (■) nm and (2.3 ± 0.3) (●) nm (orange). The thicker domains are mainly associated with particles (45 ± 4) -nm in size. Yellow arrows on AFM images indicate morphological changes to L_0 domains, whilst the white arrows indicate changes associated directly with the formation of the particles. Colours on the graph are added to highlight the changes throughout the interaction.

In addition, it was anticipated that exposure of non-phase separated, model SLBs (without noticeable phase separation) to a wide range of DNA concentrations would further help to establish the quantitative relationship between DNA concentrations and the SLB behaviour. For that reason, AFM studies on model SLBs exposed to 5; 10; 62 [$\mu\text{g/ml}$] DNA solutions were performed. The summary of these studies as well as changes of the SLB coverage over time was depicted in figure 5.4. Subsequently, in order to compare the SLB behaviour after exposure to four DNA concentrations (2.5-62 $\mu\text{g/ml}$), the slope values of the trendlines on graphs presented in figures 5.2 and 5.4 were plotted against corresponding DNA concentrations and depicted in figure 5.5. The analysis of the slope values indicated that the tendency of the model SLB coverage to increase in parallel with the increase of DNA concentration was positively proportional within the 5 - 62 [$\mu\text{g/ml}$] range. Also, the linearity of this relationship was likely ($R^2 = 0.9516$).

The AFM-observed increase in the SLB fluidity as well as both the lifting of L_0 domains and the particle formation phases suggest that the L_0 domain lipid components play a dominant role in the interaction between the bilayer and nucleic acid. The spontaneous formation of the particles associated with the L_0 domains implies two hypotheses. Firstly, the small time period between introduction of DNA molecules to the experimental environment and formation of the particular structures suggests the involvement of fast forming bonds, such as electrostatic interactions between positively and negatively charged molecules (*e.g.* sphingomyelin (SPM) and DNA). Here, the non-spherical shapes of the particles, based on the cross section analysis of AFM images at the particle formation stage, suggest that the non-spherical DNA molecule is indeed involved in this process. Secondly, the fact that the formation of particles occurs preferentially to alternative phenomena (*e.g.* the adhesion of DNA molecules to the bilayer) implies that the particle formation consisting of DNA and appropriate membrane lipid(s) is a process assuring the lowest thermodynamic free energy (Gibbs energy). Additionally, the presence of cholesterol (CHOL) within the bilayer had been associated with both a linear increase in lipid bilayer rigidity⁸ and the formation of aggregates with SPM⁹. The increase in fluidity of the model SLBs suggests an overall loss of CHOL within the model bilayer structure after exposure to DNA.

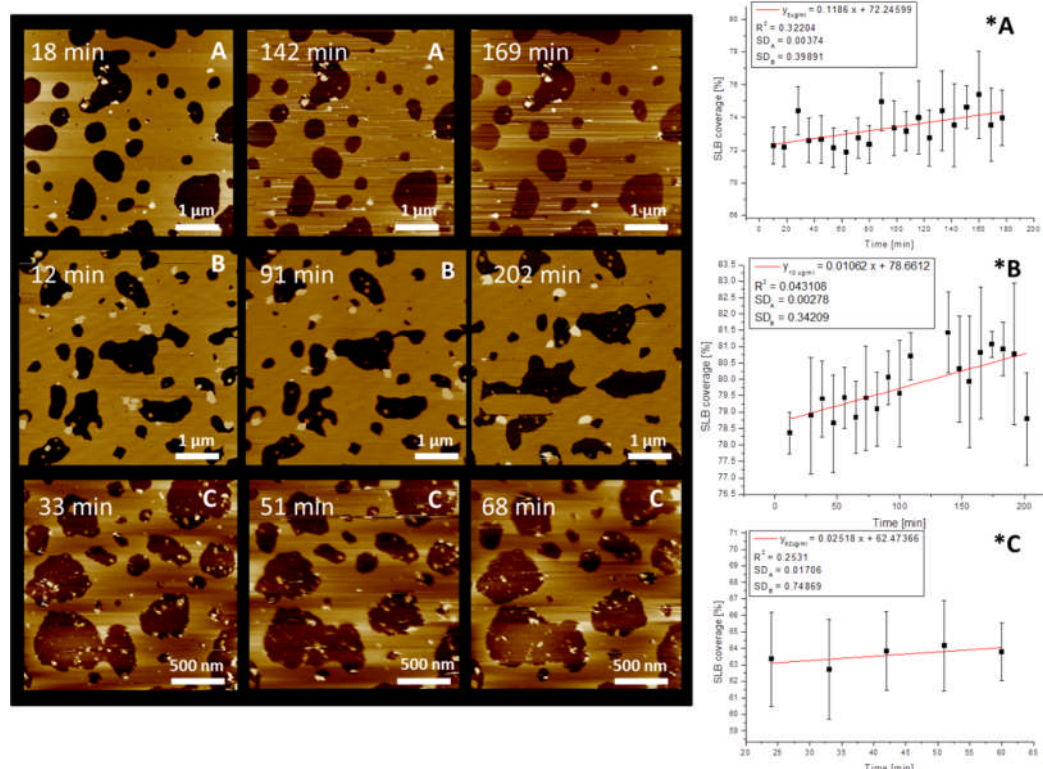


Figure 5.4. The AFM images and graphs presenting the qualitative and quantitative changes to the non-phase separated, model SLBs over time after exposure to: 5 (A), 10 (B), 62 (C) [µg/ml] DNA solutions. Both particle formation and gradual pore closure are observed for all DNA-exposed SLBs with a linear increase in SLB coverage over time (*). See appendix III for control studies. Z-scale bars have been removed for clarity purposes (average range 0-10 nm)

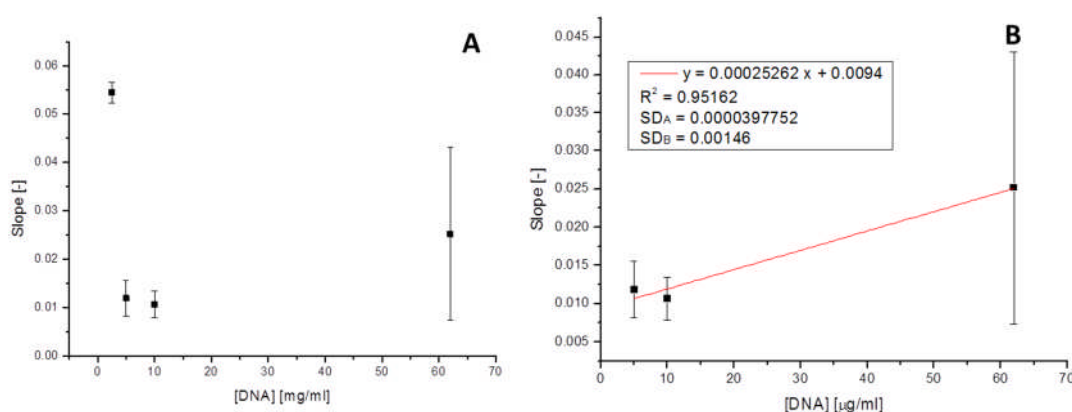


Figure 5.5. Graphs illustrating the quantitative relationship: DNA concentration vs. the increases of SLB coverage over time. (A) indicates the relationship between four DNA concentrations and slopes calculated from SLB coverage vs. time evaluations (compare figures: 5.2 and 5.4). (B) illustrates the linear correlation parameters: R^2 , slope, intercept and their errors (SD_A , SD_B , respectively) within the 5-62 µg/ml DNA concentration range.

For the reasons above, it is the author's interpretation that DNA associates with the bilayer lipids forming stable particle-like complexes composed of DNA, SPM and CHOL (DNA/SPM/CHOL lipoplex). The interaction is most likely triggered by the electrostatic attraction between the negatively-charged phosphate groups of DNA molecules and the positively-charged trimethylammonium residues within SPM hydrophilic head groups facing the liquid environment in the upper leaflet of the bilayer. For phase separated SLBs, the bilayer edge effect (see chapter 4) may also play a secondary role¹⁰. After association with the SPM/CHOL-rich regions, the DNA macromolecule cannot be inserted into the bilayer structure due to its large size and hydrophilic nature¹. Instead, it gradually lifts SPM/CHOL aggregates from the bilayer causing both the formation of the particles and remodelling of the L_0 domains within the model SLBs. The exact composition of the L_0 domains after prolonged exposure to DNA could not be fully elucidated by AFM imaging. However, based on the co-existence of two separate isle-like domain types at the remodelling stage, the occurrence of two processes is implied. The first one, associated with the (0.6 ± 0.1) -nm thick domains, results in the release of the excessive CHOL accumulated in the native L_0 domains that is responsible for 'gluing' the SPM/CHOL aggregates (compare chapter 1). The morphology and the larger surface area of these domains within the remodelled SLBs agree with this explanation. The second process, related to the (2.3 ± 0.3) -nm thick domains, is the fusion of DNA/SPM/CHOL lipoplexes with the remodelled SLBs. The presence of the particles that are smaller, yet similar in shape to the DNA/SPM/CHOL lipoplexes and associated with these domains, would imply such behaviour. Here, both adsorption to the surface and hydrophobic interactions between the lipoplex and SLB lipid components may be involved in this process. A possible mechanism of the DNA-model SLB interaction is depicted in figure 5.6.

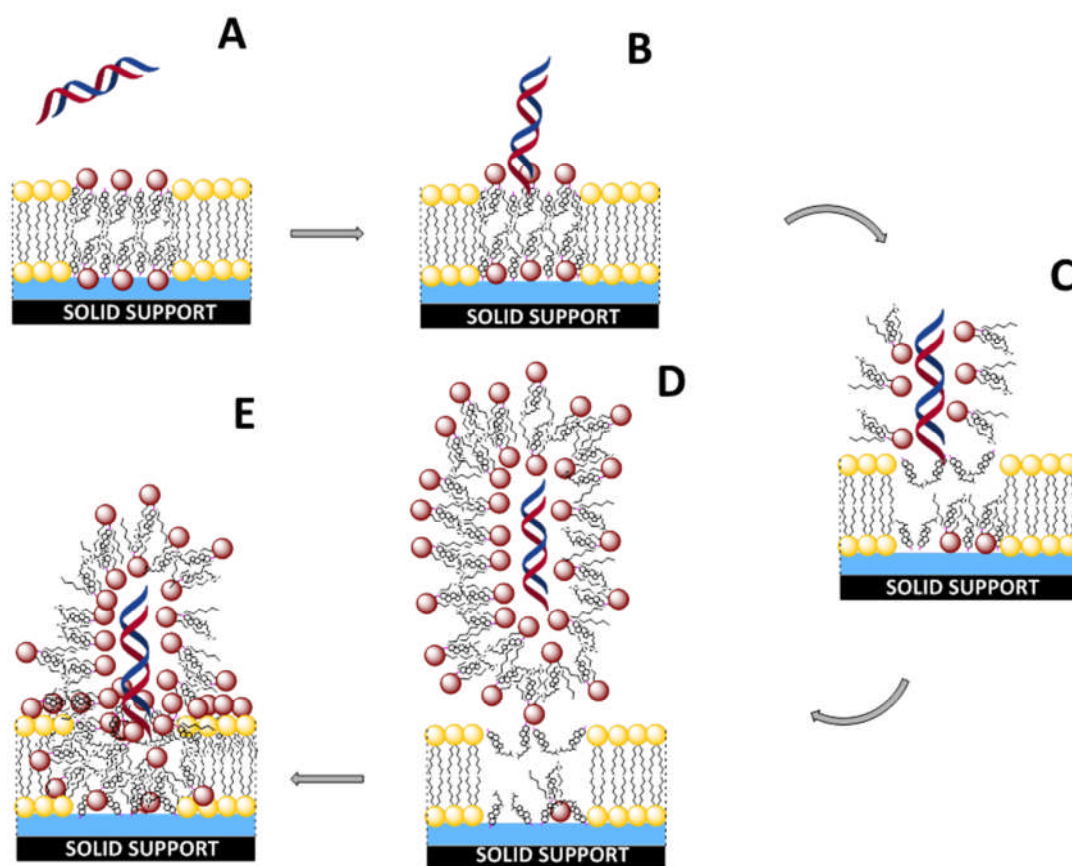


Figure 5.6. The illustration of the key steps of the interaction between DNA and a model SLB. After introduction of the DNA molecule to the SLB system (A) a gradual lifting of the L_o domain can be observed (B). Due to both: the strong electrostatic interactions and structural fit between DNA molecule and sphingomyelin-cholesterol aggregates, spontaneous formation of lipoplexes occurs (C), causing changes to the L_o domain composition and morphology (D). Finally, the lipoplex fuses with the bilayer, triggering the formation of particle-associated thick domains within the remodelled SLBs. Perpendicular orientation of DNA towards the SLB surface is suggested based on the cross section analysis of AFM-reported particle sizes.

Although the exact structure of the DNA/SPM/CHOL lipoplexes could not have been elucidated based on AFM studies alone, the particle formation phenomenon occurring spontaneously over time implied that the conformations of both lipids and DNA molecules should be energetically favourable in order to facilitate this process. Unfortunately, the exact structures of DNA lipoplexes in general, as well as SPM/CHOL aggregates remain unclear to date. Based on the SPM trap hypothesis (chapter 3), the most likely structure of the DNA/SPM/CHOL complexes is likely to resemble DNA complexes with lipid polymorphs in hexagonal H_{II} phase, as presented on figures 5.1. and 5.6.

If the spontaneous formation of DNA/SPM/CHOL lipoplexes was considered in a biological system, the phenomenon may be affected significantly by the presence of proteins, glycans and other macromolecules that both stabilize the cellular membrane and introduce steric barriers for spontaneous DNA-lipid interactions. Nevertheless, since SLBs (or direct drug-lipid interactions) have been previously utilised within drug toxicity and mode of action studies², the *in vivo* implications of the spontaneous particle formation may be important for several aspects related to the pharmacology of nucleic acids, as discussed below.

Since both SPM and CHOL are present in the vast majority of the human cell membranes and play significant structural and functional roles in the human body, the impact of the spontaneous particle formation phenomenon may be important in understanding the limitations of nucleic acid delivery science. At a cellular level, the high affinity of DNA to lipids present in the outer leaflets of biological membranes may be one reason why DNA and siRNA therapeutics are less effective *in vivo*, where there are many more lipid layers to cross, than in monolayer cell culture experiment. If such a spontaneous interaction occurs at a cell surface, the invagination of the cellular membrane would also be easier due to a local increase of the membrane fluidity. Also, the transcellular delivery of the macromolecule should be improved by the increase in overall lipophilicity of the macromolecule. However, even if the macromolecule reaches the cytosol (either through endocytosis or alternative pathways), the spontaneous complexation of the nucleic acid will reduce the effective concentration of unbound siRNA available for RISC processing. Such a hypothesis is in correlation with Langer *et al.*, who reported that ~95% of siRNA lipoplexes enters the cytosol through inhibition-resistant endocytosis pathways and remain in an endosome for a prolonged period of time, based on *in vitro* studies¹¹. Furthermore, for the vesicle-type delivery systems that pre-shield siRNAs from a direct interaction with the cellular membrane (*e.g.* GeRPs¹²), the spontaneous binding between nucleic acid and SPM/CHOL aggregates may occur in an endosome where excipient-free siRNA molecules are released. Effectively, if an siRNA/SPM/CHOL lipoplex was spontaneously formed *in vivo* and reached the cytosol of a desired cell, it is likely that the high stability of such complex significantly decreases binding with RISC, potentially explaining the low efficacy of siRNA therapeutics. Instead, the complex would either accumulate in the intercellular matrix (ICM) through interactions with lipophilic environments of a membrane or be destroyed most likely *via* the SPM-dependant pathways. Since SPM lipids (ceramides) play an important role in cell death mechanisms¹³, the latter may also be involved in the siRNA-related induction of apoptosis. Figure 5.7 depicts the considerations above.

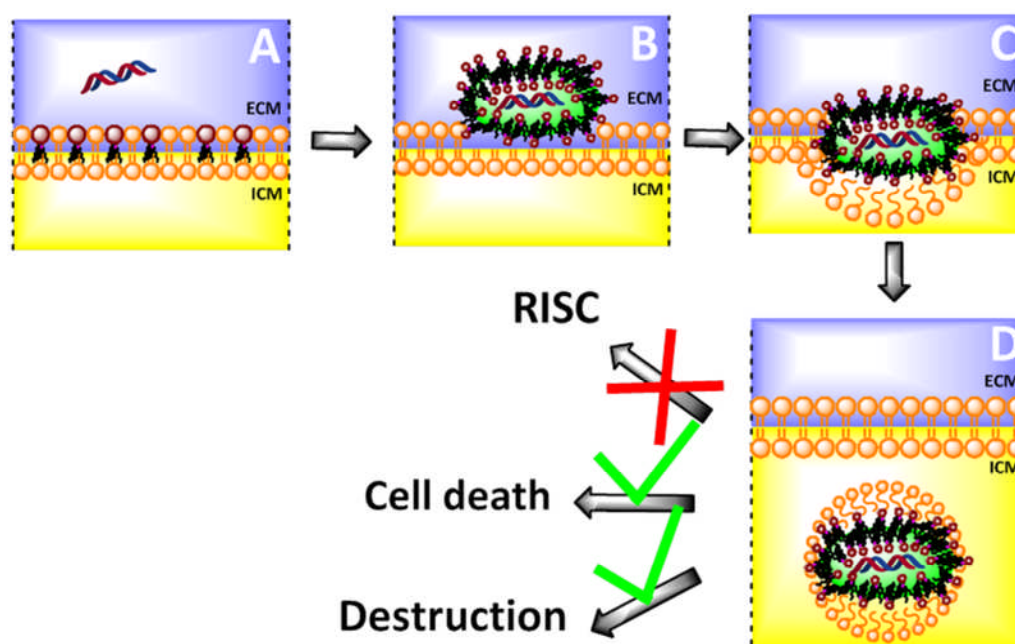


Figure 5.7. The illustration of the siRNA-cell interaction mechanism based on the AFM-observed 19bp DNA-model SLB interaction. When a chemically stable siRNA reaches the cytoplasmic membrane (A), it spontaneously forms complexes with sphingomyelin-cholesterol aggregates and fuses with the membrane (B), the subsequent local increase in the membrane fluidity triggers the membrane invagination (C). If subsequently siRNA was released to the cytosol (D), the complexation of siRNA with sphingomyelin not only interferes with the RISC processing, but also may trigger cell death or complex destruction through e.g. sphingomyelin-dependent pathways. Although a micelle-like endosomal structure is suggested at the membrane invagination stage (C), alternative lipid organisations are also possible.

The preferential binding of SPM/CHOL aggregates by DNA may also play an important role in the elucidation of the molecular mechanisms behind nucleic acid-triggered toxicity. On the one hand, an increase in the overall size of a free nucleic acid directly after *i.v.* administration is expected to trigger a response of the immune system. On the other hand, an overall increase in lipophilicity and reduction of negative charge on a nucleic acid introduced to the blood may result in an increase of likelihood of non-specific interaction occurrence with e.g. plasma or cellular membrane components. This may explain the difficulties in targeting of a specific tissue, the accumulation of nucleic acids in SPM-rich tissues, as well as various toxicity events. This hypothesis is supported by several facts associated with siRNA therapeutics and SPM research. CHOL-siRNA conjugates accumulate in liver, lung, heart, kidneys and adipose tissues¹⁴, which are all SPM-rich organs¹⁵. Also, naked siRNA accumulates in kidneys, while siRNA lipoplexes have been found in heart,

spleen, lung and liver endothelia, rather than organ matrices, only 20 minutes after tail vein injection in mice¹⁶. *Toll-like* receptors (TLRs) are associated both with siRNA-triggered immunogenicity¹ and SPM-rich regions (lipid rafts) in cellular membranes¹⁷. siRNA molecules encapsulated in stable nucleic acid-lipid particles (SNALPs) provide higher delivery efficacy *in vitro* than siRNA lipoplexes¹⁸, as SNALPs may be more efficient at shielding nucleic acids from aggregation with SPM throughout the formulation-cell interaction. In addition, DNA and siRNA complexes have been reported to trigger erythrocyte aggregation that can be reduced through PEG-based functionalization of a particle¹⁹, both *in vitro* and *in vivo*. Since erythrocytes contain large amounts of SPM/CHOL associates in the outer leaflets of erythrocyte membranes, the formation of DNA/SPM/CHOL lipoplexes may explain the mechanism involved in the erythrocyte aggregation. As the existence of lipid rafts is still uncertain and therefore the presence of SPM/CHOL aggregates in a native biological membrane may still be unconfirmed, the proposed model of the lipoplex formation *in vivo* is still likely, as the changes in membrane fluidity recorded in the AFM experiments were also observed for SLBs without a noticeable phase separation.

It is also worth mentioning that the spontaneous interaction between SPM and nucleic acids may play a role in characterising the role of SPM in the signal transduction and apoptosis or even transduction of genetic material from the host to the cell, *e.g.* during the cell-virus/bacteriophage interactions. Furthermore, since ceramides have been identified as key factors influencing cell death¹³, ceramide-enriched siRNA therapeutics may revolutionise the siRNA-based pharmacotherapy in a number of applications involving: oncology, viral, fungal and bacterial infections, metabolic, neurodegenerative or cardiovascular diseases and many more²⁰. The summary of the considerations above is depicted in figure 5.8.

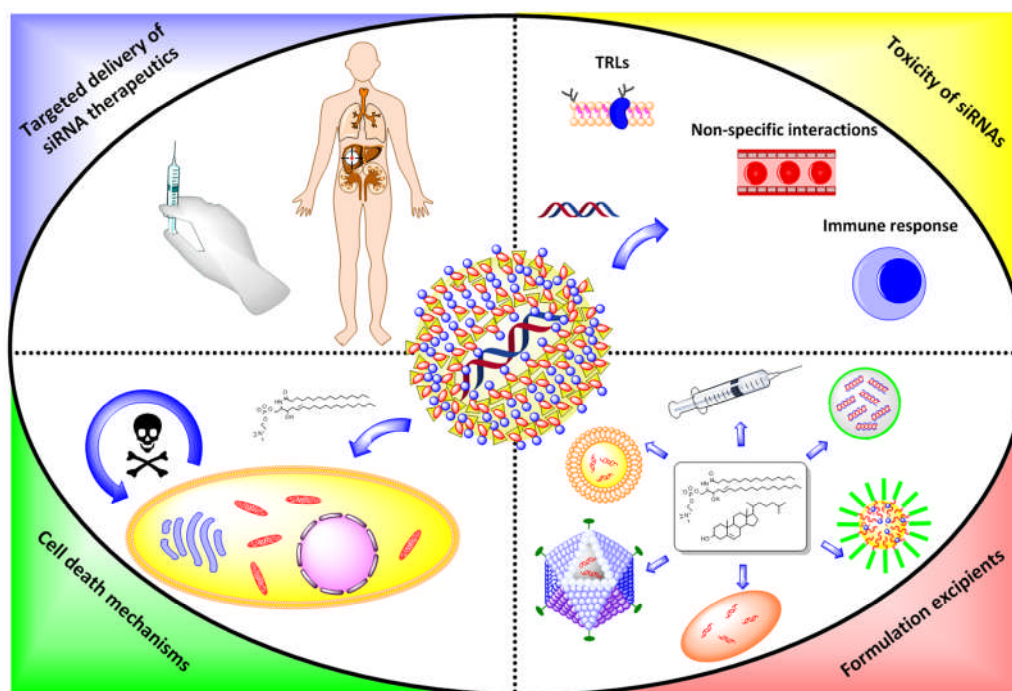


Figure 5.8. An illustration indicating the directions for future research as an implication of the spontaneous DNA-sphingomyelin-cholesterol (DNA/SPM/CHOL) lipoplex formation phenomenon. The particle formation may improve the understanding of targeted delivery of siRNA (and other nucleic acid-based) therapeutics in vivo, as explained in the text (blue). It may also provide useful insights into nucleic-acid related toxicity, e.g. associated with Toll-like receptor (TRLs) and non-specific interactions with cells and organs such as: erythrocytes, endothelium or components of the immune system (yellow). Since SPM lipids play important role in cell death mechanisms (such as apoptosis), their delivery into the cytosol with a nucleic acid molecule suggests a new biological role for this lipid in defence mechanisms (green). Additionally, since DNA/SPM/CHOL lipoplex is stable with a possible biological activity, a ceramide-enriched delivery system may be a new formulation approach for efficient nucleic acid-based therapy (red).

5.4.2 DNA polyplex–SLB interactions

As a logical extension of the observations above, the role of excipients in the nucleic acid formulation could be viewed as agents that prevent the formation of DNA/SPM/CHOL lipoplexes, when in contact with the cellular membranes. In order to assess this hypothesis, the interaction of DNA polyphosphonium polyplexes and model SLBs was investigated using AFM.

Polyphosphonium-based polymers (PPP) were chosen for AFM studies, as these were available through a collaboration with Vanessa Loczenski (a PhD student in the group, chapter 2). In addition, PPPs represent a novel class of polymers similar in structure to polyethyleneimine (PEI) – popular class of polymeric excipients for siRNA/DNA formulations,

but without some problems noted for PEI. PPP-siRNA polyplexes have been reported to provide better transfection efficacy and lower toxicity *in vitro* than the siRNA complexes with PEI⁴, therefore a mode of the mechanism of PPP-mediated gene transfection was of interest. Although PEI-SLB interactions using a 5 lipid system had not been previously investigated to the author's knowledge, the mechanisms underlying PEI transfection have been extensively investigated²¹. Thus, PPPs were excipients of preference for the AFM-based DNA polyplex-model SLB interaction studies. Additionally, due to the brush-like structure providing numerous links for both electrostatic and hydrogen bonding and a high charge density per polymer backbone (Figure 5.9), PPPs seemed to not only represent a good stereochemical fit for DNA helices (compare figure 3.15), but also introduce a significant competition against the SPM/CHOL aggregates.

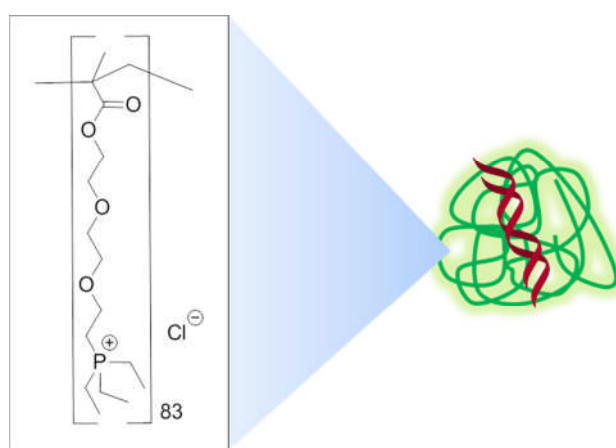


Figure 5.9. The illustration of a polyphosphonium polyplex with 19-bp DNA (right) and the chemical structure of PPP - phosphonium polymer (*P,P,P*-triethyl-*P*-[2-*O*-(2-polymethacryloyl)]-tris-(2-oxethyl)-phosphonium chloride). The degree of polymerisation (*DP*) was established through NMR (collaboration with Vanessa Loczenski). This enabled the calculation of the amounts of DNA and PPP that were required for the formation of a polyplex at an appropriate polycation:polyanion charge ratio (*P:P* ratio).

Concentrations of DNA of 5, 10, 50 $\mu\text{g/ml}$ DNA were chosen to reflect both the assumed linearity of the DNA calibration curve (figure 5.5.) and concentrations *in vitro*⁴. A 1:1 PPP/DNA charge ratio for the polyplex was chosen for the AFM interaction studies to assure the presence of unbound and bound DNA in the sample. This has been established *via* the collaboration, based on gel retardation assay studies on PPP-DNA polyplexes at different charge ratios. For the summary of particle characterisation data see appendix II. Polymer solutions of 90 $\mu\text{g/ml}$ were chosen for the interaction studies as a control to reflect the highest concentration of the polymer used for polyplex-model SLB interaction studies.

A summary of the AFM data investigating interactions between free PPP and PPP polyplexes with the model SLBs is presented in figure 5.10.

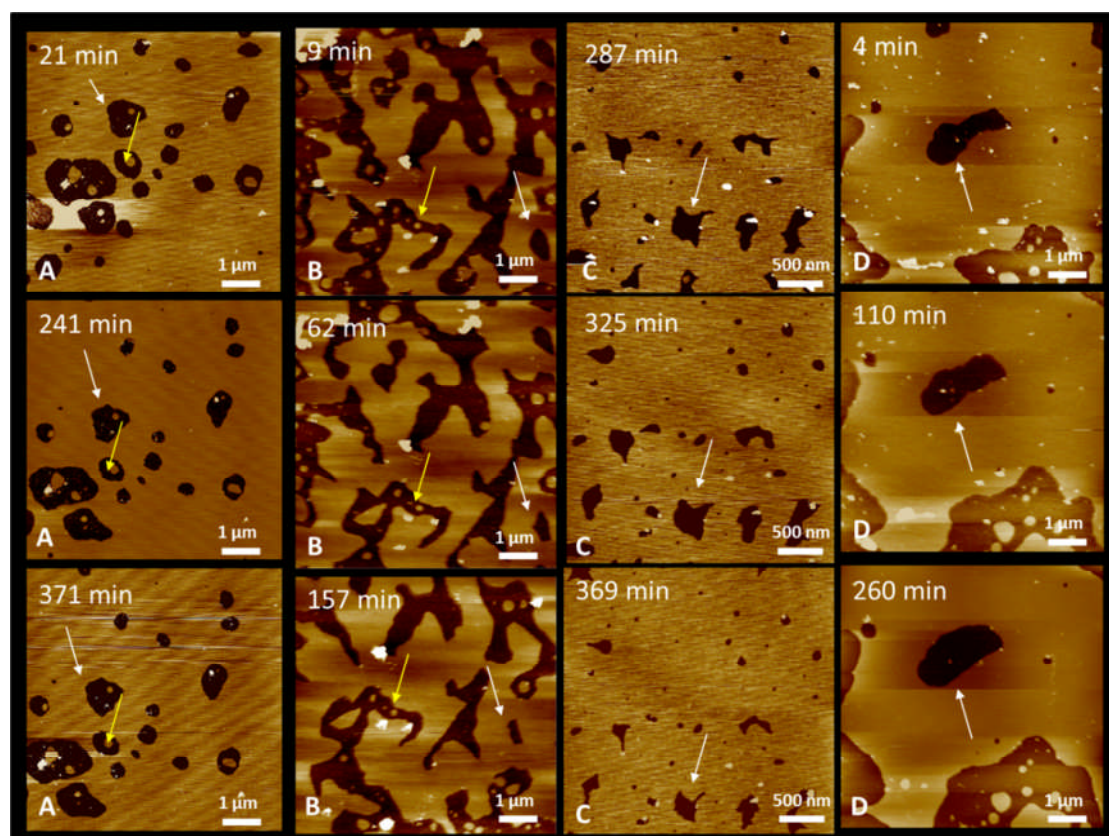


Figure 5.10. AFM images presenting the changes in the behaviour of the non-phase separated, model SLBs after exposure to: 5 (A), 10 (B), 50 (C) [$\mu\text{gDNA/ml}$] polyphosphonium polyplexes with 19-bp DNA and 90 $\mu\text{g/ml}$ phosphonium polymer solutions (D). After exposure of SLBs to polyplexes both increase in SLB fluidity and association of the particles at the SLB pore edges can be observed over time (A-C). After introduction of the polymer solution to the AFM cell, a gradual dissolution of the model SLB is observed over time. White arrows indicate changes to the SLB pore size over time, whilst the yellow arrows show association of the particles with the bilayer edges. Z-scale bars have been removed for clarity purposes (average range 0-10 nm).

The interaction of PPP with the model SLB resulted in a gradual dissolution of the bilayer manifested as an increase in the SLB-free surface area. However, the interaction of PPP polyplexes resulted in a gradual increase of the bilayer fluidity, which is demonstrated as pore closure. Additionally, the appearance of additional particles at the bilayer edges was observed. The graphs presenting the changes of SLB coverage throughout the imaging of polyplex-SLB interactions are presented in figure 5.11.

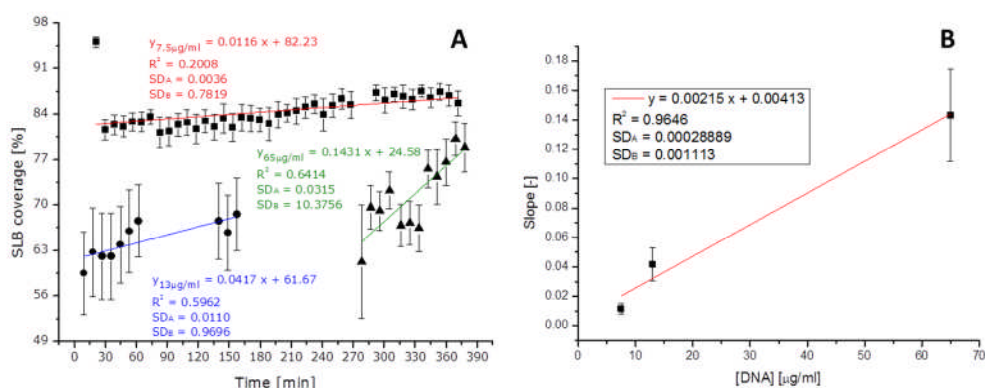


Figure 5.11. The graphs illustrating the quantitative relationship: DNA concentration vs. the increases of SLB coverage over time for the model SLB-polyphosphonium DNA polyplex interactions. (A) indicates the increase of SLB coverage over time after exposure of the model SLB to 5 (red), 10 (blue), 50 (green) [µg/ml] DNA concentrations with the linear correlation parameters from SLB coverage vs. time evaluations (compare figures: 5.2 and 5.4). (B) illustrates the relationship between the slopes from (A) and DNA concentrations with linear correlation parameters.

The AFM observations suggest that the free polymer molecules are attracted to the bilayer edges, most likely due to the edge effects (see chapter 4)¹⁰. Alternatively, adsorption triggered by electrostatic polymer-mica and polymer-lipid head group interactions may also play a role. Regardless of the forces involved in triggering the attraction of the polymer to the bilayer, PPP associates subsequently with the edge lipids initiating their gradual desorption from the surface. It is thought that the PPP-lipid interaction is based mainly on electrostatic interaction, as the SLB dissolution is not directly observed during the SLB-polyplex interaction, when the dynamic movements of the positively charged phosphonium groups are limited through DNA binding and are not freely available to edge lipids. If this assumption is correct, it also implies that the brush-like design of the polymer component seems to be a good fit for DNA grooves. The most likely lipids interacting with the polymer are DOPS, DOPE, EPC and SPM due to the presence of negative charges within the lipid head groups.

Once PPP is bound in a DNA complex and exposed to model SLBs, the bilayer fluidity increases triggering the gradual SLB pore closure. When linear fit equations for both pure DNA ($y = 2.53 \cdot 10^{-4} + 9.4 \cdot 10^{-3}$) and PPP-DNA polyplex ($y = 2.15 \cdot 10^{-3}x + 4.13 \cdot 10^{-3}$) were compared, two observations can be made. The intercept values for both equations are within the same range indicating the similarities in kinetic behaviour for both interactions. This is likely, since the amount of polymer used was not sufficient to bind all DNA molecules;

hence the binding of SPM by free DNA molecules is the dominant component influencing the kinetics of this interaction. On the other hand, the significant increase (8.5-fold) in the slope value for the SLBs exposed to the polyplexes over the DNA-exposed SLBs could be noticed. This means that the complexation of DNA with the PPP at 1:1 ratio results in the increase of the SLB coverage changes per unit of time by 8.5 times (or 8.5 times faster SLB spreading) than the increase in SLB coverage changes observed for uncomplexed DNA samples. For this reason, the author proposes that both the presence of free DNA that increases the bilayer fluidity through SPM/CHOL aggregate binding and PPP-triggered dissolution of the membrane are likely to be responsible for the overall increase of the bilayer fluidity after exposure to the polyplex solutions. This also suggest that the complexation of the DNA molecule with PPP at 1:1 charge ratio does not provide effective protection from or competition against binding SPM/CHOL aggregates, as the polymer-unbound DNA molecules in the sample are involved in the increase of SLB fluidity. Such mechanism is likely to affect the delivery of 1:1 polyplex *in vivo*.

Taking all of the above into account, it is likely that *in vitro* mechanisms for PPP polyplex delivery into the cytosol should be as follows. Firstly, particles once in contact with the cell trigger the invagination of the cytoplasmic membrane forming an endosome. This process may be facilitated by the local increase in membrane fluidity due to nucleic acid-related gradual loss of SPM/CHOL aggregates. Subsequently, due to a dramatic increase in membrane curvature when in an endosome, as well as the competition between polymer and membrane lipids over the binding with DNA, phosphonium groups of the polymer interact with the negatively-charged head groups of the membrane lipids causing changes to the membrane integrity and eventually its breakage. Here, it is also likely that such phenomena as the proton sponge effect and the complex changes in the endosomal environment exert an influence, explaining the partial release of free nucleic acid for further processing in the cytosol. The illustration of this possible mechanism is presented in figure 5.12.

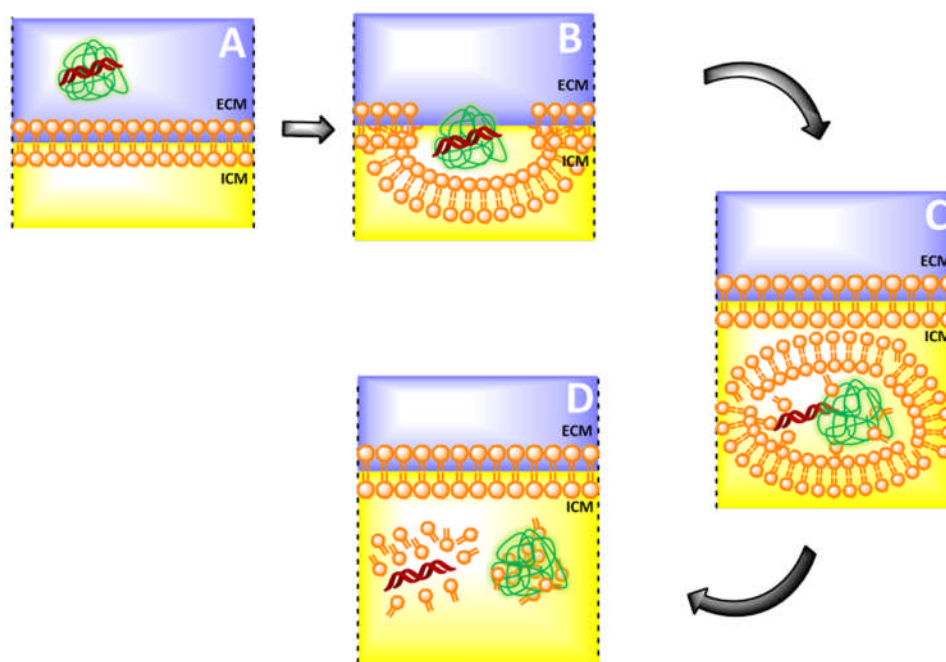


Figure 5.12. The illustration of the anticipated cell transfection mechanism for polyphosphonium-DNA polyplexes. Once the polyplex is introduced to the cell environment (A), the particles trigger invagination of the membrane through direct association with the membrane lipids (B). In an endosome both polymer and DNA bind lipids affecting endosomal membrane integrity (C). It is also possible that alternative phenomena (e.g. proton sponge effect) contribute towards endosomal escape mechanism (not shown). Once released from the endosomes, polyplexes undergo further changes in the cytosol (D). Extra- and intercellular matrices (ECM and ICM, respectively) are presented in blue and yellow, whilst DNA strands, phosphonium polymers and membrane lipids in red, green and orange, respectively.

5.5 Conclusion

In this chapter the assessment of the SLB as a model for studying the membrane-biopharmaceutical formulation interactions has been presented. Based on both the qualitative and quantitative analyses of such interactions, some potential mechanisms underlying cellular uptake and toxicity have elucidated, indicating a possible role for SLB models in pharmaceutical formulation development. In addition, this chapter outlines an innovative approach towards qualitative and quantitative assessment of such interactions, which could be used for the analysis of interactions with formulations of different chemistries.

In terms of drug development, three general conclusions may be drawn. Firstly, the findings and hypotheses outlined above specify the role of excipients in the nucleic acid formulation

as agents providing protection from nucleic acid-lipid interaction. The current role of the biopharmaceutical excipients is viewed as agents improving both tissue targeting and cellular uptake of *e.g.* siRNA. As outlined in the text above, this will not be achieved without a careful consideration of direct interaction with membrane lipids. Secondly, the spontaneous formation of particles between SPM/CHOL aggregates and nucleic acid molecules, whilst in contact with a physiological membrane, significantly impacts the current understanding of the *in vivo* behaviour of nucleic acid molecules, in cases where nucleic acids are liberated from their delivery systems in proximity to phospholipid membranes. As indicated above, these findings not only support the research behind mechanisms involved in siRNA targeted delivery and toxicity events, but also set new directions for siRNA research focus. It is hoped that these findings will soon be verified by other research groups and trigger significant improvements towards developments of effective and safe siRNA therapeutics. Thirdly, this research confirms that there is a need in drug discovery and development for testing the molecular interactions of drug candidates with biologically relevant membrane environments.

The data presented in this chapter significantly expands the current understanding of membrane behaviour in response to pharmaceutical agents. On the one hand, a possible role of SPM (or ceramides) as lipids involved in defence mechanisms within a biological organism was indicated. Since SPM lipids may trigger apoptosis and therefore result in immunogenic reactions, links between SPM and immune system are implied. This not only would correlate with the roles that ceramides play in apoptosis, signal transduction and lipid membranes, but also may explain the significant amounts of such lipids in the nervous system, as the most physiologically important one in the human body.

To conclude, further research in this area is necessary and urgent. The need for a commercial test enabling studies of such interactions in a high throughput format is obvious, which is the objective of the following chapter.

5.6 References

1. Gallas, A.; Alexander, C.; Davies, M. C.; Puri, S.; Allen, S., Chemistry and formulations for siRNA therapeutics. *Chemical Society reviews* **2013**.
2. (a) Peetla, C.; Stine, A.; Labhasetwar, V., Biophysical interactions with model lipid membranes: applications in drug discovery and drug delivery. *Molecular pharmaceutics* **2009**, *6* (5), 1264-76; (b) Lucio, M.; Lima, J. L.; Reis, S., Drug-membrane interactions: significance for medicinal chemistry. *Current medicinal chemistry* **2010**, *17* (17), 1795-809; (c) Pignatello, R.; Musumeci, T.; Basile, L.; Carbone, C.; Puglisi, G., Biomembrane models and drug-biomembrane interaction studies: Involvement in drug design and development. *Journal of pharmacy & bioallied sciences* **2011**, *3* (1), 4-14.
3. Soliman, M.; Nasanit, R.; Allen, S.; Davies, M. C.; Briggs, S. S.; Seymour, L. W.; Preece, J. A.; Alexander, C., Interaction of reducible polypeptide gene delivery vectors with supported lipid bilayers: pore formation and structure-function relationships. *Soft Matter* **2010**, *6* (11), 2517-2524.
4. Ornelas-Megiatto, C.; Wich, P. R.; Frechet, J. M., Polyphosphonium polymers for siRNA delivery: an efficient and nontoxic alternative to polyammonium carriers. *J Am Chem Soc* **2012**, *134* (4), 1902-5.
5. Rachlin, A. L.; Henderson, G. S.; Goh, M. C., An Atomic Force Microscope (Afm) Study of the Calcite Cleavage Plane - Image Averaging in Fourier Space. *Am Mineral* **1992**, *77* (9-10), 904-910.

6. Rana, T. M., Illuminating the silence: understanding the structure and function of small RNAs. *Nature reviews. Molecular cell biology* **2007**, *8* (1), 23-36.
7. Corsi, J.; Hawtin, R. W.; Ces, O.; Attard, G. S.; Khalid, S., DNA lipoplexes: formation of the inverse hexagonal phase observed by coarse-grained molecular dynamics simulation. *Langmuir* **2010**, *26* (14), 12119-25.
8. Schroen, C. G. P. H.; Stuart, M. A. C.; Vanderpadt, A.; Vanriet, K., Wettability of Tri-Block Copolymer Coated Hydrophobic Surfaces Predictions and Measurements. *Colloid Surface A* **1994**, *90* (2-3), 235-249.
9. Ohvo-Rekila, H.; Ramstedt, B.; Leppimaki, P.; Slotte, J. P., Cholesterol interactions with phospholipids in membranes. *Prog Lipid Res* **2002**, *41* (1), 66-97.
10. Tryfona, T.; Bustard, M. T., Enhancement of biomolecule transport by electroporation: a review of theory and practical application to transformation of *Corynebacterium glutamicum*. *Biotechnology and bioengineering* **2006**, *93* (3), 413-23.
11. Lu, J. J.; Langer, R.; Chen, J. Z., A Novel Mechanism Is Involved in Cationic Lipid-Mediated Functional siRNA Delivery. *Molecular pharmaceutics* **2009**, *6* (3), 763-771.
12. Aouadi, M.; Tesz, G. J.; Nicoloso, S. M.; Wang, M. X.; Chouinard, M.; Soto, E.; Ostroff, G. R.; Czech, M. P., Orally delivered siRNA targeting macrophage Map4k4 suppresses systemic inflammation. *Nature* **2009**, *458* (7242), 1180-U116.
13. Green, D. R., Apoptosis and sphingomyelin hydrolysis. The flip side. *The Journal of cell biology* **2000**, *150* (1), F5-7.
14. Soutschek, J.; Akinc, A.; Bramlage, B.; Charisse, K.; Constien, R.; Donoghue, M.; Elbashir, S.; Geick, A.; Hadwiger, P.; Harborth, J.; John, M.; Kesavan, V.; Lavine, G.; Pandey, R. K.; Racie, T.; Rajeev, K. G.; Rohl, I.; Toudjarska, I.; Wang, G.; Wuschko, S.; Bumcrot, D.; Koteliansky, V.; Limmer, S.; Manoharan, M.; Vornlocher, H. P., Therapeutic silencing of an endogenous gene by systemic administration of modified siRNAs. *Nature* **2004**, *432* (7014), 173-178.
15. (a) Chen, X. Y.; Sun, A. J.; Zou, Y. Z.; Ge, J. B.; Lazar, J. M.; Jiang, X. C., Impact of sphingomyelin levels on coronary heart disease and left ventricular systolic function in humans. *Nutr Metab* **2011**, *8*; (b) Thurberg, B. L.; Wasserstein, M. P.; Schiano, T.; O'Brien, F.; Richards, S.; Cox, G. F.; McGovern, M. M., Liver and Skin Histopathology in Adults With Acid Sphingomyelinase Deficiency (Niemann-Pick Disease Type B). *Am J Surg Pathol* **2012**, *36* (8), 1234-1246; (c) Blachnio-Zabielska, A. U.; Koutsari, C.; Tchkonja, T.; Jensen, M. D., Sphingolipid Content of Human Adipose Tissue: Relationship to Adiponectin and Insulin Resistance. *Obesity* **2012**, *20* (12), 2341-2347.
16. Santel, A.; Aleku, M.; Keil, O.; Endruschat, J.; Esche, V.; Fisch, G.; Dames, S.; Loffler, K.; Fechtner, M.; Arnold, W.; Giese, K.; Klippel, A.; Kaufmann, J., A novel siRNA-lipoplex technology for RNA interference in the mouse vascular endothelium. *Gene Ther* **2006**, *13* (16), 1222-1234.
17. Chakraborty, M.; Jiang, X. C., Sphingomyelin and its role in cellular signaling. *Advances in experimental medicine and biology* **2013**, *991*, 1-14.
18. Semple, S. C.; Akinc, A.; Chen, J.; Sandhu, A. P.; Mui, B. L.; Cho, C. K.; Sah, D. W.; Stebbing, D.; Crosley, E. J.; Yaworski, E.; Hafez, I. M.; Dorkin, J. R.; Qin, J.; Lam, K.; Rajeev, K. G.; Wong, K. F.; Jeffs, L. B.; Nechev, L.; Eisenhardt, M. L.; Jayaraman, M.; Kazem, M.; Maier, M. A.; Srinivasulu, M.; Weinstein, M. J.; Chen, Q.; Alvarez, R.; Barros, S. A.; De, S.; Klimuk, S. K.; Borland, T.; Kosovrasti, V.; Cantley, W. L.; Tam, Y. K.; Manoharan, M.; Ciufolini, M. A.; Tracy, M. A.; de Fougereolles, A.; MacLachlan, I.; Cullis, P. R.; Madden, T. D.; Hope, M. J., Rational design of cationic lipids for siRNA delivery. *Nature biotechnology* **2010**, *28* (2), 172-6.
19. (a) Ogris, M.; Brunner, S.; Schuller, S.; Kircheis, R.; Wagner, E., PEGylated DNA/transferrin-PEI complexes: reduced interaction with blood components, extended circulation in blood and potential for systemic gene delivery. *Gene Ther* **1999**, *6* (4), 595-605; (b) Jiang, G.; Min, S. H.; Oh, E. J.; Hahn, S. K., DNA/PEI/Alginate polyplex as an efficient in vivo gene delivery system. *Biotechnol Bioproc E* **2007**, *12* (6), 684-689.
20. (a) Whitehead, K. A.; Langer, R.; Anderson, D. G., Knocking down barriers: advances in siRNA delivery (vol 8, pg 129, 2009). *Nature Reviews Drug Discovery* **2010**, *9* (5), 412-412; (b) Perkel, J. M., RNAi THERAPEUTICS: A TWO-YEAR UPDATE. *Science* **2009**, *326* (5951), 454-456; (c) Czech, M. P.; Aouadi, M.; Tesz, G. J., RNAi-based therapeutic strategies for metabolic disease. *Nat Rev Endocrinol* **2011**, *7* (8), 473-484.
21. (a) Hong, S. P.; Leroueil, P. R.; Janus, E. K.; Peters, J. L.; Kober, M. M.; Islam, M. T.; Orr, B. G.; Baker, J. R.; Holl, M. M. B., Interaction of polycationic polymers with supported lipid bilayers and cells: Nanoscale hole formation and enhanced membrane permeability. *Bioconjugate Chem* **2006**, *17* (3), 728-734; (b) Mecke, A.; Majoros, I. J.; Patri, A. K.; Baker, J. R.; Holl, M. M. B.; Orr, B. G., Lipid bilayer disruption by polycationic polymers: The roles of size and chemical functional group. *Langmuir* **2005**, *21* (23), 10348-10354; (c) Mecke, A.; Lee, D. K.; Ramamoorthy, A.; Orr, B. G.; Holl, M. M. B., Synthetic and natural polycationic polymer nanoparticles interact selectively with fluid-phase domains of DMPC lipid bilayers. *Langmuir* **2005**, *21* (19), 8588-8590.

Development of supported lipid bilayer microarray for high throughput screening applications at nanoscale.

6.1 Abstract

As identified earlier, studying supported lipid bilayers (SLBs) both in a high throughput manner and to the nanometre scale may be a useful strategy for the assessment of formulation-membrane interaction performances. Therefore, a hypothesis that the combination of atomic force microscopy (AFM), time-of-flight secondary ion mass spectrometry (ToF-SIMS) and inkjet print head technology may offer an advantage towards SLB microarray development was investigated in this chapter. This led to the development of an SLB microarray prototype which is reported therein. The microarray design, experimental methodology, as well as the author's considerations are thoroughly described in order to both assure repeatability and reproducibility of the data and also to facilitate further development of this approach. Additionally, a research focus for the future directions of this research is proposed.

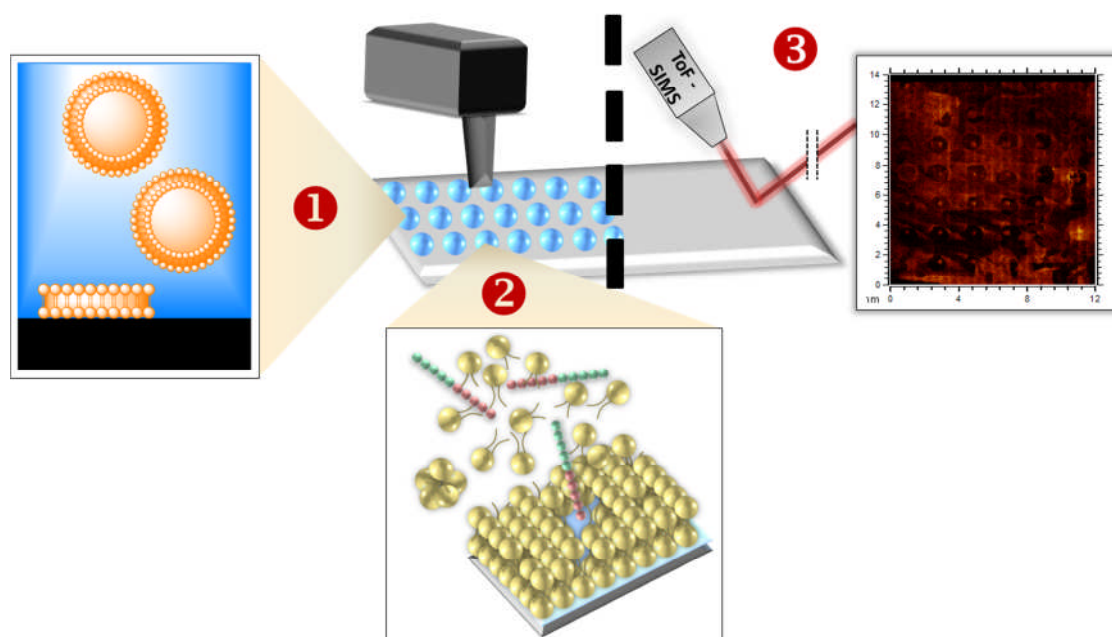


Figure 6.1 Graphical abstract indicating the supported lipid bilayer (SLB) microarray approach that was investigated. (1) Initially, liposome solutions are dispensed on a microscope slide-sized mica surface in a fully automated manner. Liposomes form an SLB layer through vesicle deposition. (2) Subsequently, SLB surfaces are dried, incubated in high humidity environments and exposed to a number of liquid spots, each containing the chemical species of interest. (3) Finally, the SLB-formulation interaction behaviours are visualised using the ToF-SIMS chemical imaging technique.

Abbreviations:

AFM – atomic force microscopy; BSST – bilayer self-spreading technique; CHOL – cholesterol; nano-HTS – nanometre-scale, high throughput screening; PBS – phosphate buffer saline; PEG – polyethylene glycol; RH – relative humidity; RT – room temperature; SLB – supported lipid bilayer; tBLMs – tethered bilayer lipid membranes; ToF-SIMS – time-of-flight secondary ion mass spectrometry; UHV – ultrahigh vacuum; VDT – vesicle deposition technique.

6.2 Introduction

Although the successful development of supported lipid bilayer (SLB) microarray approaches has been reported independently by a number of research groups¹, a commercial SLB test for studying the *in vitro* drug-membrane interactions is still lacking. Advanced surface analysis techniques, such as atomic force microscopy (AFM) and time-of-flight secondary ion mass spectrometry (ToF-SIMS), have been demonstrated as useful methods for the nanometre-scale-characterised development of high throughput screening (nano-HTS) approaches within the pharmaceutical sciences². Additionally, inkjet print head technologies, as fully automated liquid dispensing systems, provide high precision and accuracy for the liquid handling-associated microarray applications^{2b, 3}.

Within this chapter, the development of an SLB microarray prototype was attempted, based on the AFM, ToF-SIMS and inkjet printing investigations. A thorough description of the developed methodology from a practical, laboratory-based perspective is presented in order to provide assurances of both the repeatability and reproducibility of this method. The directions for further strategies towards the development of such SLB microarray approach are also discussed.

The development of an SLB microarray may ultimately lead to an SLB-based, commercially-applicable screening approach for *in vitro* studies of the interactions between membranes and pharmaceutical formulations in a high throughput manner. Such an approach could help address the issue within the pharmaceutical sciences which is associated with the lack of a predictive *in vitro* methodology for the *in vivo* behaviour of medicines, and therefore, innovate the drug discovery and development process. The discussion provided in this chapter highlights also that through careful consideration of the experimental environments SLB-related research can further contribute towards a general understanding of lipid bilayer behaviour from a material scientist's perspective.

6.3 Materials and Methods – see chapter 2.

6.4 Results and Discussion

It was anticipated that the combined application of the inkjet print head technology, AFM and ToF-SIMS chemical imaging would provide a useful strategy towards the development of an SLB microarray. On the one hand, both the accuracy and precision associated with automated dispensing systems, such as inkjet printers, would assure repeatability and reproducibility for the liquid environment-based interaction studies between an SLB-coated surface and the chemical species of interest. On the other hand, the high sensitivity of the ToF-SIMS chemical imaging would enable studies of chemical behaviours at a molecular level⁴. Since the SLB research is associated with both liquid handling and surface-based measurements, the development of an SLB microarray involving the methodologies above would enable coating the solid support surface with an SLB layer in a fully automated manner⁵. Also, such an approach would provide experimental strategy for SLB interaction studies both in high throughput and at a nanometre scale.

However, in order to build such a system, several SLB-associated issues from a technological perspective have first to be addressed. Firstly, the fabrication of an SLB on a microscope slide-sized surface has to be optimised. Secondly, since the inkjet printing technology requires clean and dry surfaces and the SLBs are not stable once exposed to air, it was thought that automated liquid dispensing in high humidity environments using dried SLB-coated mica sheets may provide a window of opportunity in terms of SLB microarray development. Therefore, the behaviour of dry SLBs needed to be studied at a nanometre scale (*e.g.* with AFM). Thirdly, both the inkjet printing and ToF-SIMS chemical imaging techniques needed to be optimised in order to provide data to illustrate the repeatability and reproducibility of the approach. Below, optimisation of such SLB microarray is discussed from a laboratory-based perspective.

6.4.1 Optimisation of SLB fabrication method on microscope slide-sized mica sheets.

Since ToF-SIMS was selected as the SLB imaging technique, an SLB fabrication approach that resulted in an even distribution of the lipid film across the entire surface of the slide was preferred over the SLB spot-type approaches reported previously⁶. It was anticipated that such approach would provide a control sample for the SLB-unaffected areas in between the spots of liquid (containing various chemical species) on the microarray surface, once inkjet printed on the slide and imaged with ToF-SIMS (see figure 6.7).

For this reason, initial experiments with microscope slide surfaces and Millipore water enabled us to establish that a total volume of 1.5-3 ml pipetted along the centre axis of the surface and heated up to 35°C under the saturated vapour conditions provided both the optimal coverage of the surface with liquid, and minimal loss of liquid throughout the heating process. Since mica surfaces are considered more hydrophilic and flat⁷ than glass surfaces, a 1.5 ml total liquid volume was applied for the vesicle deposition (VDT)⁸ and bilayer self-spreading (BSST)⁹ techniques optimised previously using smaller mica surfaces (chapter 3). A temperature of up to 40°C was preferred, as the sample stage of the inkjet printer system used in the laboratory has a limited temperature maximum of 50°C. This was an important factor, which was previously considered during the optimisation of SLB fabrication protocol on 14-mm mica discs (chapter 3), in case future manufacturing protocols involves the inkjet print head technology.

Initially, mica sheets were glued to 4 metal disc specimens in order to provide heat conductance between a hotplate and the mica surface during the SLB formation. However, AFM observed distributions of the lipid films indicated that such approach did not provide a uniform bilayer distribution for both BSST and VDT, as presented in figure 6.2. For this reason, mica sheets were glued to glass microscope slides to provide continuous solid supports for the optimisation of the VDT protocol. The BSST was not studied further, as it was anticipated that the lack of lipid self-spreading was likely to occur for glass slide-supported mica sheets, based on the previous AFM observations. Eventually, the incubation of 1.5ml 0.5 mg/ml liposome suspension at 35°C for 1 hour was established to provide uniform model SLBs of porous lipid film qualities, as presented in figure 6.2. It is worth adding that the need to glue mica surfaces to the solid support arose, as the alternative approaches (*e.g.* non-supported mica or attachment of mica to solid supports through double-sided tape or sticky carbon discs) resulted both in leakages of the liquid throughout the liposome incubation process at an elevated temperature and in the movements of the surface during AFM studies.

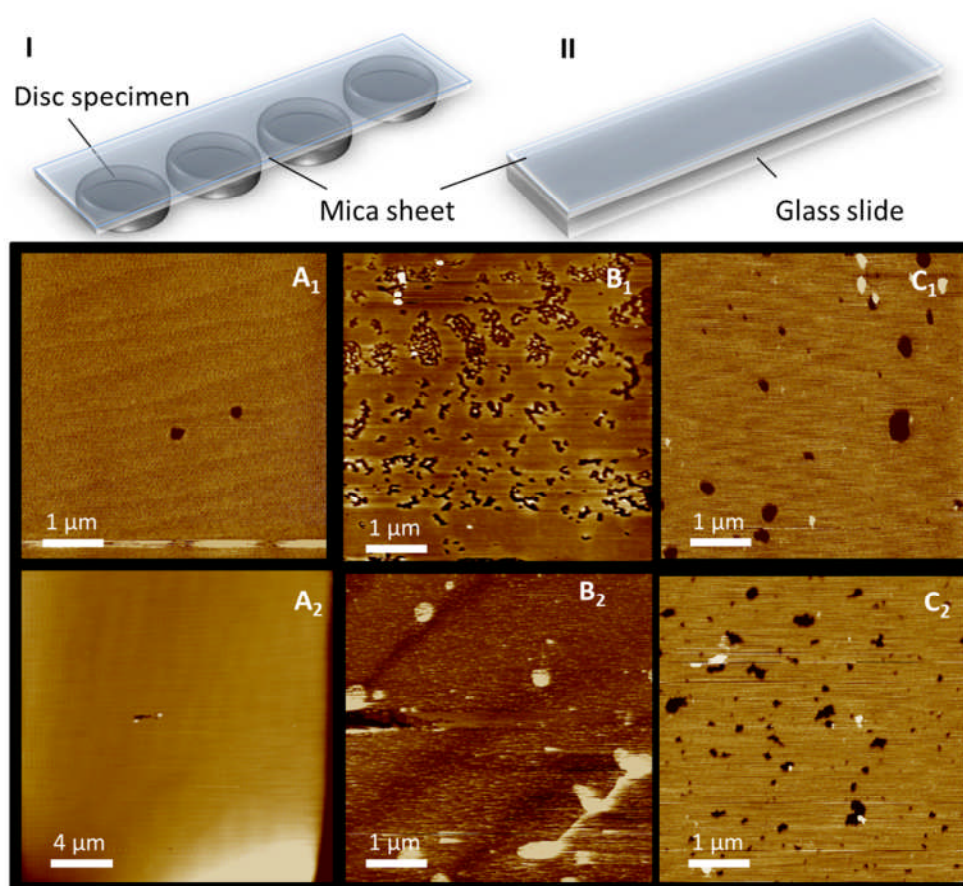


Figure 6.2. The graphics (I, II) and AFM images (A-C) presenting the engineering approaches for the optimisation of mica sheet preparation before the exposure to lipid material, and lipid film morphologies recorded for both approaches, respectively. Approach I was identified as not suitable, while approach II as suitable for SLB microarray development. Cartoon I corresponds to A and B, while cartoon II to C. When the model SLBs were fabricated using the bilayer self-spreading (A) or the vesicle deposition (B) protocols on a mica sheet that was glued to metal disc specimens underneath (I), the AFM-reported spatial distribution of the bilayers across the surface of the mica sheet was not uniform. A_{1-2} and B_{1-2} were collected from single samples prepared using the bilayer self-spreading and vesicle deposition techniques, respectively. Here, images 1 and 2 correspond to the areas of mica directly above and in between the disc specimens that are glued underneath, respectively. A_1 and B_1 indicate the presence of SLB morphologies that look similar to the ones manufactured using 14 mm mica discs (compare fig 3.2.A₁ and B₃). A_2 indicates the presence of a lipid bulk deposited on the mica surface that has not been removed throughout the bilayer self-spreading process. B_2 indicates the presence of lipid deposits of an unfamiliar morphology. C_{1-2} indicate SLB morphologies from two separate areas of the mica sheet glued to the microscope slide (II) after adapting the vesicle deposition protocol. Again, SLB morphologies presented in C are similar to the ones manufactured on 14 mm mica discs. All samples were imaged in liquid environments. The adapted protocols have been described in chapter 2. Dark features on A_{1-2} were generated with an AFM probe through scratch test (see appendix II) in order to confirm the presence of a lipid film on the surface. Z-scale bars were removed for presentation purposes (average range 0-10 nm).

6.4.2 AFM studies of dry, model SLBs in high humidity environments.

It was hypothesised that the incubation of SLBs in high humidity environments may extend their stability in air¹⁰. For that reason, AFM studies were performed on the model SLBs exposed to air at 3 different relative humidity (RH) values: ~25%, ~50% and ~70%, corresponding respectively to the RH values once dried at the room temperature, the maximum humidity that enabled AFM imaging without changing the sample temperature and the humidity maximum determined *via* EnviroScope AFM system in the laboratory. The RH values were established empirically, as discussed below. The AFM studies were performed using the model SLBs deposited on 14 mm-diameter mica discs. Although the air stability of SLBs was demonstrated in the literature to depend on the overall SLB diameter¹¹, it was assumed that the behaviour of the model SLB composition would be similar if deposited on either 14 mm mica discs or 25 mm x 75 mm mica sheets. It is also worth mentioning that PBS was replaced with Millipore water as a liquid environment throughout the AFM imaging, in order to avoid salt crystallisation-associated difficulties.

The AFM studies on the dried model SLBs at room temperature and humidity indicated that the first signs of phase separation were observed after 30-40 minutes imaging of the dry SLB surface (figure 6.3.A). Prior to imaging liquid excess was removed through wicking into tissue paper leaving small amounts of the liquid remaining on the surface, which enabled AFM studies of the SLB destabilisation process. The removal of the remaining liquid through the exposure of such SLBs to either heat, prolonged incubation in a desiccator or the stream of argon was not attempted, as it was anticipated that bilayer destruction would occur before AFM imaging, due to either the natural destabilisation process or the detrimental influence of the factor(s) introduced. The short evaporation time (~15min) of the liquid in air directly before the AFM tip was introduced to the surface area of interest was therefore utilised. Should the AFM tip be approached to a wet surface prior to this, the laser alignment in the AFM system was lost disabling AFM imaging in air¹². For this reason, the AFM studies were performed on sample areas that could be imaged after the first successful attempt to approach the SLB surface, with an AFM tip that was suitable for imaging in air (*e.g.* RTESPA). Therefore, since the AFM-studied SLB surface was not dry in all areas of the sample, it was likely that the AFM-observed 30-40 min stability of the SLBs after removal of the liquid excess was strongly affected by the presence of the remaining liquid. In reality it is likely that the destabilisation of SLB structure occurs more quickly.

Incubations at ~50% and ~70% RH suggested that high humidity environments decreased the speed of the destabilisation process for the model SLBs. AFM imaging in the ~50% RH environment allowed observation and recording of the SLB destabilisation process for liquid excess-free model SLBs (figure 6.3.B). The first signs of phase separation were noticed after 20- and 60-minutes AFM imaging in the high humidity chamber, which was followed by a delamination process after 60- and 100-minute exposure to the ~50% and ~70% RH environments, respectively. These indicated that the incomplete removal of water at ~25% RH affected the air stability of the model SLBs and the reported (30-40)-minute time period was not reflective of the true situation. The technique of water removal and AFM imaging for the samples studied in the high humidity was similar to the one above. Hence, any evaporation of remaining liquid before the AFM tip was introduced to the surface took place over a longer period (30-50 min) at the ~50% RH. For the ~70% environment (figure 6.3.C), the effective evaporation time (20-40 min) was determined by the sample stage temperature. Since the water vapour in high humidity environments had reached the dew point and started collecting on the surface at a room temperature, the sample stage temperature had to be elevated up to (28-30°C) (see figure 6.4.). Here, a temperature of up to 30°C would have been preferred in order to avoid the temperature-triggered phase separation of the model SLBs that could interfere with the air stability-related observations (figure 3.11.). The removal of condensed vapour was assessed visually using the optical microscope associated with AFM, and the tip was introduced to the liquid excess-free surface as soon as the liquid layer had disappeared from the area of interest. Since the approach of the AFM probe to the surface at that point failed during the initial attempts, most likely due to the small amounts of remaining water, the evaporation times that are reported for ~70% AFM environment, are the times between the visually-assessed, temperature-triggered removal of water excess and the time point, at which the first AFM image was set to record. It is worth adding that the evaporation times for these experiments were reported as time periods, since the variability for such studies between the samples was high. Also, the presence of vapour and water, as well as the elevated temperature of the sample stage introduced technical difficulties that decreased the AFM imaging performance. It is the author's recommendation that the evaporation time values should be regarded as a guideline, rather than the exact time periods.

The RH values that are reported for the AFM environments are also associated with some error. The system used in the laboratory enabled not only the introduction of a vapour stream in order to achieve the required RH values, but also the detection of the RH value in

the experimental environment and the automatic reintroduction of the vapour stream once the RH value in the environment dropped. If the targeted RH value of interest went above the dew point of vapour, the water droplets collected on the RH detector and interfered with the RH readings. Once the overall humidity of the environment dropped and such water droplets evaporated, the humidity controller then recognised the decrease of the RH in the environment and automatically reintroduced the vapour stream. This process manifested as a sudden drop in RH values (*e.g.* from ~70% to ~40%) and automatic reintroduction of the vapour stream to the imaging environment. Since the reintroduction of the vapour stream was detrimental to the AFM imaging performance and the use of an independent humidity detector was not possible due to the small size of the AFM environmental chamber, the RH values were therefore controlled manually throughout the experiments (chapter 2). Effectively, the vapour stream needed to be switched off during AFM image acquisition and although the RH values were constant throughout the time of the experiment, they may have been affected by the collection of the vapour droplets on the detector. The reported RH values should therefore be considered as best estimates, with further optimisation of RH conditions in an inkjet printing chamber possibly needed.

To summarise, the initial hypothesis of extended SLB stability in air at a high RH was confirmed and as identified by AFM imaging the incubation of dried, model SLBs at ~70% RH over an hour was the optimal strategy for further SLB microarray development in this project.

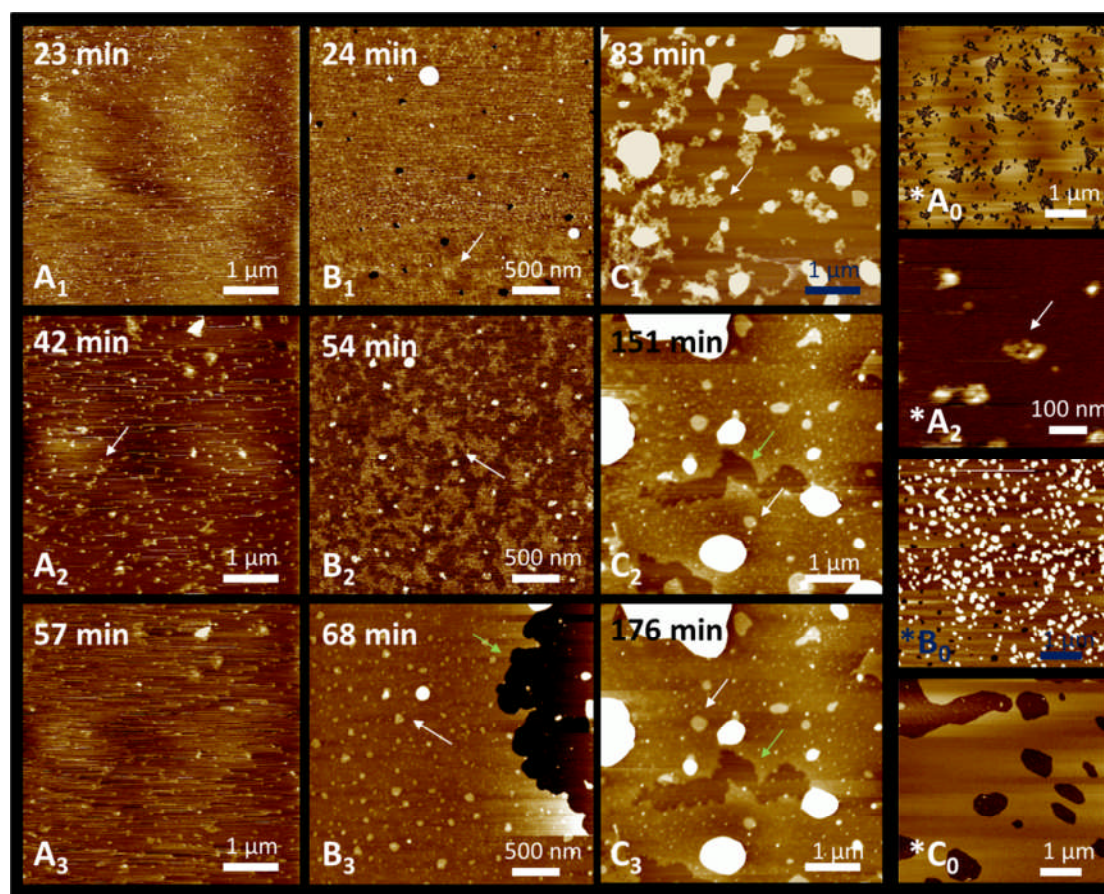


Figure 6.3. AFM images indicating the behaviour of model SLBs once the liquid excess had been removed from the surface at three different relative humidity (RH) values: $\sim 25\%$ (A), $\sim 50\%$ (B) and $\sim 70\%$ (C). 1-3 correspond to appropriate time points after the model SLB had been dried and the AFM tip for imaging in air had been introduced. 0 correspond to the model SLB morphologies of the appropriate sample (*A-*C) in the liquid environment, before the liquid excess has been removed. *A₂ presents a high-resolution image of the initial phase separation occurring after 45-minute incubation of the model SLBs in air at $\sim 25\%$ RH. White arrows indicate the phase separated areas within the SLBs, whilst the green arrows the delamination process. Before the sample in *B₀ was dried, an additional rinsing step with water was introduced in order to the remove lipid excess. Details on imaging techniques in the text. Z-scale bars were removed (average range 0-10 nm) and some labels in C and B₀ were coloured in blue for presentation purposes.

6.4.3 Optimisation of the piezoelectric inkjet printing methodology for SLB microarray development.

Optimisation of the inkjet printing methodology needed to involve two steps, if the fully automated SLB microarray system was considered. One was the extrapolation of the VDT protocol from the human-operated pipette systems in order to fabricate SLBs to robot-operated systems, while the second was the optimisation of the dispensing of the liquid spots on the SLBs for formulation-membrane interaction studies. Step one was however not attempted for the purpose of this work. Since additional problems associated with

dispensing higher viscosity liposomal solutions required for the VDT protocol, may have affected the inkjet printing performance, the experimental focus was directed at the step two. The additional advantage of such a focus was the possibility of observing the behaviour of spots on mica-type surfaces, which would be helpful for the optimisation of step one, if mica-deposited SLBs were the systems of interest for both inkjet printing and ToF-SIMS imaging in the future. Here, as step one was previously demonstrated to be achievable¹³, step two appeared as a greater challenge.

Due to author's previous experience with handling PEO-PPO-PEO tri-block co-polymer solutions (chapter 4), 0.001-0.0001 % (w/v) L-62, L-64 and F-68 Pluronic® solutions in Millipore water were initially selected for these studies. Again, PBS was replaced with Millipore water as a solvent in order to decrease the possibility of both salt crystallisation and potential interferences between the secondary ions on ToF-SIMS chemical images.

The initial experiments aimed to optimise the parameters for dispensing the polymer dilutions on mica sheets in high humidity environments. Low surfactant concentrations were selected in order to both avoid bubble formation and a low solution viscosity throughout the inkjet printing process. Based on the experience with AFM imaging of dry SLBs in high humidity environments, 70% RH and 28°C-30°C sample stage temperature were selected as optimal conditions preventing the collection of vapour on dry mica surfaces (figure 6.4).

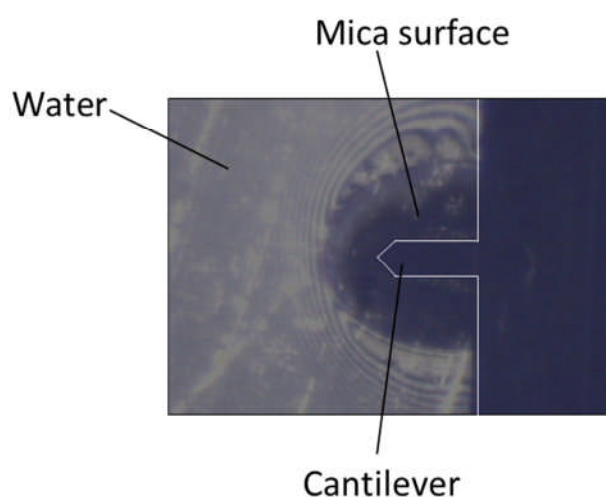


Figure 6.4. *The optical image of an AFM probe approaching the liquid-excess-free, SLB-coated mica surface incubated in a ~70% relative humidity environment at RT. Adsorption of water at the sample surface indicates the need for increasing the temperature of the sample surface above the theoretical dew point in order to enable the AFM imaging in air. The white line has been added to highlight the presence of the AFM probe (cantilever).*

Since the printing chamber was significantly larger than the high humidity chamber of the AFM system, RH values were monitored *via* two independent hygrosopes: one associated with the inkjet printer and another directly inserted into the printing chamber. Both the RH

and stage temperature were expected to provide not only a homogenous surface quality of the surface, but also a minimal possibility of the liquid spots merging, once deposited on the surface. Since achieving such an environment within the printing chamber took, on average, more than 40 minutes, it was also established that the best practice was to dry the SLB slide and insert it just directly before the printing process, and also after the humidity and stage temperature were adjusted and printing nozzles tested for patency with surfactant solutions and Millipore water. The then required readjustment of the RH and evaporation of liquid remaining on the SLB surface in the printer environment was found to be more time efficient than achieving the required parameters on a dry slide inserted into the printer chamber at RT and ~25% RH conditions. Such a strategy was applied in order to decrease the time of SLB exposure to air to the minimum; hence providing the SLB of the closest similarity to the one in liquid environments. It is also worth mentioning that thorough and gentle drying of the slide directly before inserting into the printing chamber was an important step. For that reason, not only the excess of the liquid on the slide before insertion was carefully poured onto a tissue paper, but also larger droplets of the remaining liquid, non-specifically adsorbed at the SLB surface, were gently wicked away with tissue paper, making sure that the tissue did not come in a direct contact with the surface. Assessment of the degree of surface 'dryness' before insertion into the chamber was performed visually, due to the time constraints associated with limited air stability of the SLBs. The techniques of insertion and drying of the slide were described for reproducibility purposes however, it is worth highlighting that they may not be necessary, if step one (the automated dispensing of liposome solutions on mica sheet) was optimised.

Since evaporation of the liquids dispensed *via* inkjet printing may significantly affect the interaction between SLBs and polymer surfactants, parameters such as the total volume of the solution deposited on the surface, as well as the distances between spots on the microscope slide-sized mica sheets needed to be optimised. The trial printing experiments using mica sheets glued to a microscope slide and 0.0001 % Pluronic® L-64 surfactant solution indicated that deposition of a 142nl total liquid volume resulted in spots (2.0 ± 0.1) mm in diameter that remained on the surface for at least 60 minutes (figure 6.5.). The spots of lower volumes evaporated within 60 minutes, while the spots of volumes higher than 1.42 μ l had the tendency to merge on the surface (data not recorded). It was also noted that some liquid spots 'travelled' on the mica surface after deposition, increasing the possibility of spot merging. Hence, the optimal total volume of liquid for experiments with SLBs was established within the 142 nl – 284 nl range. The droplet traveling was most likely associated

with the physicochemical properties of mica that have affected the behaviour of liquids on the surface. The fact that water-based solutions have had the tendency to move across the mica surface due to its high hydrophilicity (and possibly negative charge and flatness) was a general observation, based on the experience with handling mica as a solid support. Each drop for this experiment was printed at 3.5 mm apart fitting 6 spots in a row parallel to the shorter edge of the mica sheet. Lack of spot merging indicated that the distances between spot centres could be further still decreased, even up to 2 mm apart, as presented in figure 6.5.

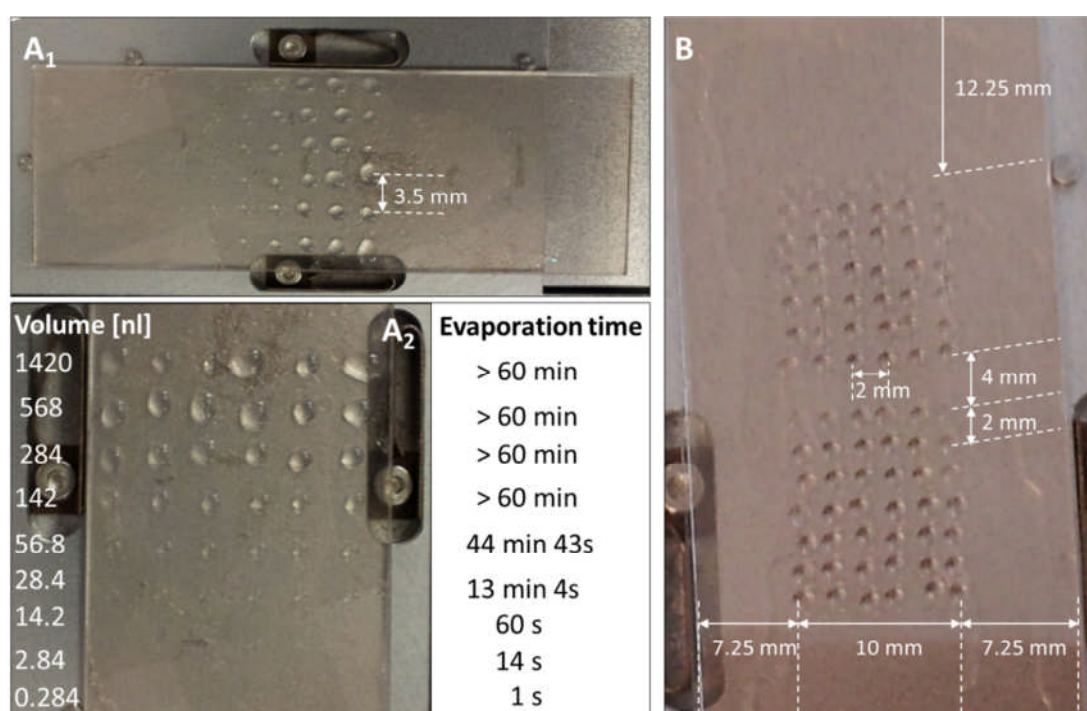


Figure 6.5. Optical images presenting inkjet printed spots on mica sheets surfaces incubated at 70% relative humidity and 28°C the sample stage temperature. Different volumes of 0.0001 % (w/v) Pluronic® L-64 solution in Millipore water were printed on the slide in image A, while 198 nl/spot of 0.001-0.0001 % Pluronic® L-62, L-64 and F-68 solutions were printed on the slide in image B. Distances between the spots are indicated in image A₁ and B. A₂ indicates volumes of the liquid printed on the slide in A₁ and associated times, at which the solvent was observed to disappear. The images were taken after 15-minute incubation in ~70% relative humidity, once the printing process was completed.

As a consequence of lowering the distances between spots, the distances between the spots and slide edges increased. Due to technical difficulties with the AFM imaging at the edges of the SLB microarray, as well as handling the slide with tweezers at all times, the presence of a representative SLB coverage around the slide edges was not clear. For the same reason, printing of all spots as close as possible to the centre of the slide was preferred. It is also

worth mentioning that the surface-nozzle distance was increased, when compared with values used for other applications ($Z = 700 \mu\text{m}$; standard values have been around $\sim 400 \mu\text{m}$), because the deposition of relatively large volumes of liquid was observed to interfere with the printing process.

6.4.4 Optimisation of the ToF-SIMS chemical imaging of SLB microarrays.

Throughout the ToF-SIMS imaging experiments three core technical issues were identified as critical factors affecting the data collection process.

Firstly, since surface topography may affect ToF-SIMS imaging, provision of flat and non-tilted supports was required. As indicated in figure 6.6., some potential data was lost when the images were collected from a 14 mm x 8 mm surface with a tilted solid support. For this reason, the processes of both gluing mica to the microscope slide and cleaving it before exposure to liquid solutions throughout the SLB preparation was optimised. In order to achieve the even distribution of glue layer underneath the mica, the glue was dispensed drop-wise along the centre axis of the glass slide, parallel to the longer edge. Subsequently, the mica sheet has been pressed thoroughly, yet gently towards the slide and the glue layer was distributed through circular motions of the mica sheet, trying to remove the air bubbles that may be formed throughout the process. The amount of glue dispensed on the glass slide was not quantified as the slight excess was easily removable whilst cleaving mica. However, a large glue excess was avoided, as the ToF-SIMS imaging performance may have been affected, especially when mica had been cleaved several times; such a phenomenon was observed for other microarray applications in the laboratory. A sticky tape that was as wide as the mica sheet was used for cleaving. The process of attaching the tape to the mica was performed in a single movement and required practice beforehand. The attachment of the tape was followed by a thorough and firm pressing in all areas of the slide. The tape was then removed in a careful, yet paced single motion at a low angle making sure that a continuous mica layer was detached. Here, it is worth adding that mica sheet itself ought not to be bent in advance.

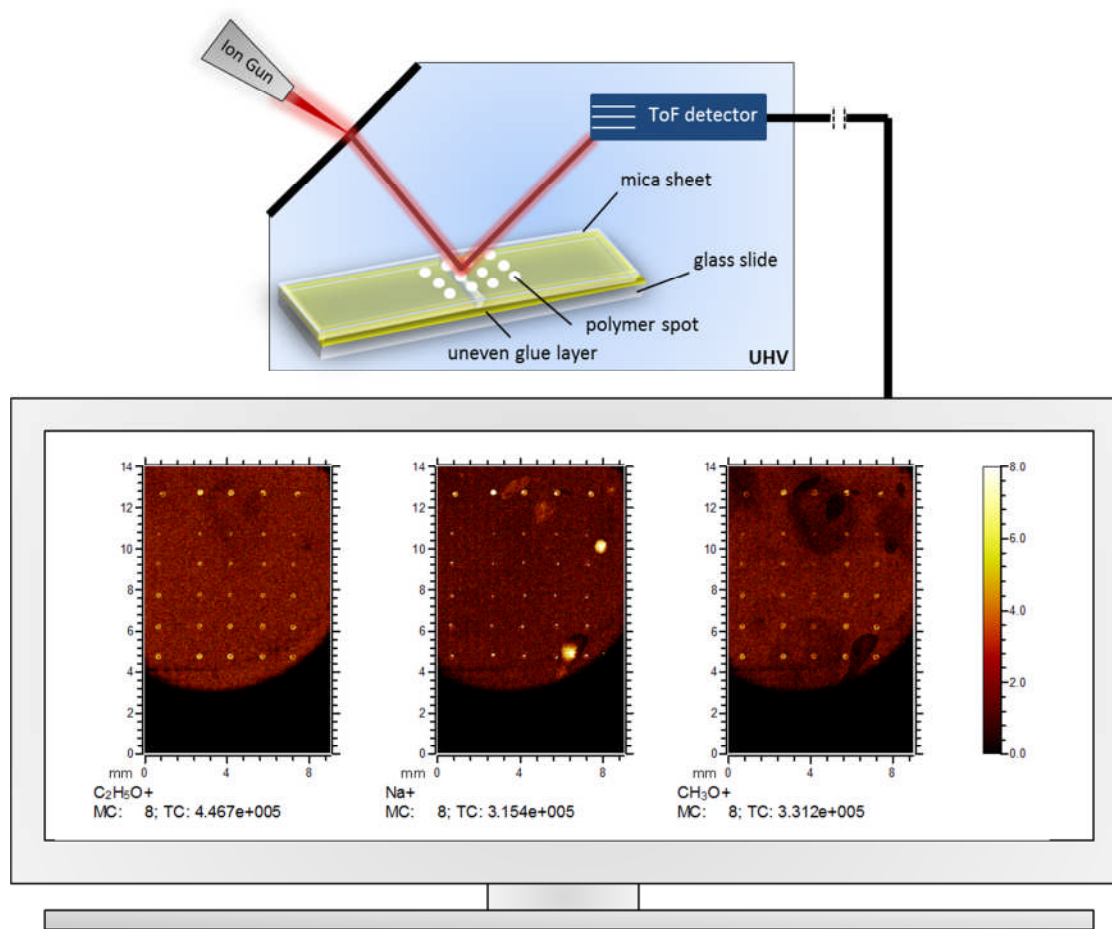


Figure 6.6. An illustration presenting ToF-SIMS chemical images collected from glass slide-attached mica sheets with tilted surface topography. Various volumes of 0.0001% (w/v) Pluronic[®] L-64 solution were printed on the mica sheet in high humidity environments (compare figure 6.5.A₂) before the ToF-SIMS images were collected using bismuth (III) primary ion source. The image analysis suggested that ToF-SIMS imaging performance was affected by either uneven distribution of the glue underneath or possible cracks in the mica, since all spots printed on the slide were not imaged (black areas on the ToF-SIMS chemical images) after the introduction of the primary ion source. The presence of polymer-representative ions ($C_2H_5O^+$ and CH_3O^+) on the slides in the shape of a spot (circular, light features on the appropriate ToF-SIMS images) demonstrates that printing of the polymer spots on the surface was successful. The presence of the sodium ions within such spots indicated that the polymer solutions were contaminated with this ion. The cartoon above the image has been added in order to communicate the requirement for a uniform surface topography determined via ToF-SIMS imaging technique (compare figure 2.2.).

Secondly, knowledge of the precise position of the spots on the slide was an important piece of information in order to identify the areas within the slide for ToF-SIMS analysis. Since the visual assessment of the presence of SLBs on the slide was not possible and the polymer excess in each spot was rinsed off the surface, the position of the material on the slide sometimes could not be easily identified with the optical camera of the mass spectrometer.

Therefore, the first indication whether the areas of SLBs exposed to the solutions of interest had been imaged with ToF-SIMS could only be performed after the primary ion beam had been introduced. Here, since the inkjet printed spots of liquids had the tendency to move in a random direction on the mica surface, and some ‘escaped’ from the theoretically-expected scan areas, it was a good practice that the scan size areas for ToF-SIMS images were slightly larger than the calculated array dimensions. It was also common sense that the position of the spots was known to the person handling the slide, while it was transferred from the printing chamber onto the ToF-SIMS sample stage in order to avoid errors.

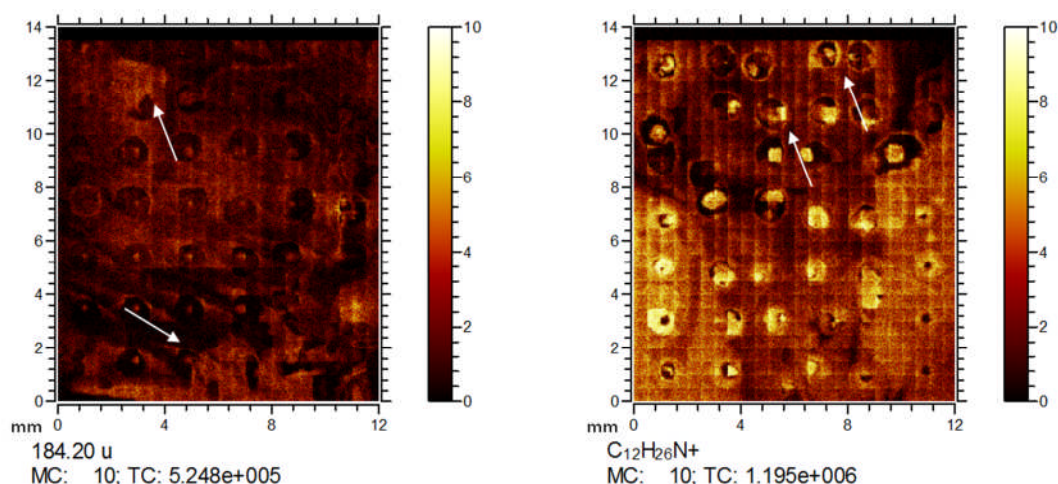


Figure 6.7. ToF-SIMS images of an SLB-Pluronic® interaction in a microarray format. The circular areas within the chemical images correspond to the spots of liquid printed on the slide. The left image represents the sample that was incubated in the printing chamber at 70 % relative humidity for 1 hour after printing spots and then rinsed through a gentle immersion in water, while the right image is a similar sample that was left to dry in air after the 1-hour incubation process. Effectively, SLB within each spot area has been exposed to a different surfactant concentration: 0.001 – 0.0001 % Pluronic L-62, L-64, F-68. Spot travelling, as well as excessive material ‘escaping’ from the surface after rinsing can be observed on the images and have been indicated with white arrows. This suggests that the rinsing step could be further optimised. ToF-SIMS images were obtained using C_{60} primary ion source.

Thirdly, optimisation of the rinsing step at the end of the SLB-surfactant interaction was required to prevent possible interferences originating from the distribution of secondary ions within the image. For the sample presented in figure 6.7. on the left hand side, a single, gentle immersion of the whole slide in copious amounts of Millipore water plus gentle shaking of the flask with the slide through circular motions over 1 minute was performed. The presence of chemical species that appear to be ‘coming off’ the surface on the ToF-SIMS image suggested that the incubation time could have been extended in order to obtain images of higher quality. An alternative to use two or more separate immersions was initially

considered however, this was avoided, as it could substantially decrease the overall amount of lipid material on the surface.

From a commercial point of view, the use of mica as a solid support is questionable. Although mica has offered several important advantages as a solid support for lipid bilayers, such as flatness, cleanness, a degree of reusability and low cost, some disadvantages with regards to SLB microarray development have been identified, *e.g.* the travelling of spots deposited on the surface, bendability, the need to glue the mica sheets to glass slides that may affect the data collection process or overall short stability of model SLBs exposed to air on this support. For that reason, the preliminary assessment of a surface similar to the FluidArray® (chapter 1) that may be more suitable for commercial applications, was performed using AFM.

FluidArray® surfaces have been reported to provide not only minimal non-specific lipid adsorption at the surface, but also air stable supported lipid bilayers, based on the fluorescent microscopy studies^{1b}. AFM studies on similar supports performed by a different research group have confirmed that such surfaces may be of use with regards to SLB microarray applications¹⁴. Preliminary AFM studies on CHOL-functionalised PEG-brush surfaces indicated that high quality bilayers have been fabricated using the VDT protocol (Figure 6.8.).

Interestingly, 23-hour exposure to air and subsequent rehydration of dry SLBs resulted in surfaces that were covered with both lipid bulks and bilayer morphologies when imaged with AFM. This suggested that FluidArray®-like surfaces indeed provided a degree of air stability for the model SLBs, when studied at a nanometre scale. It was therefore anticipated that the incubation of model SLBs deposited on such surfaces in high humidity environments would offer further improvements towards SLB microarray development. However, the high cost and high degree of surface chemistry associated with the FluidArray® surfaces were viewed as drawbacks in terms of the commercial employability of such systems. In fact, FluidArray®-deposited lipid bilayers should be classified as tethered bilayer lipid membranes (tBLMs) rather than SLBs (see chapter 1). Therefore, development of alternative, more user-friendly strategies for surface functionalization with both polymer and lipid molecules should be investigated in the future.

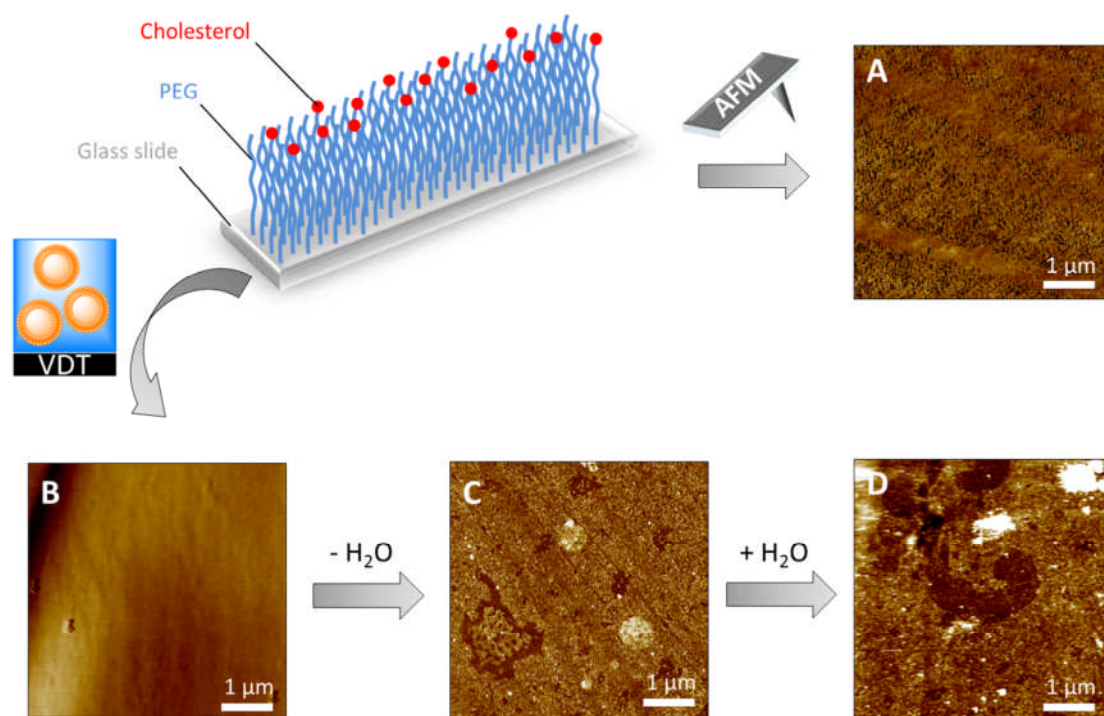


Figure 6.8. AFM images and illustration depicting the FluidArray[®] surface-based preliminary studies. The cartoon depicts the key components of FluidArray[®]-type surfaces (elements have not been drawn in scale for clarity purposes). Image A represents AFM-observed morphologies of the FluidArray[®]-type surface in air. Image B represents the AFM-observed morphology of the surface in liquid, after coating with the model supported lipid bilayer (SLB) through the vesicle deposition protocol. Image C depicts the AFM-observed morphology of the surface in B that was dried and left in a desiccator for 23 hours (image collected in air). Image D represents the morphology of the surface in C after a careful addition of PBS solution (image collected in liquid). The $-H_2O$ and $+H_2O$ symbols represent the processes of drying and rehydration of the SLB-coated FluidArray[®]-type surface, respectively. The PEG (blue) stands for carboxyl-group functionalised polyethylene glycol chains attached the glass slide (grey). Cholesterol (red) is attached to PEG through an ester group.

In addition to the optimisation of the solid support, a detection methodology that enables data collection in high throughput has to be considered, in order to develop commercially successful SLB microarrays. Since membranes are highly alterable systems and their interactions with xenobiotics can run pharmacodynamically through a number of different mechanisms, the selection of an appropriate detection method should be well thought through. For this application, ToF-SIMS was selected, as it not only was suitable for high throughput screening, but also enabled tracking the behaviour of the material on the surface chemically; hence it gave an indication of the interaction performances at a molecular level. For this reason, ToF-SIMS imaging may be employed as a technique supplementing *e.g.* AFM-based investigations on SLBs, in order to explain the mechanisms of the interactions between membrane lipids and the molecules of interest. Unfortunately, ToF-SIMS is not

user-friendly or cheap as a scientific technique in its current form. Therefore, it is likely that commercially viable SLB-based tests for the assessment of surfactant performances would evolve around other approaches, *e.g.* fluorescence¹⁵ or impedance¹⁶-based measurements. High sensitivity, as well as suitability for the high throughput screening for such measurements may additionally support this claim. Nevertheless, the ability to capture chemical images of such interactions makes ToF-SIMS an important technique in the SLB research.

It is the author's opinion that further research in this field should focus either on a thorough characterisation of FluidArray®-type surfaces or enrichment of the model SLB composition with a moisturising agent, in order to achieve more air-stable lipid coating. The preparation of FluidArray® supports was based on the original research paper however, the exact chemistry and properties of the surfaces are not currently clear; the manufacturer of PEG-brush coated glass slides only provided limited information about the product hence the spatial distribution of the polymer on the surface was not known. Perhaps, using tin oxide¹⁶ substrates coated with lipid-PEG conjugates through the temperature-induced ultradense grafting technique¹⁷ may offer several advantages in terms of further SLB microarray development. On the other hand, the cholesterol functionalization process may need to be characterised more thoroughly. Chemically, the reaction at the surface holds the potential to provide clean PEG-CHOL esters through a simple, mild esterification¹⁸. It would be interesting to see how other lipid chemistries and their distributions on the surface would affect stability of the model SLBs in high humidity environments. However, as indicated earlier, optimisation of such surfaces would be associated with higher manufacturing costs for the ultimate SLB microarray. Therefore, the optimisation of printing methodology on protein¹⁹- or polymer²⁰-enriched model SLBs may be an alternative strategy to investigate. On the one hand, since addition of such lipopreservatives to the model composition would most likely improve the air-stability of the model SLBs, the fabrication process, as well as the high humidity requirement would be simplified. On the other hand, however, such a modification would likely increase both the overall hydrophilicity of the microarray surface and complexity of the SLB chemistry interfering with the inkjet printing or ToF-SIMS imaging processes.

6.5 Conclusions

In conclusion, the development of an SLB microarray prototype was achieved, demonstrating that such approach could in the future be employed to study excipient-

membrane interactions not only in a higher throughput, but also at a nanometre scale. Although this setup could, without a doubt, be further improved, the results and discussion presented above substantially contribute towards the development of an SLB-based screening methodology that holds considerable potential to study the formulation-membrane interactions using nano-HTS approaches.

6.6 References

- (a) Furukawa, K.; Aiba, T., Supported Lipid Bilayer Composition Microarray Fabricated by Pattern-Guided Self-Spreading. *Langmuir* **2011**, *27* (12), 7341-7344; (b) Deng, Y.; Wang, Y.; Holtz, B.; Li, J. Y.; Traaseth, N.; Veglia, G.; Stottrup, B. J.; Elde, R.; Pei, D. Q.; Guo, A.; Zhu, X. Y., Fluidic and air-stable supported lipid bilayer and cell-mimicking microarrays. *J Am Chem Soc* **2008**, *130* (19), 6267-6271; (c) Han, X. J.; Qi, G. D.; Xu, X. T.; Wang, L., Formation of Lipid Bilayer Microarrays on Photo-Oxidized Polystyrene Surfaces. *Chem-Eur J* **2011**, *17* (52), 14741-14744; (d) Kaufmann, S.; Sobek, J.; Textor, M.; Reimhult, E., Supported lipid bilayer microarrays created by non-contact printing. *Lab Chip* **2011**, *11* (14), 2403-2410; (e) Smith, K. A.; Conboy, J. C., Using micropatterned lipid bilayer arrays to measure the effect of membrane composition on merocyanine 540 binding. *Bba-Biomembranes* **2011**, *1808* (6), 1611-1617; (f) Yamazaki, V.; Sirenko, O.; Schafer, R. J.; Nguyen, L.; Gutschmann, T.; Brade, L.; Groves, J. T., Cell membrane array fabrication and assay technology. *Bmc Biotechnol* **2005**, *5*; (g) Wang, Z. Z.; Wilkop, T.; Han, J. H.; Dong, Y.; Linman, M. J.; Cheng, Q., Development of air-stable, supported membrane arrays with photolithography for study of phosphoinositide - Protein interactions using surface plasmon resonance imaging. *Analytical chemistry* **2008**, *80* (16), 6397-6404; (h) Smith, K.; Gale, B. K.; Conboy, J., Micropatterned fluid lipid bilayer arrays created using a continuous flow microspotter. *Abstr Pap Am Chem S* **2009**, *237*; (i) Reimhult, E.; Baumann, M. K.; Kaufmann, S.; Kumar, K.; Spycher, P. R., Advances in nanopatterned and nanostructured supported lipid membranes and their applications. *Biotechnol Genet Eng* **2010**, *27*, 185-216; (j) Tiefenauer, L. X.; Studer, A., Nano for bio: Nanopore arrays for stable and functional lipid bilayer membranes (Mini Review). *Biointerphases* **2008**, *3* (2), Fa74-Fa79.
- (a) Yang, J.; Mei, Y.; Hook, A. L.; Taylor, M.; Urquhart, A. J.; Bogatyrev, S. R.; Langer, R.; Anderson, D. G.; Davies, M. C.; Alexander, M. R., Polymer surface functionalities that control human embryoid body cell adhesion revealed by high throughput surface characterization of combinatorial material microarrays. *Biomaterials* **2010**, *31* (34), 8827-8838; (b) Hook, A. L.; Chang, C. Y.; Yang, J.; Luckett, J.; Cockayne, A.; Atkinson, S.; Mei, Y.; Bayston, R.; Irvine, D. J.; Langer, R.; Anderson, D. G.; Williams, P.; Davies, M. C.; Alexander, M. R., Combinatorial discovery of polymers resistant to bacterial attachment. *Nature biotechnology* **2012**, *30* (9), 868-75.
- (a) Davies, M. C.; Alexander, M. R.; Hook, A. L.; Yang, J.; Mei, Y.; Taylor, M.; Urquhart, A. J.; Langer, R.; Anderson, D. G., High throughput surface characterization: A review of a new tool for screening prospective biomedical material arrays. *Journal of drug targeting* **2010**, *18* (10), 741-751; (b) Dietrich, P. M.; Horlacher, T.; Gross, T.; Wirth, T.; Castelli, R.; Shard, A. G.; Alexander, M.; Seeberger, P. H.; Unger, W. E. S., Surface analytical characterization of carbohydrate microarrays. *Surf Interface Anal* **2010**, *42* (6-7), 1188-1192; (c) Hook, A. L.; Chang, C. Y.; Yang, J.; Scurr, D. J.; Langer, R.; Anderson, D. G.; Atkinson, S.; Williams, P.; Davies, M. C.; Alexander, M. R., Polymer microarrays for high throughput discovery of biomaterials. *Journal of visualized experiments : JoVE* **2012**, (59), e3636; (d) Mei, Y.; Saha, K.; Bogatyrev, S. R.; Yang, J.; Hook, A. L.; Kalcioğlu, Z. I.; Cho, S. W.; Mitalipova, M.; Pyzocha, N.; Rojas, F.; Van Vliet, K. J.; Davies, M. C.; Alexander, M. R.; Langer, R.; Jaenisch, R.; Anderson, D. G., Combinatorial development of biomaterials for clonal growth of human pluripotent stem cells. *Nature materials* **2010**, *9* (9), 768-78; (e) Scoutaris, N.; Alexander, M. R.; Gellert, P. R.; Roberts, C. J., Inkjet printing as a novel medicine formulation technique. *Journal of Controlled Release* **2011**, *156* (2), 179-185; (f) Scoutaris, N.; Hook, A. L.; Gellert, P. R.; Roberts, C. J.; Alexander, M. R.; Scurr, D. J., ToF-SIMS analysis of chemical heterogeneities in inkjet micro-array printed drug/polymer formulations. *Journal of materials science. Materials in medicine* **2012**, *23* (2), 385-91; (g) Scurr, D. J.; Horlacher, T.; Oberli, M. A.; Werz, D. B.; Kroeck, L.; Bufali, S.; Seeberger, P. H.; Shard, A. G.; Alexander, M. R., Surface Characterization of Carbohydrate Microarrays. *Langmuir* **2010**, *26* (22), 17143-17155; (h) Yang, J.; Rose, F. R. A. J.; Gadegaard, N.; Alexander, M. R., A High-Throughput Assay of Cell-Surface Interactions using Topographical and Chemical Gradients. *Adv Mater* **2009**, *21* (3), 300-304.
- Hook, A. L.; Scurr, D. J.; Anderson, D. G.; Langer, R.; Williams, P.; Davies, M.; Alexander, M., High throughput discovery of thermo-responsive materials using water contact angle measurements and time-of-flight secondary ion mass spectrometry. *Surf Interface Anal* **2013**, *45* (1), 181-184.
- Celiz, A. D.; Hook, A. L.; Scurr, D. J.; Anderson, D. G.; Langer, R.; Davies, M. C.; Alexander, M. R., ToF-SIMS imaging of a polymer microarray prepared using ink-jet printing of acrylate monomers. *Surf Interface Anal* **2013**, *45* (1), 202-205.
- (a) Majd, S.; Mayer, M., Hydrogel stamping of arrays of supported lipid bilayers with various lipid compositions for the screening of drug-membrane and protein-membrane interactions. *Angew Chem Int Edit* **2005**, *44* (41), 6697-6700; (b) Majdzarringhalamaraghy, S.; Mayer, M., Multiple stamping of arrays of supported lipid bilayers with different lipid compositions using micropatterned hydrogel stamps. *Biophys J* **2005**, *88* (1), 238a-238a; (c) Moran-Mirabal, J. M.; Edel, J. B.; Meyer, G. D.; Throckmorton, D.; Singh, A. K.; Craighead, H. G., Micrometer-sized supported lipid bilayer arrays for bacterial toxin binding studies through total internal reflection fluorescence microscopy. *Biophys J* **2005**, *89* (1), 296-305.
- Faghijnejad, A.; Zeng, H., Interaction Mechanism between Hydrophobic and Hydrophilic Surfaces: using Polystyrene and Mica as a Model System. *Langmuir* **2013**.
- Seifert, U., Configurations of fluid membranes and vesicles. *Adv Phys* **1997**, *46* (1), 13-137.
- Radler, J.; Strey, H.; Sackmann, E., Phenomenology and Kinetics of Lipid Bilayer Spreading on Hydrophilic Surfaces. *Langmuir* **1995**, *11* (11), 4539-4548.
- Mennicke, U.; Salditt, T., Preparation of solid-supported lipid bilayers by spin-coating. *Langmuir* **2002**, *18* (21), 8172-8177.
- Fang, Y., Air stability of supported lipid membrane spots. *Chem Phys Lett* **2011**, *512* (4-6), 258-262.
- Sebastiani, F.; Harvey, R.; Khanniche, S.; Artero, J. B.; Haertle, M.; Fragneto, G., Diffraction studies on natural and model lipid bilayers. *Eur Phys J-Spec Top* **2012**, *213* (1), 355-365.
- Yamada, M.; Imaishi, H.; Morigaki, K., Microarrays of Phospholipid Bilayers Generated by Inkjet Printing. *Langmuir* **2013**, *29* (21), 6404-6408.
- Indrieri, M.; Suardi, M.; Podesta, A.; Ranucci, E.; Ferruti, P.; Milani, P., Quantitative investigation by atomic force microscopy of supported phospholipid layers and nanostructures on cholesterol-functionalized glass surfaces. *Langmuir* **2008**, *24* (15), 7830-41.
- Castellana, E. T.; Cremer, P. S., Imaging large arrays of supported lipid bilayers with a microscope. *Biointerphases* **2007**, *2* (2), 57-63.
- Sugihara, K.; Delai, M.; Szendro, I.; Guillaume-Gentil, O.; Voros, J.; Zambelli, T., Simultaneous OWLS and EIS monitoring of supported lipid bilayers with the pore forming peptide melittin. *Sensor Actuat B-Chem* **2012**, *161* (1), 600-606.
- Ogaki, R.; Andersen, O. Z.; Jensen, G. V.; Kolind, K.; Kraft, D. C. E.; Pedersen, J. S.; Foss, M., Temperature-Induced Ultradense PEG Polyelectrolyte Surface Grafting Provides Effective Long-Term Bioreistance against Mammalian Cells, Serum, and Whole Blood. *Biomacromolecules* **2012**, *13* (11), 3668-3677.
- Kim, S.; Lee, J. I.; Kim, Y. C., A Simple and Mild Esterification Method for Carboxylic-Acids Using Mixed Carboxylic Carbonic Anhydrides. *J Org Chem* **1985**, *50* (5), 560-565.
- Holden, M. A.; Jung, S. Y.; Yang, T. L.; Castellana, E. T.; Cremer, P. S., Creating fluid and air-stable solid supported lipid bilayers. *J Am Chem Soc* **2004**, *126* (21), 6512-6513.
- Albertorio, F.; Diaz, A. J.; Yang, T.; Chapa, V. A.; Kataoka, S.; Castellana, E. T.; Cremer, P. S., Fluid and air-stable lipopolymer membranes for biosensor applications. *Langmuir* **2005**, *21* (16), 7476-82.

Concluding remarks and future prospects.

Abbreviations:

3R- replacement, reduction, refinement; AFM – atomic force microscopy; API – active pharmaceutical ingredient; CHOL – cholesterol; DNA – deoxyribonucleic acid; HTS – high throughput screening; nano-HTS – nanometre-scale high throughput screening; nano-PKPD – nanometre-scale pharmacokinetics and pharmacodynamics; PBS – phosphate buffer saline; QbD – quality by design; siRNA – short interfering ribonucleic acid; SLB – supported lipid bilayer; SPM – sphingomyelin; ToF-SIMS – time-of-flight secondary ion mass spectrometry; XPS – X-ray photoelectron spectroscopy.

Throughout this thesis supported lipid bilayers (SLBs) have been assessed and analysed as possible tools for the *in vitro* screening of pharmaceutical formulation performance.

In chapter 1, SLBs were compared with the literature-reported, lipid-based membrane models indicating the significant potential that SLBs hold as systems for high throughput screening (HTS) applications. A unique classification of the SLB advantages and limitations was proposed and the need for elucidation of the behaviour of complex, physiologically-relevant lipid compositions, at the nanometre scale, was identified.

In chapter 2, experimental, as well as data analysis approaches were described in detail. This not only will enable the reproducibility of the experiments, but also help the processing of experimental data for similar studies.

In chapter 3, the development of a model SLB composed of five natural lipids was reported. Not only user-friendly fabrication approaches were optimised for this model, but also an innovative characterisation of lipid bilayer systems at a nanometre scale was performed. In addition, a novel hypothesis regarding the phase separation behaviour of SLBs was proposed and compared with membrane behaviours *in vivo*, based on both experimental observations and consideration of the literature.

In chapter 4 and 5, the interactions between model SLBs and formulation components were studied and novel interaction mechanisms between membranes and excipients (*e.g.* Pluronic®, phosphonium polymer), active pharmaceutical ingredients (*e.g.* siRNA) and formulations (*e.g.* DNA polyplex) were identified. On the one hand, the both results and experimental approaches from this thesis have improved the general understanding of the formulation-membrane interaction studies. On the other hand, the *in vitro*-studied

behaviours of model SLBs have been correlated with the literature-reported drug behaviours *in vivo*.

In chapter 6, a model SLB microarray prototype that suitable for HTS approaches, was engineered. An optimisation process was detailed that will allow further development of this approach.

Due to a multidisciplinary nature of this thesis, the findings significantly contribute to a number of disciplines within the pharmaceutical sciences.

Firstly, the new insights into sphingomyelin/cholesterol (SPM/CHOL) behaviours provide progress within lipid chemistry and lipid bilayer research. Based on the findings in this thesis, the focus of future research should be directed at physicochemical and biological properties of ceramide-cholesterol aggregates and their behaviours as both: independent chemical species and co-participants of lipid bilayers that strongly influence overall membrane properties. Also, the focus on bilayers of physiologically-relevant lipid compositions has been highlighted and shown valuable throughout the thesis not only for SLB-, but also for liposome-type models.

Secondly, since the new biological role of SPM as a lipid linking apoptosis and immunogenicity has been suggested, the focus of biochemistry and molecular biology of lipids (lipidomics) may therefore shift towards the interaction of lipids and immune system giving an early start to a new scientific discipline, immunolipidomics. Also, cell senescence-associated phenomena have been correlated with the *in vitro* behaviours of membrane models, possibly elucidating some aging-related mechanisms in biology.

Thirdly, the mechanisms related to the toxicity and poor delivery efficacy of nucleic acid therapeutics have been indicated, changing the view on the role of an excipient in such formulations. From a drug delivery perspective, research into the ability of an excipient to protect nucleic acid from the spontaneous binding of SPM/CHOL aggregates is likely to emerge. Also, further studies of the interaction between nucleic acids and ceramides may result in new biopharmaceutical formulations that hold the potential to further improve the nucleic acid delivery.

Fourthly, the need for early screening of direct drug-lipid (drug-membrane) interactions has been highlighted and demonstrated throughout this thesis, suggesting future research directions within the biophysical and material sciences. Without a doubt, further investigations into development of high throughput screening approaches, as well as

methods for the engineering of air-stable SLBs are necessary. Advances with regards to the development and characterisation of model SLB microarray discussed in this thesis improve the understanding of lipid bilayers as tools in the material sciences. Hopefully, this will allow the engineering of a test or a device of relevance to drug discovery and development.

Fifthly, a model for testing drug-membrane interactions in low throughput has essentially been developed, characterised and demonstrated to be useful throughout this thesis. Drug development researchers could therefore use it in its current shape to further elucidate AFM-based interactions of both small and big molecule drug candidates of various chemistries, *e.g.* protein-, nucleic acid-, polymer- or carbohydrate-based biopharmaceutics. Such an approach is encouraged, as the innovation is a pressing and still an unaddressed issue for the research and development of new medicines.

Finally, this thesis is a significant contribution in the field of pharmacology. Not only the development of a SLB-based testing approach has a significant impact of the 3Rs of animal model use in pharmaceutical sciences, but also indicates the urgent need for testing the biopharmaceutical performance at a nanometre scale. Regardless, the shift from a traditional pharmacology towards nanopharmacology can be gradually observed implying that investigations of drug behaviour at a molecular level are the future direction for this field. Although the term nanopharmacology is loosely associated with homeopathy¹, there are clear indications in the literature that this emerging science field will evolve in the near future². Here, AFM in PeakForce® Tapping mode³ plays an important role³. In this thesis, SLBs were proposed to be tools for nano-PKPD studies, hopefully establishing their deserved place in nano-PKPD field and setting the scene for future advancements. The methodology developed throughout this research links the potential of AFM with both the approaches and observations in pharmacology. Additionally, the possibility of using other techniques (ToF-SIMS, XPS) for the elucidation of lipid behaviours at a nanometre scale has been successfully attempted. In the times when animal and human health is legally and ethically valued more than ever, and nature and its components have been largely characterised, the focus on nanopharmacology is appropriate and necessary, as it may uncover phenomena that have not been elucidated through traditional approaches.

To conclude, it is the author's hope that progress demonstrated above would make this research both attractive and worthy of further investigations. Obviously, the topic has not been saturated with discoveries and still many questions remain unanswered. However, the scientific advancements presented in this thesis, based on 3 years of laboratory-based work

Chapter 7: Concluding remarks and future prospects.

of a person not previously familiar with the topic, indicate that the further success in this area is achievable and the outlook for subsequent discoveries should remain optimistic.

References

1. Ullman, D., Let's have a serious discussion of nanopharmacology and homeopathy. *Faseb J* **2006**, *20* (14), 2661-2661.
2. Lal, R.; Ramachandran, S.; Arnsdorf, M. F., Multidimensional Atomic Force Microscopy: A Versatile Novel Technology for Nanopharmacology Research. *Aaps Journal* **2010**, *12* (4), 716-728.
3. Lamprou, D. A.; Venkatpurwar, V.; Kumar, M. N. V. R., Atomic Force Microscopy Images Label-Free, Drug Encapsulated Nanoparticles In Vivo and Detects Difference in Tissue Mechanical Properties of Treated and Untreated: A Tip for Nanotoxicology. *Plos One* **2013**, *8* (5).

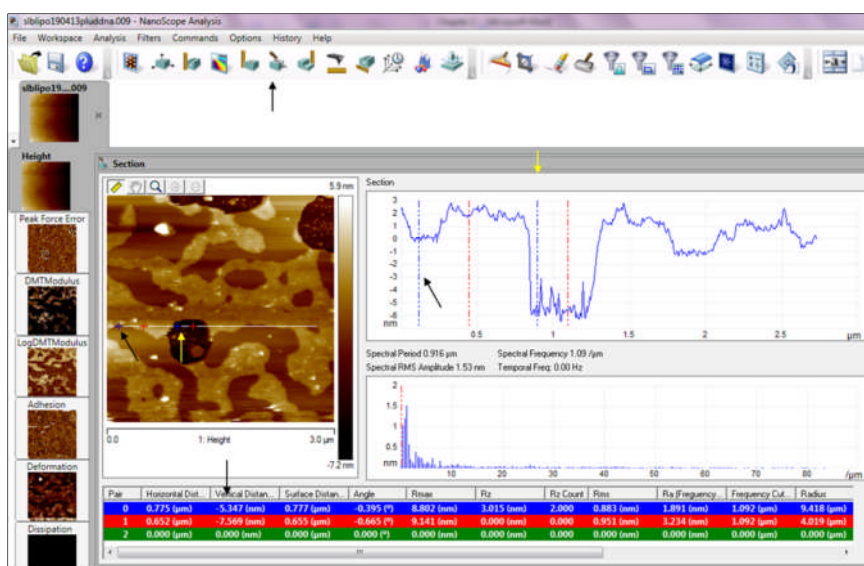
Appendix I

Analysis of AFM Images.

Attachments:

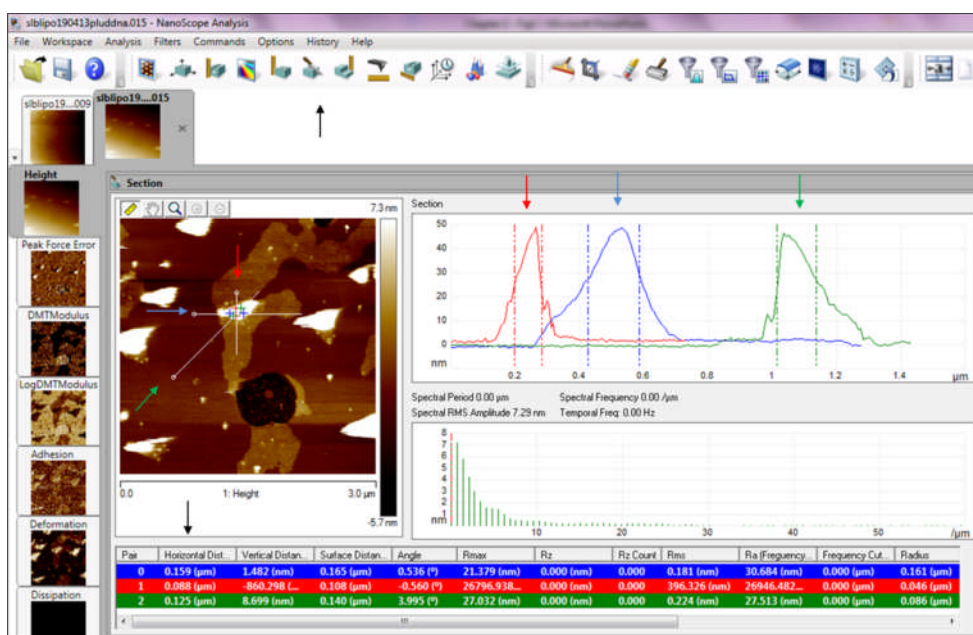
- Evaluation of SLB thickness.....138
- Evaluation of particle size.....138
- Quantification of SLB coverage (step-by-step approach).....139

Evaluation of SLB thickness.



The image above indicates an example for the evaluation of SLB coverage using NanoScope Analysis software. Arrows indicate ‘Section Analysis’ (black on the top), marker points (black and yellow in the middle) and SLB thickness (black at the bottom). See section 2.2.2.2.7.1. for more details.

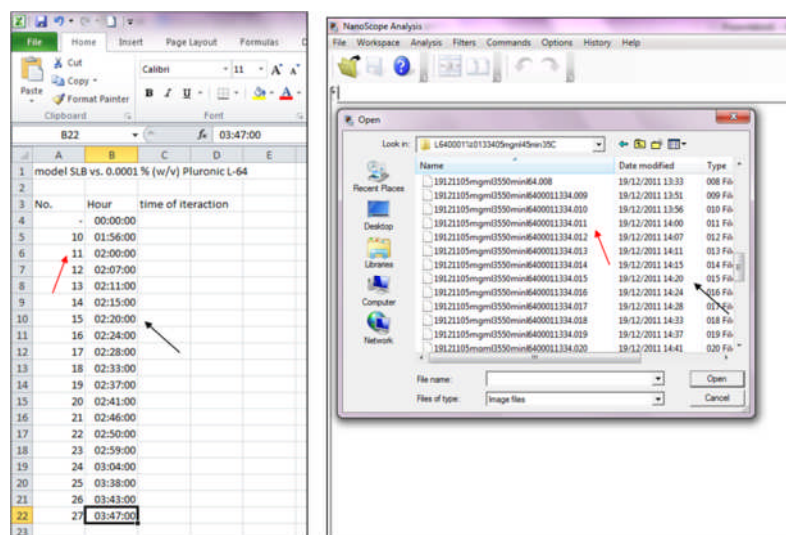
Evaluation of particle size.



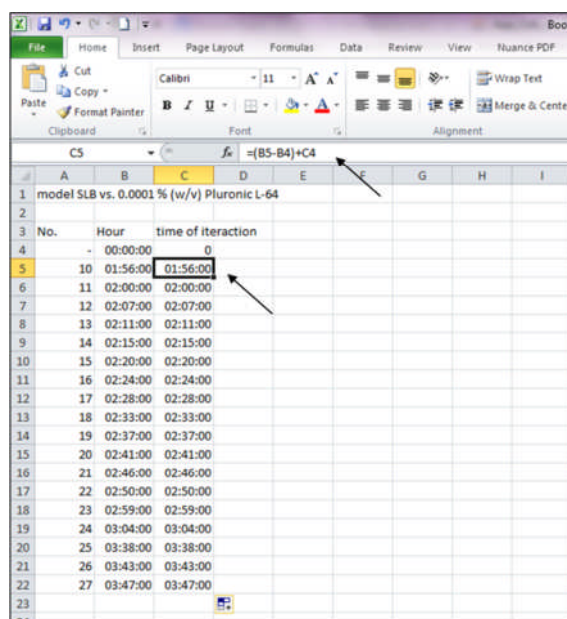
The image above indicates an example for the evaluation of particle size using NanoScope Analysis software. Arrows indicate ‘Section Analysis’ (black on the top), marker lines that were drawn horizontally (blue), vertically (red) and in diagonal (green), as well as particle size values that are used for further calculations (black at the bottom). See section 2.2.2.2.7.3. for more details.

Quantification of SLB coverage (step-by-step approach).

1. Open Excel software, name the interaction of interest and copy AFM image numbers with associated time in a format presented on the figure below. Naming the interactions and copying the image numbers is not essential, however it would be helpful during the retrospective analysis, if the need for finding the original AFM image associated with particular data point on the graph arose. The first time point is the time at which the interaction in AFM setup started and is not the time when the first image of the area of interest was collected.

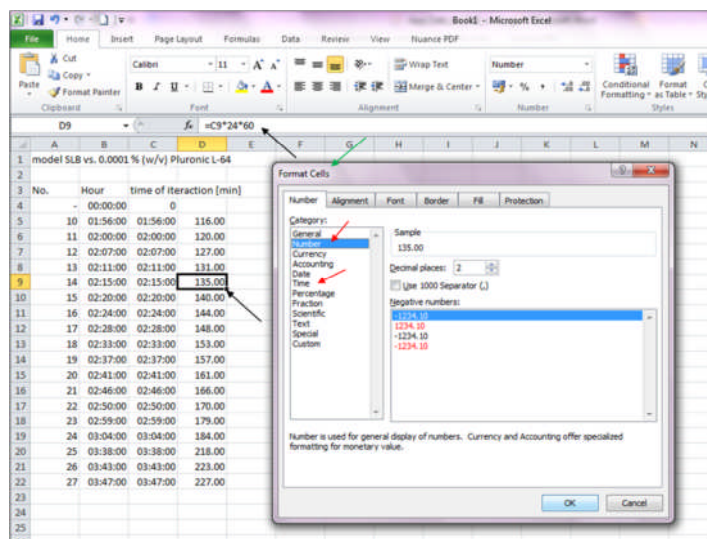


2. Express the time point values in an interaction time format. The first time point equals 0, while the second time point is the difference between the hours at the second and first time point plus the time point above the cell of interests. For instance, for the cell C5 on the image the function is $'=(B5-B4)+C4'$, whilst for the cell C10 $'=(B10-B9)+C9'$.

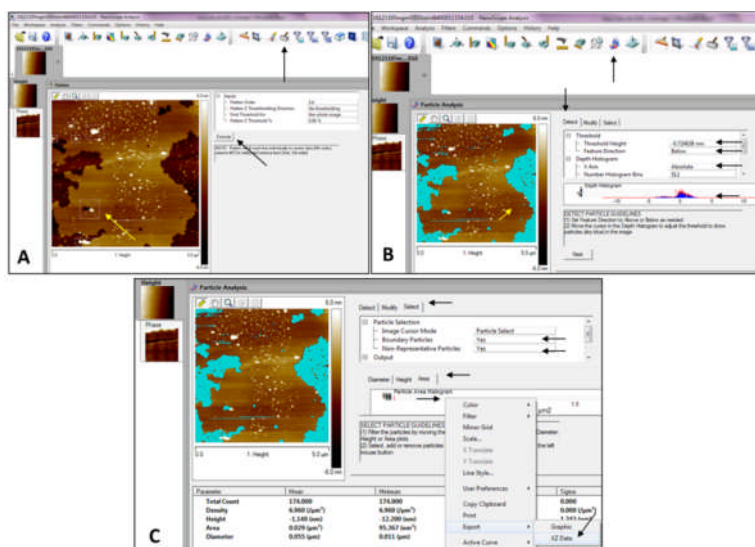


Appendix I: Analysis of AFM Images.

- Change the display of the interaction time from HH:MM:SS format into minute values. This can be achieved through multiplying each cell by 1440 and formatting cell, so that the value is displayed as number rather than time (e.g. for D5 the function looks `=D5*24*60` & right click). This step is not essential however, display of the time in such a format looks better on the final graph. At this point, the first time point may be abandoned, as the values for the corresponding surface areas extracted from AFM data are non-existent.

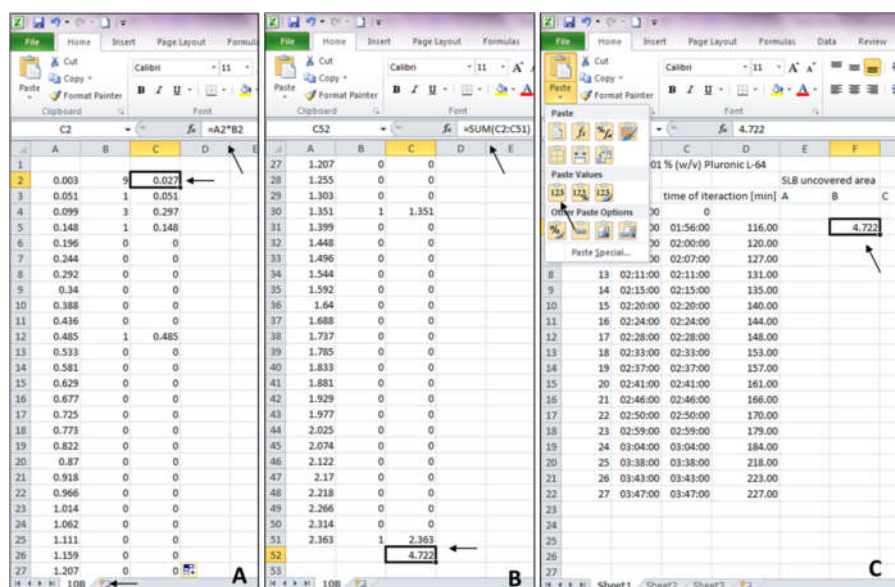


- Open the first AFM image of interest in NanoScope Analysis software, establish the best flattening approach that ideally will be applied for all other images of the interaction (Image A), click onto Particle Analysis mode (Image B), choose: YES for Boundary Particles and Non-representative Particles (Image C), BELOW for Feature Direction and ABSOLUTE for X-Axis, adjust the threshold in order to mark the SLB-uncovered area to the best possible fit (Image B) and export the data into a .txt file which can be named after the number of the AFM image of interest (Image C). Since finding the best possible fit of the uncovered area is subjective, the minimum of 3 data sets corresponding to 3 neighbouring threshold values are saved for each image.



Appendix I: Analysis of AFM Images.

- Open the .txt file of interest as an Excel file, multiply values from column A by the corresponding values from column B (e.g. C5 is '=A5*B5' in image A), sum up all the values in column C using '=sum(C[number of top row]:C[number of bottom row])' as presented in image B. This is the SLB-uncovered surface area value that should be copied into the Excel file with the interaction time data points. Use 'copy values' option in Excel to avoid errors (image C).



- Repeat steps 4 and 5 for each data set exported from the NanoScope software. This should result in sets of 3 SLB-uncovered surface area values for each time point as presented on the image below. The data exported from the NanoScope software may not be reported in the same units at all times. Therefore, in some cases the SLB-uncovered surface area values may need to be divided or multiplied by 1000 in order to assure the consistency within the same and across different time points of the interaction.

The image shows a screenshot of an Excel spreadsheet with a table of SLB-uncovered surface area values. The table has columns for No., Hour, time of iteration [min], and three columns for SLB-uncovered area (A, B, C). The values are as follows:

No.	Hour	time of iteration [min]	A	B	C
1					
2					
3					
4		00:00:00	0		
5	10	01:56:00	116.00	4.632	4.722
6	11	02:00:00	120.00	5.26	5.371
7	12	02:07:00	127.00	6.213	6.193
8	13	02:11:00	131.00	6.655	6.789
9	14	02:15:00	135.00	7.157	7.249
10	15	02:20:00	140.00	8.09	8.232
11	16	02:24:00	144.00	10.756	10.846
12	17	02:28:00	148.00	12.578	12.697
13	18	02:33:00	153.00	15.345	15.443
14	19	02:37:00	157.00	16.677	16.733
15	20	02:41:00	161.00	18.446	18.548
16	21	02:46:00	166.00	19.356	19.413
17	22	02:50:00	170.00	20.284	20.393
18	23	02:59:00	179.00	20.875	20.963
19	24	03:04:00	184.00	21.223	21.357
20	25	03:38:00	218.00	22.122	22.222
21	26	03:43:00	223.00	22.298	22.38
22	27	03:47:00	227.00	22.409	22.494
23					
24					
25					
26					
27					

Appendix I: Analysis of AFM Images.

- Choose 3 random images for the interaction of interest in the Nanoscope software and repeat steps 4-6 with minor modifications in step 4. In step 4 export the data for areas marked for both above and below the same threshold value. This can be achieved through choosing above/below options in the tab. Here, the software may automatically change the initial threshold value when the above/below options are changed for the first time. Therefore, a trial selection of both options should be performed prior to exporting the data into the .txt files. These files will be used for the calculation of the total surface area per image, therefore the names '100_[image_number]A.txt' and '100_[image_number]B.txt' are recommended for the data above and below the same threshold value, respectively. In the main Excel file sum up the total surface area values above and below the threshold for each image, e.g. for J4 it is '=SUM(H4:I4)'

model SLB vs. 0.0001 % (w/v) Pluronic L-64			SLB uncovered area						100%	
No.	Hour	time of interaction [min]	A	B	C	A	B			
4	-	00:00:00	0					9.396	14.899	24.295
5	10	01:56:00	01:56:00	116.00	4.632	4.722	4.844	5.12	19.148	24.268
6	11	02:00:00	02:00:00	120.00	5.26	5.371	5.455	8.614	15.342	23.956
7	12	02:07:00	02:07:00	127.00	6.213	6.193	6.3			
8	13	02:11:00	02:11:00	131.00	6.655	6.789	6.897			
9	14	02:15:00	02:15:00	135.00	7.157	7.249	7.35			
10	15	02:20:00	02:20:00	140.00	8.09	8.232	8.401			
11	16	02:24:00	02:24:00	144.00	10.756	10.846	10.944			
12	17	02:28:00	02:28:00	148.00	12.578	12.697	12.709			
13	18	02:33:00	02:33:00	153.00	15.345	15.443	15.557			
14	19	02:37:00	02:37:00	157.00	16.677	16.733	16.891			
15	20	02:41:00	02:41:00	161.00	18.446	18.548	18.654			
16	21	02:46:00	02:46:00	166.00	19.356	19.413	19.567			
17	22	02:50:00	02:50:00	170.00	20.294	20.393	20.495			
18	23	02:59:00	02:59:00	179.00	20.875	20.963	21.05			
19	24	03:04:00	03:04:00	184.00	21.223	21.357	21.456			
20	25	03:38:00	03:38:00	218.00	22.122	22.222	22.543			
21	26	03:43:00	03:43:00	223.00	22.298	22.38	22.459			
22	27	03:47:00	03:47:00	227.00	22.409	22.494	22.582			

- Calculate both the average SLB-uncovered surface area values (e.g. for K5 it is '=AVERAGE(E5:G5)' or for J7 '=AVERAGE(J4:J6)') and the standard deviation from these averages (e.g. for L9 it is '=STDEV.P(E9:G9)' and for J8 '=STDEV.P(J4:J6)') not only for each time point of the interaction (left), but also for the total surface area values (right).

model SLB vs. 0.0001 % (w/v) Pluronic L-64			SLB uncovered area						100%		
No.	Hour	time of interaction [min]	A	B	C	A	B			(A+B+C)/3	
5	10	01:56:00	01:56:00	116.00	4.632	4.722	4.844	5.12	19.148	24.268	6.7326667
6	11	02:00:00	02:00:00	120.00	5.26	5.371	5.455	8.614	15.342	23.956	5.362
7	12	02:07:00	02:07:00	127.00	6.213	6.193	6.3				6.2353333
8	13	02:11:00	02:11:00	131.00	6.655	6.789	6.897				6.7803333
9	14	02:15:00	02:15:00	135.00	7.157	7.249	7.35				7.252
10	15	02:20:00	02:20:00	140.00	8.09	8.232	8.401				8.241
11	16	02:24:00	02:24:00	144.00	10.756	10.846	10.944				10.848667
12	17	02:28:00	02:28:00	148.00	12.578	12.697	12.709				12.661333
13	18	02:33:00	02:33:00	153.00	15.345	15.443	15.557				15.448333
14	19	02:37:00	02:37:00	157.00	16.677	16.733	16.891				16.767
15	20	02:41:00	02:41:00	161.00	18.446	18.548	18.654				18.549333
16	21	02:46:00	02:46:00	166.00	19.356	19.413	19.567				19.445333
17	22	02:50:00	02:50:00	170.00	20.294	20.393	20.495				20.394
18	23	02:59:00	02:59:00	179.00	20.875	20.963	21.05				20.962667
19	24	03:04:00	03:04:00	184.00	21.223	21.357	21.456				21.345333
20	25	03:38:00	03:38:00	218.00	22.122	22.222	22.543				22.295667
21	26	03:43:00	03:43:00	223.00	22.298	22.38	22.459				22.379
22	27	03:47:00	03:47:00	227.00	22.409	22.494	22.582				22.495

Appendix I: Analysis of AFM Images.

- Express the average surface area value for each time point as a per cent (%) of the average total surface area. For M5 it is $'=(K5*100)/\$J\$7'$.

model SLB vs. 0.0001 % (w/v) Pluronic L-64													
SLB uncovered area													
100%													
No.	Hour	time of iteration [min]	A	B	C	A	B	(A+B+C)/3	SD	%			
4	-	00:00:00	0					9.396	14.899	24.295			
5	10	01:56:00	01:56:00	116.00	4.532	4.722	4.844	5.12	19.148	24.268	4.6993333	0.128378	19.44042
6	11	02:00:00	02:00:00	120.00	5.26	5.371	5.455	8.614	15.342	23.956	5.362	0.079862	22.18177
7	12	02:07:00	02:07:00	127.00	6.213	6.193	6.3	Average 100%:		24.173	6.2353333	0.046449	25.79462
8	13	02:11:00	02:11:00	131.00	6.655	6.789	6.897	SD 100%:		0.153838	6.7803333	0.098986	28.0492
9	14	02:15:00	02:15:00	135.00	7.157	7.249	7.35				7.252	0.07882	30.00041
10	15	02:20:00	02:20:00	140.00	8.09	8.232	8.401				8.241	0.127125	34.09176
11	16	02:24:00	02:24:00	144.00	10.756	10.846	10.944				10.848667	0.076774	44.87927
12	17	02:28:00	02:28:00	148.00	12.578	12.697	12.709				12.661333	0.059129	52.378
13	18	02:33:00	02:33:00	153.00	15.345	15.443	15.557				15.448333	0.086631	63.90739
14	19	02:37:00	02:37:00	157.00	16.677	16.733	16.891				16.767	0.090613	69.36251
15	20	02:41:00	02:41:00	161.00	18.446	18.548	18.654				18.549333	0.084921	76.73575
16	21	02:46:00	02:46:00	166.00	19.356	19.413	19.567				19.445333	0.089123	80.44237
17	22	02:50:00	02:50:00	170.00	20.294	20.393	20.495				20.394	0.082061	84.36686
18	23	02:59:00	02:59:00	179.00	20.875	20.963	21.05				20.962667	0.071444	86.71934
19	24	03:04:00	03:04:00	184.00	21.223	21.357	21.456				21.345333	0.095479	88.30238
20	25	03:38:00	03:38:00	218.00	22.122	22.222	22.543				22.295667	0.179593	92.23376
21	26	03:43:00	03:43:00	223.00	22.298	22.38	22.459				22.379	0.065732	92.5785
22	27	03:47:00	03:47:00	227.00	22.409	22.494	22.582				22.495	0.07063	93.05837

- Subtract the % values from 100 (e.g. for N5 it is $'=100-M5'$). These values stand for SLB coverage of the surface [%] and are used for plotting the SLB coverage vs. time relationship in a graph format (column D [X axis] vs. column N [Y axis], respectively).

model SLB vs. 0.0001 % (w/v) Pluronic L-64														
SLB uncovered area														
100%														
No.	Hour	time of iteration [min]	A	B	C	A	B	(A+B+C)/3	SD	%	SLB coverage			
4	-	00:00:00	0					9.396	14.899	24.295				
5	10	01:56:00	01:56:00	116.00	4.532	4.722	4.844	5.12	19.148	24.268	4.6993333	0.128378	19.44042	80.55957749
6	11	02:00:00	02:00:00	120.00	5.26	5.371	5.455	8.614	15.342	23.956	5.362	0.079862	22.18177	77.81822695
7	12	02:07:00	02:07:00	127.00	6.213	6.193	6.3	Average 100%:		24.173	6.2353333	0.046449	25.79462	74.20538066
8	13	02:11:00	02:11:00	131.00	6.655	6.789	6.897	SD 100%:		0.153838	6.7803333	0.098986	28.0492	71.9507991
9	14	02:15:00	02:15:00	135.00	7.157	7.249	7.35				7.252	0.07882	30.00041	69.9958632
10	15	02:20:00	02:20:00	140.00	8.09	8.232	8.401				8.241	0.127125	34.09176	65.90824474
11	16	02:24:00	02:24:00	144.00	10.756	10.846	10.944				10.848667	0.076774	44.87927	55.12072698
12	17	02:28:00	02:28:00	148.00	12.578	12.697	12.709				12.661333	0.059129	52.378	47.62200251
13	18	02:33:00	02:33:00	153.00	15.345	15.443	15.557				15.448333	0.086631	63.90739	36.09261021
14	19	02:37:00	02:37:00	157.00	16.677	16.733	16.891				16.767	0.090613	69.36251	30.63748811
15	20	02:41:00	02:41:00	161.00	18.446	18.548	18.654				18.549333	0.084921	76.73575	23.26424799
16	21	02:46:00	02:46:00	166.00	19.356	19.413	19.567				19.445333	0.089123	80.44237	19.55763317
17	22	02:50:00	02:50:00	170.00	20.294	20.393	20.495				20.394	0.082061	84.36686	15.63314442
18	23	02:59:00	02:59:00	179.00	20.875	20.963	21.05				20.962667	0.071444	86.71934	13.28065748
19	24	03:04:00	03:04:00	184.00	21.223	21.357	21.456				21.345333	0.095479	88.30238	11.69762407
20	25	03:38:00	03:38:00	218.00	22.122	22.222	22.543				22.295667	0.179593	92.23376	7.766240571
21	26	03:43:00	03:43:00	223.00	22.298	22.38	22.459				22.379	0.065732	92.5785	7.42150333
22	27	03:47:00	03:47:00	227.00	22.409	22.494	22.582				22.495	0.07063	93.05837	6.94162909

Appendix I: Analysis of AFM Images.

11. Calculate the error using the equation from chapter 2, e.g. for O5 it is $'=ABS((100/\$J\$7)*L5)+ABS(((100*K5)/(\$J\$7)^2)*\$J\$8)'$. The final values of error bars were expressed using one or two significant figures.

The screenshot shows an Excel spreadsheet with the following data table:

Hour	time of iteration [min]	A	B	C	A	B	(A+B+C)/3	SD	%	SLB coverage	Y error		
00:00:00	0				9.396	14.899	24.295						
01:56:00	01:56:00	116.00	4.532	4.722	4.844	5.12	19.148	24.268	4.6993333	0.128378	19.44042	80.55957749	0.7
02:00:00	02:00:00	120.00	5.26	5.371	5.455	8.614	15.342	23.956	5.362	0.079862	22.18177	77.81822695	0.5
02:07:00	02:07:00	127.00	6.213	6.193	6.3 Average 100%			24.173	6.2353333	0.046449	25.79462	74.20538066	0.4
02:11:00	02:11:00	131.00	6.655	6.789	6.897 SD 100%			0.153838	6.7803333	0.098986	28.0492	71.9507991	0.6
02:15:00	02:15:00	135.00	7.157	7.249	7.35				7.252	0.07882	30.00041	69.99958632	0.5
02:20:00	02:20:00	140.00	8.09	8.232	8.401				8.241	0.127125	34.09176	65.90824474	0.7
02:24:00	02:24:00	144.00	10.756	10.846	10.944				10.848667	0.076774	44.87927	55.12072698	0.6
02:28:00	02:28:00	148.00	12.578	12.697	12.709				12.661333	0.059129	52.378	47.62200251	0.6
02:33:00	02:33:00	153.00	15.345	15.443	15.557				15.448333	0.086631	63.90739	36.09261021	0.8
02:37:00	02:37:00	157.00	16.677	16.733	16.891				16.767	0.090613	69.36251	30.63748811	0.8
02:41:00	02:41:00	161.00	18.446	18.548	18.654				18.549333	0.084921	76.73575	23.26424799	0.8
02:46:00	02:46:00	166.00	19.356	19.413	19.567				19.445333	0.089123	80.44237	19.55763317	0.9
02:50:00	02:50:00	170.00	20.294	20.393	20.495				20.394	0.082061	84.36686	15.63314442	0.9
02:59:00	02:59:00	179.00	20.875	20.963	21.05				20.962667	0.071444	86.71934	13.28065748	0.8
03:04:00	03:04:00	184.00	21.223	21.357	21.456				21.345333	0.095479	88.30238	11.69762407	1.0
03:38:00	03:38:00	218.00	22.122	22.222	22.543				22.295667	0.179593	92.23376	7.766240571	1.3
03:43:00	03:43:00	223.00	22.298	22.38	22.459				22.379	0.065732	92.5785	7.42150333	0.9
03:47:00	03:47:00	227.00	22.409	22.494	22.582				22.495	0.07063	93.05837	6.94162909	0.9

Appendix II

Supporting Information on AFM Studies.

Attachments:

- Development of scratch test.....146
- Optimisation of BST and VDT protocols for fabrication of model SLBs.....147
- Summary of control experiments after injection of PBS into the AFM cell.....151
- Summary of control experiments for model SLB-exciipient interaction studies.....152
- Summary of control experiments for model SLB-nucleic acid formulation
interaction studies.....153

Development of scratch test.

Since the atomic force microscopy (AFM)-reported morphologies of pure mica surfaces and continuous supported lipid films were similar, the presence of continuous lipid films needed to be confirmed each time with AFM. As AFM imaging involves a direct, software-controlled contact of the AFM probe with the sample surface and supported lipid films are a soft matter, it was anticipated that the presence of lipid coating above the surface can be verified through application of high force of AFM tip in the tapping mode that is detrimental to the integrity of the area lipid layer of interest and, at the same time, is not detrimental to the integrity of the solid support. If such a force was applied to a particular surface area of the lipid film-coated sample, the lipid layer within the such area would be swept away, not only uncovering the surface of the solid support, but also enabling both the confirmation of the presence of lipid film on the sample surface and the subsequent assessment of the lipid film thickness through cross section analysis. This experimental approach is referred in the thesis as a scratch test.

Since preliminary AFM experiments with pure mica surfaces indicated that application of high forces of the AFM tip affected mica integrity, the initial optimisation of the force of the AFM tip in the tapping mode, which was suitable for the scratch test, was performed. The summary of the optimisation process was depicted in figure below.

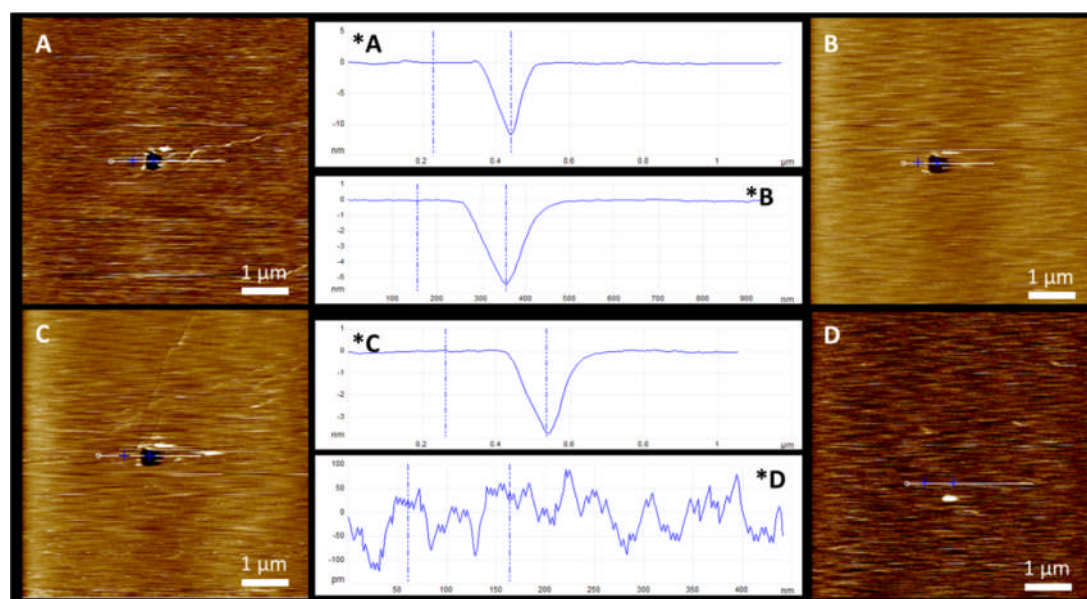


Figure S-II.1. AFM images (A-D) and corresponding cross section analyses (*) of pure mica scratched with AFM probe at different setpoint values: 0.000005 mV (A); 0.00005 mV (B); 0.0005mV (C); 0.005 mV (D). The setpoint is a software-controlled parameter that enables modifying the force of AFM tip applied to the sample surface. As indicated in the figure above, application of different forces to the mica support does (A-C) or does not (D) affect the integrity of the mica surface. Lack of surface integrity (A-C) is manifested as a dark, square-shaped ‘hole’ in the centre of the image. (D) indicates that the integrity of mica surface is not affected after ‘scratching’ the surface at 0.005 mV setpoint value. AFM images were collected in liquid environments using MultiMode2 AFM setup, as described in chapter 2. Z-scale bars were removed for presentation purposes.

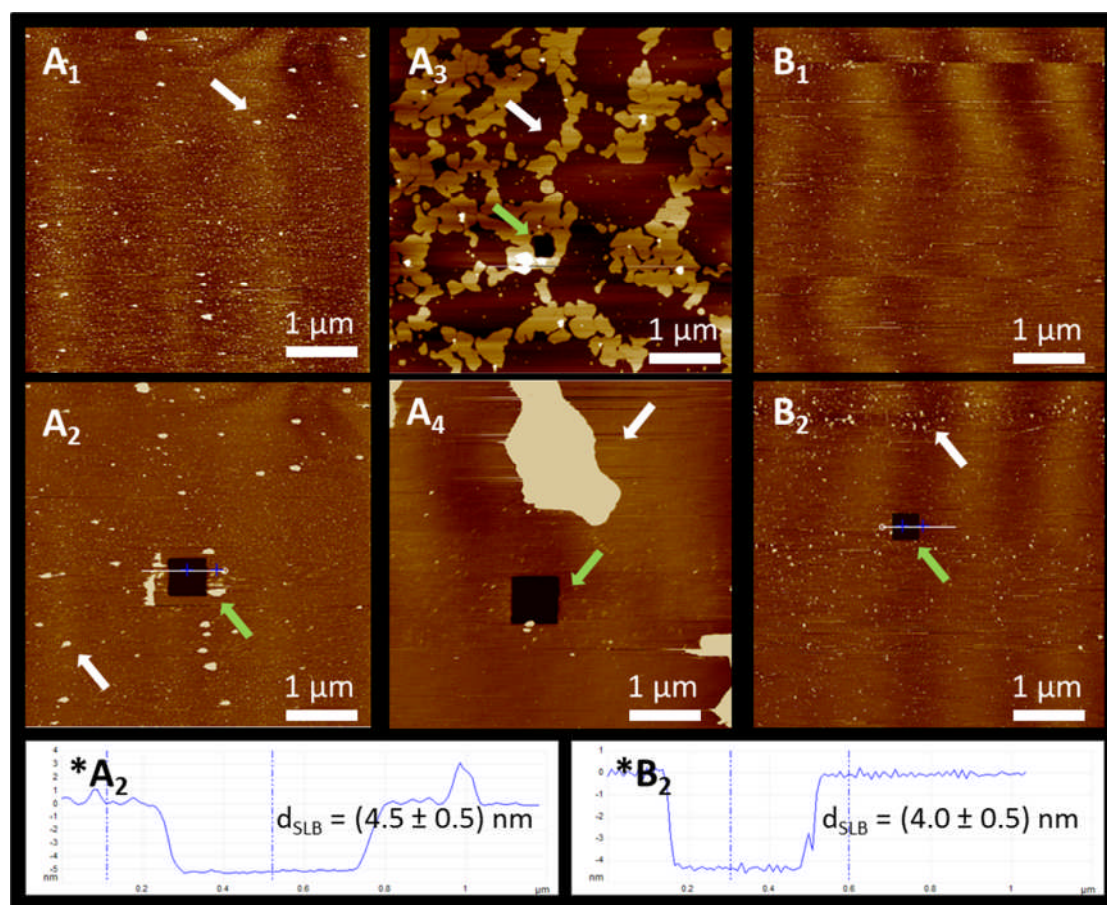
Eventually, it was established that the scratch test protocol was consisted of the following steps:

- (1) Capture 5 μm x 5 μm continuous SLB image using the appropriate imaging parameters (chapter 2).
- (2) Zoom-in in the image centre at 100 nm x 100 nm – 500 nm x 500 nm scan size.
- (3) Minimize image resolution.
- (4) Maximize tip velocity.
- (5) Decrease the amplitude setpoint value to 0.001 mV for 10 seconds.
- (6) Increase the amplitude setpoint value to the value in step (1).
- (7) Increase image resolution to the resolution in step (1).
- (8) Decrease the tip velocity to the velocity in step (1).
- (9) Increase the scan size to 5 μm x 5 μm .
- (10) Zero the X and Y offset values.
- (11) Capture image as in (1).

Optimisation of BSST and VDT protocols for fabrication of model SLBs.

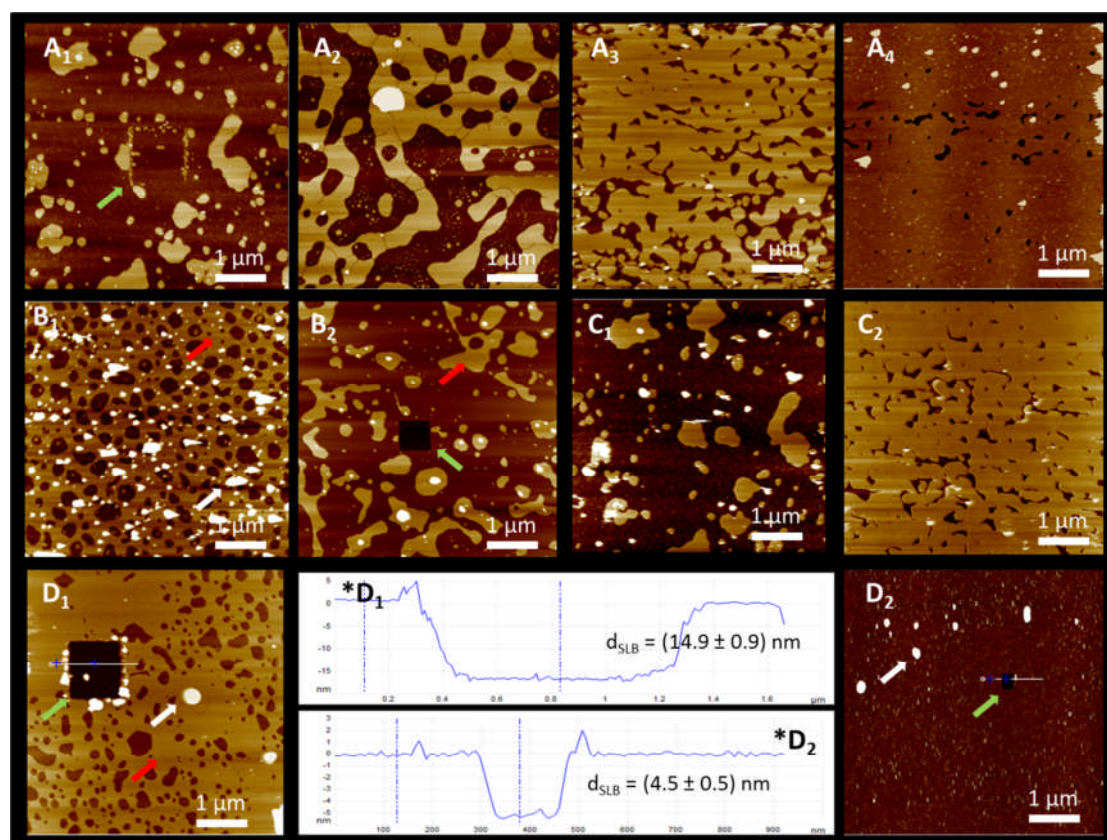
Single lipid dioleoylphosphatidyl choline (DOPC) and dipalmitoylphosphatidyl choline (DPPC) liposomes were used as liquid and gel phase-representative lipids to optimise the protocols for model SLB fabrication using both bilayer self-spreading (BSST) and vesicle deposition (VDT) techniques.

Initially, it was noticed that DOPC formed only a single lipid bilayers using BSST approach, while DPPC could form bi- or multilayers depending on the manufacturing parameters, *e.g.* temperature, incubation time, amount of lipid material pipetted on the solid support, number of rinses and solution type used for rinsing. Also, BSST resulted in a fast formation of continuous SLBs for both lipids, while VDT-fabricated lipid film morphologies were strongly dependant on the manufacturing parameters. The summary of atomic force microscopy (AFM)-recorded morphologies for DOPC and DPPC supported lipid bilayers (SLBs), when fabricated using BSST, was depicted in the figure below. Since model lipid mixture was expected to behave in a similar way to 1:1 DPPC:DOPC-composed lipid mixture, 10 μg and 45-minute incubation at 45°C in Millipore water were chosen as conditions of preference for model SLB fabrication using BSST.

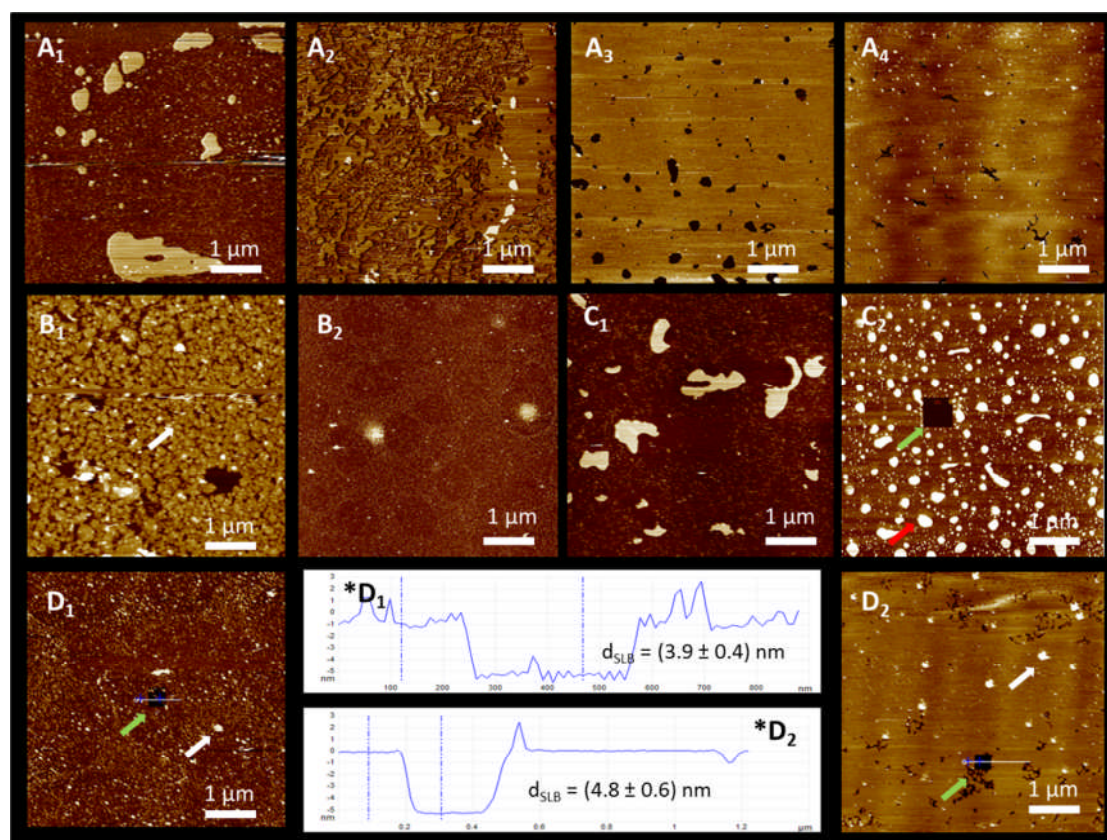


AFM images indicating BSST-fabricated DPPC (A) and DOPC (B) supported lipid films. A 60-minute incubation of mica-deposited 10 μg DPPC lipid in Millipore water at 45°C followed by 3 gentle PBS rinses results in a 4.5 nm-thick (*A₂), continuous SLBs with a small excess of SLB-attached lipid material (A₁₋₂). When 90-minute incubation or 100 μg DPPC are used, the BSST results in DPPC multilayer lipid films (A₃ or A₄, respectively). A 45-minute incubation of mica-deposited 10 μg DOPC in Millipore water at 35°C followed by 3 gentle PBS rinses results in a 4.0 nm-thick (*B₂), continuous SLBs with a small excess of SLB-attached lipid material (B₁₋₂). The white arrows indicate excessive lipid material on the SLB surface, while the green arrows indicate areas scratched with the AFM probe in order to confirm the presence of SLBs. AFM images were collected in liquid environments using MultiMode2 AFM setup, as described in chapter 2. Z-scale bars were removed for presentation purposes.

VDT resulted in a slow formation of lipid excess-attached SLBs for DOPC and lipid films of various morphologies for DPPC. Here, incubation temperature and time, ionic strength of the incubation buffer, liposome concentration and rinsing technique were identified as critical factors determining the morphologies of DPPC lipid films. The summaries of AFM-recorded morphologies for DPPC and DOPC-composed supported lipid films, when fabricated using VDT, were depicted in the appropriate figures below. Since model liposomes were expected to behave in a similar way to 1:1 DPPC:DOPC-composed liposomes, a 5-minute pre-incubation of freshly-cleaved mica with 10mM magnesium chloride and subsequent rinse with Millipore water plus 45-minute incubation of 0.5 mg/ml liposome suspension in Millipore water at 35°C were chosen as conditions of preference for model SLB fabrication using VDT.



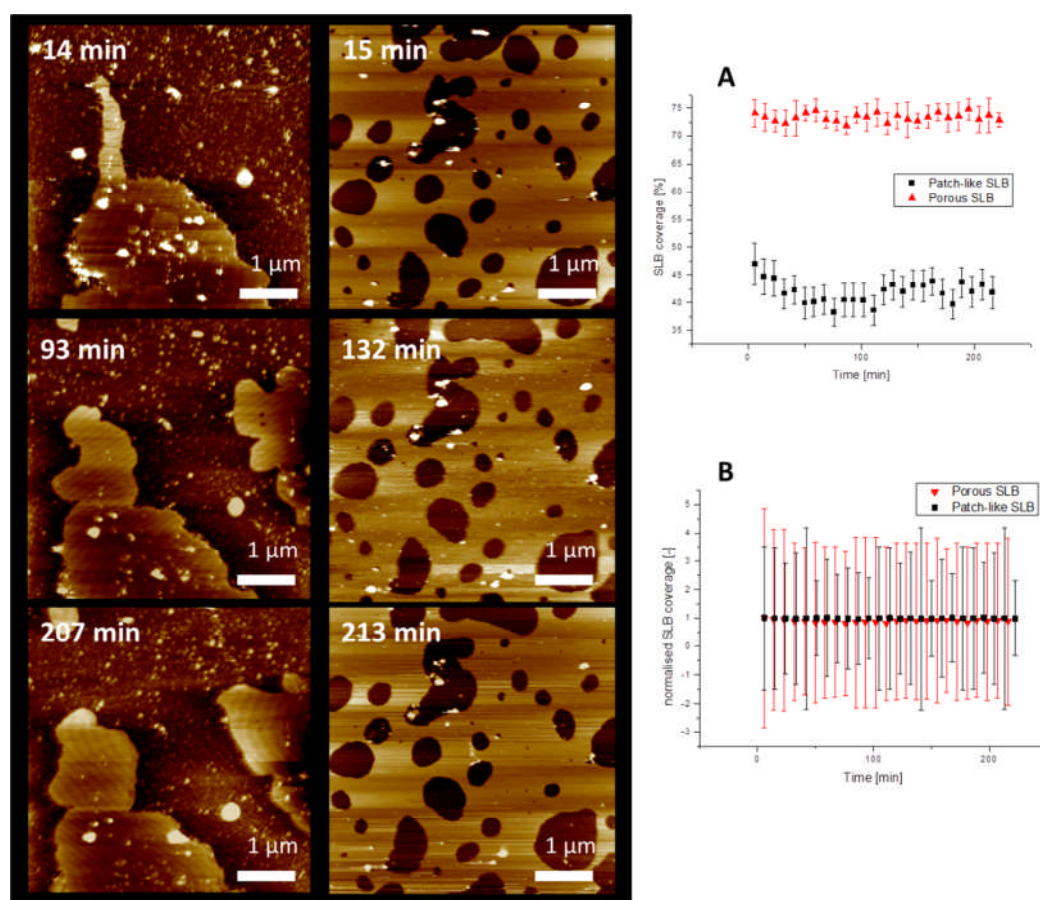
AFM images indicating morphologies of DPPC-composed supported lipid films prepared using vesicle deposition technique (VDT). A_1 , A_2 , A_3 and A_4 indicate lipid film morphologies after 2-hour incubation of 0.1, 0.2, 0.4 and 0.5 mg/ml DPPC liposomes in 10mM Tris at room temperature, followed by 2 gentle rinses with 0.2 μm Millipore water of room temperature, respectively. B_1 and B_2 indicate lipid film morphologies after 60-minute incubation of 0.5 mg/ml DPPC liposomes in 10 mM Tris at 45°C, followed by 2 gentle rinses with 0.2 μm Millipore water of room and 45°C temperature, respectively. C_1 and C_2 indicate lipid film morphologies after 60-minute incubation of 10mM magnesium chloride-pre-coated, freshly-cleaved mica surfaces with 0.5 mg/ml DPPC liposomes in 0.2 μm Millipore water at 45°C, followed by 2 vigorous and gentle rinses with 0.2 μm Millipore water of 45°C temperature, respectively. D_1 and D_2 indicate lipid film morphologies and associated cross section analyses (*) after 60-minute incubation of 10mM magnesium chloride-pre-coated, freshly-cleaved mica surfaces with 0.5 mg/ml DPPC liposomes in 0.2 μm 10mM Tris and Millipore water at 45°C, followed by 2 gentle rinses with 0.2 μm PBS of room temperature, respectively. The white arrows indicate excessive lipid material on the SLB surfaces, the green arrows indicate areas scratched with the AFM probe in order to confirm the presence of SLBs, while the red arrows indicate the presence of additional bilayers that are deposited above the mica-neighbouring DPPC bilayer. AFM images were collected in liquid environments using MultiMode2 AFM setup, as described in chapter 2. Z-scale bars were removed for presentation purposes.



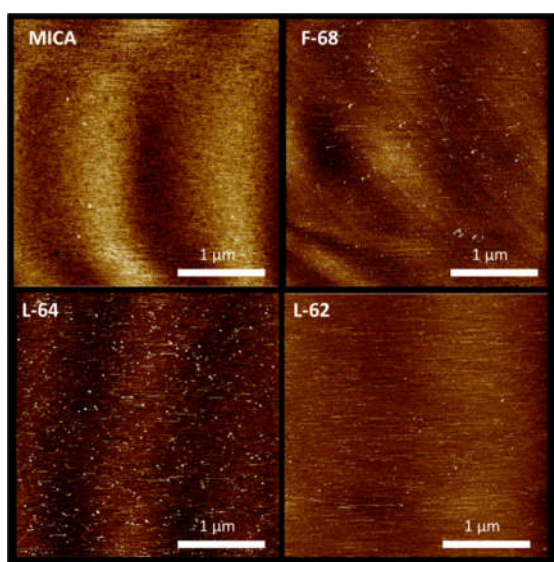
AFM images indicating morphologies of DOPC-composed supported lipid films prepared using vesicle deposition technique (VDT). A_1 , A_2 , A_3 and A_4 indicate lipid film morphologies after 2-hour incubation of 0.1, 0.3, 0.4 and 0.5 mg/ml DOPC liposomes in 10mM Tris at room temperature, followed by 2 gentle rinses with 0.2 μm Millipore water of room temperature, respectively. B_1 and B_2 indicate morphologies after 60-minute incubation of 0.5 mg/ml DOPC liposomes in 10 mM Tris at 35°C, followed by 2 gentle rinses with 0.2 μm Millipore water of room and 35°C temperature, respectively. C_1 and C_2 indicate lipid film morphologies after 60-minute incubation of 10mM magnesium chloride-pre-coated, freshly-cleaved mica surfaces with 0.5 mg/ml DOPC liposomes in 0.2 μm Millipore water at 35°C, followed by 2 vigorous and gentle rinses with 0.2 μm Millipore water of room temperature, respectively. D_1 and D_2 indicate lipid film morphologies and associated cross section analyses (*) after 60-minute incubation of 10mM magnesium chloride-pre-coated, freshly-cleaved mica surfaces with 0.5 mg/ml DOPC liposomes in 0.2 μm 10mM Tris and Millipore water at 35°C, followed by 2 gentle rinses with 0.2 μm PBS of room temperature, respectively. The white arrows indicate excessive lipid material on the SLB surfaces, the green arrows indicate areas scratched with the AFM probe in order to confirm the presence of SLBs, while the red arrows indicate the presence of additional bilayers that are deposited above the mica-neighbouring DOPC bilayer. AFM images were collected in liquid environments using MultiMode2 AFM setup, as described in chapter 2. Z-scale bars were removed for presentation purposes.

Summary of control experiments on model SLBs after injection of PBS into AFM cell.

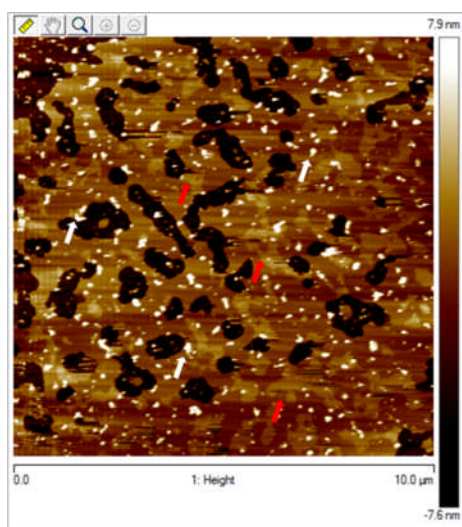
AFM studies on patch-like and porous, model SLBs were performed in order to establish the behaviour of lipid film of different qualities after injection of PBS solution into the imaging environment. The technique of PBS injection was similar to the one reported for Pluronics®, DNA and DNA polyplex solutions: 50 μl liquid were gently pipetted onto the sample and imaged. Subsequently, AFM images were recorded over time and SLB coverage was quantified in the same manner as described in chapter 2. As indicated in figure below, SLB coverage for porous lipid films is constant within 5 μm x 5 μm scan area monitored over 200 minutes in liquid environments using AFM in PeakForce® Tapping mode. The minor fluctuations on graph A (red) are most likely due to the drift associated with AFM imaging. The SLB coverage for patch-like films over time also remains statistically constant after 200 minutes imaging of 5 μm x 5 μm SLB areas (graph A, black). However, the fluctuations of coverage values are not as minor, most likely due to both image drift and secondary adsorption of the excessive lipid material from the liquid environment surrounding the patch-like bilayers on mica (compare images on the left hand side). This was likely, as the patch-like SLBs were produced *via* vigorous rinsing of porous films and the presence of excessive material in the surrounding environment was expected. Such noise is 'decreased' once the SLB coverage values are normalised (compare B and figures 4.6. and 4.7.). The control studies were not added on the graphs in figures 4.6., 4.7. or 5.5. for clarity purposes.



Summary of control experiments for model SLB-exciipient interaction studies.

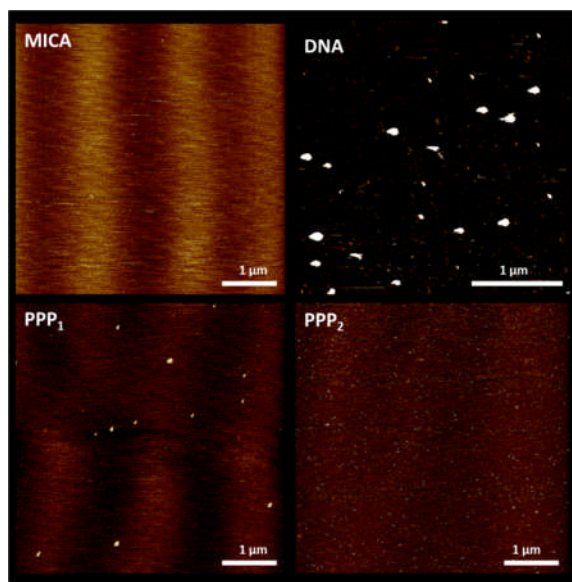


AFM images indicating morphologies of pure mica and Pluronic®: L-62, L-64 and F-68 after injection of 0.001 % (w/v) solutions in PBS into the AFM environment. Images are collected in liquid environments using MultiMode2 AFM setup in tapping mode as described in chapter 2. Z-scale bars were removed for presentation purposes.

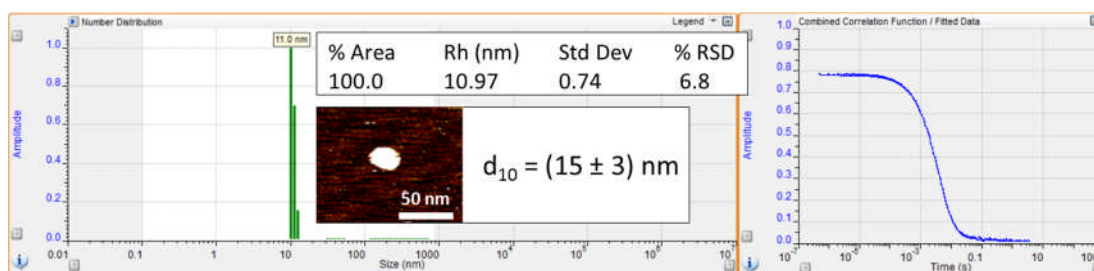


AFM image indicating the morphology of porous, model SLB before addition of 0.0001% (w/v) Pluronic® L-62 to the AFM environment. White and red arrows are added to indicate the presence of excessive lipid material and liquid-ordered domains, respectively. The image was recorded in liquid environment using MultiMode2 setup as explained in chapter 2.

Summary of control experiments for model SLB-nucleic acid formulation interaction studies.



AFM images indicating morphologies of the mica, DNA and polyphosphonium polymer (PPP). Presence of particles on pure mica surfaces was assessed each time before injection of liquid for particle imaging. After injection of 50 μg/ml DNA two particle populations were observed: (9±5) and (50±10) [nm] in size. After injection of 90 μg/ml (1) and 30 μg/ml (2) PPP solutions populations of (45±5) and (10±5) nm-sized particles were observed, respectively. The presence of particles of sizes larger than theoretically predicted the presence of particle self-aggregation at high concentrations of both DNA and polymer. AFM images were collected in liquid environments using PeakForce® Tapping mode.



The summary of 1:1 Polyphosphonium-DNA polyplex characterisation data. Dynamic light scattering (DLS) based on 25 measurements indicates a hydrodynamic radius of (11 ± 1) nm, whilst cross section analysis of AFM-imaged particles of diameters of (15±3) nm, based measurements of 10 particles. The inconsistencies in the DNA- and AFM-reported particle sizes are most likely due to the presence of polymer-bound and unbound DNA in the sample, as established through the collaboration with Vanessa Loczenski, based on gel retardation assays (data not shown). AFM images were collected in liquid environments using PeakForce® Tapping mode.

Appendix IV

Molecular Ion Assignments for ToF-SIMS Spectra of Single Lipids.

Attachment:

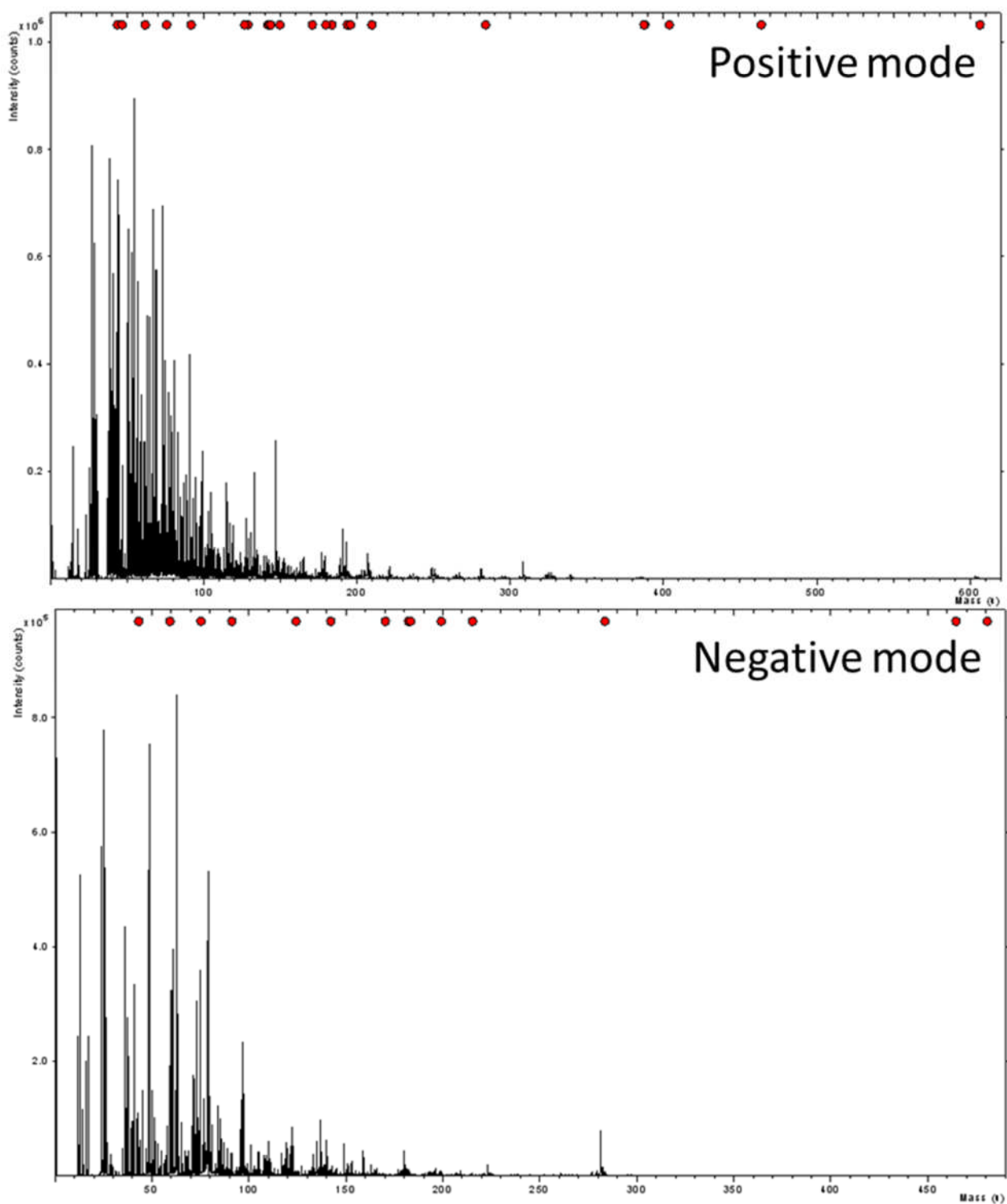
- The peaks and ions identified within the ToF-SIMS C₆₀ spectra of DOPE.....155
- ToF-SIMS C₆₀ spectra of DOPE in positive and negative modes.....156
- The peaks and ions identified within the ToF-SIMS C₆₀ spectra of EPC.....157
- ToF-SIMS C₆₀ spectra of EPC in positive and negative modes.....158
- The peaks and ions identified within the ToF-SIMS C₆₀ spectra of SPM.....159
- ToF-SIMS C₆₀ spectra of SPM in positive and negative modes.....160
- The peaks and ions identified within the ToF-SIMS C₆₀ spectra of CHOL.....161
- ToF-SIMS C₆₀ spectra of CHOL in positive and negative modes.....162
- The peaks and ions identified within the ToF-SIMS C₆₀ spectra of DOPS.....163
- ToF-SIMS C₆₀ spectra of DOPS in positive and negative modes.....164

Appendix III: Molecular Ion Assignments for ToF-SIMS Spectra of Single Lipids.

The peaks and ions identified within the ToF-SIMS C₆₀ spectra of DOPE.

Lipid	Molecular Mass [Da]	Molecular ion assignment	Molecular Mass [Da]	Molecular ion assignment
DOPE	41.0	C ₃ H ₅ ⁻	214.0	C ₅ H ₁₃ NO ₆ P ⁻
	57.0	C ₃ H ₅ O ⁻	281.2	C ₁₈ H ₃₃ O ₂ ⁻
	73.0	C ₃ H ₅ O ₂ ⁻	339.3	C ₂₂ H ₄₃ O ₂ ⁺
	89.1	C ₃ H ₅ O ₃ ⁻	433.2	C ₂₁ H ₃₈ O ₇ P ⁻
	124.0	C ₂ H ₇ NO ₃ P ⁺	434.2	C ₂₁ H ₃₉ O ₇ P ⁻
	139.1	C ₉ H ₁₅ O ⁺	462.3	C ₂₃ H ₄₅ NO ₆ P ⁻
	140.1	C ₉ H ₁₆ O ⁺	478.3	C ₂₃ H ₆₅ NO ₇ P ⁻
	167.0	C ₃ H ₅ O ₆ P ⁻	479.3	C ₂₃ H ₆₆ NO ₇ P ⁻
	168.9	C ₃ H ₆ O ₆ P ⁻	619.5	C ₃₉ H ₇₁ O ₅ ⁻
	181.1	C ₅ H ₁₂ NO ₄ P ⁻	620.5	C ₃₉ H ₇₂ O ₅ ⁻
	197.0	C ₅ H ₁₂ NO ₅ P ⁻	698.5	C ₃₉ H ₇₁ O ₅ P ⁻
	198.0	C ₅ H ₁₃ NO ₅ P ⁻	699.5	C ₃₉ H ₇₂ O ₅ P ⁻
	213.0	C ₅ H ₁₂ NO ₆ P ⁻		

Abbreviations: DOPE – dioleoylphosphatidyl ethanolamine



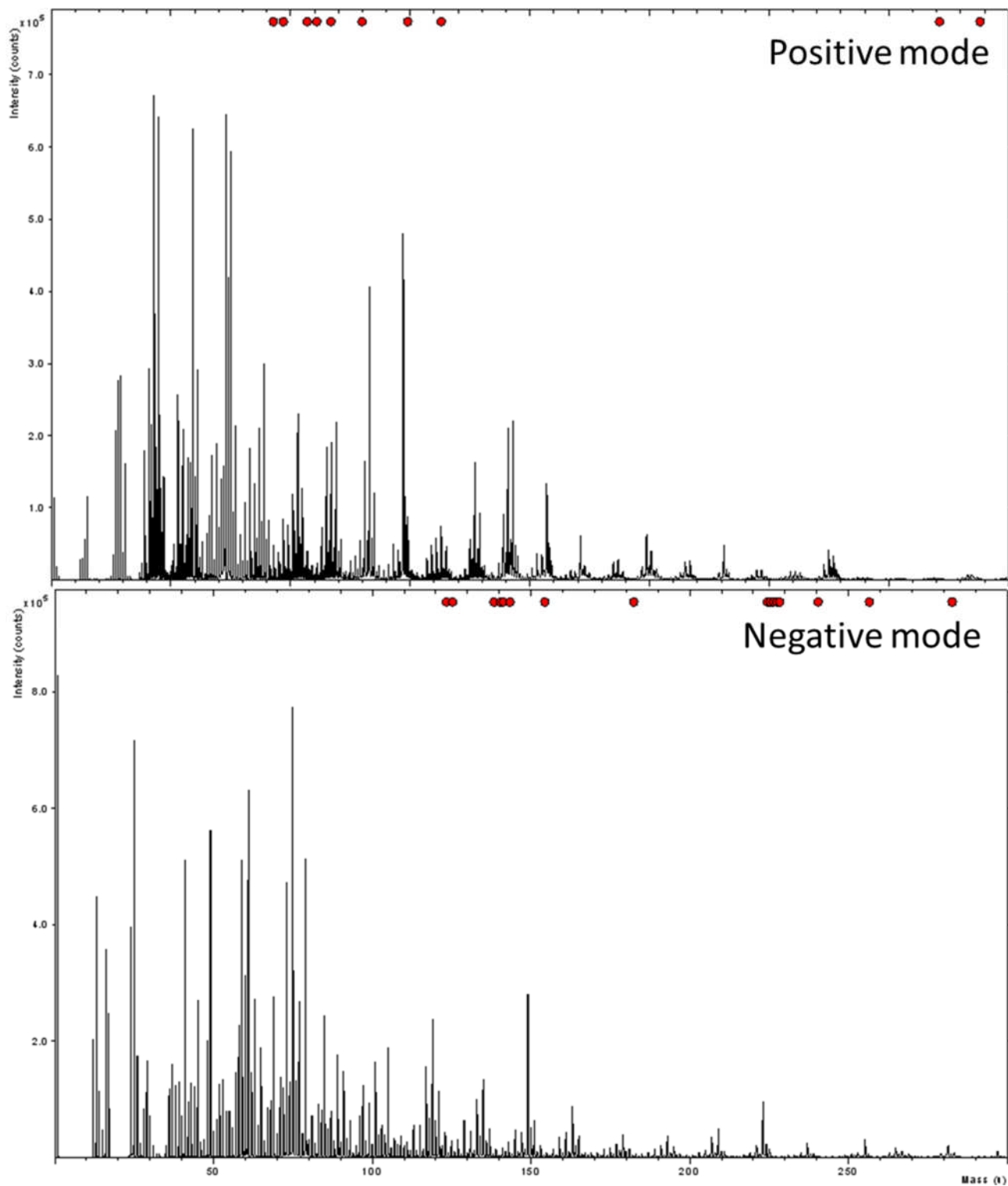
Appendix III: Molecular Ion Assignments for ToF-SIMS Spectra of Single Lipids.

The peaks and ions identified within the ToF-SIMS C_{60} spectra of EPC.

Lipid	Molecular Mass [Da]	Molecular ion assignment	Molecular Mass [Da]	Molecular ion assignment
EPC	193.0	$C_5H_{13}NO_4P^-$	253.2	$C_{16}H_{31}NO^-$
	223.1	$C_8H_{18}NO_4P^-$	255.1	$C_8H_{18}NO_6P^-$
	224.1	$C_{15}H_{14}NO^+$	256.2	$C_{15}H_{30}NO_2^-$
	225.0	$C_6H_{13}NO_6P^-$	383.3	$C_{23}H_{43}NO_4^+$
	226.1	$C_8H_{21}NO_4P^-$	394.2	$C_{17}H_{33}NO_7P^-$
	227.1	$C_8H_{22}NO_4P^-$	397.2	$C_{17}H_{36}NO_7P^-$
	228.0	$C_6H_{15}NO_6P^-$	480.4	$C_{33}H_{52}NO_2^+$
	239.1	$C_8H_{18}NO_5P^-$	759.6	$C_{42}H_{82}NO_8P^-$

Abbreviations: EPC – egg phosphatidyl choline

Appendix III: Molecular Ion Assignments for ToF-SIMS Spectra of Single Lipids.



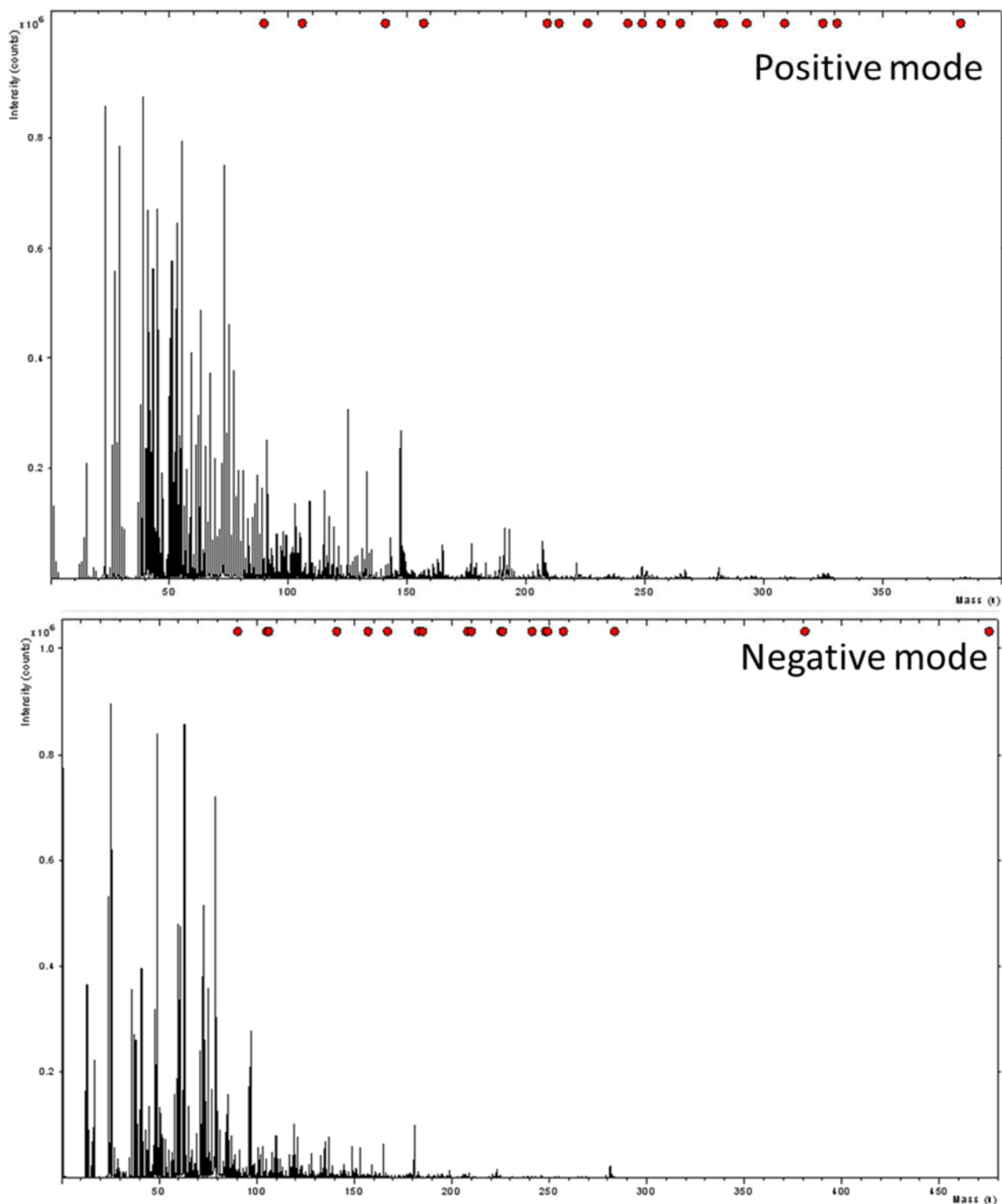
Appendix III: Molecular Ion Assignments for ToF-SIMS Spectra of Single Lipids.

The peaks and ions identified within the ToF-SIMS C₆₀ spectra of SPM.

Lipid	Molecular Mass [Da]	Molecular ion assignment	Molecular Mass [Da]	Molecular ion assignment
SPM	104.1	C ₅ H ₁₄ NO ⁺	254.0	C ₁₆ H ₃₂ NO ⁻
	167.9	C ₁₀ H ₁₈ NO ⁺	375.3	C ₁₈ H ₃₁ O ₈ ⁺
	168.0	C ₉ H ₁₂ O ₃ ⁻	404.2	C ₂₀ H ₃₉ NO ₅ P ⁻
	185.1	C ₉ H ₁₄ NO ₃ ⁺	413.3	C ₂₆ H ₃₇ O ₄ ⁺
	186.1	C ₅ H ₁₇ NO ₄ P ⁺	598.3	C ₃₄ H ₆₅ NO ₅ P ⁻
	198.1	C ₃ H ₄ O ₇ Na ⁺	600.5	C ₃₄ H ₆₇ NO ₅ P ⁻
	224.1	C ₈ H ₁₇ PO ₅ ⁺	616.5	C ₃₄ H ₆₇ NO ₆ P ⁻
	225.1	C ₈ H ₁₈ PO ₅ ⁺	642.4	C ₃₆ H ₆₅ NO ₆ P ⁻

Abbreviations: SPM – sphingomyelin

Appendix III: Molecular Ion Assignments for ToF-SIMS Spectra of Single Lipids.



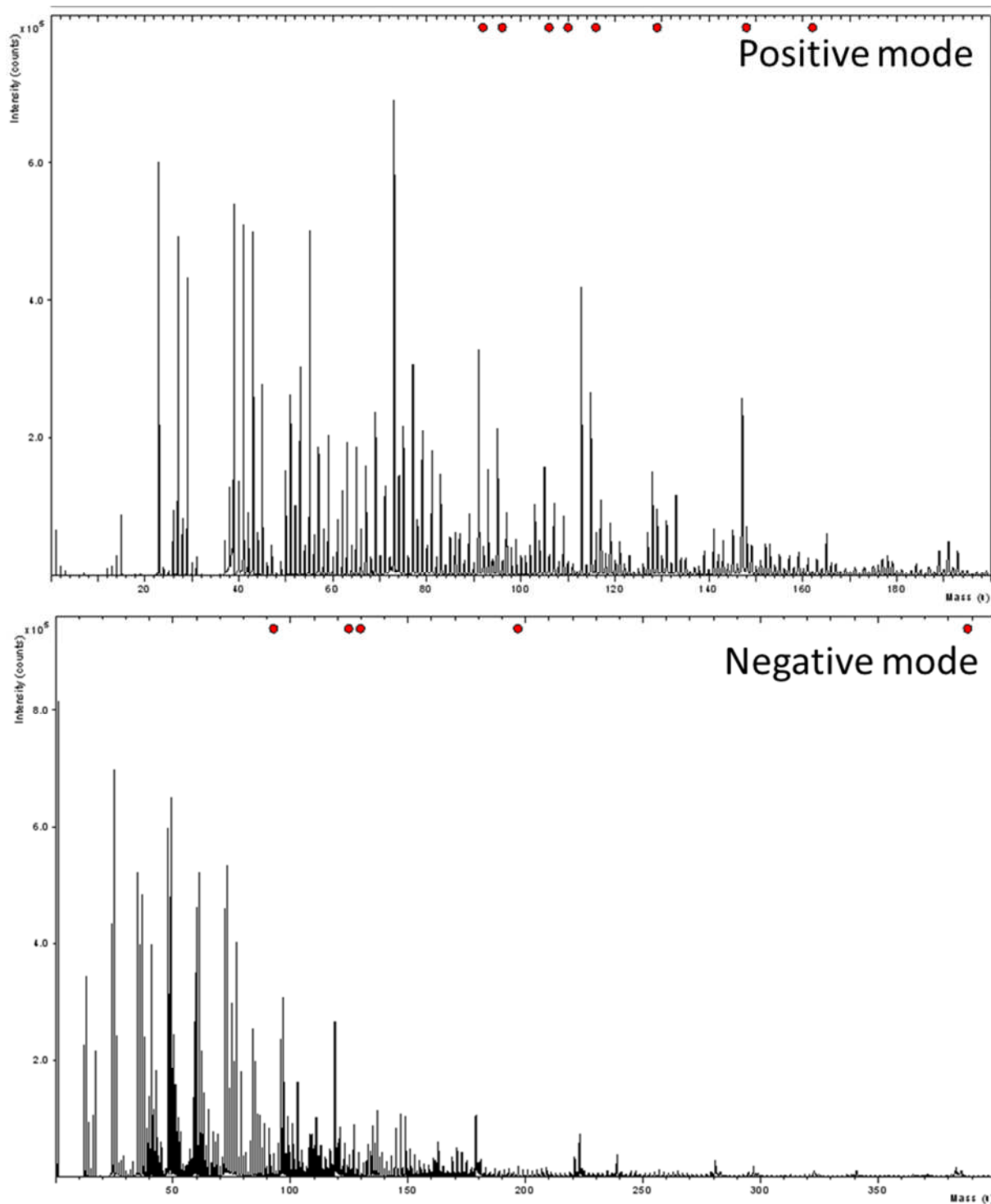
Appendix III: Molecular Ion Assignments for ToF-SIMS Spectra of Single Lipids.

The peaks and ions identified within the ToF-SIMS C_{60} spectra of CHOL.

Lipid	Molecular Mass [Da]	Molecular ion assignment	Molecular Mass [Da]	Molecular ion assignment
CHOL	145.1	$C_{11}H_{13}^+$	185.1	$C_{13}H_{13}O^+$
	146.1	$C_{11}H_{14}^+$	275.3	$C_{20}H_{35}^+$
	147.1	$C_{10}H_{11}O^+$	290.0	$C_{24}H_2^+$
	150.1	$C_{10}H_{14}O^+$	367.4	$C_{27}H_{43}^+$
	159.1	$C_{12}H_{15}^+$	369.4	$C_{27}H_{45}O^+$
	160.1	$C_{12}H_{16}^+$	384.3	$C_{27}H_{44}O^-$
	161.2	$C_{12}H_{17}^+$	385.4	$C_{27}H_{45}O^+$
	166.1	$C_{24}H_2^+$	386.3	$C_{27}H_{46}O^+$
	182.1	$C_{13}H_{10}O^+$		

Abbreviations: CHOL – cholesterol

Appendix III: Molecular Ion Assignments for ToF-SIMS Spectra of Single Lipids.



Appendix III: Molecular Ion Assignments for ToF-SIMS Spectra of Single Lipids.

The peaks and ions identified within the ToF-SIMS C_{60} spectra of DOPS.

Lipid	Molecular Mass [Da]	Molecular ion assignment	Molecular Mass [Da]	Molecular ion assignment
DOPS	89.0	$C_3H_7NO_2^-$	255.1	$C_{16}H_{18}O_3^+$
	105.0	$C_3H_7NO_3^-$	269.8	$C_{21}H_{18}^+$
	125.1	$C_8H_{15}N^+$	281.2	$C_{18}H_{33}O_2^-$
	167.1	$C_9H_{11}O_3^+$	288.8	$C_{19}H_{13}O_3^+$
	206.0	$C_3H_6NO_6PNa^-$	319.1	$C_{15}H_{20}O_6Na^+$
	224.2	$C_{14}H_{24}O_2^+$	343.1	$C_{16}H_{24}O_6P^+$
	240.0	$C_6H_{11}NO_7P^-$	379.3	$C_{26}H_{35}O_2^+$
	246.0	$C_6H_{10}NO_6PNa^-$	521.3	$C_{24}H_{44}O_9P^-$
			619.5	$C_{39}H_{71}O_5^-$

Abbreviations: DOPS – dioleoylphosphatidyl serine

Appendix III: Molecular Ion Assignments for ToF-SIMS Spectra of Single Lipids.

